SCIENCE

U.S.
DEPOSITORY

JOURNAL OF RESEARCH

OF THE U.S. GEOLOGICAL SURVEY

MARCH–APRIL 1976
VOLUME 4, NUMBER 2

UICC LIBRARY
APR 15 1976
DOCUMENTS

Scientific notes and summaries of investigations in geology, hydrology, and related fields

U.S. DEPARTMENT OF THE INTERIOR

UNITED STATES DEPARTMENT OF THE INTERIOR
THOMAS S. KLEPPE, Secretary
GEOLOGICAL SURVEY
V. E. McKelvey, Director

For sale by the Superintendent of Documents, U.S. Government Printing Office, Washington, DC 20402. Annual subscription rate $18.90 (plus $4.75 for foreign mailing). Single copy $3.15. Make checks or money orders payable to the Superintendent of Documents.

Send all subscription inquiries and address changes to the Superintendent of Documents at the above address.

Purchase orders should not be sent to the U.S. Geological Survey library.

Library of Congress Catalog-card No. 72-600241.

The Journal of Research is published every 2 months by the U.S. Geological Survey. It contains papers by members of the Geological Survey and their professional colleagues on geologic, hydrologic, topographic, and other scientific and technical subjects.

Correspondence and inquiries concerning th Journal (other than subscription inquiries ar address changes) should be directed to Anna M Orellana, Managing Editor, Journal of Researc Publications Division, U.S. Geological Surve National Center 321, Reston, VA 22092.

Papers for the Journal should be submitte through regular Division publication channels.

The Secretary of the Interior has determined that the publication of this periodical is necessary in the transaction of the public business required by law of this Department. Use of funds for printing this periodical has been approved by the Director of the Office of Management and Budget through June 30, 1980.

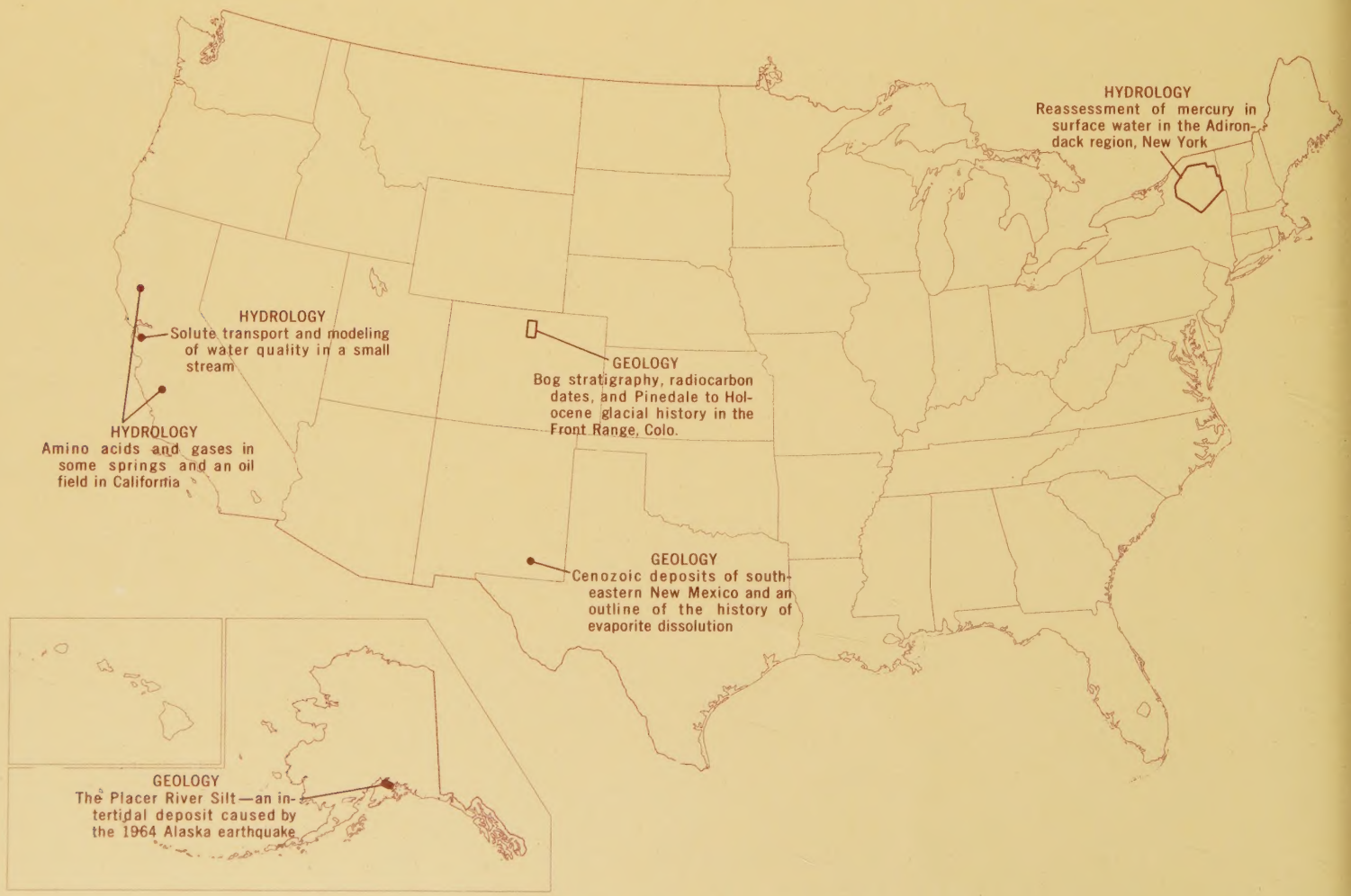
HYDROLOGY
Reassessment of mercury in surface water in the Adirondack region, New York
HYDROLOGY
Solute transport and modeling of water quality in a small stream
HYDROLOGY
Amino acids and gases in some springs and an oil field in California
GEOLOGY
Bog stratigraphy, radiocarbon dates, and Pinedale to Holocene glacial history in the Front Range, Colo.
GEOLOGY
Cenozoic deposits of southeastern New Mexico and an outline of the history of evaporite dissolution
GEOLOGY
The Placer River Silt—an intertidal deposit caused by the 1964 Alaska earthquake

GEOGRAPHIC INDEX TO ARTICLES

See "Contents" for articles concerning areas outside the United States and articles without geographic orientation.

JOURNAL OF RESEARCH

of the

U.S. Geological Survey

Vol. 4 No. 2 Mar.–Apr. 1976

CONTENTS

Abbreviations II
Metric-English equivalents II

GEOLOGIC STUDIES

Geology of central Costa Rica and its implications in the geologic history of the region ..... *R. D. Krushensky, Enrique Malavassi V., and Rolando Castillo M.* 127
Cenozoic deposits of southeastern New Mexico and an outline of the history of evaporite dissolution ..... *G. O. Bachman* 135
The Placer River Silt—an intertidal deposit caused by the 1964 Alaska earthquake ..... *A. T. Ovenshine, D. E. Lawson, and S. R. Bartsch* 151
Bog stratigraphy, radiocarbon dates, and Pinedale to Holocene glacial history in the Front Range, Colo ..... *R. F. Madole* 163
Geology of the massifs at the Apollo 17 landing site ..... *E. W. Wolfe and V. S. Reed* 171
Rise of a variable-viscosity fluid in a steadily spreading wedge-shaped conduit with accreting walls ..... *A. H. Lachenbruch and Manuel Nathenson* 181
The volumetric properties of H_2O—a graphical portrayal ..... *J. R. Fisher* 189
The heat capacities at low temperatures and entropies at 298.15 K of low albite, analbite, microcline, and high sanidine ..... *R. E. Openshaw, B. S. Hemingway, R. A. Robie, D. R. Waldbaum, and K. M. Krupka* 195
Definition X-ray powder data for covellite, anilite, djurleite, and chalcocite ..... *R. W. Potter and H. T. Evans, Jr.* 205
A review of the minerals of the alunite-jarosite, beudantite, and plumbogummite groups ..... *Theodore Botinelly* 213
Flameless atomic absorption determination of bismuth in soils and rocks ..... *W. H. Ficklin and F. N. Ward* 217

HYDROLOGIC STUDIES

Interstation correlation of peak-flow estimates ..... *C. H. Hardison* 221
Reassessment of mercury in surface water in the Adirondack region, New York ..... *William Buller* 223
Amino acids and gases in some springs and an oil field in California ..... *J. B. Rapp* 227
Solute transport and modeling of water quality in a small stream ..... *S. M. Zand, V. C. Kennedy, G. W. Zellweger, and R. J. Avanzino* 233
The measurement of adenosine triphosphate in pure algal cultures and natural aquatic samples ..... *W. T. Shoaf and B. W. Lium* 241
Determination, storage, and preservation of low molecular weight hydrocarbon gases in aqueous solution ..... *D. J. Shultz, J. F. Pankow, D. Y. Tai, D. W. Stephens, and R. E. Rathbun* 247

Recent publications of the U.S. Geological Survey ..... Inside of back cover

ABBREVIATIONS

A ---------ampere
A ---------angstrom
ADP ------ammonium dihydrogen phosphate
atm -------atmosphere
avg -------average
B.P. ------before present
b.y. -------billion years
calc -------calculated
dc ---------direct current (d-c as unit modifier)
deg -------degree
diam. ------diameter
eq ---------equation
EROS ----Earth Resources Observation System
g-mol -----gram-mole
ID ---------inside diameter
J ----------joule
K ----------kelvin
kPa --------kilopascal
kV ---------kilovolt
lm ----------lumen
M ---------molarity; molar (concentration)
meq ------milliequivalent
MIBK ----methyl isobutyl ketone
min -------minute
ml ---------millilitre
mol -------mole
m.y. ------million years
μg ---------microgram
μl ----------microlitre
μm -------micrometre
N ----------normality
nm -------nanometre
OD -------outside diameter
ppb -------part per billion
ppm ------part per million
quad. -----quadrangle
RAP ------rubidium acid phthalate
wt ---------weight
w/v ------weight per volume
yr ---------year

METRIC-ENGLISH EQUIVALENTS

Metric unit		English equivalent	
Length			
millimetre (mm)	=	0.03937	inch (in)
metre (m)	=	3.28	feet (ft)
kilometre (km)	=	.62	mile (mi)
Area			
square metre (m^2)	=	10.76	square feet (ft^2)
square kilometre (km^2)	=	.386	square mile (mi^2)
hectare (ha)	=	2.47	acres
Volume			
cubic centimetre (cm^3)	=	0.061	cubic inch (in^3)
litre (l)	=	61.03	cubic inches
cubic metre (m^3)	=	35.31	cubic feet (ft^3)
cubic metre	=	.00081	acre-foot (acre-ft)
cubic hectometre (hm^3)	=	810.7	acre-feet
litre	=	2.113	pints (pt)
litre	=	1.06	quarts (qt)
litre	=	.26	gallon (gal)
cubic metre	=	.00026	million gallons (Mgal or 10^6 gal)
cubic metre	=	6.290	barrels (bbl) (1 bbl=42 gal)
Weight			
gram (g)	=	0.035	ounce, avoirdupois (oz avdp)
gram	=	.0022	pound, avoirdupois (lb avdp)
tonne (t)	=	1.1	tons, short (2,000 lb)
tonne	=	.98	ton, long (2,240 lb)
Specific combinations			
kilogram per square centimetre (kg/cm^2)	=	0.96	atmosphere (atm)
kilogram per square centimetre	=	.98	bar (0.9869 atm)
cubic metre per second (m^3/s)	=	35.3	cubic feet per second (ft^3/s)

Metric unit		English equivalent	
Specific combinations—Continued			
litre per second (l/s)	=	.0353	cubic foot per second
cubic metre per second per square kilometre [$(m^3/s)/km^2$]	=	91.47	cubic feet per second per square mile [$(ft^3/s)/mi^2$]
metre per day (m/d)	=	3.28	feet per day (hydraulic conductivity) (ft/d)
metre per kilometre (m/km)	=	5.28	feet per mile (ft/mi)
kilometre per hour (km/h)	=	.9113	foot per second (ft/s)
metre per second (m/s)	=	3.28	feet per second
metre squared per day (m^2/d)	=	10.764	feet squared per day (ft^2/d) (transmissivity)
cubic metre per second (m^3/s)	=	22.826	million gallons per day (Mgal/d)
cubic metre per minute (m^3/min)	=	264.2	gallons per minute (gal/min)
litre per second (l/s)	=	15.85	gallons per minute
litre per second per metre [(l/s)/m]	=	4.83	gallons per minute per foot [(gal/min)/ft]
kilometre per hour (km/h)	=	.62	mile per hour (mi/h)
metre per second (m/s)	=	2.237	miles per hour
gram per cubic centimetre (g/cm^3)	=	62.43	pounds per cubic foot (lb/ft^3)
gram per square centimetre (g/cm^2)	=	2.048	pounds per square foot (lb/ft^2)
gram per square centimetre	=	.0142	pound per square inch (lb/in^2)
Temperature			
degree Celsius (°C)	=	1.8	degrees Fahrenheit (°F)
degrees Celsius (temperature)	=	[(1.8 × °C) + 32]	degrees Fahrenheit

Any use of trade names and trademarks in this publication is for descriptive purposes only and does not constitute endorsement by the U.S Geological Survey.

Jour. Research U.S. Geol. Survey
Vol. 4, No. 2, Mar.–Apr. 1976, p. 127–134

GEOLOGY OF CENTRAL COSTA RICA AND ITS IMPLICATIONS IN THE GEOLOGIC HISTORY OF THE REGION

By RICHARD D. KRUSHENSKY; ENRIQUE MALAVASSI V.,[1] and ROLANDO CASTILLO M.,[1] Reston, Va.; San José, Costa Rica

Prepared in cooperation with the Dirección de Geología, Minas, y Petróleo, Ministerio de Economía, Industria, y Comercio of Costa Rica

Abstract.—The oldest rocks in Costa Rica, the Nicoya Complex, crop out in an arcuate belt along the Pacific coast and outside the mapped area. The complex is an ophiolite assemblage and indicates that a Late Cretaceous arc-trench system, probably a southerly extension of the Middle America Trench, lay along and west of the present Pacific coast. Polarity of the system is indicated by the presence of a volcanic olivine basalt arc east of the ophiolite belt and by a younger magmatic arc farther east. Relative lack of metamorphism of the ophiolite assemblage suggests that the rocks were obducted rather than subducted. Fossil evidence indicates that the complex was emplaced no later than the late Campanian. By the late Eocene both the ophiolite assemblage and the olivine basalt arc had been established as major sediment sources for basins that lay to the east, and they continued as such through the Oligocene and possibly into the middle Miocene. Widespread deposition of trachyandesite lava and volcaniclastic sediments, local marine planation, uplift, and renewed volcanism mark what is presumed to be the end of the Miocene. Extreme south-to-north coarsening of the unconformably superposed Doán Formation and the presence of corals in the shaly facies of the Doán in the southern part of the mapped areas suggest that marine sedimentation there was undisturbed by orogeny and that intrusion of the Talamancan magmatic rocks must have followed deposition of the Doán. Volcaniclastic block breccia, characteristic of northern exposures of the Doán, indicates that volcanism in the proto-Cordillera Central had begun by at least Doán time. Volcanism has been a dominant process in central Costa Rica since that time.

The reconnaissance geologic map of central Costa Rica (fig. 1) includes four 15-minute quadrangles and major parts of three others, covering an area of about 3,150 km². The major part of the Cordillera Central; the capital, San José; and the principal towns of Cartago, Heredia, and Alajuela are in this area (fig. 2).

[1] Dirección de Geología, Minas, y Petróleo, Ministerio de Economía, Industria, y Comercio.

The correlations and geologic history outlined here are highly tentative as the country has been little studied geologically. Outstanding reports are those by Williams (1952) in the Meseta Central Occidental (western central valley), by Weyl (1957, 1961) in the Cordillera de Talamanca in south-central Costa Rica, and by Dengo (1961, 1962a, b) in western and west-central Costa Rica. Henningsen (1966) studied the sequence exposed along the Pan-American Highway in southern Costa Rica, and Krushensky (1972) and Castillo M. and Krushensky (unpub. data, 1975) studied the geology of the Istarú and Abra quadrangles in central Costa Rica.

Description of map units

(See fig. 3 for location of places mentioned.)

Central and western areas:

Qm Mudflow deposits of 1963–65 (Holocene): Unsorted and nonbedded material ranging from silt to boulders.

Qac Stream and lake deposits, minor colluvium (Holocene and Pleistocene):

All locally derived; thickness as much as 60 m.

Stream deposits: Bedded and sorted silt, sand, gravel, and nonsorted mudflow deposits.

Lake deposits: Southeast of Cerros de la Carpintera, Istarú quad. fine sand and clay; between Troya, Tapantí quad., and Finca Ajenjal, Istarú quad., bedded coarse sand and gravel.

Colluvial deposits: Southeast Carrillo and northeast Istarú quads., talus, ash, and minor alluvium.

Qtl Ash-flow tuff sheets and lava flows of the Central Valley (Pleistocene):

Four single ash-flow tuff cooling units, three lava flows, minor alluvium, and ash-fall tuff, all undivided on the map; all volcanic deposits from Volcán Barba, Barba quad.; thickness as much as 350 m.

Single ash-flow-tuff cooling unit: Crops out from its source at the summit of Volcán Barba, Barba

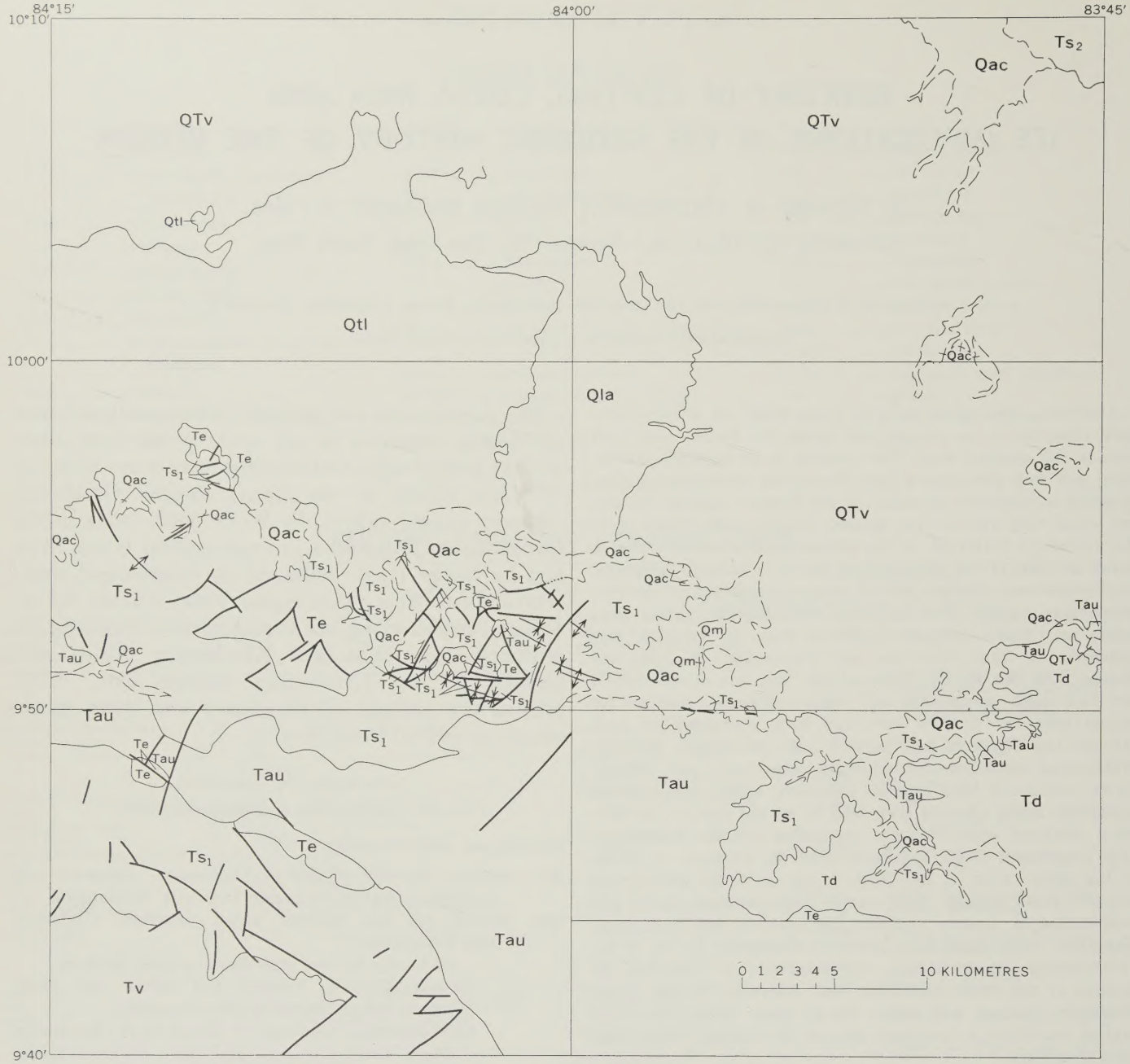

FIGURE 1.—Reconnaissance geologic map of central Costa Rica.

Description of map units—Continued

Central and western areas—Continued

quad., to San Felipe, Abra quad., light-yellow-brown, massive, very fine grained devitrified nonwelded ash-flow tuff; locally abundant lithic clasts of dense to vesicular andesite from the underlying lava flows, common to abundant essential pumice fragments.

Andesitic lava flow: Crops out from Huacalillo and Angeles, Barba quad., to Ojo de Agua, Abra quad., dark gray to dark reddish brown, vesicular to dense, containing abundant plagioclase and some augite phenocrysts.

Description of map units—Continued

Central and western areas—Continued

Single ash-flow-tuff cooling unit: Crops out from San Miguel Norte to Hacienda Caja, Abra quad., upper vapor-phase zone of light-yellow-brown, devitrified, nonwelded to partly welded ash-flow tuff, common light-brown essential pumice fragments, abundant accidental lithic clasts of densely welded light-gray ash-flow tuff and dark-grayish-brown vesicular andesite; lower devitrified to glassy zone of light-brown to light-bluish-gray densely welded ash-flow tuff, abundant lithic clasts, and partly to completely collapsed essen-

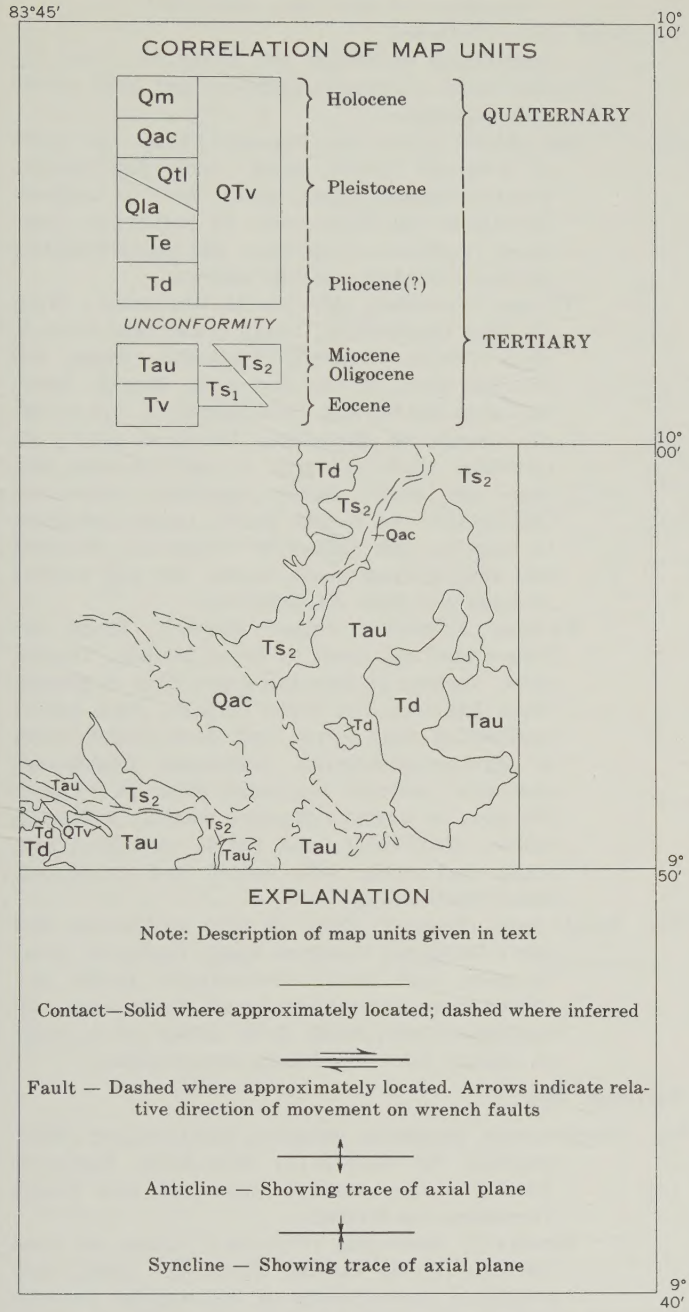

Description of map units—Continued

Central and western areas—Continued

tial pumice fragments, compaction foliation well developed.

Andesitic lava flow: Crops out from San Miguel Norte to Vuelta Virilla on Río Tues and Río Virilla, Abra quad., medium-grayish-brown clinkery top, dense middle, and dense but platy base, sparse to rare plagioclase phenocrysts.

Andesitic lava flow: Crops out south of the junction of Río Tues and Quebrada Tierra Blanca, Abra quad., dark-reddish-brown to dark-gray scoriaceous, containing abundant plagioclase, some augite phenocrysts, and some iddingsite after olivine.

Description of map units—Continued

Central and western areas—Continued

Single ash-flow tuff cooling unit: Crops out from Curridabat to Puente Mulas, Abra quad., upper vapor phase zone of nonwelded to partly welded light- to medium-gray devitrified ash-flow tuff containing abundant light-green to yellowish-brown essential pumice fragments, sparse accidental lithic clasts, and sparse plagioclase and augite phenocrysts; lower partly devitrified zone of bluish-gray densely welded ash-flow tuff containing partly to completely collapsed essential pumice fragments, locally lithophysal, containing sparse to common plagioclase and augite phenocrysts.

Single ash-flow tuff cooling unit: Crops out from Potrerillos to western edge of the mapped area, Abra quad., upper zone of light-gray glassy partly welded ash-flow tuff containing sparse to common plagioclase and augite phenocrysts; lower dark-gray to black glassy zone of densely welded ash-flow tuff containing abundant plagioclase and some augite phenocrysts, compaction foliation well developed in upper part of the densely welded zone, pumice locally lithophysal throughout zone.

Mudflow, alluvium, and ash: Unconsolidated nonsorted mudflow deposits, bedded coarse gravel and sand, minor bedded ash.

Qla Lahar, alluvium, and ash (Pleistocene): Unconsolidated nonsorted lahar deposits, bedded coarse gravel and sand, minor bedded ash; lahar and ash deposits commonly saprolitized.

QTv Lava mudflow, tuff, and ash deposits of Barba, Irazú, and Turrialba volcanic centers (Holocene to Pliocene?): Not divided on the map. Thickness exceeds 3,000 m.

Deposits of Barba volcanic center: Crop out in eastern Barba, northern Abra, and western Carrillo quads., interbedded dark-grayish-brown olivine-augite andesite and olivine basalt lava flows, light-gray welded to nonwelded andesitic ash-flow tuff, and predominant mudflow deposits; mudflow deposits are deeply weathered and consist of andesite and basalt clasts in a clay matrix; some fine- to coarse-grained light-brown and dark-grayish-brown ash-fall tuff.

Deposits of Irazú volcanic center: Crop out in central and northern Istarú and central Carrillo quads., interbedded thick mudflow deposits of light-gray-brown andesite clasts in a clay-silt matrix; augite andesite lava flows containing abundant to sparse plagioclase and augite phenocrysts, sparse to rare bronzite, rare olivine, hypersthene, and biotite; some ash-fall tuff and and ash.

Deposits of Turrialba volcanic center: Crop out in eastern Carrillo and in western Tucurrique quads., interbedded mudflow, lava flows, ash-fall tuff, and ash as in the Irazú center and on breached northeast flank of Volcán Turrialba; younger light-reddish-brown froth flow in crater wall at summit of Volcán Turrialba; youngest ejecta are trachyandesite bombs plastered on walls of southernmost crater of the volcano.

Description of map units—Continued

Central and western areas—Continued

Te Intrusive rocks near Escazú (Pliocene?): Crop out from Aserrí to Cerro Bandera, near Patarrá, and near Cerro Palomas, Abra quad.; Meseta to Bajos la Zorra, Loma Ococa to La Cruz, Caraigres quad.; and Finca Belén to Alto Tres Picos, Tapantí quad.; quartz diorite, granodiorite, gabbrodiorite, and locally syenite; chiefly hornblende bearing. All apparently belong to the Talamanca comagmatic series.

Td Doán Formation (Pliocene?): Crops out from Pilón de Azúcar, Tucurrique quad., to Cerro Cruces, Istarú quad., and between Río Villegas and Finca Belén, Tapantí quad.; consists of coarse clastic and fine clastic facies. Thickness in excess of 800 m.

Coarse clastic facies: Crops out from Pilón de Azúcar, Tucurrique quad., to Peñas Blancas–Cerro Doán, Tapantí quad., thick- to thin-bedded poorly sorted densely cemented dark-gray boulder and block volcaniclastic conglomerate breccia; subrounded to angular, dense to vesicular andesite and basalt clasts as much as 3 m across in a coarse sandstone matrix or breccia matrix of the same composition; forms prominent cliffs.

Fine clastic facies: Crops out at Tausito, predominant at Río Villegas, Tapantí quad., interbedded fine-grained volcaniclastic-epiclastic thin-bedded dark-gray-blue fissile shale, mudstone, and siltstone, some fine-grained conglomerate; rare corals.

Tau Aguacate Formation, undivided (Pliocene? to Upper Miocene?): Ash-flow and ash-fall tuff interbedded with mudflow deposits and lava flows, undivided on map. Thickness more than 900 m.

Ash-flow and ash-fall tuff: Crops out from Patio de Agua, Caraigres quad., to San Isidro, Tapantí quad.; not divided on map, fine-grained light-gray partly welded ash-flow tuff, compaction foliation well developed, abundant dark-grayish-green and dark-gray accidental lithic clasts, common light-gray essential pumice fragments; forms prominent cliffs; generally deeply saprolitized. Thickness in excess of 500 m.

Ash-fall tuff, mudflow deposits, and basalt lava flows: Crop out from Cerro Jucosal–Estrella, Tapantí quad., to Corralillo–San Pablo, Caraigres quad., to Tabarcia, Abra quad.; fine-grained thin- to thick-bedded pale-brown, light-greenish-gray, and dark-reddish-brown ash-fall tuff; mudflow deposits and some basalt flows; dark-gray glassy densely welded ash-flow tuff in the Río Conejo area, Caraigres quad., not divided on map, correlated with lowest welded ash-flow tuff beneath the Irazú sequence.

Southwest area:

Ts_1 Sandstone, limestone, siltstone, shale, and conglomerate includes the Coris Formation, San Miguel Limestone, Térraba Formation, and Pacacua Formation, not divided on the map. Thickness exceeds 3,000 m.

Coris Formation (Miocene): Crops out from Cerros de la Carpintera, Istarú and Abra quads., to Altos Tablazo, Caraigres quad., to San Miguel–San Rafael Abajo, Abra quad.: yellow to red argillaceous sandstone and mudstone; local friable white quartzose sandstone and hard purple orthoquartzite.

San Miguel Limestone (Miocene): Crops out south of Bermejo, Istarú quad., near San Miguel, Patarrá–Guatuso, Abra quad., fine- to medium-crystalline light-bluish-gray to pale-brown limestone; argillaceous partings and rippled-bedding surfaces abundant; pectens common.

Térraba Formation (Miocene to Oligocene): Crops out from Quebradillas, Istarú quad., near Patarrá, Altos Tablazo, Tarbaca, Alajuelita, Mesón, the southern flank of the Cerros de Escazú, Abra–Caraigres quads., and from Montes de Oro to the Río Grande de Candelaria, Caraigres quad.; interbedded black and gray to medium-green siltstone and shale, densely cemented, calcareous, thin-bedded, and locally fissile; locally mudstone to siltstone and tuffaceous sandstone; weathers pale gray, grayish green, brown, red, and yellow; contains abundant Foraminifera.

Pacacua Formation (upper Eocene): Crops out from Cachí and Orosi to Barro Morado, Tapantí quad., Verbena to Belo Horizonte, west of Escazú, Cerro Palomas, and Cerro Pacacua, Abra quad.; interbedded dark-purple and dark-reddish-brown to dark-greenish-brown tuffaceous breccia-conglomerate; andesite and basalt clasts in a clayey pale-gray to purple tuffaceous matrix; tuffaceous yellow, gray, green, and purple sandstone, siltstone, and shale, well bedded and calcareous, rarely fossiliferous.

Tv Basalt flows (Eocene): Crop out south of Tiguires and Cerro Caraigres, Caraigres quad., dark-gray, grayish-green, and green olivine-augite basalt and olivine-augite-hypersthene basalt flows; local volcaniclastic beds; basalt flows locally cut by veins of opaline silica and locally serpentinized.

Northeast area:

Ts_2 Conglomerate, sandstone, limestone, siltstone, and shale: Includes the Suretka(?) Formation, Gatún(?) Formation, Las Animas Limestone, and Uscari Formation, not divided.

Suretka(?) Formation (Pliocene?): Crops out from Encanto to Río Colima, Tucurrique quad., conglomerate predominantly of well-rounded andesite boulders in a clayey matrix.

Gatún(?) Formation (Miocene): Crops out at the the junction of the Río Chiz and Río Reventazón, Tucurrique quad., dark-gray medium- to fine-grained-thin-bedded volcaniclastic sandstone, 40–60 percent volcanic clasts.

Las Animas Limestone (Miocene): Crops out between Río Jesús María and alluvium bordering Río Azul, Tucurrique, quad., irregularly bedded dark-grayish-brown mottled limestone.

Uscari Formation (Miocene to Oligocene): Crops out from Jesús María to Río Calvario, Tucurrique quad., irregularly bedded dark-gray shale, some black carbonaceous shale and brown mottled hard calcareous shale.

FIGURE 2.—Index map of Costa Rica and bordering areas of Nicaragua and Panama showing the location of major geographic features; the Barba, Abra, Caraigres, Tapantí, Istarú, Carrillo, and Tucurrique quadrangles; and the Quaternary volcanoes of Costa Rica.

The oldest rocks in Costa Rica make up an ophiolite assemblage (Dengo, 1961, 1962a, b), the Nicoya Complex, which lies in an arcuate belt along the Pacific coast. The complex consists of folded and overthrust volcaniclastic sedimentary rocks, pillowed basalt flows, chert, limestone, and mafic intrusive rocks (Dengo, 1962a, p. 11–13). Late Campanian Foraminifera from limestone in the complex in southern Costa Rica (Henningsen, 1966, p. 564) and middle Maestrichtian to late Campanian Foraminifera from the unconformably superposed Rivas Formation (Dengo, 1962a, p. 18, 22) suggest that the ophiolite assemblage was emplaced by the late Campanian.

Within the mapped area (see "Description of map units"), the oldest rocks exposed consist of an unnamed sequence of olivine basalt lava flows (To), an unnamed sequence of volcaniclastic sedimentary rocks, the Parritilla Limestone, and the Pacacua Formation (Ts_1). These units are little known, and correlations with surrounding areas are tentative as all but the

Parritilla are also unfossiliferous. Olivine basalt flows and associated volcaniclastic rocks in Cerro Caraigres in the southwestern corner of the mapped area (fig. 3) may correlate with similar rocks beneath the Machuca "formation" (Hayes, 1899, pl. 32) of southern Nicaragua and with similar basalt and tuff (Weyl, 1957, p. 24) of early Tertiary age (Dengo, 1962a, p. 142) in Cerro Buena Vista and Cerro Paramo of southern Costa Rica. The fossiliferous Parritilla Limestone and the overlying vivid purple, generally calcareous volcaniclastic sedimentary rocks of the Pacacua Formation are tentatively correlated with the upper Eocene of Brito Formation in northwestern Costa Rica–southwestern Nicaragua on the basis of fossils and lithology (Castillo M., 1968, p. 4). The Pacacua, according to Gabriel Dengo (in Castillo M., 1969, p. 11), is also lithologically like the Tuis (Eocene) and Senosri (lower Oligocene) Formations of the Atlantic coast of Costa Rica. The coarse character of much of the Pacacua in the Orosi and Villa Colon (fig. 3) areas suggests derivation from a nearby source of volcanic rocks, possibly the olivine basalt clastic units noted in the Cerro Caraigres area.

Interstratified beds of dark-colored siltstone, calcareous and tuffaceous sandstone, and shale of the Térraba Formation (Ts_1 in fig. 1) crop out widely in central and southwestern parts of the mapped area; they extend westward beyond the mapped area to Ventanas on the Río Virilla and southward to the Valle del General and Valle de Coto (fig. 2) on the Panama–Costa Rica border (Dengo, 1961, p. 49). The Térraba is argillaceous to the south and progressively more silty, arenaceous, and tuffaceous to the north (Henningsen, 1966, p. 562). It also contains increasing amounts of augite, hypersthene, and hornblende toward the west, the direction of sediment supply (Henningsen, 1966, p. 565). Foraminifera indicate an early Oligocene age (Henningsen, 1966, p. 562) for the lower beds of the Térraba in southern Costa Rica, and a middle or early Miocene age (Ruth Todd, in Krushensky, 1972, p. 7) for beds near the upper contact in the Orosi–Bermejo area of the Istarú and Tapantí quadrangles. The Térraba unconformably overlies the upper Eocene Davíd Formation in the Valle del General (Dengo, 1961, p. 49) and unconformably overlies the Pacacua near Orosi in the Tapantí quadrangle. It is

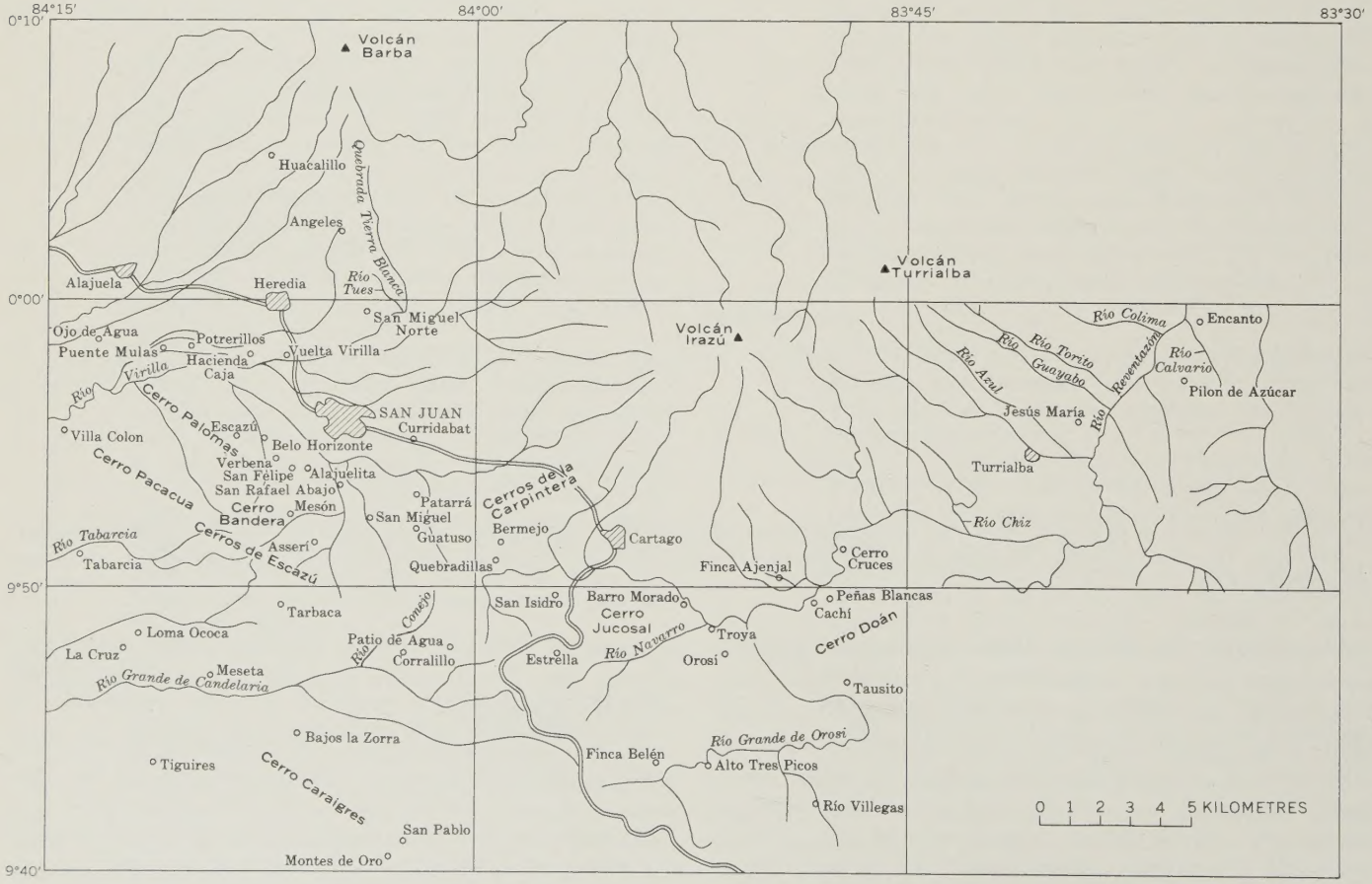

FIGURE 3.—Index map showing locations of places noted in description of map units.

correlated with shale identified as Uscari (Ts_2) in the Tucurrique quadrangle.

The San Miguel Limestone (Ts_1) (Romanes, 1912, p. 106) is thin, fine grained, and areally restricted; it contains abundant specimens of *Lyropecten*? (*Nodipecten*) sp. (Woodring and Malavassi V., 1961, p. 491). The San Miguel is correlated (Castillo M., 1968, p. 10) with calcareous epiclastic and volcaniclastic rocks of the Punta Carballo Formation (Dengo, 1962a, p. 38) on the flank of Cerro Turrucares in the Río Grande quadrangle adjoining the Abra quadrangle on the west and on the Pacific coast near Puntarenas. The Punta Carballo on the Pacific coast consists predominantly of coarse sandstone and conglomerate derived from erosion of the Nicoya Complex. Foraminifera from the Cerro Turrucares locality suggest that the Punta Carballo and the correlative San Miguel are middle Miocene. Mollusks from the same locality suggest a middle or early Miocene age (Woodring and Malavassi V., 1961, p. 496).

The Coris Formation (Ts_1) (Castillo M., 1969, p. 17), characterized by tuffaceous sandstone, siltstone, local lignite lenses, and ripple-marked quartzose sandstone, crops out in the mapped area only from the east end of the Cerros de la Carpintera to Aserrí in the Istarú and Abra quadrangles. The Coris is unfossiliferous, but is tentatively considered late to middle Miocene. It overlies the San Miguel disconformably in the Istarú quadrangle and overlies the Punta Carballo unconformably in the Caraigres quadrangle. Rocks identified as the Gatún Formation in the Río Chiz–Río Reventazón area of the Tucurrique quadrangle are tentatively correlated with the Coris and the base of the Aguacate Formation on the basis of similar lithology and sequence.

The Aguacate Formation (Tau) ranges from bedded fine-grained ash-fall tuff at the base to coarse volcaniclastic breccia-conglomerate and basalt flows in the middle to massive partly welded ash-flow tuff in the upper part. The formation crops out west of the Cerro Aguacate (Dengo, 1962a, p. 57) and south into the northern part of the Cordillera de Talamanca (fig. 2). The basal tuff is interbedded with the Coris in the northern part of the Caraigres quadrangle and may make up the upper tuffaceous part of the Gatún Formation to the west. In the northwest part of the Tapantí quadrangle, the middle part of the Aguacate and older rocks are folded and unconformably overlain by an ash-flow tuff sequence. The Aguacate is unfossiliferous and is assumed to be late Tertiary (Pliocene? to late Miocene?) (Dengo, 1962a, p. 57); it is correlated with volcanic rocks of the Paso Real sequence in the Valle del General (Dengo, 1962b, p. 149).

Volcaniclastic block breccia, conglomerate, and interbedded volcaniclastic siltstone, sandstone, and shale of the Doán Formation (Td) (Escalante, 1966, p. 64) and as redefined by Krushensky (1972, p. 12) are known only in the southern part of the mapped area. Outcrops show progressively finer grained epiclastic-volcaniclastic rocks toward the south. In the upper reaches of the Río Grande de Orosi in the Tapantí quadrangle, the Doán consists of marine coral-bearing siltstone-shale. The Doán unconformably overlies the middle part of the Aguacate Formation in the Tapantí and Istarú quadrangles. It is lithologically like the Suretka Formation in the Tucurrique quadrangle, but the included blocks and boulders are less well rounded and clinopyroxene is more plentiful in the Doán.

Volcanic rocks of the Cordillera Central and the coeval Cordillera del Guanacaste in northwestern Costa Rica (fig. 2) have not been subdivided regionally, and correlation of specific sequences from one to another of the volcanic piles is not presently possible. Williams (1952) studied the ash-flow tuff and the trachyandesite lava-flow sequence in the Valle Central Occidental (formerly Meseta Central Occidental) in the northern part of the Abra quadrangle and farther west, and Dengo (1962a) studied the post-Tertiary rocks on the western flank of the Cordillera del Guanacaste. Krushensky (1972, and unpub. data, 1975) subdivided the volcanic rocks of the Irazú volcanic center in the Istarú quadrangle and the interlayered partly welded ash-flow tuff and lava-flow sequence of the Volcán Barba in the Abra quadrangle.

Turrialba, Irazú, Barba, and Poás (fig. 2) are the principal and currently active volcanoes of the Cordillera Central. Turrialba, Irazú, and Barba are within the mapped area; all are stratocones composed of moderately to steeply dipping trachyandesite lava flows, lahar deposits, lesser quantities of bedded tuff, and local rhyodacite to quartz latite ash flows and froth flows (QTv). Deposits from adjacent volcanoes are interlayered, and none of the older volcanic rocks are known as erosion has penetrated only the upper parts of the volcanic piles. The northeastern part of the cone of Turrialba was apparently blown out and has been only partly rebuilt by recent eruptions. Older rocks may be exposed in the cliffs enclosing that new cone segment, but the volcano is largely unmapped.

The rock sequence of Costa Rica suggests formation of a Late Cretaceous arc-trench system and the emplacement by the late Campanian of an ophiolite assemblage in western Costa Rica. Lack of metamorphism beyond low-grade chloritization suggests that the complex was obducted, that is, thrust over the Caribbean plate, rather than subducted beneath it. Polarity

of the arc-trench system is indicated by the presence of an olivine basalt arc east of the ophiolite belt and by a younger magmatic arc farther east.

Insular volcanic centers erupting olivine basalt lavas and surrounded by volcaniclastic sedimentary aprons had been established by at least the late Eocene. Uplift of the ophiolite belt and the basalt arc furnished sediments to a back-arc basin, present central and west-central Costa Rica, through the Oligocene and into the middle Miocene. Farther and possibly rapid uplift of the ophiolite belt–basalt arc is evident in rocks of the Punta Carballo, but central Costa Rica remained a basin of sedimentation. Rocks of the Coris and the disconformable to unconformable contact of the Coris and the underlying San Miguel–Punta Carballo indicate that uplift of central Costa Rica had begun by late to middle(?) Miocene. The general absence of quartz-bearing rocks in the ophiolite assemblage and the continued existence of the central part of the country as a sedimentary basin require a farther removed source of the abundant quartz in the Coris. Henningsen (1966, p. 566) has suggested quartz-bearing plutons in northern Nicaragua as such a source.

The earliest fold period in the Tertiary of Costa Rica seems to follow deposition of the middle part of the Aguacate Formation. Flows and volcaniclastic rocks of that unit, in addition to older rocks, were folded into low-amplitude structures, locally overturned and overthrust, and cut by northeast-trending left-lateral wrench faults, probably in the latest Miocene. Later deposition of the nearly horizontal ash-flow tuff (youngest) part of the Aguacate suggests at least local marine planation, uplift, and deposition under subaerial conditions. Volcanism in the Cordillera Central, perhaps contemporaneous with the ash-flow tuff of the Aguacate, is indicated by the block breccia of the Doán Formation. However, the inclusion of corals in the predominantly shaly facies of the Doán in the southern part of the mapped area indicates that marine deposition there continued uninterrupted by orogeny. The Talamancan orogeny and intrusion of the Talamancan comagmatic series occurred only after deposition of the Doán. Compositional similarity of the Doán volcaniclastic materials and rocks of the Cordillera Central suggest that current volcanism in the Cordillera Central is a continuation of that which began in Doán time. Recent volcanism in the Cordillera Central (Qtl) and the Cordillera del Guanacaste has produced predominantly trachyandesite lava flows and tuff, and lesser quantities of rhyodacite–quartz latite as ash flows and froth flows.

REFERENCES CITED

Castillo M., Rolando, 1968, Geology of the Abra and part of the Río Grande quadrangles, central Costa Rica: Costa Rica Dirección Geología, Minas y Petróleo, Nota Divulgatica, 16 p.

——— 1969, Geología de los mapas basicos Abra y partes de Río Grande, Costa Rica: Costa Rica Dirección Geología, Minas y Petróleo Informes Téc. Notas Geol., v. 8, no. 33, 40 p.

Dengo, Gabriel, 1961, Notas sobre la geología de la parte central del litoral pacifico de Costa Rica: Costa Rica Inst. Geog. Nac. Informe Semestral, Julio a Deciembre 1960, p. 43–63.

——— 1962a, Estudio geológico de la region de Guanacaste, Costa Rica: San José, Costa Rica, Inst. Geog. Nac., 112 p.

——— 1962b, Tectonic-igneous sequence in Costa Rica, *in* Petrologic studies—A volume in honor of A. F. Buddington: New York, Geol. Soc. America, p. 133–161.

Escalante, Gregorio, 1966, Geología de la cuenca superior del Río Reventazón, Costa Rica, *in* Trabajos tecnicos presentados en la primera reunion de geólogos de America Central: Inst. Centroamericano Inv. y Tecnología Indus., Pubs. Geol., no. 1, p. 59–70.

Hayes, W. C., 1899, Physiography and geology of region adjacent to the Nicaragua canal route: Geol. Soc. America Bull., v. 10, p. 285–348.

Henningsen, Dierk, 1966, Notes on stratigraphy and paleontology of Upper Cretaceous and Tertiary sediments in southern Costa Rica: Am. Assoc. Petroleum Geologists Bull., v. 50, pt. 1, no. 3, p. 562–566.

Krushensky, R. D., 1972, Geology of the Istarú quadrangle, Costa Rica: U.S. Geol. Survey Bull. 1358, 46 p.

Krushensky, R. D., and Escalante, Gregorio, 1967, Activity of Irazú and Poás volcanoes, Costa Rica, November 1964–July 1965: Bull. Volcanol., v. 31, p. 75–84.

Romanes, James, 1912, Geology of a part of Costa Rica: Geol. Soc. London Quart. Jour., v. 68, p. 103–139.

Weyl, Richard, 1957 ,Contribución a la geología de la Cordillera de Talamanca de Costa Rica (Centro America): San José, Costa Rica, Inst. Geog. Nac., 77 p.

——— 1961, Die Geologie Mittelamerikas, Band 1, *of* Bentz, A. T., ed., Beiträge zur regionalen Geologie der Erde: Berlin, Gebrüder-Borntraeger, 226 p.

Williams, Howel, 1952, Volcanic history of the Meseta Central Occidental, Costa Rica: California Univ. Pubs. Geol. Sci., v. 29, no. 4, p. 145–180.

Woodring, W. P., and Malavassi V., Enrique, 1961, Miocene Foraminifera, mollusks, and a barnacle from the Valle Central, Costa Rica: Jour. Paleontology, v. 35, no. 3, p. 489–497.

Jour. Research U.S. Geol. Survey
Vol. 4, No. 2, Mar.–Apr. 1976, p. 135–149

CENOZOIC DEPOSITS OF SOUTHEASTERN NEW MEXICO AND AN OUTLINE OF THE HISTORY OF EVAPORITE DISSOLUTION

By GEORGE O. BACHMAN, Denver, Colo.

Abstract.—Sedimentary records of Cenozoic history in southeastern New Mexico begin with the Ogallala Formation of Miocene and Pliocene age. Later records include the Gatuna Formation of early or middle Pleistocene age, Mescalero caliche, an informal term, of middle Pleistocene age, and fluvial deposits of late Pleistocene age but there are many gaps in the record. The modern landscape is the result of erosion and deposition in climates that have ranged from semihumid to semiarid as well as dissolution of soluble rocks in Permian formations in the subsurface. This dissolution may have begun as early as Jurassic time and has continued intermittently to the present.

The geologic features discussed here are mostly in Eddy, Lea, and Chaves Counties of southeastern New Mexico (figs. 1, 2). This portion of New Mexico is in the southern part of the Pecos River section of the Great Plains physiographic province and, climatically, in the northern part of the Chihuahuan desert. The present climate is semiarid; however, climate has ranged from arid to semihumid during Cenozoic time.

Cenozoic history has been generally neglected in many of the previous studies of southeastern New Mexico but major contributions have been made by Fiedler and Nye (1933), Morgan (1942), Price (1943, 1958), Horberg (1949), Nicholson and Clebsch (1961), and Vine (1963). The purpose of this report is to summarize the present knowledge of Cenozoic stratigraphy and to outline the history of dissolution as a geologic process that has contributed to the formation of the modern landscape (table 1).

I worked in southeastern New Mexico during parts of 1972 and 1973 as part of a U.S. Geological Survey group studying underground beds of salt for disposal of nuclear waste. This work was supported by the Oak Ridge National Laboratory of the U.S. Atomic Energy Commission. Fieldwork consisted of reconnaissance geologic mapping from the Pecos River eastward to Grama Ridge and from the Querecho Plains southward to the New Mexico–Texas State line. Selected areas were mapped in detail. In addition to traverses on the ground, much of the area was observed during low-level flights in light aircraft.

Acknowledgments.—Many people contributed ideas to the basic concepts in this report. Among these, L. E. Gard, C. L. Jones, and P. W. Lambert discussed geologic relations with me in the field. During the 1973 field season I conferred with J. C. Frye, A. B. Leonard, C. C. Reeves, Jr., and J. W. Hawley, who contributed freely of their knowledge of the area. S. E. Galloway of the New Mexico State Engineers Office discussed ground-water relations and geology of the Roswell-Artesia basin. Subsurface information for the interpretation of parts of figure 8 was provided by C. L. Jones.

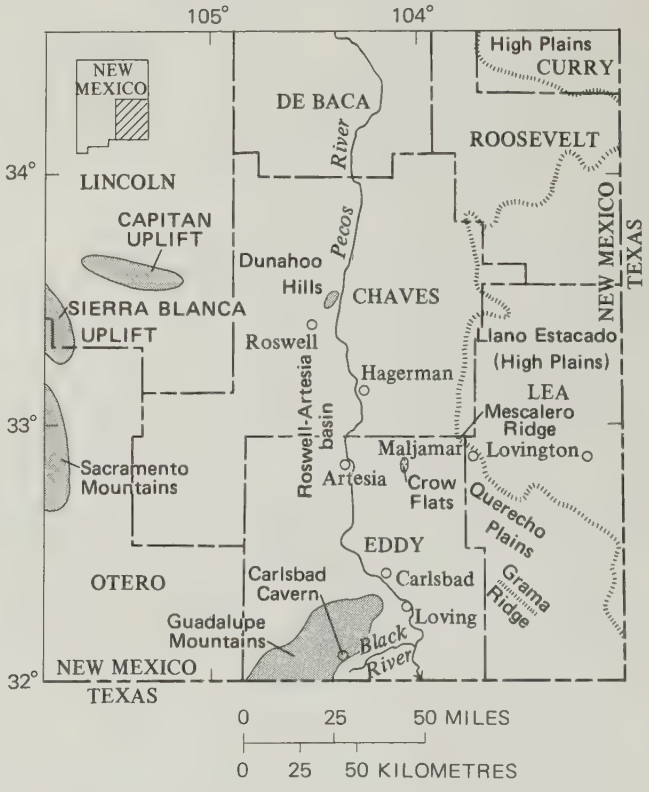

FIGURE 1.—Index map of southeastern New Mexico.

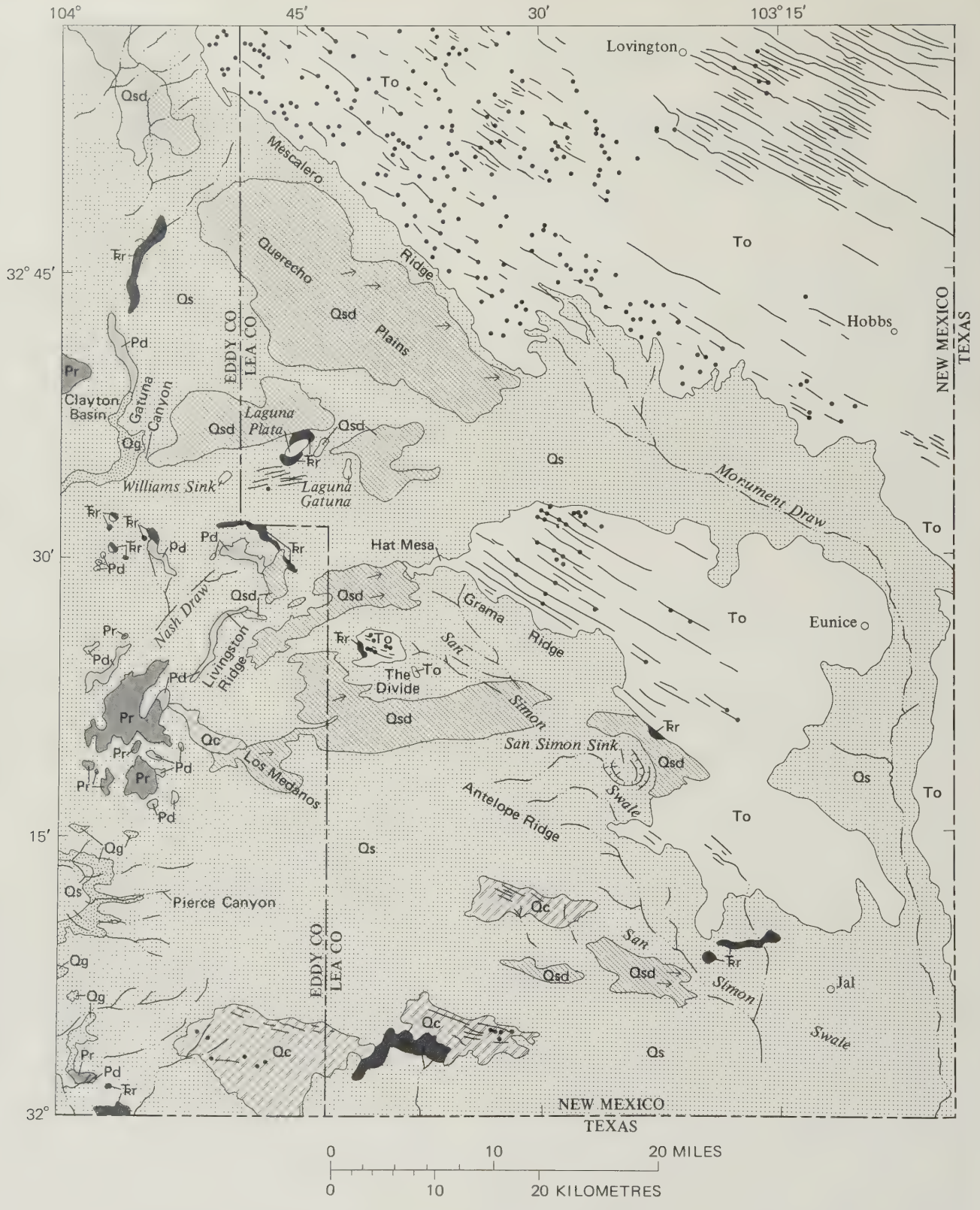

FIGURE 2.—Reconnaissance geologic map of surficial deposits, southern Lea County and eastern Eddy County, N. Mex. Base from U.S. Geological Survey Hobbs topographic quadrangle, scale 1:250,000, 1964–62.

EXPLANATION

Qs	Surficial sand	Holocene and Pleistocene	QUATERNARY
Qsd	Sand-dune deposits		
Qc	Caliche		
Qg	Gatuna Formation	Pleistocene	
To	Caliche caprock and Ogallala Formation	Pliocene and Miocene	TERTIARY
Rt	Sedimentary rocks		TRIASSIC
Pd	Dewey Lake Red Beds		PERMIAN
Pr	Rustler Formation		

Contact

Depressions

Swales or depressions

Trace of annular collapse

→ Dominant modern wind direction – Indicated by orientation of sand dunes

PRE-TERTIARY ROCKS

The oldest rocks exposed in southeastern New Mexico are of Permian and Triassic age. These rocks contribute to the physiographic relief, but the Permian rocks are especially noteworthy because the included evaporites have been dissolved at various times causing subsidence of younger deposits. The evaporite-bearing Permian rocks were deposited in shallow basins (fig. 3)

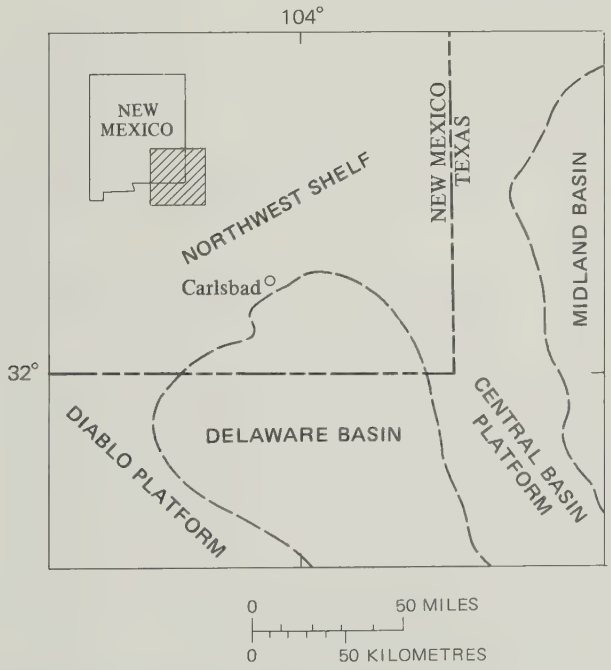

FIGURE 3.—Index map showing subsurface Permian features in southeastern New Mexico.

and have been discussed by King (1942, 1948), Hayes (1964), and Jones (1973). These rocks include the Castile, Salado, Rustler, and Dewey Lake Formations. Of these Permian formations, only the Rustler Formation and the Dewey Lake Red Beds are exposed in the study area.

OGALLALA FORMATION

The Ogallala Formation of Miocene and Pliocene age is the oldest record of Tertiary history and climate preserved in southeastern New Mexico. It underlies the High Plains and is well exposed along Mescalero Ridge, at Hat Mesa, Grama Ridge, and The Divide. Along Mescalero Ridge it typically includes the following three units, in descending order:

	Thickness in metres (ft)	
1. Caliche (caprock), brecciated, light-gray to white, densely pisolitic in upper part. Dense and hard under hammer. Forms prominent ledge	2.5–3	(8–10)
2. Sand, light-brown, fine-grained; grains are mostly quartz, subangular to well rounded, and well sorted. Cement is weak and calcareous. Forms vertical cliff in places	2–4	(6.5–14)
3. Sand, very friable, moderate orange-pink to grayish-orange-pink, fine-grained; grains are mostly quartz, well rounded, and well sorted. Strongly cross laminated in places. Forms gentle slope	5–6	(16–20)

Because the base of the Ogallala Formation commonly is covered, these three units do not represent the total thickness along Mescalero Ridge.

Much of the Ogallala Formation in eastern New Mexico was deposited on an irregular erosional surface as a series of complex alluvial fans. Frye (1970) concluded that deposition ceased when the region was covered by an extensive alluvial plain. By the end of Ogallala time the High Plains surface probably was continuous westerly across the region of the present Pecos River drainage to the backslope of the Sacramento Mountains.

When Ogallala deposition began in the central Great Plains, climatic conditions were somewhat moist, streamflow was regular, and temperature may have been somewhat warmer than at present. As Ogallala time progressed the climate became drier, the water table declined, and streamflow became intermittent (Frye and Leonard, 1957, p. 8). The thick deposits of sand along Mescalero Ridge probably accumulated as eolian deposits during this dry period.

When Ogallala deposition ceased during late Pliocene time the region was tectonically stable and the

TABLE 1.—*Summary of late Tertiary and Quaternary events in southeastern New Mexico*

Age		Stratigraphic unit	Deposits	Events	Probable climate	Tentative correlations
Holocene		Young sand dunes	Sand	Working wind from southwest.	More dry than present.	
		Old soil			More moist than present.	
		Old sand dunes			More dry than present.	
Pleistocene	Late	Lakewood terrace deposits.	River conglomerate, pond, marsh, and lake silts.	Pecos River developed as axial stream from Fort Sumner to Roswell.	More moist than present. Probably cooler.	Wisconsin.
		Orchard Park alluvial deposits.	Limestone-porphyry conglomerate. Caliche caprock.	Reworking of Blackdom deposits.	More moist than present. Probably cooler.	Probably early Wisconsin.
		Blackdom alluvial deposits.	Limestone-porphyry conglomerate. Caliche caprock.	Major erosion of back slope of Sierra Blanca and Sacramento and Capitan Mountains.	More moist than present. Probably cooler.	Do.
		Hiatus				
	Middle	Mescalero caliche, an informal name.	Caliche	Land surface stable. Soil development over much of southeast New Mexico.	More dry than present. Probably warmer.	Yarmouth(?). Unnamed gravel surface west of Pecos.
	Middle or early	Gatuna Formation	Gravel. Stream gravels, pond sediments, solution basin fill. Conglomerate, sand, silt, some gypsum.	Pediments formed in area between Carlsbad and San Simeon Swale. Streams cut High Plains escarpment eastward. Extensive solution of salt and gypsum in subsurface. Collapse of Nash Draw and Clayton Basin. San Simon Swale may have been of major stream.	Much more moist than present. Probably cooler.	Analogous to Kansan deposits in Trans-Pecos Texas.
	Early(?)	Hiatus				
Pliocene		Ogallala "climax-soil."	Caliche	Land surface stable. Soil development.	Similar to, or more dry than, present.	
Pliocene and Miocene		Ogallala Formation.	Gravel, sand, silt			

climate was semiarid to arid. The High Plains were extensive and featureless. In southeastern New Mexico the High Plains surface slopes southeastward about 2.1 m/km (10 ft/mi) and this slope is presumed to reflect the original depositional surface. On this surface a pedocal soil, the Ogallala "climax-soil" (Frye, 1970), formed and the present caliche caprock accumulated in the zone of illuviation.

Stages of formation of pedogenic caliche in southern New Mexico have been described by Gile, Peterson, and Grossman (1966). Similar stages are present in southeastern New Mexico where the caliche varies from weak calcareous accumulations in youthful soils through nodular and laminar deposits on older geomorphic surfaces, and finally to the brecciated and pisolitic caliche of the Ogallala. The pisolitic texture forms during late stages of caliche genesis after repeated solution and desiccation. Caliche deposits younger than the Ogallala may contain pisoliths locally but on younger geomorphic surfaces the pisoliths are not as abundant, widespread, nor as completely formed. I used this distinctive aspect of the Ogallala caliche in extreme southeastern New Mexico to identify clasts in later deposits that have been eroded from the Ogallala caprock.

Bretz and Horberg (1949, p. 483) suggested that the Pecos River system near Carlsbad is of pre-Ogallala origin and that "if it be assumed that no postconglomerate deformation has occurred, a former Ogallala fill of more than 1,300 feet [425 m] along the Pecos de-

pression is indicated." My work does not support this hypothesis. Instead, the Ogallala Formation thins towards the south and southwest from the High Plains. Drill-hole information indicates that the Ogallala Formation is about 102–112 m (315–345 ft) thick along Mescalero Ridge north of Maljamar. At Hat Mesa it ranges in thickness from about 33 to 60 m (100–180 ft) and on the west side of The Divide it is no more than 9 m (27 ft) thick. At all these localities the pisolitic caliche caps the Ogallala Formation which indicates that the southwesterly thinning must have occurred before the caliche formed. Erosion probably was not the cause of regional thinning because other evidence points to a progressive desiccation as Ogallala deposition ceased. Much of the lowering of the Pecos River valley has occurred as a result of dissolution of evaporites in the underlying Permian rocks since Ogallala time.

THE PLIOCENE-PLEISTOCENE HIATUS

The Ogallala "climax-soil" (Frye, 1970) formed after most Ogallala deposition and before the extensive erosion that characterized Pleistocene time. Late in this period of soil formation and after the caliche was indurated, northwest-trending fields of longitudinal, or seif, dunes probably formed on the High Plains surface in southeastern New Mexico. These dune fields have since been eroded away but oriented depressions remain on the High Plains surface that are believed to have formed by the etching and removal of the Ogallala caliche between the former longitudinal dunes (Price, 1943; 1958, p. 3). Havens (1966, p. 8) reported that drilling in depressions west of Lovington indicates that caliche "thins toward or is absent beneath the central part of the depressions." The depressions are partly filled by alluvial and lacustral sediments, and plant growth is relatively more abundant within them. Flint (1955, p. 156–160) reviewed various concepts of the origin of parallel drainage on shale and concluded that some form of eolian control was probable, but that the mechanism of stream development was not clear.

These alined swales and dolines are especially common in the vicinity of Lovington (fig. 2). They are commonly about 35–100 m (100–300 ft) wide and about 3–5 km (2–3 mi) long, although some are as much as 16 km (10 mi) long. These depressions have gentle relief (fig. 4) and most are less than 13 m (40 ft) deep. They are generally oriented about N. 60° W. This orientation indicates that effective winds were from the northwest during late Pliocene or early Pleistocene time which contrasts with the dominant southwesterly winds of present time.

FIGURE 4.—Aerial view of alined drainage on the mesa west of Eunice, Lea County, N. Mex. View is west-northwestward. Swales are marked by darker vegetation. Caliche of the Ogallala surface is exposed along the margins of the swale in the foreground. These swales are 30–90 m (100–300 ft) wide and about 5 km (3 mi) long. Internally drained depressions are visible in the distance.

In areas of longitudinal dunes in the Navajo country of Arizona "troughs between the ridges, as well as the flanks of ridges, are covered with vegetation; only the long ridge tops are bare" (Hack, 1941, p. 243). In other modern dune fields, plant growth is more abundant in troughs between dunes than on the dunes themselves. Plant growth between longitudinal dunes on the High Plains probably accelerated the etching of the underlying Ogallala caliche by chemical action that included the release of humic acids. Erosion by wind and water could then more effectively remove sediments from these etched swales.

Some swales are locally minor drainages in eastern Lea County. Monument Draw, northwest of Eunice, and San Simon Swale (fig. 2) are parallel in part to the system of swales on the High Plains surface. These drainages may have begun in etched swales on the Ogallala caliche. Drainage has developed along similar swales about 240 km (150 mi) farther north on the High Plains in Curry County, N. Mex. (Price, 1958, p. 63).

PLEISTOCENE AND HOLOCENE DEPOSITS

In Pleistocene time large areas of Ogallala deposits were removed or reworked by water and wind. The Pecos River and its tributaries became entrenched;

some underlying Permian evaporites were dissolved, resulting in surface collapse. Pleistocene deposits found in this region are presumed to represent parts of early or middle Pleistocene time. They include the Gatuna Formation and the Mescalero caliche.

GATUNA FORMATION

The Gatuna Formation was named for exposures of light-reddish-brown sandstone and conglomerate more than 25 m (80 ft) thick in Gatuna Canyon, eastern Eddy County, by Robinson and Lang (1938, p. 84–85), who did not describe a type section. The formation is well exposed along the east side of Clayton Basin (fig. 2), where it rests on rocks of Permian age and is overlain by the Mescalero caliche, an informal name. Although the Gatuna is estimated to be thicker at other localities, it is better exposed and less disturbed by slumping on the north side of Gatuna Canyon. The following stratigraphic section is here proposed as a reference section for the Gatuna Formation.

Reference section of the Gatuna Formation

[North side of Gatuna Canyon, SW¼SW¼, sec. 36, T. 19 S., R. 30 E. Color notations are from Goddard and others (1948)]

	Thickness in metres (ft)	
Mescalero caliche:		
5. Caprock is eroded. Well-cemented nodular zone grades downward to nodular zone that engulfs top of Gatuna	1.7	(5.5)
Gatuna Formation:		
4. Sandstone, pale-reddish-brown (10*R* 5/4), slightly calcareous, medium-grained; grains are subround to round and well sorted; weathers to irregular masses. Bedding is indistinct	3.5	(11.4)
3. Conglomerate, poorly sorted. Upper part of unit includes abundant coarse subangular clasts as much as 25 cm (9.8 in) in diameter which are derived from Ogallala pisolitic caliche; grades downward to less coarse sand and pebbles. Clasts at base are subangular to subround and do not exceed 4 cm (1.6 in) in diameter in basal metre of unit	12.3	(40.0)
2. Sandstone, friable, moderate-reddish-orange (10*R* 6/6) to pale-reddish-brown (10*R* 5/4), fine- to medium-grained; grains are subangular to subround, well sorted, and include rock fragments, quartz, and sparse biotite. Cement is weak and calcareous. Beds in unit are about 10 cm (4 in) thick, and are irregular to indistinct	1.0	(3.3)
Total Gatuna Formation	16.8	(54.7)
1. Covered; in slopes below base of measured section (estimated thickness)	7	(23)

The Gatuna Formation is extensively slumped in Gatuna Canyon. Its thickness there is estimated to range from about 15 to 30 m (50–100 ft). At a gravel pit on the north side of Gatuna Canyon (S½ sec. 35, T. 19 S., R. 30 E.) it is well exposed and is at least 17 m (56 ft) thick in a slump block.

Although much of the Gatuna Formation is fine grained, the conglomeratic beds have provided most of the evidence for the history of the formation. The conglomerate comprising unit 3 of the reference section contains the following types and percentages of clasts:

Ogallala pisolitic caliche	36
Sandstone	10
Orthoquartzite	24
Tertiary porphyries (mostly Sierra Blanca rock types, but one clast noted may be from Capitan Mountains)	16
Permian limestone	6
Quartz	4
Chert	2
Jasper	2

Clasts in the conglomeratic sand in Gatuna Canyon are largest in the basal part of the formation where they average about 7–10 cm (3–4 in) in diameter, with clasts as much as 20 cm (8 in) not uncommon. In the upper part of the formation in Gatuna Canyon, clasts are generally less than 9 cm (3.5 in) in diameter.

Rounded cobbles and boulders derived from the pisolitic caprock caliche of the Ogallala Formation are widespread and common in the Gatuna. Gravel in a pit on the north side of Gatuna Canyon contains the following percentages and types of clasts: 35 percent are derived from the Ogallala caliche, 50 percent are quartzite and orthoquartzite, 10 percent are Tertiary porphyries, and 5 percent are red sandstone. The clasts derived from the Ogallala caliche are 7–20 cm (3–8 in) in diameter which indicates that they have been transported shorter distances than the quartzite and porphyry clasts which have a generally smaller average diameter.

A conglomeratic, lenticular channel deposit is well exposed in the Gatuna Formation along the west side of Long Arroyo about 13 km (8 mi) east of Hagerman. There the Gatuna rests on an uneven erosion surface on Permian red beds. The sandy matrix is pale red, poorly sorted, and crossbedded. The clasts are as much as 15 cm (6 in) in diameter. Of the clasts in the deposit, 45 percent are quartzite and orthoquartzite, 35 percent are Ogallala pisolitic caliche, 10 percent are red sandstone, and 10 percent are chert. In the southern part of Eddy County conglomerates are widespread in the upper part of the Gatuna Formation where they were deposited as alluvial gravels on a piedmont surface. More than 50 percent of the clasts in the gravels of this area are of Permian limestone and the rest of the clasts are of quartz, orthoquartzite, chert, and Tertiary porphyries.

Conglomerates with quartzite clasts are common along the Pecos and Black Rivers and remnants are widespread in the Pecos River Valley. They were first described by Nye (in Fiedler and Nye, 1933, p. 35–38). Bretz and Horberg (1949) and Thomas (1972) have

suggested that these gravels are basal Ogallala, but clasts derived from the Ogallala pisolitic caliche are present in at least one outlier west of the Pecos River near Loving (SE¼ sec. 33, T. 23 S., R. 28 E.). Pebble counts at other places suggest pebble associations found in the Gatuna Formation; therefore I consider these gravels to be remnants of the Gatuna.

Underlying the caliche caprock of the Dunahoo Hills (fig. 1) is an outlier of conglomerate that also may be part of the Gatuna Formation. It is an irregular, cross-bedded channel deposit with some interbeds of fine sand. Clasts in the conglomeratic beds are subround to round and spherical to oblate spheroidal. Most commonly they are 6–8 cm (about 3 in) in diameter but a few are as much as 20 cm (8 in) in diameter. Nearly 70 percent of these clasts were derived from Permian limestone; the remaining 30 percent are orthoquartzite, chert, and Tertiary porphyries. Rare clasts of Ogallala pisolitic caliche were observed in these exposures. In roadcuts near the highway other rock types are present, but many roadcuts were contaminated by exotic debris during highway construction.

Fine-grained deposits in the Gatuna are well exposed in Nash Draw, Pierce Canyon, and at Crow Flats. In the southern part of Nash Draw (SE¼ sec. 33, T. 23 S., R. 29 E.) thin, even beds of yellowish clay and silt dip steeply into a sink that formed during Gatuna time. At this place a bed of gypsum 2 m (6 ft) thick is intercalated with the yellowish clays. Near Crow Flats (figs. 1, 7) east of Artesia the Gatuna includes massive fine-grained beds which locally fill sinks of Gatuna age.

The Gatuna Formation was derived locally and was deposited before the Pecos River had cut headward to the Sangre de Cristo Mountains. Sources for the Gatuna include: (1) The Ogallala Formation, (2) Permian and Triassic rocks, and (3) Tertiary porphyries in the Capitan and Sierra Blanca uplifts west of the Pecos River. Apparently there are no clasts derived from the Sangre de Cristo Mountains or Pedernal uplift to the north. The pink, alkalic feldspars that might be expected in such a gravel are abundant only in the much younger (Wisconsin) Lakewood terrace along the Pecos River near Roswell.

Other workers have suggested that the Gatuna Formation could be pre-Ogallala (Kelley, 1971, p. 30), or that some siliceous gravels in the Pecos River valley, herein correlated with part of the Gatuna, could be Ogallala (Thomas, 1972 p. 17) or pre-Ogallala (Bretz and Horberg, 1949, p. 487). The Ogallala pisolitic caliche clasts in the Gatuna Formation in its type locality are evidence for its post-Ogallala age. More specific evidence of age has not been found.

The Gatuna Formation is here considered to be early or middle Pleistocene in age. The widespread channel deposits as well as the sink fillings indicate that the climate was unusually wet. Other workers have regarded middle Pleistocene (Kansan) time as the wettest time in the Pleistocene in the High Plains (Frye and Leonard, 1965, p. 211; Hibbard, 1970, p. 401), and probably the Gatuna was deposited at this time. In addition, the Gatuna is almost everywhere overlain by an extensive, indurated caliche (the Mescalero caliche). This caliche covers a geomorphic surface that is analogous in extent and maturity to high surfaces along the Rio Grande in southern New Mexico which are believed to have developed during middle Pleistocene time (Kottlowski and others, 1965, p. 292).

MESCALERO CALICHE

The Mescalero plain lies generally east of the Pecos River and west of the High Plains in southeastern New Mexico (Bretz and Horberg, 1949, p. 481). It extends southward from the vicinity of Fort Sumner to the New Mexico–Texas State line. Wherever the surface can be observed beneath the widspread deposits of windblown sand, it is underlain by a distinctive caliche. I observed this caliche at many places and treated it as an informal stratigraphic unit, here called the Mescalero caliche.

The Mescalero caliche consists of two parts: a basal, earthy to firm, nodular calcareous deposit, and an upper well-cemented laminar caprock. These units correspond to the K zone of Gile, Peterson, and Grossman (1966) and include the K_3 and K_2 zones, respectively. The two units commonly weather to a ledge in which the caprock overhangs the nodular base. Together the two parts range in thickness from about 1 to 4 m (3–13 ft) with the caprock usually making up about one-third to more than one-half of the total thickness.

Although both parts of the Mescalero caliche may engulf underlying sediments, most commonly this is more apparent in the basal part. Near the base of the caliche, irregular masses of bedrock may be partially surrounded or completely engulfed by the caliche. In the caprock where diagenesis is most advanced, scattered quartz pebbles and sand grains may be the only vestige of the engulfed sediment.

Prominent laminations throughout much of the caprock characterize the Mescalero caliche. These laminae consist of alternating dark and light layers generally less than 5 mm thick and parallel to the land surface. They may be weakly crenulated or even disrupted by pisoliths. The pisoliths are common only locally and are less common and less well developed than in the

Ogallala caliche along Mescalero Ridge. Brecciation is rare in the Mescalero caliche.

Microscopically the carbonate of the caprock is mostly micrite with subordinate sparry calcite in veinlets, replacements, and irregular masses. The dark layers are clotted micrite. The micrite occurs in places as yellowish bands around pisoliths which suggest the presence of iron oxide.

Sand grains are common in both the lower nodular zone and the caprock of the caliche. However, in the caprock, sand grains are abundant in the massive, unlaminated part but are rare in the laminae. More commonly, detrital grains in the laminated zones are very fine silt (0.01–0.02 mm in diameter). Sand grains in the massive parts of the caprock are subangular to rounded quartz that range in diameter from about 0.1 to 0.3 mm. Some of these grains are etched and replaced by sparry calcite. The general absence of sand grains in the laminated zones suggests that processes of solution and reprecipitation that formed the laminae separated the carbonate from larger detrital grains.

The Mescalero caliche was formed during an interval of climatic and tectonic stability that followed deposition of the Gatuna Formation. The Mescalero caps the Gatuna Formation almost everywhere that the Gatuna is exposed. It locally caps Triassic and Permian rocks as well. The Mescalero caliche formed in the semiarid environment that followed the moist conditions of Gatuna time. It is analogous in maturity and extent to the caliche that caps the La Mesa surface along the Rio Grande valley in southern New Mexico (Gile and others, 1966, p. 348), and is considered to be middle Pleistocene in age.

PLEISTOCENE DEPOSITS AND THE DEVELOPMENT OF MODERN DRAINAGE

Major drainage was probably eastward to southeastward during early Tertiary time and this continued to be the dominant direction of drainage while the Ogallala Formation was being deposited during late Tertiary time. Bretz and Horberg (1949, p. 487) postulated an early Tertiary ancestral Pecos drainage, and there may have been a local Pecos drainage but this southward-flowing system was limited in extent and its headwaters may have extended no farther north than the vicinity of Carlsbad and San Simon Swale. Streams probably flowed eastward from the Capitan and Sierra Blanca uplifts, but the pattern of that drainage system is not known.

Southeasterly flowing streams formed at least three major drainage systems in eastern New Mexico during late Pliocene and early Pleistocene time (fig. 5). The Canadian River system to the north cut through the

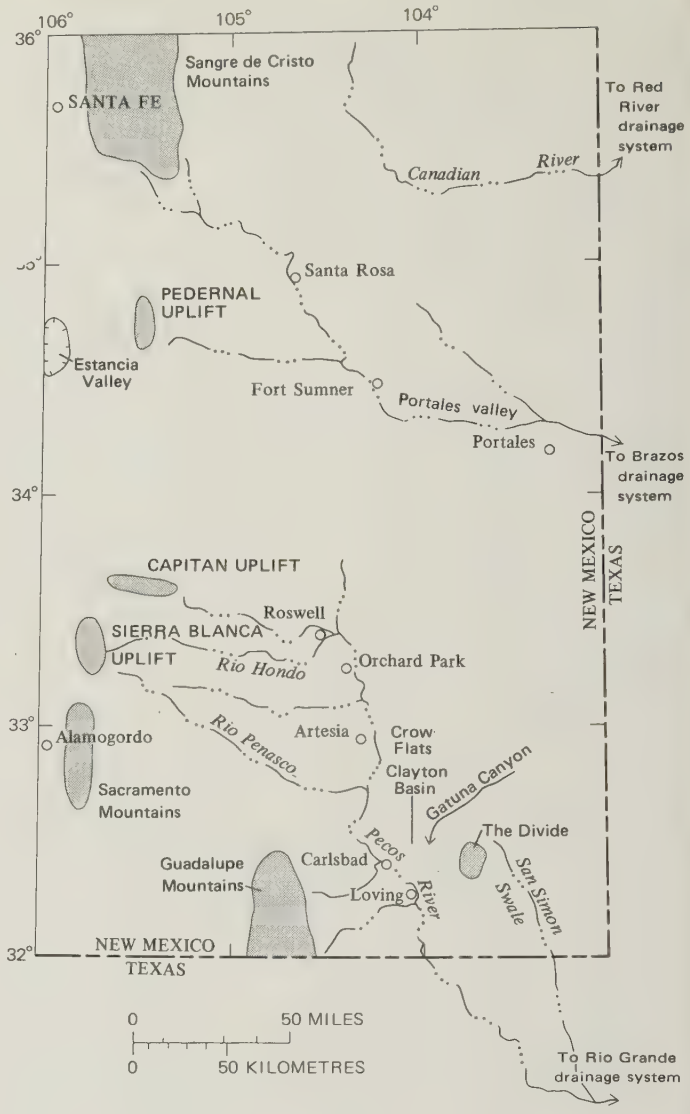

FIGURE 5.—Map showing probable drainage in eastern New Mexico during middle Pleistocene time.

Ogallala Formation and flowed eastward into the Red River system. A second major system drained southeastward towards the Portales valley and finally into the Brazos drainage in western Texas (Baker, 1915, p. 52–54). The third system generally followed the southern part of the Pecos River valley. Igneous debris was carried from the Sierra Blanca and Capitan uplifts eastward down the Rio Penasco, Rio Hondo, and other valleys west of the Pecos into the southward-flowing Pecos River. By middle Pleistocene time a stream system also flowed westward from the High Plains toward Clayton Basin and deposited portions of the Gatuna Formation.

After Gatuna time there was a period of tectonic stability during which the Mescalero plain formed and

extensive deposits of caliche accumulated in a semiarid climate. Streams were smaller than in Gatuna time but the pattern of their drainage is not known.

After Mescalero time pediment surfaces were cut east of the Sacramento Mountains, and the Pecos River entrenched itself near its present channel along the toes of these pediments. The wetter climate that contributed to the formation of pediments also caused widespread solution and collapse in the Roswell-Artesia basin and probably farther to the south. Stream gradients and sediment-carrying capacity thus decreased along the Pecos River during most of late Pleistocene and Holocene time.

During early and middle Pleistocene time sediments were derived largely from the Sierra Blanca and Sacramento and Capitan Mountains, but in late Pleistocene (post-Mescalero) time the Pecos River intersected the Portales valley drainage system near Fort Sumner. The Pecos River thus became a permanent stream flowing from the southern Rocky Mountains to the Rio Grande.

Part of the history of the Pecos River drainage is recorded in five physiographic surfaces that have been recognized in southeastern New Mexico west of the Pecos. Horberg (1949, p. 464) summarized the studies of previous workers and enumerated these surfaces, from oldest to youngest: (1) The Sacramento plain, (2) the Diamond A plain, (3) the Blackdom terrace, (4) the Orchard Park terrace, and (5) the Lakewood terrace. A tentative correlation of these physiographic features and their accompanying deposits is proposed in table 2.

TABLE 2.—*Tentative correlation of Quaternary features and formations in southeastern New Mexico*

West of Pecos River	East of Pecos River	Age
Lakewood terrace deposits.	Playa deposits	Woodfordian Substage (late Pleistocene).
Orchard Park alluvial gravel.	Not recognized	(?).
Blackdom alluvial gravel.	Not recognized	(?).
Diamond A plain	Mescalero caliche	Middle Pleistocene.
Gatuna (?) Formation, locally.	Gatuna Formation.	Early or middle Pleistocene.
Sacramento plain	High Plains surface.	Late Pliocene to early Pleistocene.

At the close of Ogallala time an extensive physiographic surface extended from the High Plains to the Sacramento Mountains. In the Sacramento Mountains this surface is highly dissected and has been named the Sacramento plain (Fiedler and Nye, 1933, p. 14–15). The limits of this plain have not been defined, but Horberg (1949, p. 464, 465) suggested its correlation with the High Plains surface and also believed it to be equivalent to the upland surface on the Guadalupe Mountains.

Remnants of a lower physiographic surface, the Diamond A plain (Fiedler and Nye, 1933, p. 14), are present about 32–40 km (20–25 mi) west of the Pecos River. This surface is less dissected than the older Sacramento plain, but it is hummocky and marked by numerous dolines. It is well preserved about 37 km (23 mi) west of Hagerman, where it is capped by caliche. This caliche has a prominent laminar caprock and is morphologically very similar to the Mescalero caliche east of the Pecos River.

The next lower surface has been named the Blackdom terrace (Fiedler and Nye, 1933, p. 12, 32–35), and this usage has been followed by other workers in the area (Morgan, 1942; Horberg, 1949, p. 464–465, 470–471). The Blackdom alluvial deposits are coalesced fans that rest on a broad surface cut on older rocks and it seems more proper to refer to these deposits as the Blackdom alluvial deposits. They were deposited by aggrading western tributaries of the Pecos River during an early stage of formation of the Pecos drainage before the river was entrenched in its present course. The Blackdom, as well as the younger Orchard Park alluvial deposits, should be distinguished genetically from the Lakewood terrace deposits. The latter contain clasts from the Sangre de Cristo Mountains and are related genetically to the modern Pecos River.

Blackdom alluvial deposits occur only west of the Pecos River. They are present intermittently from about 16 km (10 mi) south of Roswell to the Seven Rivers Hills. These deposits appear to be present in the vicinity of Arroyo del Macho but have not been examined in that area.

The Blackdom deposits are about 6.0–8.5 m (20–30 ft) thick. The surface of the deposits slopes eastward about 5.5–7.5 m/km (30–40 ft/mi), is hummocky to undulating, marked by small dolines, and is more uneven than the younger Orchard Park surface. The gravel in the deposits consists mostly of limestone from the underlying Permian rocks but clasts of porphyries derived from the Sierra Blanca and Capitan uplifts increase in abundance in exposures toward the north. The clasts average about 6–8 cm (2.4–3.2 in) in diameter but sorting is poor and some clasts are as much as 0.5 m (1.6 ft) in diameter. Clasts are subangular to round and are cemented by an earthy to well-indurated caliche. Many of the limestone clasts are solution faceted. Laminar zones in this caliche are poorly developed and pisoliths were not observed.

The Orchard Park alluvial deposits (the Orchard Park terrace of Fiedler and Nye, 1933, p. 11–12, 31–32)

occur west of the Pecos River between Roswell and Lakewood. They represent a later stage of the erosional cycle that abraded the Blackdom deposits. Some clasts are reworked from the Blackdom and they are generally smaller than clasts in the Blackdom. In a gravel pit near Orchard Park (SE¼SE¼ sec. 21, T. 12 S., R. 25 E.) clasts average about 3–4 cm (1.2–1.6 in) in diameter with some as much as 15 cm (6 in) in diameter. At this quarry, 58 percent of the clasts are of Tertiary porphyry derived from the Sierra Blanca and Capitan uplifts to the west, and 42 percent are of Permian limestone. About 45 km (28 mi) south of Orchard Park and 3.2 km (2 mi) east of Artesia, the Orchard Park deposits are composed entirely of Permian limestone clasts, many of which are solution faceted. The matrix is structureless caliche that is poorly to moderately indurated. The incomplete exposures at the quarry near Orchard Park are 3.8 m (12.5 ft) thick. Near Lakewood the Orchard Park deposits are estimated to be 6–9 m (20–30 ft) thick.

The Lakewood terrace is the youngest named physiographic feature along the Pecos River (Fiedler and Nye, 1933, p. 10). It is present in a narrow strip along the river from the vicinity of Roswell to about 6.4 km (4 mi) south of Carlsbad where it loses its identity. Surfaces near the Pecos channel east of Loving are here interpreted as older collapsed surfaces which have been exhumed and are not properly a part of the Lakewood terrace. The Lakewood terrace is present westward along some of the tributaries to the Pecos and is especially prominent in the Roswell-Artesia basin.

The Lakewood terrace deposits are widely varied along the Pecos River. The northernmost exposures near Roswell contain a large variety of rock types that reflect the source areas of the Pecos River as far north as the Sangre de Cristo Mountains. For example, about 22 km (14 mi) northeast of Roswell (SW¼NE¼ sec. 3, T. 9 S., R. 25 E.), gravels in the Lakewood terrace contain subround to round pebbles that average about 3 cm (1.2 in) in diameter, with some clasts as much as 10 cm (4 in) in diameter. The types and percentages of clasts in the gravels are:

Orthoquartzite	22
Granite, pink to yellow, medium- to coarse-crystalline	12
Chert	15
Quartz	12
Permian limestone	22
Sandstone	12
Schist, mica, hornblende, quartz	2
Diorite(?) weathered	2
Pink alkalic feldspar, "fresh," sparse fragments	1
Total	100

This is the most heterogeneous conglomerate observed along the Pecos River from the Roswell-Artesia basin southward to the New Mexico–Texas State line. The granites are similar to those in gravels along the Pecos River near Fort Sumner about 100 km (63 mi) north. It is noteworthy that clasts of the Tertiary porphyries exposed farther west are apparently absent, although such clasts are commonly represented in the older Orchard Park alluvial deposits in the same area.

At the south end of the Roswell-Artesia basin, Lakewood deposits are generally fine sand, silt, and clay. The size of the material in the deposits reflects the low gradient of the Pecos River south of Roswell and the effectiveness of the Roswell-Artesia basin as a settling basin. Near Carlsbad the Lakewood terrace deposits are mostly sand and gravel derived from Permian limestones, which indicate local sources.

FANGLOMERATES EAST OF THE GUADALUPE MOUNTAINS

Lime sand and limestone pebble fanglomerates cover an extensive area of low relief between the Guadalupe Mountains and the Pecos River. These deposits are continuous from Carlsbad southward nearly to Black River and in a narrow belt in the Black River drainage along the eastern front of the Guadalupe Mountains. Some of this clastic debris has been described as an alluvial apron (Hayes and Koogle, 1958). Horberg (1949, fig. 3) recognized a "Blackdom plain" south of Carlsbad, and Motts (1962) mapped "younger" and "older" alluvium which he correlated with the Lakewood terrace and with the Orchard Park and Blackdom "plains." These plains may be underlain by some equivalents of the Orchard Park and Blackdom alluvial deposits but they are part of an extensive fan system east of the Guadalupe Mountains, and this system has not been traced with certainty north of Carlsbad.

Clasts in these fanglomerates are derived from the Permian limestones and other rocks from the Guadalupe Mountains. Most of the limestone pebbles are solution faceted, and caliche cements the deposit at many places. The caliche is generally structureless and was probably deposited from surface water solutions.

These fanglomerates appear to be deposited on an erosional and karst topography. South of Carlsbad Caverns lenticular beds of conglomerate fill channel-shaped depressions along the tops of ridges. North of Carlsbad Caverns the fanglomerates appear to fill sinks, and, at places, the surface itself is locally marked by dolines and sinks. Modern drainage on these fanglomerates generally parallels low discontinuous ridges that radiate from the Guadalupe Mountains. This suggests that the fans are now being dissected.

The age of these fanglomerates is not known. They may be as old as the Blackdom deposits, or older. How-

ever, northeast of Loving, along the west side of the Pecos River, remnants of these fanglomerates rest on probable Gatuna Formation and Mescalero caliche. Here the underlying deposits are distinguished from the fanglomerate by the many Tertiary porphyry and siliceous pebbles cemented in the caprock. This caprock is here interpreted as an exhumed Mescalero caliche surface that has collapsed along the Pecos River. Therefore, at least the eastern fringes of the fanglomerate are assumed to be post-Mescalero in age.

WINDBLOWN SAND

Windblown sand is widespread over much of the area east of the Pecos River. Some of these deposits occur as coppice dune fields with local informal names such as Los Medanos and Mescalero sands. Most of these dunes are relatively inactive, but they have been active during Holocene time and local blowouts suggest that they would soon be reactivated if the plant cover were disturbed.

At least two distinct deposits occur at most places in coppice dune fields. These include a lower deposit of compacted, somewhat clayey sand that may be as much as 0.5 m (1.5 ft) thick and an overlying deposit of loose blow sand as much as 6–8 m (20–25 ft) thick. Locally, soils are very poorly formed on some deposits of blow sand.

The widespread deposits of windblown sand indicate a large source of fine sand. Sand deposits are discontinuous along the banks of the Pecos River and there is very little evidence that much sand has been derived from there. I believe that most of the windblown sand in areas such as Los Medanos was derived from the Ogallala Formation. During wet intervals in the Pleistocene the sand was eroded from the Ogallala, and during arid intervals it was blown across the Mescalero plain.

HISTORY OF EVAPORITE DISSOLUTION

The parts of southeastern New Mexico underlain by salt, gypsum, and other soluble Permian rocks near the surface attract popular interest because of the widespread karst topography that has formed on modern surfaces. The removal of these soluble rocks by dissolution has caused subsidence and collapse of the surface at many places (Lee, 1925). However, my work indicates that dissolution and collapse have not been confined to the modern landscape but have been active processes in this area for long intervals in geologic time.

In east-central New Mexico near Santa Rosa, karst topography developed during Late Triassic time, but evidence for Triassic karst development in southeastern New Mexico has not been seen. However, dissolution of Permian salt in the western part of the Delaware basin may have begun as early as Jurassic time. During this time southern New Mexico was above sea level and there was probably considerable erosion. South of New Mexico, in western Texas, near-shore marine conditions prevailed during at least part of Jurassic time (Albritton, 1938, p. 1764). In central New Mexico continental Jurassic rocks were derived from the south. These relations, as well as the regional pattern of thinning of Triassic rocks, indicate an area of extensive erosion in southern New Mexico during Jurassic time (fig. 6).

Rocks of Triassic age wedge out to a featheredge on Permian rocks in southern New Mexico. Rocks of Cre-

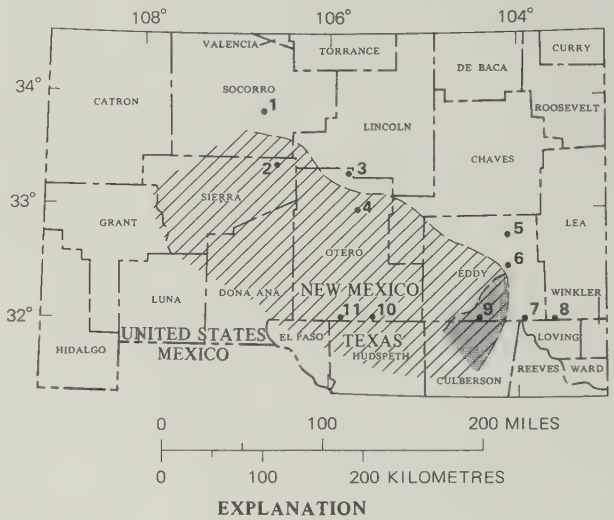

FIGURE 6.—Map showing extent of Jurassic erosion in southern New Mexico. Control points: 1, Carthage coal field (Triassic less than 500 ft thick; Wilpolt and Wanek, 1951). 2, North San Andres Mountains (Triassic absent, Cretaceous rests on Permian; Bachman and Harbour, 1970). 3, Southern Sierra Blanca (Triassic about 100 ft thick; G. O. Bachman, unpub. data). 4, North Sacramento Mountains (Triassic absent, Cretaceous rests on Permian; Pray and Allen, 1956). 5, Crow Flats (Triassic about 50+ ft thick, chaos structure). 6, Northeast Carlsbad (Triassic remnants present in sinkholes). 7, Red Bluff Reservoir (Triassic present). 8, South Lea County (Triassic present). 9, Black River valley (Triassic absent, Cretaceous remnant present in sinkhole; Lang, 1947). 10, Cornudas Mountains (Triassic absent, Cretaceous rests on Permian). 11, Otero Mesa (Triassic absent, Cretaceous rests on Permian).

taceous age lap across this wedgeout at some places. These places indicate the configuration of the line of pre-Cretaceous zero thickness of Triassic strata and outline the area of southern New Mexico, including a portion of the Delaware basin, where Permian rocks were unprotected by Triassic strata during Jurassic erosion. Probably some dissolution of Permian salt and gypsum occurred in the western part of the Delaware basin at this time. During Cretaceous time the entire region was submerged below sea level and presumably neither erosion nor dissolution was an effective process.

Extensive erosion, presumably accompanied by dissolution of Permian salts, occurred during parts of Tertiary time. However, there are no sedimentary records of these events that can be related directly to the formation of modern karst topography.

The earliest and most widespread datum for determining the relative time of solution and collapse of many modern karst features is the Pleistocene Mescalero caliche. I believe that the Mescalero caliche is pedogenic and that it formed on an undulatory, stable surface. Pedogenic caliche—like other soils—probably would not form on steep slopes. However, along the margins of some major depressions the Mescalero dips steeply—nearly vertically in places; yet this caliche is comparable in thickness and morphology to adjacent horizontal profiles. In addition, fracturing and slumping of the Mescalero along the margins of these depressions indicate collapse after Mescalero time. Major solution and collapse of the surface preceded and followed the accumulation of the Mescalero caliche in Nash Draw, Clayton Basin, and at Crow Flats.

Crow Flats is a large collapse feature about 24 km (15 mi) east of Artesia (fig. 7). Evidence for at least three episodes of solution and collapse is preserved there. These episodes occurred (1) after Triassic and before Gatuna time, (2) during or after Gatuna time, and (3) after Mescalero time.

At Crow Flats dolomite and gypsum of the Permian Rustler Formation are the oldest rocks exposed. These rocks are overlain by conglomeratic, crossbedded, dark-reddish-brown sandstone of the Upper Triassic Dockum Group. South of Pavo Mesa for about 11 km (8 mi) along the east side of Crow Flats, Triassic and Permian rocks are contorted and fractured and exposed as chaotic, angular blocks. At many places Triassic rocks fill collapse sinks at least 15 m (50 ft) deep in Rustler gypsum. These sinks formed after the Triassic rocks were indurated and possibly as early as Jurassic time when the entire region was uplifted and eroded. Certainly this collapse occurred before Gatuna time because the Gatuna Formation rests unconformably on these chaotic structures.

Southwest of the Nakee Ishee Lakes the Gatuna Formation itself dips persistently northeast with apparent dips of as much as 20°. East and southeast of the lakes the Gatuna is relatively flat lying and cuts unconformably across the steeply dipping Gatuna beds. The steep dips in the Gatuna are interpreted as partly depositional and partly a result of collapse before Mescalero time.

At another place along the eastern edge of the exposure of chaotic rocks (NW¼ sec. 14, T. 17 S., R. 28 E.), the Gatuna Formation is at least 10 m (33 ft) below the uppermost exposures of Triassic rocks. These exposures of Gatuna are about 700 m (2,000 ft) wide and are roughly circular in plan. They are sinkhole fillings capped by relatively undisturbed Mescalero caliche.

At the north end of Pavo Mesa the Mescalero caliche is relatively flat lying and truncates dipping beds of the Gatuna Formation. However, along the east side of Pavo Mesa the Mescalero dips east and northeast; dips range from about 10° to nearly vertical. On Pavo Mesa the Mescalero caliche is at the 3,700-ft contour. Along a low escarpment southeast of the Nakee Ishee Lakes the Mescalero is fractured and is at the 3,590-ft contour. This indicates a displacement of 30 m (110 ft) since the caliche formed. Observations of similar displacements indicate that Clayton Basin has subsided more than 30 m (100 ft) and parts of Nash Draw have subsided as much as 55 m (180 ft) since Mescalero time.

Surface measurements and drilling data were used to compile a contour map with the Mescalero caliche as the datum for an area in eastern Eddy and western Lea Counties (fig. 8). This map shows gross topographic features of both Mescalero and post-Mescalero time and delineates some areas that have collapsed since Mescalero time. Relatively uniform spacing of contours beneath the Querecho Plains suggests that this represents an original slope on the Mescalero surface. The Mescalero surface dips southwestward, away from the High Plains, about 5.5–7.5 m/km (30–40 ft/mi). The uniform spacing of contours between The Divide and Livingston Ridge suggests that this surface also approaches its original slope. The closed contour at 3,700 ft around The Divide indicates that this area has been a drainage divide between San Simon Swale and Nash Draw at least since Mescalero time. A prominent swale east of Gatuna Canyon may indicate a relict Gatuna drainage system. At present this swale is occupied by several prominent depressions that include Williams Sink and Laguna Plata. These depressions do not appear to be collapse features and there is no evidence in the subsurface for dissolution of salts beneath these depressions. They are here interpreted as

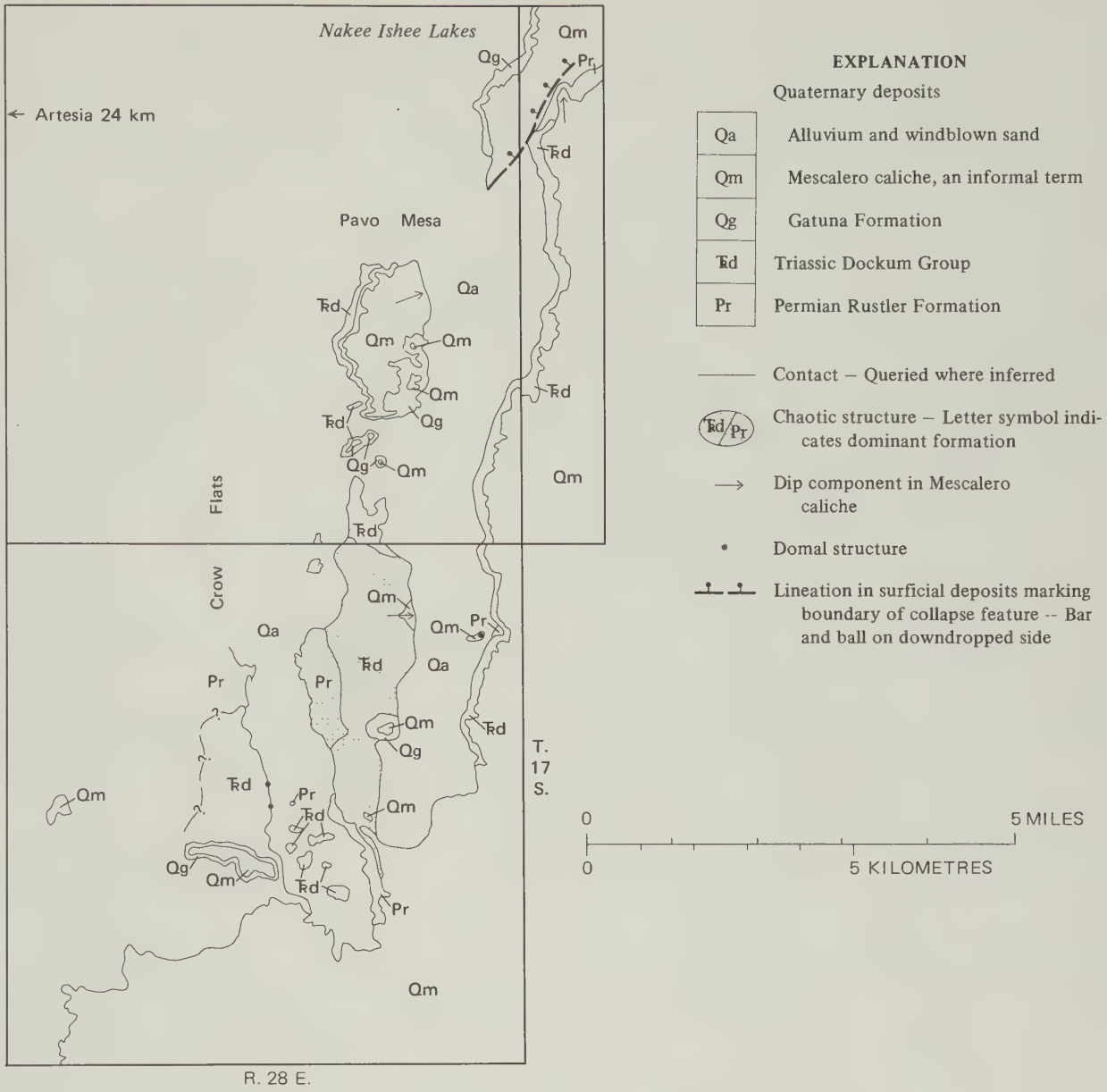
Nakee Ishee Lakes
← Artesia 24 km
Pavo Mesa
Flats
Crow
T. 17 S.
R. 28 E.
EXPLANATION
Quaternary deposits
Qa Alluvium and windblown sand
Qm Mescalero caliche, an informal term
Qg Gatuna Formation
Trd Triassic Dockum Group
Pr Permian Rustler Formation
Contact – Queried where inferred
Chaotic structure – Letter symbol indicates dominant formation
Dip component in Mescalero caliche
Domal structure
Lineation in surficial deposits marking boundary of collapse feature -- Bar and ball on downdropped side
0 5 MILES
0 5 KILOMETRES

FIGURE 7.—Geologic sketch map of Crow Flats area east of Artesia, N. Mex.

blowouts within the relict drainage. Closely spaced contours around Clayton Basin and Nash Draw delineate these post-Mescalero features.

REFERENCES CITED

Albritton, C. C., Jr., 1938, Stratigraphy and structure of the Malone Mountains, Texas: Geol. Soc. America Bull., v. 49, no. 12, p. 1747–1806.

Bachman, G. O., and Harbour, R. L., 1970, Geologic map of the northern part of the San Andres Mountains, central New Mexico: U.S. Geol. Survey Misc. Geol. Inv. Map I–600.

Baker, C. L., 1915, Geology and underground waters of the northern Llano Estacado: Texas Univ. Bull. 57, 225 p.

Bretz, J. Harlen, and Horberg, C. L., 1949, The Ogallala Formation west of the Llano Estacado: Jour. Geology, v. 57, no. 5, p. 477–490.

Fiedler, A. G., and Nye, S. S., 1933, Geology and groundwater resources of the Roswell artesian basin, New Mexico: U.S. Geol. Survey Water-Supply Paper 639, 372 p.

Flint, R. F., 1955, Pleistocene geology of eastern South Dakota; U.S. Geol. Survey Prof. Paper 262, 173 p.

Frye, J. C., 1970, The Ogallala Formation—a review, *in* Mattox. R. B., and Miller, W. D., eds., The Ogallala aquifer—A symposium: Internat. Center for Arid and Semi-Arid Land Studies Spec. Rept. 39, p. 5–14.

Frye, J. C., and Leonard, A. B., 1957, Ecological interpretations of Pliocene and Pleistocene stratigraphy in the Great Plains region: Am. Jour. Sci., v. 255, no. 1, p. 1–11.

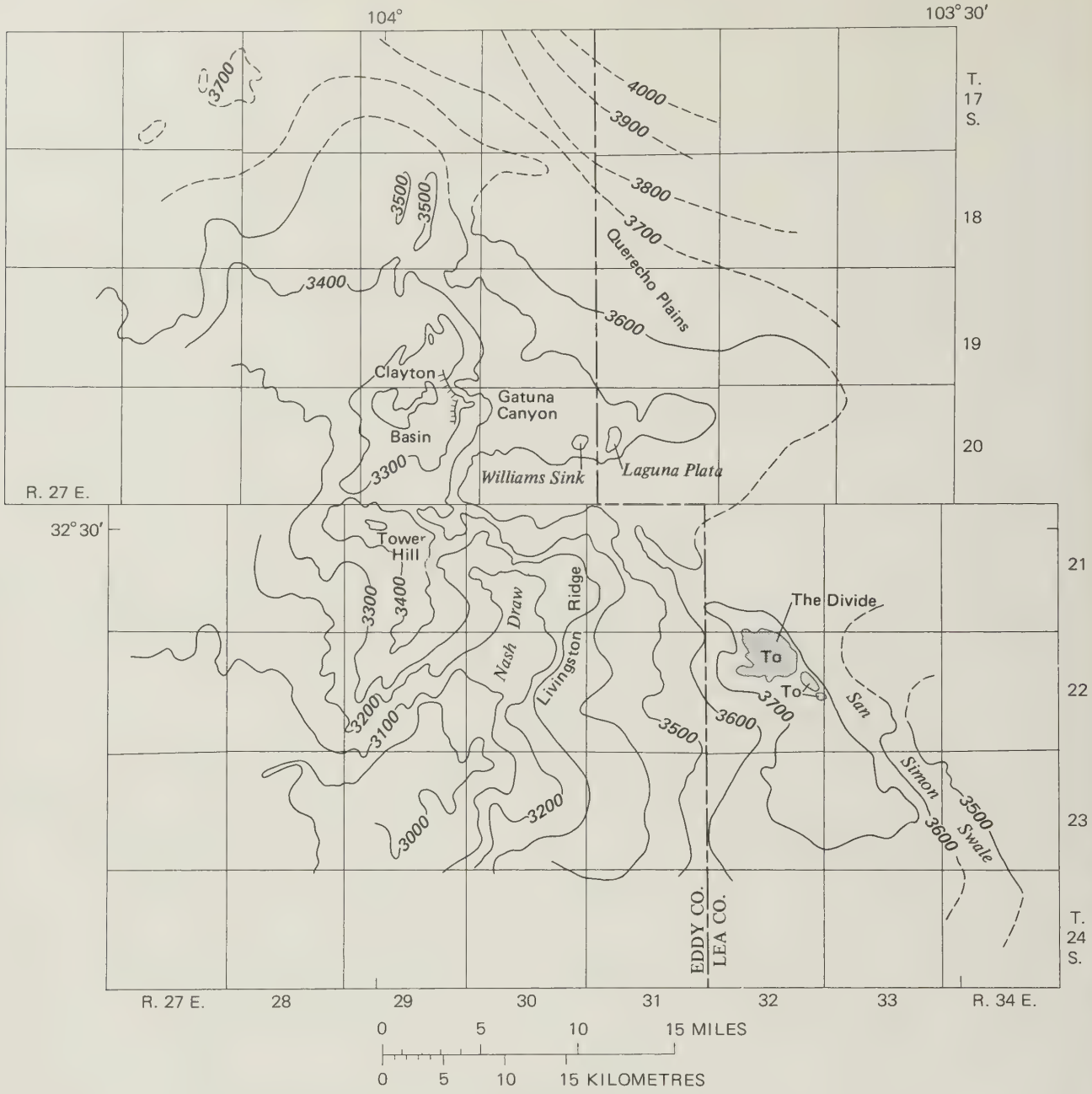

EXPLANATION

Slump in Mescalero caliche

To — Ogallala Formation at The Divide

—— 3300 —— Structure contours on Mescalero caliche — Dashed where control is sparse. Interval is 100 feet (30.5 m)

---3200---

FIGURE 8.—Structure contour map of Mescalero caliche.

——— 1965, Quaternary of the southern Great Plains, *in* Wright, H. E., and Frey, D. G., eds., The Quaternary of the United States: Princeton, N. J., Princeton Univ. Press, p. 203–216.

Gile, L. H., Peterson, F. F., and Grossman, R. B., 1966, Morphological and genetic sequences of carbonate accumulations in desert soils: Soil Sci., v. 101, no. 5, p. 347–360.

Goddard, E. N., chm., and others, 1948, Rock-color Chart: Natl. Research Council (repr. by Geol. Soc. America, 1951, 1970), 6 p.

Hack, J. T., 1941, Dunes of the western Navajo Country: Geog. Rev., v. 31, no. 2, p. 240–263.

Havens, J. S., 1966, Recharge studies on the High Plains in northern Lea County, New Mexico: U.S. Geol. Survey Water-Supply Paper 1819–F, 52 p.

Hayes, P. T., 1964, Geology of the Guadalupe Mountains, New Mexico: U.S. Geol. Survey Prof. Paper 446, 69 p.

Hayes, P. T., and Koogle, R. L., 1958, Geology of the Carlsbad Caverns West quadrangle: U.S. Geol. Survey Geol. Quad. Map GQ–112 [1959].

Hibbard, C. W., 1960, Pleistocene mammalian local faunas from the Great Plains and central lowland provinces of the United States, *in* Dort, Wakefield, and Jones, J. K., eds., Pleistocene and Recent environments of the central Great Plains: Kansas Univ. Dept. Geol. Spec. Pub. 3, p. 395–433.

Horberg, C. L., 1949, Geomorphic history of the Carlsbad Caverns area, New Mexico: Jour. Geology, v. 57, no. 5, p. 464–476.

Jones, C. L., 1973, Salt deposits of Los Medanos area, Eddy and Lea Counties, New Mexico, with sections on Groundwater hydrology, by M. E. Cooley, *and* Surficial geology, by G. O. Bachman: U.S. Geol. Survey open-file report, 65 p.

Kelley, V. C., 1971, Geology of the Pecos country, southeastern New Mexico: New Mexico Bur. Mines and Mineral Resources Mem. 24, 75 p.

King, P. B., 1942, Permian of west Texas and southeastern New Mexico: Am. Assoc. Petroleum Geologists Bull., v. 26, no. 4, p. 535–763.

——— 1948, Geology of the southern Guadalupe Mountains, Texas: U.S. Geol. Survey Prof. Paper 215, 183 p. [1949].

Kottlowski, F. E., Cooley, M. E., and Ruhe, R. V., 1965, Quaternary geology of the southwest, *in* Wright, H. E., and Frey, D. G., eds., The Quaternary of the United States: Princeton, N.J., Princeton Univ. Press, p. 287–298.

Lang, W. B., 1947, Occurrence of Comanche rocks in Black River Valley, New Mexico: Am. Assoc. Petroleum Geologists Bull., v. 31, no. 8, p. 1472–1478.

Lee, W. T., 1925, Erosion by solution and fill: U.S. Geol. Survey Bull. 760–C, p. 107–121.

Morgan, A. M., 1942, Solution-phenomena in the Pecos basin in New Mexico: Am. Geophys. Union Trans., v. 23, p. 27–35.

Motts, W. S., 1962, Geology of the West Carlsbad quadrangle, New Mexico: U.S. Geol. Survey Geol. Quad. Map GQ–167.

Nicholson, Alexander, Jr., and Clebsch, Alfred, Jr., 1961, Geology and ground-water conditions in southern Lea County, New Mexico: New Mexico Bur. Mines and Mineral Resources Ground-Water Rept. 6, 123 p.

Pray, L. C., and Allen, J. E., 1956, Outlier of Dakota(?) strata, southeastern New Mexico: Am. Assoc. Petroleum Geologists, Bull., v. 40, p. no. 11, 2735–2740.

Price, W. A., 1943, Greater American deserts: Texas Acad. Sci. Proc. and Trans. 1943, v. 27, p. 163–170.

Price, W. A., 1958, Sedimentology and Quaternary geomorphology of south Texas: Gulf Coast Assoc. Geol. Socs. Trans., v. 8, p. 41–75.

Robinson, T. W., and Lang, W. B., 1938, Geology and groundwater conditions of the Pecos River Valley in the vicinity of Laguna Grande de la Sal, New Mexico, with special reference to the salt content of the river water: New Mexico State Engineer 12th and 13th Bienn., Rept. 1934–38, p. 77–100 [1939].

Thomas, R. G., 1972, The geomorphic evolution of the Pecos River system: Baylor Geol. Studies Bull. 22, 40 p.

Vine, J. D., 1963, Surface geology of the Nash Draw quadrangle, Eddy County, New Mexico: U.S. Geol. Survey Bull. 1141–B, 46 p.

Wilpolt, R. H., and Wanek, A. A., 1951, Geology of the region from Socorro and San Antonio east to Chupadera Mesa, Socorro County, New Mexico: U.S. Geol. Survey Oil and Gas Inv. Map OM–121.

Jour. Research U.S. Geol. Survey
Vol. 4, No. 2, Mar.–Apr. 1976, p. 151–162

THE PLACER RIVER SILT—AN INTERTIDAL DEPOSIT CAUSED BY THE 1964 ALASKA EARTHQUAKE

By A. T. OVENSHINE, DANIEL E. LAWSON,[1] and SUSAN R. BARTSCH-WINKLER,
Menlo Park, Calif., Urbana, Ill., Menlo Park, Calif.

Abstract.—At the head of Turnagain Arm near Anchorage, the major lasting geologic consequence of the Alaska earthquake of 1964 was deposition of the Placer River Silt, an intertidal deposit covering an area of more than 18 km^2 and containing more than 20×10^6 m^3 of sediment. This formation, which was derived from erosion of intertidal bars in Turnagain Arm, averages 1.5 m thick seaward of the Seward Highway and 0.9 m thick landward. Its distribution is controlled both by the arrangement of the major streams that enter tidewater and by manmade features such as the highway and railroad embankments. The Placer River Silt is still being deposited. The contemporary lowland sedimentation system of the Portage area includes a number of depositional settings: (1) In the Placer River Silt— upper tidal flats, levees, and channelway fans, (2) elsewhere in the intertidal zone—tidal stream channels, lower tidal flats, and saltwater marsh, and (3) in the supratidal zone—gravel levees, freshwater marsh, bogs, and lakes. Since 1964, the critical environmental results of the earthquake-caused deposition have been abandonment of the settlement of Portage, formation of an unsightly blanket of silt, destruction of natural plant communities, localized erosion, and creation of quicksand hazards.

The Alaska earthquake of March 27, 1964, caused land subsidence in the Portage area (fig. 1) amounting to at least 2.4 m. Of this, slightly more than 1.6 m resulted from regional tectonic subsidence and 0.8 m was from local subsidence (McCulloch and Bonilla, 1970, p. D128 and fig. 114), probably related to seismically induced compaction in the 300 m (Dennis Kalpacoff, oral commun., 1973) of unconsolidated sediment that underlies the area. The subsidence allowed high tides to inundate approximately 18 km^2 of land that had been above sea level, resulting in deposition of more than 20×10^6 m^3 of fine-grained intertidal sediment. This report describes this sediment and the contemporary sedimentation system at Portage and notes some of the environmental consequences of its deposition.

The Portage area, about 77 km southeast of Anchorage, was within the area of maximum damage and shaking related to the Alaska earthquake of 1964. The small roadside settlement of Portage was abandoned after the earthquake; present habitation is limited to one house and several mobile homes associated with a service station. The area is crossed by the Seward Highway and contains the junction of the Whittier and Seward spurs of The Alaska Railroad.

Portage is situated at the mouths of three broad, alluviated valleys—Twentymile, Portage, and Placer—separated by steep bedrock ridges that rise 900–1,200 m above the valley floors. Bedrock in the region is Jurassic(?) and Cretaceous graywacke, siltite, and argillite assigned to the Valdez(?) Group (Clark, 1972). The valleys in the Portage area, 1.5–2.5 km wide and within 10 m of sea level, are underlain by Holocene sands and gravels that interfinger with tidal silts and sands about 1 km landward of the present shoreline. The water table is within 1.5 m of the ground surface throughout most of the area. Large fast-flowing braided streams near the midlines of each of the three valleys typically are flanked by well-drained natural levees underlain by sand and gravel. Much of the water in the streams originates in snowfields of the Chugach Mountains and in glaciers that descend to low altitudes at the heads of the valleys. Between the levees and the bedrock valley walls is grassy or sparsely forested freshwater marsh and bog.

The streams reach tidewater at the head of Turnagain Arm, a southeast-trending, 72-km-long marine embayment at the northeast end of Cook Inlet. Turnagain Arm is noteworthy for its high tidal range (10 m), frequent occurrence of bore tides, and extensive development of intertidal sand bars. No data on tide characteristics are available for the Portage area, but our observations during the summer of 1973 suggest a tidal range of 8 m or more and lag in the start of flooding of 4 hours or more relative to Anchorage.

[1] University of Illinois.

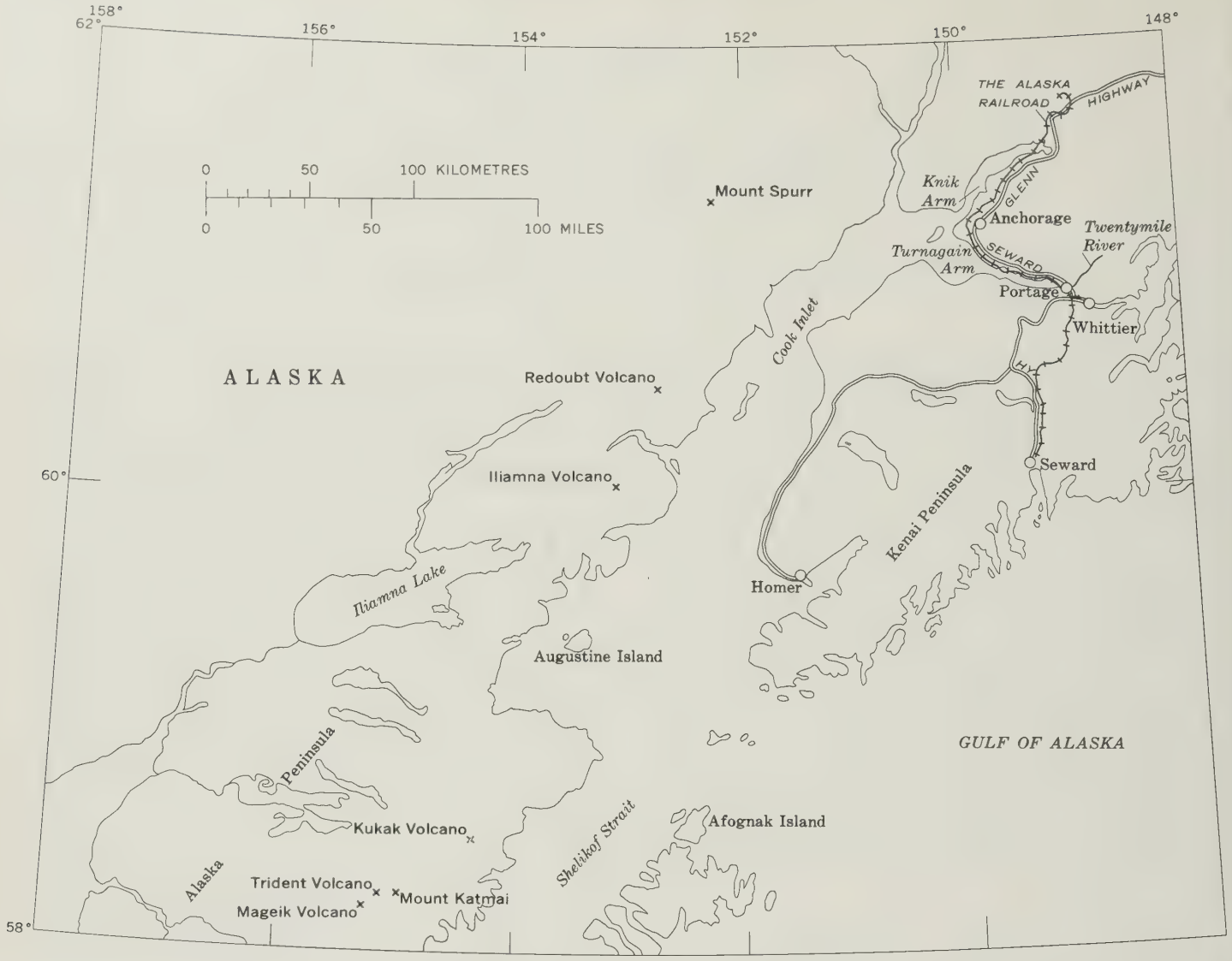

FIGURE 1.—Location of the Portage area in Alaska. Active volcanoes on the west side of Cook Inlet indicated by X.

THE PLACER RIVER SILT

The deposits of intertidal origin that resulted from the Alaska earthquake make up a recognizable geologic unit that has been mapped throughout the Portage area (fig. 2). This unit, here named the Placer River Silt for its occurrence on Placer River, commonly overlies a soil horizon rich in organic material. In 1973 the Placer River Silt was still being deposited.

The best exposures of the formation are in the steep banks of Portage Creek and Placer and Twentymile Rivers. The exposure in the north bank of the north fork of Portage Creek west of the Seward Highway is designated the type section (fig. 3*D*). Excellent exposures occur in many of the small channels that cross the tidal flats seaward of the Seward Highway.

Sections of the Placer River Silt have been measured at five localities shown in figure 3: Ingram Creek (*A*), Placer River (*B* and *C*), Portage Creek (*D*), and Twentymile River (*E*).

Base of the Placer River Silt

As shown in the measured sections (fig. 3), the Placer River Silt overlies a buried soil and vegetation horizon developed on an older unit of intertidal silts. These older silts, in contrast to the post-1964 silts, are relatively firmly compacted and contain abundant yellowish-orange and yellowish-brown oxidized zones that encapsulate rootlets, twigs, or other buried plant debris.

The soil horizon developed at the top of the older silt ranges in thickness from a few centimetres to more

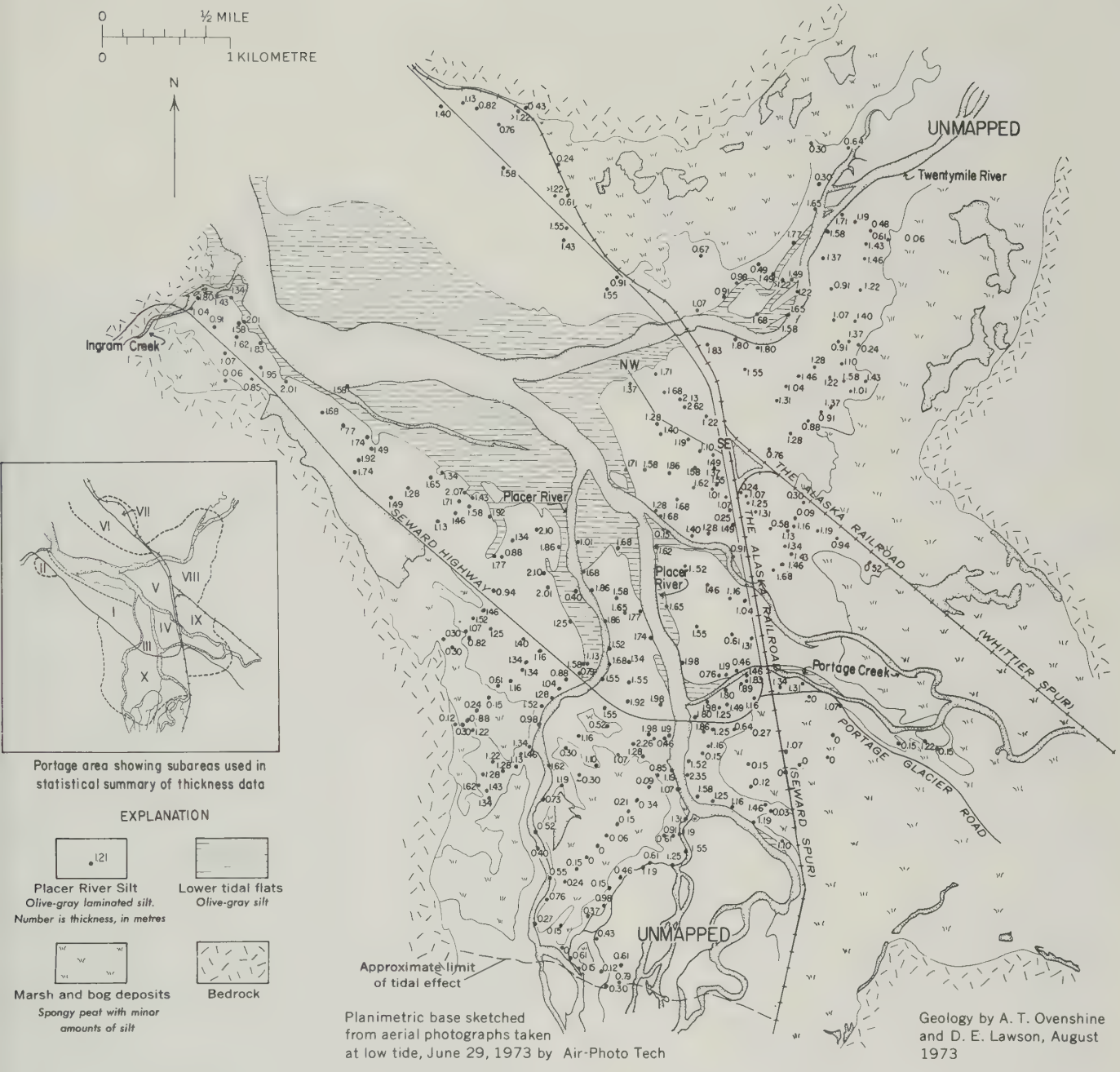

FIGURE 2.—Geologic sketch map showing distribution of the Placer River Silt and depositional framework of the Portage area.

than several tens of centimetres and is recognized mainly by a high proportion of nearly undecayed vegetable matter. The nature of the soil varies according to the plant community that lived on it at the time of the earthquake: in areas that were forest or alder thicket, the soil is a centimetre or more of black leaf duff overlying 1–10 cm of brown rootlet-bearing silt; in areas that were bog or marsh, from 1 to 5 cm of spongy black malodorous peat composed of partly decayed grass blades, sphagnum moss, and rootlets; in areas that were grassland, as much as 30 cm of compacted silt bound together by a lacework of grass roots. The grassland soil is well exposed in the shoreline bluffs of Turnagain Arm between Placer and Ingram Creeks. During storm high tides, blocks of this rootbound silt as much as 1 m² in area and 0.3 m in thickness are eroded and transported hundreds of metres across the tidal flats.

Before the Alaska earthquake, the Portage area had a variety of plant communities including spruce and cottonwood forest, willow and alder thickets, well-

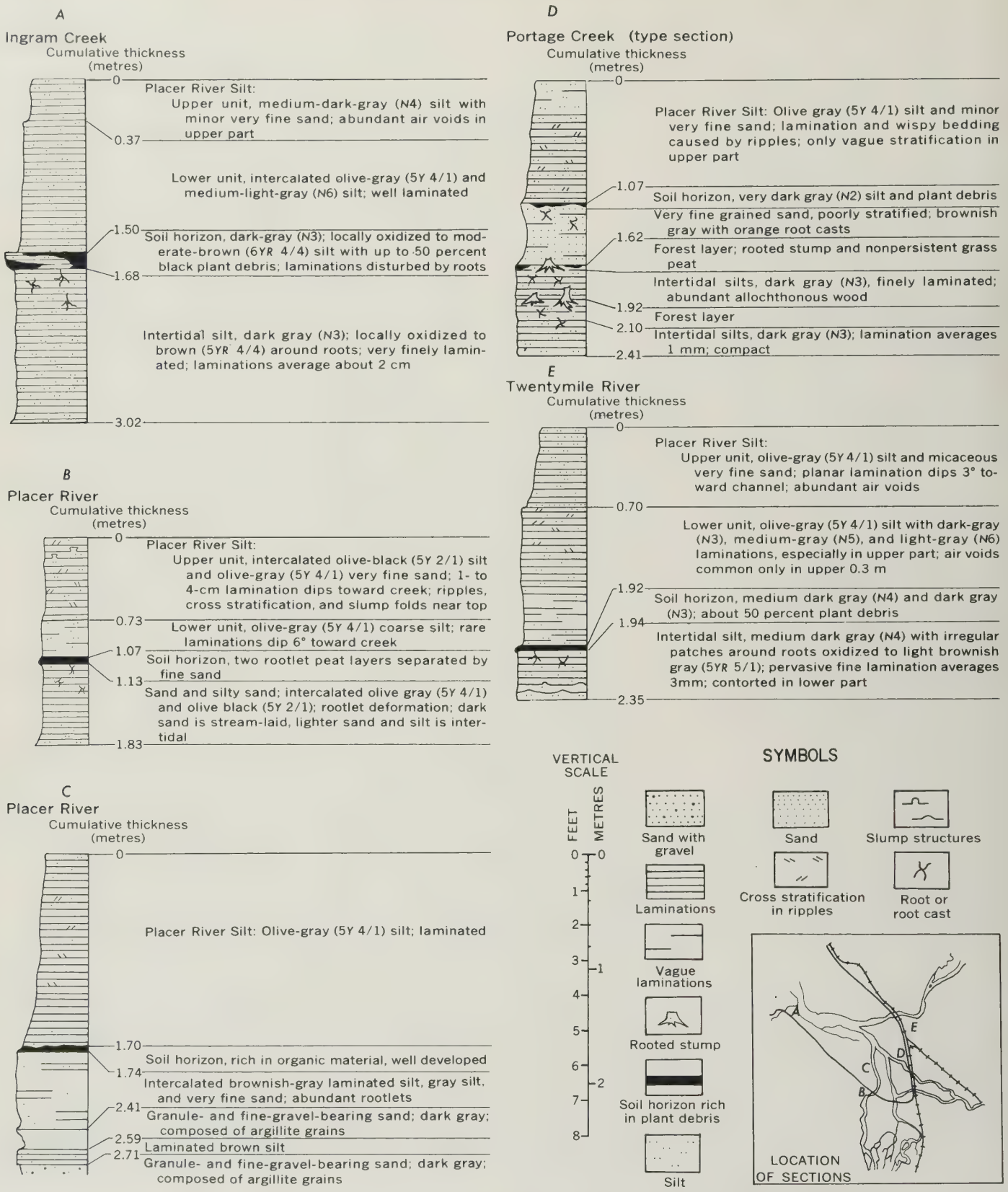
A
Ingram Creek
Cumulative thickness (metres)
0
Placer River Silt:
Upper unit, medium-dark-gray (N4) silt with minor very fine sand; abundant air voids in upper part
0.37
Lower unit, intercalated olive-gray (5Y 4/1) and medium-light-gray (N6) silt; well laminated
1.50
Soil horizon, dark-gray (N3); locally oxidized to moderate-brown (6YR 4/4) silt with up to 50 percent black plant debris; laminations disturbed by roots
1.68
Intertidal silt, dark gray (N3); locally oxidized to brown (5YR 4/4) around roots; very finely laminated; laminations average about 2 cm
3.02
B
Placer River
Cumulative thickness (metres)
0
Placer River Silt:
Upper unit, intercalated olive-black (5Y 2/1) silt and olive-gray (5Y 4/1) very fine sand; 1- to 4-cm lamination dips toward creek; ripples, cross stratification, and slump folds near top
0.73
Lower unit, olive-gray (5Y 4/1) coarse silt; rare laminations dip 6° toward creek
1.07
Soil horizon, two rootlet peat layers separated by fine sand
1.13
Sand and silty sand; intercalated olive gray (5Y 4/1) and olive black (5Y 2/1); rootlet deformation; dark sand is stream-laid, lighter sand and silt is intertidal
1.83
C
Placer River
Cumulative thickness (metres)
0
Placer River Silt: Olive-gray (5Y 4/1) silt; laminated
1.70
Soil horizon, rich in organic material, well developed
1.74
Intercalated brownish-gray laminated silt, gray silt, and very fine sand; abundant rootlets
2.41
Granule- and fine-gravel-bearing sand; dark gray; composed of argillite grains
2.59
Laminated brown silt
2.71
Granule- and fine-gravel-bearing sand; dark gray; composed of argillite grains
D
Portage Creek (type section)
Cumulative thickness (metres)
0
Placer River Silt: Olive gray (5Y 4/1) silt and minor very fine sand; lamination and wispy bedding caused by ripples; only vague stratification in upper part
1.07
Soil horizon, very dark gray (N2) silt and plant debris
Very fine grained sand, poorly stratified; brownish gray with orange root casts
1.62
Forest layer; rooted stump and nonpersistent grass peat
Intertidal silts, dark gray (N3), finely laminated; abundant allochthonous wood
1.92
Forest layer
2.10
Intertidal silts, dark gray (N3); lamination averages 1 mm; compact
2.41
E
Twentymile River
Cumulative thickness (metres)
0
Placer River Silt:
Upper unit, olive-gray (5Y 4/1) silt and micaceous very fine sand; planar lamination dips 3° toward channel; abundant air voids
0.70
Lower unit, olive-gray (5Y 4/1) silt with dark-gray (N3), medium-gray (N5), and light-gray (N6) laminations, especially in upper part; air voids common only in upper 0.3 m
1.92
Soil horizon, medium dark gray (N4) and dark gray (N3); about 50 percent plant debris
1.94
Intertidal silt, medium dark gray (N4) with irregular patches around roots oxidized to light brownish gray (5YR 5/1); pervasive fine lamination averages 3mm; contorted in lower part
2.35
VERTICAL SCALE
FEET
METRES
0
1
2
3
4
5
6
7
8
0
1
2
SYMBOLS
Sand with gravel
Laminations
Vague laminations
Rooted stump
Soil horizon rich in plant debris
Silt
Sand
Cross stratification in ripples
Slump structures
Root or root cast
LOCATION OF SECTIONS
A
B
C
D
E

FIGURE 3.—Measured sections of the Placer River Silt.

drained and marshy grasslands, and sphagnum bogs. After the earthquake, these communities were killed by the change to a saltwater environment, but sedimentation was so rapid that nearly all trees and shrubs were buried intact, in upright position (figs. 4 and 5). Ten years after the earthquake, the parts of the plants that project above the silt were desiccated and brittle and were being broken off in increasingly large numbers with each passing year. The buried parts of the plants, however, were little decayed and retained their bark, fresh wood color, and much of the strength of living plant tissue. One of the principal future characteristics of the Placer River Silt will be its extensive preservation of upright rooted stumps in a peat-bearing soil layer.

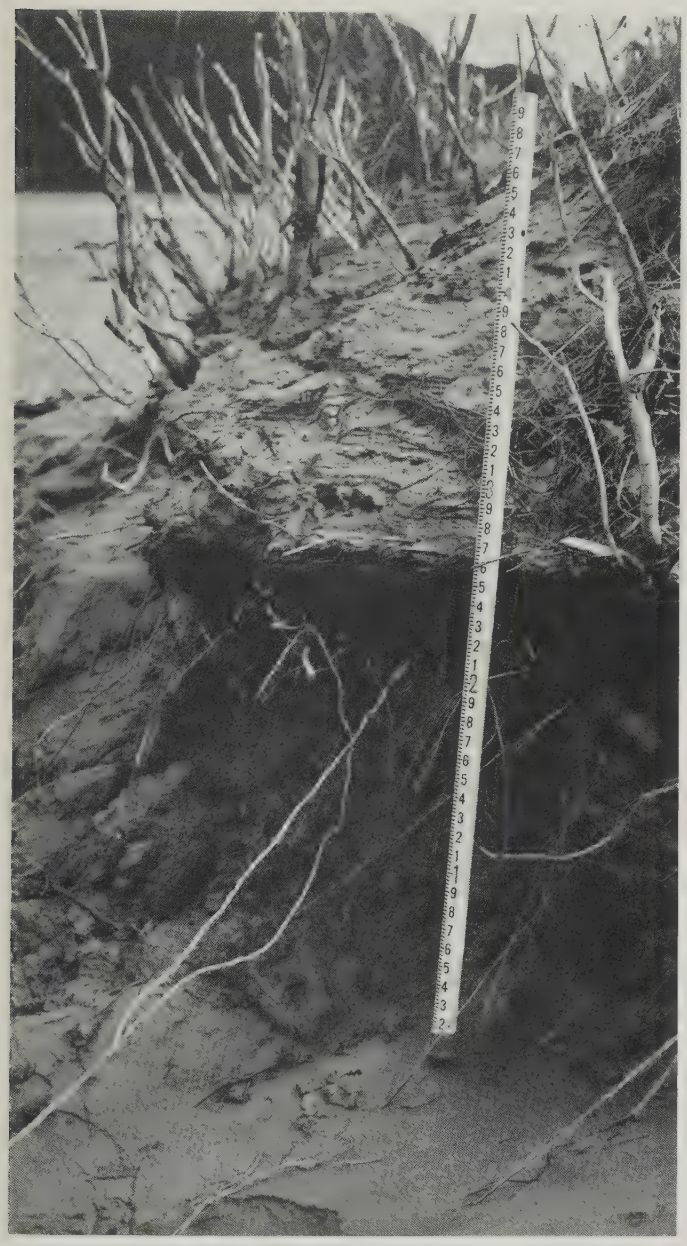

FIGURE 4.—Tidal stream cutbank exposing alder thicket killed and buried by deposition of the Placer River Silt. The pre-Placer River soil horizon is at 1.6 ft on the measuring rod. Bank of Portage Creek, seaward of the Seward Highway.

LITHOLOGY

The Placer River Silt is a thin-bedded to laminated micaceous silt that locally contains thin intercalations of silty clay or very fine grained sand. The predominant color is olive gray (5*Y* 4/1), darkening when wet; individual clay or very fine sand laminations range from medium dark gray (*N*4) to medium light gray (*N*6).

Under the hand lens, the sediment is uniform in composition, appears well sorted, and consists of medium and coarse silt-size grains of quartz and feldspar (60 percent), green and black rock fragments (25 percent), and mica (15 percent). The quartz and feldspar grains are angular and equant, whereas the lithic fragments are angular to subround and range from equant to rod or plate shaped. Muscovite, biotite, and chlorite occur in cleavage flakes and elongate shreds as much as 1 mm in length.

Examination of samples taken along the profile from Twentymile River to the highway indicates that the silt consists of quartz (30 percent), quartzose lithic fragments (25 percent), feldspar (20 percent), hornblende (15 percent), and chlorite plus mica (15 percent). Trace constituents are glauconite(?), opaque minerals, garnet, apatite, colorless and brown volcanic glass, and diatoms. All the grains are angular, and except for iron staining of some of the lithic fragments, all are fresh and unaltered.

Plant debris is the only constituent of organic origin that is at all common in the Placer River Silt. In most sections, material such as twigs, limbs and logs, bark fragments, willow and cottonwood leaves, and spruce needles are dispersed rather than concentrated in layers and make up less than 3 percent of the sediment volume. At no place in the Portage area was evidence of sediment infauna found, although centimetre-size valves of *Macoma* sp. are transported from Turnagain Arm and, rarely, incorporated in the formation.

In figure 6 are the results of pipet grain-size analysis of eight surface samples from the locations shown on the profile of figure 7. Attempts to draw separate curves on the same plot for each of the eight samples analyzed were unsuccessful, because many of the data points were coincident or nearly so. Shown in figure 6 are "average" curves drawn through points that represent the means at each phi class boundary of percentage

FIGURE 5.—Spruce forest buried by the Placer River Silt, Portage Creek tidal flats. Augering in the tidal channel (foreground) showed that 1.83 m of silt had accumulated between 1964 and 1973.

values obtained by analysis of the eight samples. Standard deviations for the means used in constructing the frequency percent curve are also shown on the figure and indicate that the variations in percentages are generally small.

Slightly less than 97 percent of the sediment is silt size, and most (91 percent) is medium and coarse silt. The median diameter is 37μm and the Folk graphic mean diameter is 35 μm. The grain-size distribution is moderately well sorted (Folk inclusive graphic standard deviation = 0.64 phi units) and moderately fine skewed (Folk inclusive graphic skewness = 0.43 phi units).

The samples analyzed show no systematic grain-size trends that can be correlated with distance along the profile. Field observations suggest that although the silt may become finer grained in the marsh areas near the zero edge, the grain-size distribution depicted in figure 6 is probably representative of most of the formation.

The most common sedimentary structures are planar lamination and small-scale cross stratification within ripple marks. The planar lamination, which ranges in thickness from 0.5 to 4 cm and averages about 1 cm, is caused by burial of thin layers of fine silt or clayey silt that are darker in color and less erodable than the medium and coarse silt that makes up an estimated 91 percent of the formation. The planar lamination commonly is laterally persistent for 2 m or more. In channel-bank exposures, it dips 3° to 15° toward the channel axis.

Small-scale cross stratification resulting from the migration and eventual burial of ripple marks is common in most exposures but generally is clearly visible only on outcrop faces that have been cleared of slopewash. Sets of ripples have amplitudes of approximate-

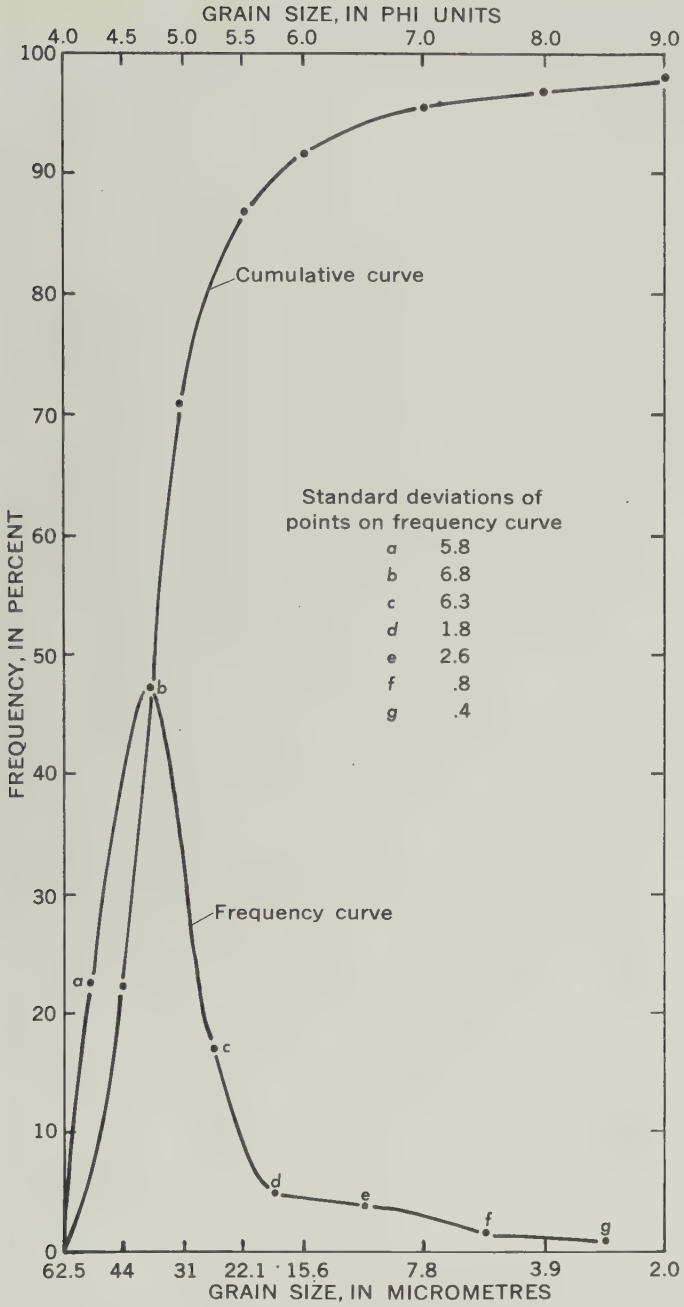

FIGURE 6.—"Average" grain-size frequency and cumulative frequency per phi unit class for eight samples of the Placer River Silt. Sample localities shown in figure 7.

ly 2 cm and wave lengths of 10–15 cm. Commonly, both ebb and flood directions are observed in a single outcrop. Less than 5 percent of the ripples and cross strata observed show oversteepened, convoluted, or folded forms caused by syn- or post-depositional processes.

Thickness and distribution

The distribution of the Placer River Silt is determined to a large extent by the geometry of the three valleys and five streams that intersect at tidewater in the Portage area. The thickness of the formation reflects not only the influences of these elements but also the effects of the highway and railroad embankments, structures that existed before and were rebuilt after the Alaska earthquake.

Thickness measurements of the Placer River Silt (figs. 2 and 7; table 1) were obtained either by hand augering to the vegetation-rich soil layer underlying the formation or hand leveling to the "general sediment surface" from exposures of the buried soil layer in the banks of tidal channels.

For purposes of discussion and statistical summary, the thickness data are grouped into the 10 subareas shown on figure 2 inset. Subareas I, III, IV, V, and VI are tidal flats separated by the major stream channels entering Turnagain Arm and situated inside, or sea-

TABLE 1.—*Thickness and volume of the Placer River Silt by subarea*

Subarea	Number of thickness observations	Average thickness* (m)	Area ($m^2 \times 10^6$)	Sediment volume ($m^3 \times 10^6$)
I	42	1.57	2.01	3.16
II	3	.66	.26	.17
III	16	1.65	.75	1.24
IV	23	1.35	.89	1.20
V	27	1.44	1.11	1.60
VI	6	1.41	1.72	2.43
VII	6	.66	.58	.38
VIII	53	1.21	2.95	3.57
IX	24	.92	1.44	1.33
X	101	.90	6.28	5.65
Totals	301	---	17.99	20.73

* Average thickness:
All subareas 1.18
Subareas I, III, IV, V, VI 1.48
Subareas II, VII, VIII, IX, X ..... .87

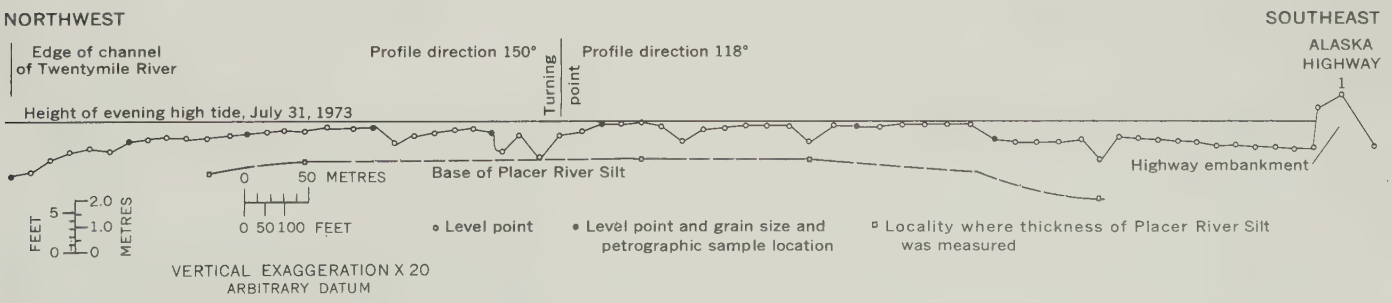

FIGURE 7.—Cross section of the Placer River Silt from the edge of the Twentymile River tidal channel to Alaska Highway 1. Section location shown in figure 2.

ward, of the curve of the Seward Highway as it goes around the head of Turnagain Arm. Subareas II, VIII, IX and X are "outside" the highway and most include the landward or zero edge of the formation. The thickness data grouped in subarea VII are, with two exceptions, from a tidal flat situated between the highway and railroad embankments and connected to Turnagain Arm by only a single culvert 2 ft in diameter.

Seaward of the Seward Highway, the Placer River Silt averages about 1.5 m in thickness; landward of the highway, it averages about 0.9 m. Although factors such as proximity to the sediment source and greater subsidence could cause more accumulation inside the highway, doubtless the single most important factor is the containment effect imposed on the flood tide by the gravel highway embankment. Flow through the embankment can occur only at the culvert connecting subareas VI and VII, at the bridges across the Twentymile and Placer Rivers, and at the two forks of Portage Creek.

In subareas I, III, IV, V and VI, deposition has produced tabular sediment bodies of relatively even thickness. Levees are not typically present along the banks of the major channels, and in the few localities in which they are observed, levees show an estimated relief above the sediment surface of less than 0.3 m. Tidal channels as much as 2 m deep and 25 m wide are present but are less numerous and more widely spaced than in the intricate channelway fan systems that occur landward of the highway in the Placer River area.

Landward of the Seward Highway, the thickness and distribution of the Placer River Silt presents a more complicated pattern controlled largely by the geometry of the major stream channels and to an unknown extent by differential subsidence. In this area, the active depositional elements are levees and channelway fans, both of which are prograding into marshland surrounding freshwater bogs and lakes. In figure 2, the narrow bands of the formation mapped along the main forks of the Placer River are levees 60–250 m wide with relief of as much as 1 m.

The term "channelway fan" is used here to designate areas of active deposition that are lobate to irregular in outline and crossed by numerous small tidal channels. Channelway fans form where one or more tidal channels breach the levees and allow silt-laden flood waters to extend hundreds of metres into the marsh. In the Portage area, channelway fans occur in two places west of the west fork of the Placer River, between the north fork of Portage Creek and the embankment of the Whittier spur of The Alaska Railroad, and on the north side of the Twentymile River.

The thickness data from the south side of the Twentymile River are contoured in figure 8 in order to show the geometry of the sediment body that has formed between 1964 and 1973. The deposit is thickest adjacent to the river and is shown by relatively wide-spaced contours over most of the area. At the distal edge of the deposit, however, the contours are closely spaced, indicating abrupt thinning toward the zero edge. Possibly this almost tabular deposit has formed by the coalescing of a series of channelway fans whose outlines are still partly discernible in the lobate form of the distal edge of the formation.

In the years since 1964 the marshlands beyond the levees and channelway fans have received only minor amounts of silt—generally less than 0.3 m (fig. 2). The grass-dominated plant community seems to be flourishing and keeping pace with the slow buildup of parts of the marsh surface.

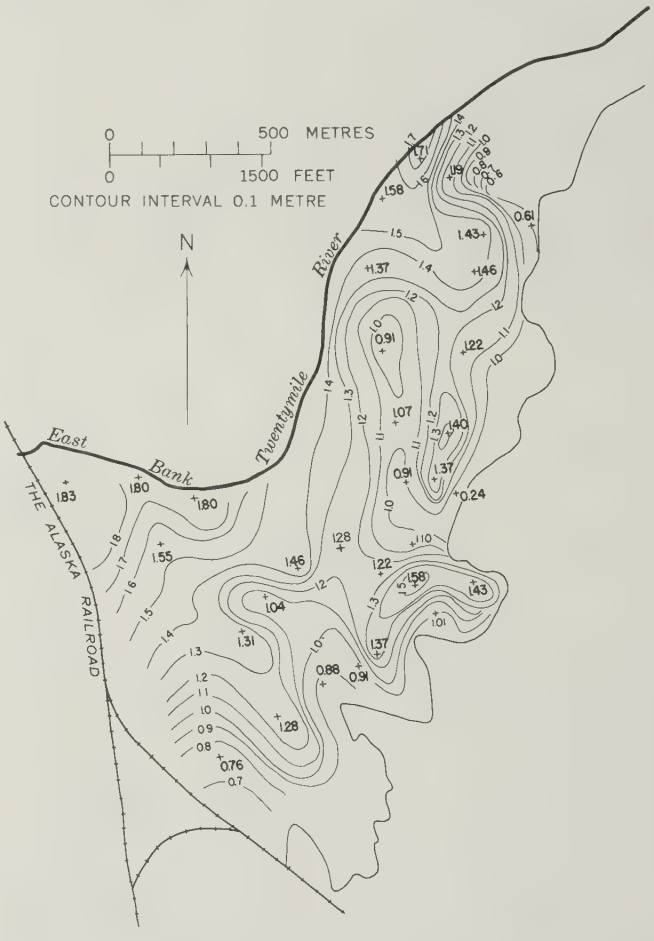

FIGURE 8.—Isopach map of the Placer River Silt on the south side of Twentymile River. Contours are closely spaced near the edge of the deposit and more widely spaced elsewhere.

Source

Source is considered at two levels as follows: The original source is the bedrock terrane from which the sediment was eroded; the immediate source is the location of the sediment prior to movement into the Portage area from 1964 to 1973.

At least three bedrock sources appear to be represented in the Placer River Silt. The quartzose lithic fragments, the chlorite, and much of the quartz are consistent with derivation from the weakly metamorphosed graywacke and argillite that make up the Chugach Mountains surrounding Turnagain Arm. The volcanic glass and the unaltered hornblende associated with it, however, do not occur in the bedrock of the Turnagain watershed and probably were derived from one or more of the active volcanoes on the northwest side of Cook Inlet (fig. 1). They could have reached their present locations through combinations of wind and water currents. There is no major local source for the biotite and plagioclase feldspar that make up a significant part of the sediment. These constituents were probably derived from the batholithic terrane of the Talkeetna Mountains and transported to Knik Arm through the Susitna or Matanuska Rivers. This suggests the existence of currents that sweep sediment from the Knik area into Turnagain Arm.

Prior to the investigations reported here, we believe that the immediate source of all the silt was the alluvium in the valleys of the major streams that meet in tidewater at Portage. However, the inferred bedrock sources far to the north and west and the thickness pattern of the formation are clear indications that the immediate source of the formation is seaward of Portage rather than landward. Probably this immediate source is the extensive intertidal bars of sandy silt that occur throughout Turnagain Arm.

THE SEDIMENTATION SYSTEM OF THE PORTAGE AREA

The Placer River Silt is only one of the recognizable sedimentary elements in the environment of the Portage area. In this section we list and describe briefly some of the intertidal and supratidal settings that occur in this environment of contemporary sedimentation. The characteristics and interrelations of the various settings are the subject of continuing study.

A diagrammatic portrayal of the arrangement of the recognized subdivisions of the intertidal and fluviatile environments, figure 9, points up the importance of zones of maximum sedimentation in the formation of the lowland physiography. The most rapid sedimentation occurs on the tidal flats and on the levees of the supratidal rivers. As these regions build up, drainage from the peripheral areas is impeded and a zone of marshes, bogs, and lakes develops in the vicinity of the valley walls. The distribution of this zone is clearly shown in figure 2.

Intertidal settings

In the intertidal environment, 3 km wide at some places, we now recognize six subdivisions, discussed here in order of decreasing proportion of time covered by the tide.

Tidal stream channels.—The discharge of the streams that flow through the valleys and into Turnagain Arm is sufficient to maintain swift currents in the channels during times of low tide. Surface-water velocities in the channels are in the range from 50 to 150 cm/s on the basis of a single series of observations on the Twentymile River at the start of ebb flow. Standing waves and antidunes are typical features of the water surface. The channel deposits cannot be directly observed, but from study of midchannel bars and channel banks, the streams appear to be moving coarse sand and fine gravel. Large ripples with wave lengths of approximately 1 m and amplitudes of 7 cm are exposed on some bars during low water.

Lower tidal flats.—These flat constructional terraces are graded to the average low-tide water level. The landward juncture of the lower tidal flats with the upper tidal flats is typically an erosional scarp 1–2 m

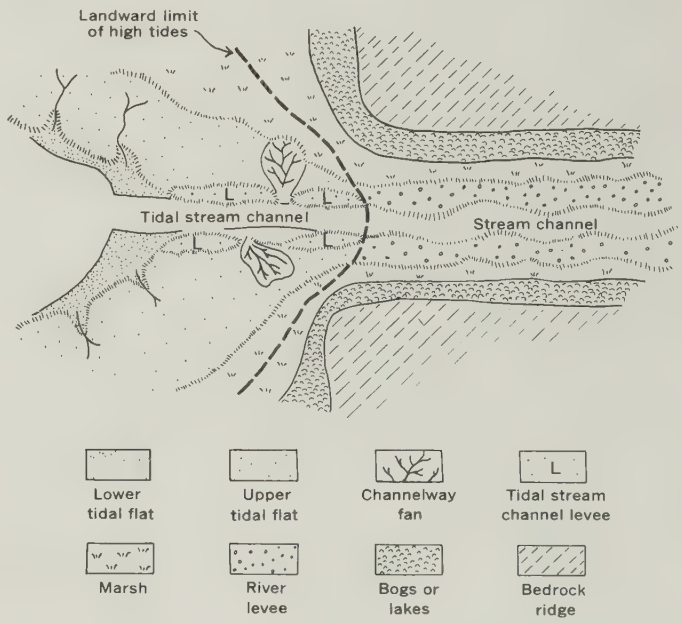

FIGURE 9.—Idealized diagram depicting the major elements in the lowland depositional system of the Portage area.

high and rarely a smooth constructional slope dipping about 35° toward the channel. Rippled silt and very fine sand accumulate on the lower tidal flats. As the water table is nearly at the surface, the sediment is saturated, readily liquefiable, and hazardous to traverse.

Channelway fans.—Channelway fans occur behind the leveed parts of tidal streams where one or more tidal channels breach the levee system. In the Portage area, the channelway fans are flooded during about half of the high tides and appear to be actively prograding into the saltwater marshes. The sediment surface is extremely irregular because of the close spacing of numerous small channels 0.5–1.5 m wide and 0.3–0.5 m deep. Many of the channels are constructional in origin because laminations in their banks dip toward the channel axis at the same angle as the bank face. Interchannel areas support a sparse to abundant flora of salt-tolerant grasses. As deposition continues, channelway fans may coalesce and evolve into upper tidal flats.

Upper tidal flats.—The upper tidal flats are nearly horizontal constructional terraces that are building toward the level of the highest tides that reach the Portage area (fig. 7). The deposits of the upper tidal flats are laminated and rippled silts, commonly exhibiting small voids that originate from air entrapment during rapid flooding. The more landward parts support a sparse flora consisting of two or three types of salt-tolerant grasses.

Levees.—Levees are common only in the upper reaches of the tidal streams, where they probably originate through the formation of current nulls caused by the meeting of seaward-directed streamflow and shoreward-directed tidal flow. Levees do not generally occur at the junction between the lower and upper tidal flats, probably because the boundary is erosional. Levee deposits show air-entrapment voids, laminations, and ripples and are indistinguishable from the sediments of the upper tidal flats.

Saltwater marsh.—The saltwater marsh zone supports a dense growth of several species of salt-tolerant grass and had received less than 0.3 m of sediment from 1964 to 1973. Deposits are fetid fine silt and mud that may exhibit millimetre-scale lamination.

Supratidal settings

Stream gravels and organic deposits are forming beyond the influence of the tide in the Portage area. We recognize three supratidal zones.

Braided streams.—Deposits of pebble and cobble gravel and variable amounts of coarse, poorly sorted sand occur in and near the present stream courses. The deposits are linear in shape and parallel to the stream axis.

Freshwater marsh.—Between the stream gravels and the bogs and lakes that border the valley walls is a densely vegetated freshwater marsh. Growth of vegetation is apparently much more rapid than sedimentation because samples obtained by augering consist of slightly muddy plant debris in various states of decay.

Bogs and lakes.—Little or no sediment reaches the bog area between the marsh and valley wall, and auger samples consist almost entirely of water-saturated spongy peat. Sphagnum moss, several varieties of grass, and prostrate shrubs are the dominant vegetation. Deposits in the lakes are finely comminuted plant debris.

ENVIRONMENTAL CONSEQUENCES OF INUNDATION AND SEDIMENTATION

The direct effects of the earthquake in the Portage area included destruction of bridges (Kachadoorian, 1968), subsidence of railroad and highway embankments (McCulloch and Bonilla, 1970; Kachadoorian, 1968), and damage to buildings (Plafker and others, 1969). Although railroad and highway damage was quickly repaired, there are longer lasting effects on the environment of the Portage area that resulted from the inundation and sedimentation. These effects include abandonment of the area, destruction of flora, esthetic deterioration, localized erosion, and development of "quicksand" hazards.

The Portage area has been all but abandoned by man because of the high tides and the blanket of silt that now covers the lowlands. The sole house and the service station currently maintained were constructed on thick gravel pads after the earthquake. Although the house is safely located, the service station is on the seaward side of the highway where it is threatened by the spring and storm high tides.

Having to abandon the Portage area was a hardship to the residents for many reasons, perhaps mainly because it thwarted development that might reasonably have been expected. The area is one of the very few roadside parcels of fee simple land excluded from the Chugach National Forest. It is situated on the heavily traveled Seward Highway at the junction of the road to Portage Glacier, one of the major tourist attractions of the Anchorage area; it is approximately midway between Anchorage and the popular recreation areas around Kenai Lake; and it is at the vehicle-loading point for The Alaska Railroad where, during the summer months, thousands of touring cars and buses are

shuttled to the Alaska Ferry System at the deepwater port of Whittier. The Portage area, before its inundation and siltation, was ideally situated for commercial development based on tourist and roadside services.

Special construction techniques, though adding to costs, might still facilitate development of Portage were it not for the esthetic deterioration of the area. The abandoned, partly buried and vandalized buildings (fig. 10), the uniform mantle of gray silt, and the stands of dead spruce and cottonwood are depressing sights. A measure of the deterioration of the area is that tourist buses now use it as the main stopping point at which to discuss effects of the Alaska earthquake.

Contributing to the esthetic deterioration is the widespread destruction of preearthquake plant communities. Forest at least 250 years old, well-drained and marshy grassland, and alder thicket have been killed over an area of more than 18 km². Salt-tolerant grasses and reeds and a few willows that have sprouted roots from branches at levels as much as 2 m above the former root zones constitute the only vegetation of the active tidal flats. The dead forest and thicket at Portage are the sources of extensive layers of plant debris that accumulate on intertidal bars elsewhere in Turnagain Arm and of the huge limbs and whole trees that are transported seaward to become hazards to boating in Cook Inlet.

Although many of the environmental effects result from sedimentation, currents generated during the ebb and flood locally focus to produce erosion that forms, enlarges, and extends tidal channels. A major consequence of headward erosion of channels is providing tidal access to the low-lying marsh, bog, and lake areas that rim the active intertidal zones. The result is continued progradation of intertidal sediment into the freshwater marsh, leading to further destruction of plant communities. A channelway fan system is developing in a marsh on the northwest side of the Twentymile River (fig. 11). Access to the marsh and a pathway for sediment influx is provided by a 150-m-long channel that is being eroded in the trench fill of the Anchorage-Whittier refined products pipeline. As much as 0.7 m of silt has entered the marsh by this developing tidal channel. A similar channel is developing along the axis of an old wooden waterline between Portage Creek and the junction of the Seward and Whittier spurs of the railroad.

Another group of environmental effects are quicksand hazards resulting from the properties of the Placer River Silt. The uncompacted nature and predominance of silt-size sediment results in ready liquefaction if the sediment is saturated (as it is in the tidal channels at all times and over the entire area immediately following high tide). The instability of the sediment is well known to local sportsmen, who shun foot travel in the region. In our experience, the lower tidal flats, tidal channel bottoms, point bars, and midchannel bars are extremely dangerous to traverse because it is possible to sink instantly to midthigh depths.

FIGURE 10.—Roadside business adandoned after the 1964 Alaska earthquake. As much as 2 m of silt has accumulated in this area. Photograph taken during high tide.

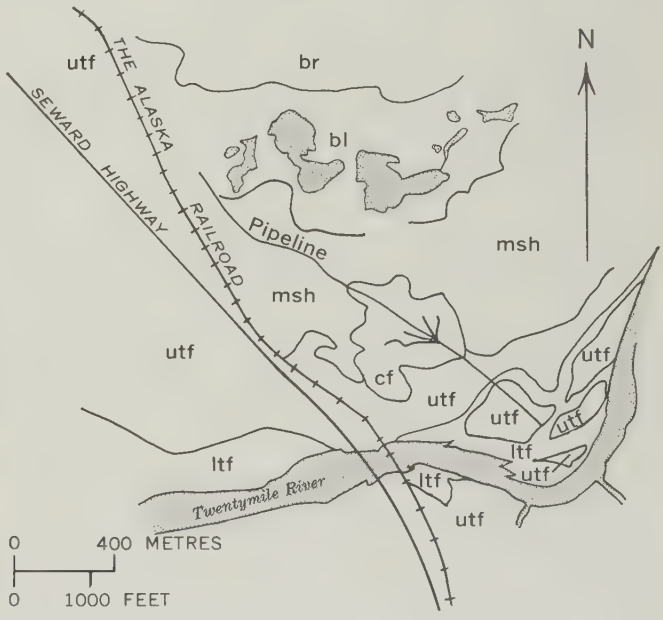

FIGURE 11.—Sketch map of north side of Twentymile River showing depositional environments and a channelway fan prograding into marsh deposits where tidal access is provided through erosion along the pipeline trench. Symbols: ltf, lower tidal flat; utf, upper tidal flat; cf, channelway fan; msh, marsh; bl, bog or lake; br, bedrock ridge.

THE FUTURE OF THE PORTAGE AREA

The effects on the environment of the Portage area brought about by intertidal deposition—the destruction of natural plant communities, erosion, and creation of quicksand hazards—are severe and lasting results of the Alaska earthquake of March 27, 1964. But they are not necessarily permanent consequences. As shown in figures 3 and 4, beneath the buried soil horizon that records the earthquake is a unit of older intertidal silts resembling the Placer River Silt in many ways. From this, and from the evident buildup of the Placer River Silt toward the level of the highest tides (fig. 7), we can expect that the surface will eventually reach a level at which saltwater incursion is exceedingly rare. As this level is approached, the former plant communities will recolonize, ultimately prosper, and play an important role in stabilizing the courses of the tidal streams and channels. The area will then much resemble Portage as it was before the earthquake.

The circumstances that developed the Placer River Silt—earthquake, subsidence, and a gradation leading to natural "repair" of the landscape—may have occurred many times during Holocene deposition in the Portage area. The older intertidal silts may record one comparable episode of subsidence and sedimentation that occurred more than 250 years ago, as judged by the age of an old spruce rooted in the silts, and possibly less than 723 years ago on the basis of tenuous correlation with a carbon-dated section in the Girdwood area, 18 km west of Portage (Karlstrom, 1964, pl. 7). As the area is underlain by at least 300 m of silt (McCulloch and Bonilla, 1970, p. D131; Dennis Kalpacoff, oral commun., 1973), it is possible that many episodes of earthquake-caused sedimentation are preserved in the geologic record. Deciphering this record may have a critical bearing on the future of Portage and of the greater Anchorage area.

REFERENCES CITED

Clark, S. H. B., 1972, Reconnaissance bedrock geologic map of the Chugach Mountains near Anchorage, Alaska: U.S. Geol. Survey Misc. Field Studies Map MF–350, scale 1:250,000.

Kachadoorian, Reuben, 1968, Effects of the earthquake of March 27, 1964, on the Alaskan Highway system: U.S. Geol. Survey Prof. Paper 545–C, 66 p.

Karlstrom, T. N. V., 1964, Quaternary geology of the Kenai Lowland and glacial history of the Cook Inlet region, Alaska: U.S. Geol. Survey Prof. Paper 443, 69 p.

McCulloch, D. S., and Bonilla, M. G., 1970, Effects of the earthquake of March 27, 1964 on The Alaska Railroad: U.S. Geol. Survey Prof. Paper 545–D, 161 p.

Plafker, George, Kachadoorian, Reuben, Eckel, E. B., and Mayo, L. R., 1969, Effects of the earthquake of March 27, 1964, on various communities: U.S. Geol. Survey Prof. Paper 542–G, 50 p.

Jour. Research U.S. Geol. Survey
Vol. 4, No. 2, Mar.–Apr. 1976, p. 163–169

BOG STRATIGRAPHY, RADIOCARBON DATES, AND PINEDALE TO HOLOCENE GLACIAL HISTORY IN THE FRONT RANGE, COLORADO

By RICHARD F. MADOLE, Denver, Colo.

Abstract.—Radiocarbon dates and stratigraphic cores from bogs, kettle ponds, and former ice-marginal lakes on the east and west sides of the Front Range, Colo., between lat 40°00′ and 40°24′ N. suggest that (1) valley glaciers of Pinedale age began to recede from their terminal positions between about 14,600 and 13,000 yr ago, (2) revegetation of glaciated areas at altitudes of 2,600–2,900 m (8,600–9,500 ft) was complete by 11,000–10,000 yr ago, (3) at one site, 3,500±1,000 yr elapsed before peat began to form after deglaciation, (4) the formation of bogs within the glaciated areas kept pace with glacier recession in a general way, beginning at progressively later times as deglaciation proceeded upward, (5) Pinedale glaciers had disappeared or were reduced to small remnants by about 8,000 yr ago, (6) moraines that have been mapped as belonging to the early stade of Pinedale Glaciation are no younger than 13,000 yr B.P. and may be older than 14,600 yr, and those delimiting what has been mapped as late stade are no younger than about 7,600 yr B.P. and are probably older than 7,800 yr, and (7) most of the till mapped as Pinedale was deposited between about 14,600 and 8,000 yr ago.

This paper describes the stratigraphy and radiocarbon dates of four localities in the Front Range and gives interpretations that bear on the beginning and end of Pinedale deglaciation, on the ages of moraines mapped as delimiting the early and late stades of Pinedale Glaciation, and on postglacial revegetation. Although the dates and stratigraphic data are too few to be interpreted rigidly, they offer insights not provided by morphology and weathering, criteria which of necessity have been relied on heavily by Quaternary stratigraphers in the Front Range and southern Rocky Mountains in general.

My work on a radiocarbon correlation of stades of Pinedale Glaciation began in 1969. Sediment for dating was collected from the base of bogs, kettle ponds, and former ice-marginal lakes. Samples from bogs and kettles were recognized as providing only minimum dates, and their interpretation was known to be subject to the kinds of errors discussed by Florin and Wright (1969) and Porter and Carson (1971). However, no radiometrically datable materials have yet been found in till in the Front Range or any other part of the southern Rocky Mountains.

Bogs were found to vary in degree of utility for radiocarbon dating, not only because of their location relative to a stratigraphic boundary or moraine system, but also because of conditions which influenced how soon after deglaciation they formed. Closed depressions, preferably those unassociated with landforms produced by stagnant ice, are the best sites for sampling because the imperfect drainage needed to form bogs was present as soon as they became free of ice. Where closure is not complete, bogs can take hundreds or even thousands of years to get started.

Acknowledgments.—Most of the work described was made possible by National Science Foundation Grant GA–29137. Geological Society of America Grant 16644 supported mapping at the Winding River site. Mark Anders, Jim Clark, Jeff Davis, Bonnie Gray, Barbara Madole, Mark Madole, Thomas Madole, Tom Meierding, Joe Noffsinger, and Katie Thorsheim helped with coring. Rolf Kihl made grain-size analyses and prepared samples for radiocarbon dating. Estella Leopold, Harold Malde, G. M. Richmond, and Van Williams provided several valuable suggestions for improving the organization and presentation of the results of this study.

SETTING AND STRATIGRAPHY OF SAMPLE SITES

The location, stratigraphy, and radiocarbon dates of four key sites are described in the following sections. Figure 1 shows the locations of the four sites plus others mentioned later in the paper. (See table 1.)

Winding River kettle pond

Winding River kettle pond is on the Pinedale terminal moraine, 250 m west of the Colorado River in the southwest corner of the Grand Lake quadrangle. This is the lowest of the four key sites (alt 2,640 m or 8,660 ft), and Madole, Fahnestock, and Meierding (1972) correlated the moraine on which it is located with the early stade of Pinedale Glaciation of Richmond (1960) and Madole (1969). Four metres of sediment overlie the till of the kettle floor. This sediment is divisible

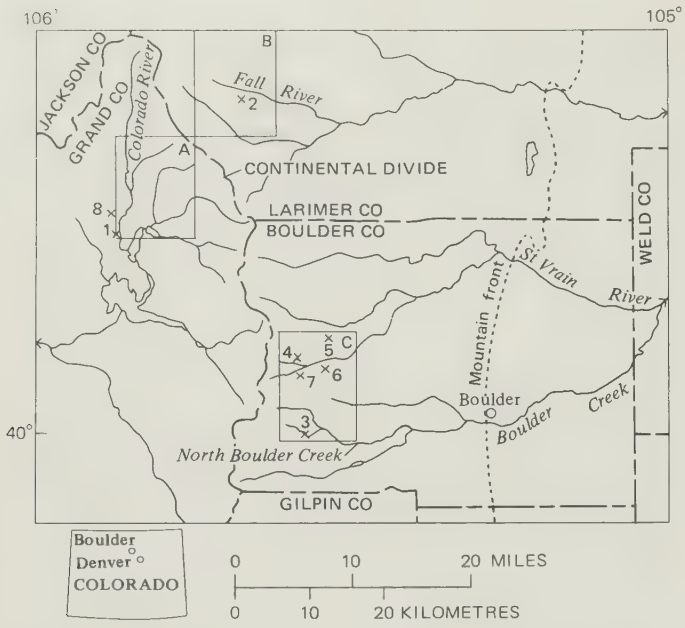

FIGURE 1.—Location of key sample sites: (1) Winding River kettle pond, (2) Hidden Valley, (3) Devlins park, (4) Mitchell bog. Others referred to: (5) Stapp Lakes, (6) Red Rock, (7) Long Lake, (8) Supply Creek bog. Quadrangles (7½-minute): (A) Grand Lake, (B) Trail Ridge, (C) Ward. Sites 4 and 7 are near the upper limit of continuous till at altitudes of 3,250 and 3,200 m (10,660 and 10,500 ft); the others are nearer the lower limit of glaciation at altitudes between 2,640 m (8,660 ft) and 2,953 m (9,690 ft).

into three principal parts (fig. 2): (1) an upper unit of peat 2.1 m thick, (2) a middle unit of black organic mud about 0.3 m thick, and (3) a lower unit of grayish-olive silt and clay 1.5 m thick, of which at least the lower half is finely laminated. Compared to other localities in the region, this is a large amount of sediment for so small a basin. Several kettle ponds of similar size at comparable altitudes in the Ward quadrangle contain only 25 to 100 cm of sediment.

The lower unit (3a and 3b) contains very little coarse sediment. Sand makes up only 2–12 percent of six samples that were analyzed (fig. 3), whereas silt ranges from 40 to 59 percent. The dominance of silt suggests a windblown origin. Laminations in this sediment indicate that the kettle hole contained water when the sediment was deposited. A lack of deformed laminae shows that subsequent collapse or slumping due to the melting of buried ice was insignificant. An absence of laminations in the upper part may reflect a decrease in water depth and a corresponding change to more turbulent conditions.

The lower unit also has only a few percent organic matter, whereas the middle unit (unit 2) is nearly half

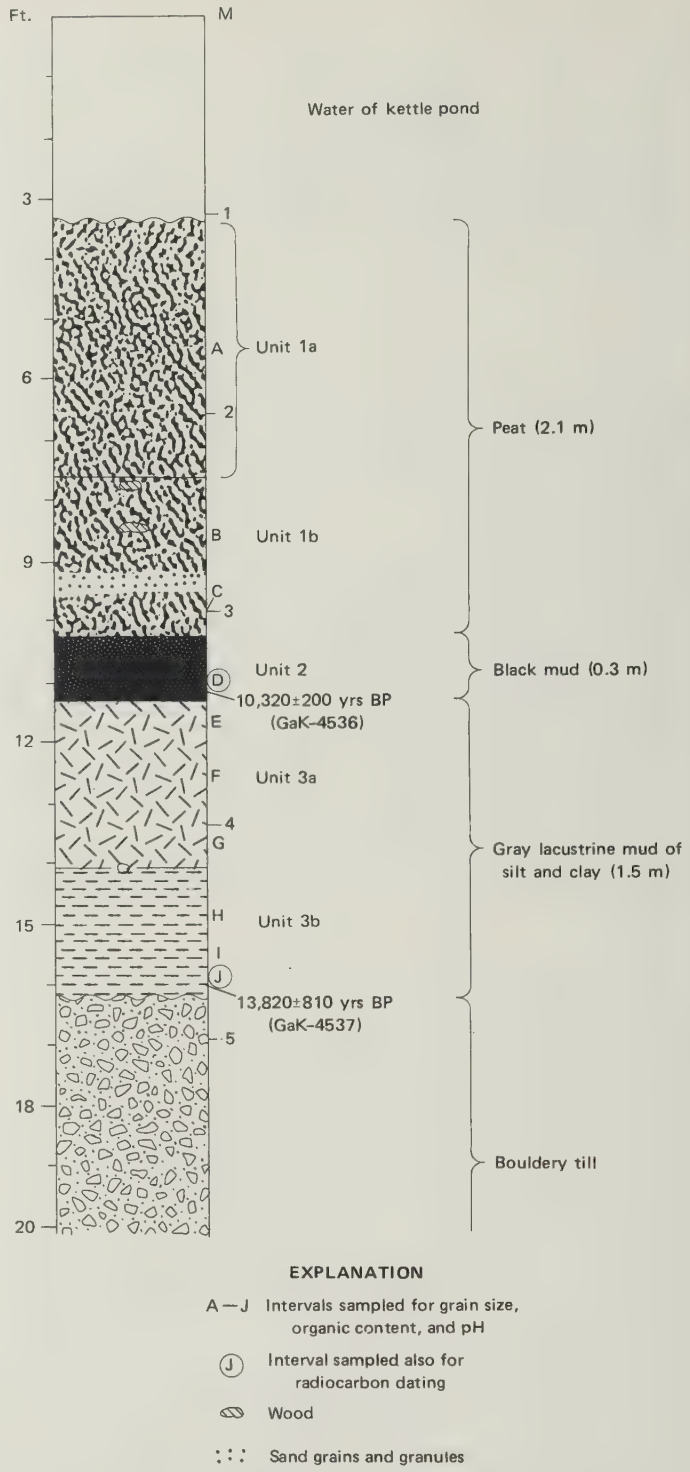

FIGURE 2.—Winding River kettle pond core.

Description of units shown in figure 2

Unit 1a: Olive-brown to dark-olive-brown (2.5Y 4/3 to 2.5Y 3/3 rootlet mud (fresh). Darker in lower 20 cm. Approximately 80 percent organic matter, dominated by a dense network of rootlets as much as 1 cm across. Remainder is mud consisting of 12 percent sand, 42 percent silt, and 46

Description of units shown in figure 2—Continued

percent clay. pH 4.8. When squeezed, the organic matter yields relatively clear water that has suspended dark material.

Unit 1b: Brownish-black to olive-black (2.5Y 3/2 to 5Y 3/1) rootlet mud (decomposed); 49 to 57 percent organic matter, much more decomposed than above. Few rootlets, but sedgelike remains occur throughout. Sand-silt-clay content of mud component ranges from 22–48–34 percent at top to 12–40–48 percent at bottom. Amount of sand is two to six times greater than in other units. pH 5.0. Waterlily seeds abundant in upper 55 cm. Horizontally bedded fragments of wood and laminae of sand and granules occur throughout. Flakes of muscovite are particularly prominent in middle 23 cm. Lower boundary is recognized by an abrupt decrease in plant remains.

Unit 2: Black (5Y 2/1) silty clay mud; 46 percent organic matter, almost all fine grained (microscopic). Remaining sediment is 6 percent sand, 41 percent silt, 53 percent clay. pH 5.1. Sand grains, flakes of muscovite, lily seeds, and decomposed rootlets are sparse.

Unit 3a: Grayish-olive (7.5Y 6/2) mud of silt and clay (nonlaminated). Samples E, F, and G have 6.7, 6.0, and 9.5 percent organic matter, respectively, all colloidal sized; amounts of sand-silt-clay in these samples are, respectively, 6.5–54.1–39.4, 3.4–53.4–43.2, and 1.7–41.9–56.4 percent. pH 4.6, 4.5, and 4.6. Not visibly laminated but has perceptible differences in shades of gray from layer to layer. Microscopic laminations may be present in lower 38 cm. Micaceous throughout. Generally devoid of visible sand grains. Basal part particularly low in sand.

Unit 3b: Light-olive-gray (5Y 6/2) mud of silt and clay (laminated). Samples H, I, and J have 5.2, 3.3, and 3.7 percent organic matter, all colloidal sized; amounts of sand-silt-clay in these samples are 3.3–48.1–48.6, 9.1–57.9–33, and 10.3–47.6–42.1 percent. pH 4.4 in all. Micaceous, especially near the bottom.

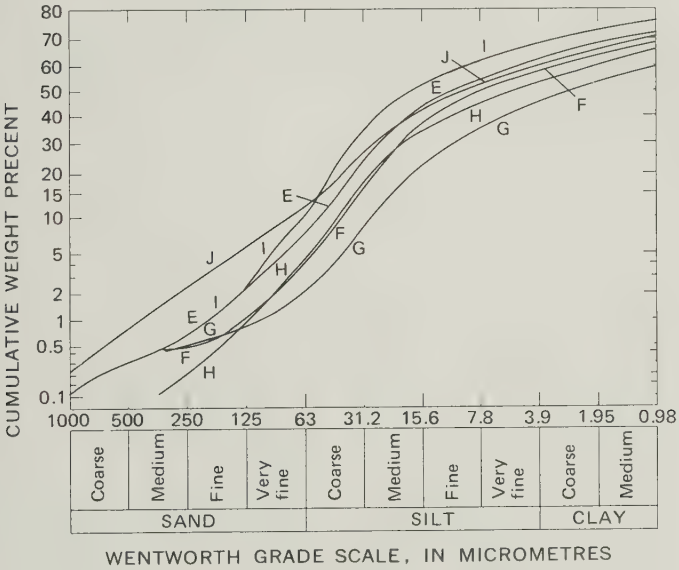

FIGURE 3.—Grain-size distribution for samples E–J from Winding River kettle pond core (fig. 2). The grain size (40–59 percent silt, 2–12 percent sand, and no grains larger than 1 mm) suggests that this interval consists of windblown material.

organic. This abrupt increase in organic content is interpreted as marking the return of an abundant growth of plants near the site following deglaciation.

The upper unit (1b and 1a) consists predominantly of organic matter, which, unlike that in unit 2, is chiefly in the form of visible plant remains. Unit 1b is about half organic matter, while 1a is four-fifths organic. Unit 1b contains scattered grains of coarse sand and granules and fragments of wood—materials derived from adjacent slopes. These constituents suggest that the setting had changed from what it was during deposition of unit 2 to something similar to that of today—a small pond surrounded by forest and filling with peat.

A small quantity of colloidal-sized organic matter, presumably consisting of pollen, humus, and other windblown organic debris of the kind described by Bonde (1969), which was concentrated from the bottom 12 cm of the lower unit, yielded a radiocarbon date of 13,820±810 yr B.P. (Gakushuin Univ. sample GaK–4537). Black mud of the middle unit gave a radiocarbon date of 10,320±200 yr B.P. (Gakushuin Univ. sample GaK–4536).

Hidden Valley bog

Hidden Valley, in the southeast corner of the Trail Ridge quadrangle, Rocky Mountain National Park, was once tributary to Fall River, but it has been blocked by a large lateral moraine of the early stade of Pinedale Glaciation (Richmond, 1960). Drainage from Hidden Valley is diverted eastward along the flank of the moraine, and sediment deposited behind the moraine has formed a broad relatively flat marsh. The marsh is at an altitude of about 2,802 m (9,180 ft), approximately 4.8 km west of the Pinedale terminal moraine that closes off Horseshoe Park, a broad meadow, 180 m below Hidden Valley, on the valley floor of Fall River.

A boring at the marsh penetrated 2.4 m of peat and the upper 1.5 m of coarse sand and granules that underlie it. Two or three thin layers of sand (a few centimetres or less thick) were found in the peat, of which the most conspicuous is at a depth of 2 m. The bottom 5 cm of the peat, which is a mixture of organic mud and highly decomposed plants, provided a radiocarbon date of 10,630±250 yr B.P. (Gakushuin Univ. sample GaK–3977). As at other localities discussed here, dates from basal peat or organic mud are interpreted as marking the time when plants reoccupied the area of the sample site after glaciers of Pinedale age retreated.

Devlins park

Devlins park (a name for a mining claim not shown on most maps) is the site of a former ice-marginal lake at the south edge of the Ward quadrangle, western Boulder County (fig. 1). Drainage from Devlins park was blocked by a moraine in a manner similar to Hidden Valley. The site is at an altitude of 2,953 m (9,690 ft), approximately 2.3 km upvalley from the glacial terminus. During Pinedale Glaciation, Devlins park was covered by water 30–50 m deep, which was backed up 1.5 km behind the impounding moraine. The lake persisted long enough to form a large delta, wave-cut terraces, and a spillway across crystalline rocks (fig. 4).

While sand and fine gravel were being deposited in the delta and along the shoreline, clay and silt were accumulating over most of the lake basin. Water depth and temperature probably inhibited organisms from disturbing most of this sediment, and the lake's orientation and configuration limited disturbance by waves. Hence, thin horizontal laminations thought to represent seasonal layers are perfectly preserved.

Approximately 7 m of core from Devlins park was obtained during the summer of 1971 using a hand-operated modified Livingston piston-sampler. During the following summer a power-driven rig using a split-barrel sampler recovered nearly 12 m of section. Unfortunately, the split-barrel sampler seriously deformed the sediments. Most of the section cored is sticky, unoxidized, gray, rhythmically layered silty clay consisting of dark-gray laminae generally <2 mm thick that alternate with light-gray laminae of variable thickness, ranging from 0.5 to 20 mm, but being typically from 2 to 4 mm. Most such rhythmites, the pairs of dark- and light-gray laminae, are from 1 to 6

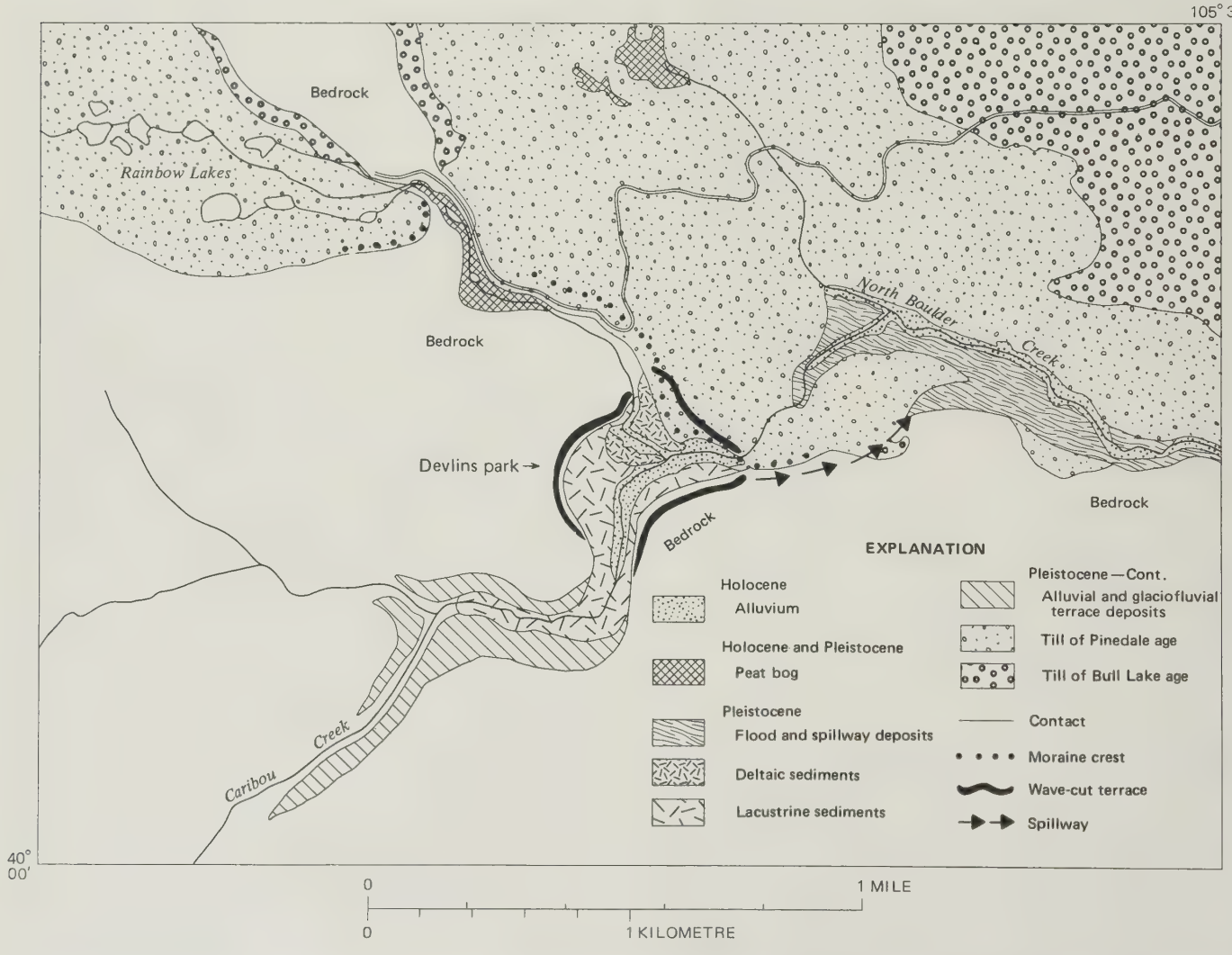

FIGURE 4.—Surficial geology of the Devlins park area. From Madole, Bachhuber, and Larson (1973) and Gable and Madole (1975).

mm thick. These are interrupted intermittently, as for example every 20–25 rhythmites, by layers of fine sand or silt, most of which are from 12 to 20 mm thick. The thicker the interrupting layers, the coarser is the sediment composing them. Those 25–30 mm thick tend to be coarse sand.

The dark layer of the rhythmites contains organic and inorganic colloids. The organic fraction consists of pollen and probably also of humus and other organic debris. Much of this organic material is believed to have been transported by wind. Organic material concentrated from the uppermost lakebeds exposed in the south bank of the creek that drains from Rainbow Lakes (fig. 4) yielded a date of 12,180±240 yr B.P. (Gakushuin Univ. sample GaK–4834). This is believed to date the end of glacial Lake Devlin, which drained catastrophically when the glacial dam was breached and left a swath of flood deposits in the valley of North Boulder Creek (fig. 4).

Mitchell bog

Mitchell bog fills an oval depression in a moraine 0.5 km east of Mitchell Lake in the northwestern part of the Ward quadrangle (fig. 1). The bog is at an altitude of 3,255 m (10,680 ft), approximately 3.6 km from cirques at the valley head and about 0.9 km downvalley from the upper limit of nearly continuous till. Mitchell bog is the highest of the four key sites. The moraine on which it is located was mapped as delimiting the late stade of Pinedale Glaciation (Madole, 1969). The bog is 80–115 m across and slightly more than 2 m deep on the west side, becoming progressively more shallow toward the east and southeast. It is saturated with melt water most of the summer and drains by seepage through a swale on the southeast that is filled with about 30 cm of peat.

Seven cores removed from Mitchell bog were from 0.3 m to 2.2 m long and composed entirely of peat. The absence of a basal unit of silt and clay such as that found at the Winding River kettle is tentatively attributed to a sparse supply of sediment upvalley from the site. Cores near the west edge of Mitchell bog contain more black inorganic sediment, especially in their upper parts, than those on the east. Thin streaks of scattered sand occur within the peat on the west, whereas wood is relatively abundant in the cores from the center and the east. The wood is of interest because woody plants do not grow in this bog. The wood may mark episodes of milder climate when the timberline rose and forests encroached on the bog. The site is essentially at timberline now. A spruce-fir krummholz (stunted, wind-battered trees) flanks it on the west, and a normal subalpine forest lies only a fraction of a kilometre to the east and south. The bottom 10 cm of the longest core, taken about halfway between the center of the bog and the west edge, yielded a radiocarbon date of 7,690±115 yr B.P. (Stockholm Univ. sample St 3898).

DISCUSSION

Radiocarbon dates and stratigraphic evidence from Winding River kettle and Devlins park provide an indication of when Pinedale deglaciation began in the Front Range. Judging from the date of 13,820±810 yr B.P. for lake sediment at the base of Winding River kettle, Pinedale ice in this area began to recede from its maximum reach between about 14,600 and 13,000 yr ago. Undisturbed laminae in the lowermost sediment in this kettle indicate a lack of disturbance by collapse over melting ice and imply that all ice had disappeared from this locality by the time the sediment was deposited. Furthermore, the absence of megascopic plant remains and the paucity of organic matter in the sediment seem to refute the notion that it could have accumulated over stagnant ice long after deglaciation, as described by Florin and Wright (1969) in Minnesota. The location of Glacial Lake Devlin and the radiocarbon date for the uppermost rhythmites indicate that the Pinedale glacier in the valley of North Boulder Creek had receded at least 2.3 km from its terminal moraine by 12,180±240 yr B.P.

Data from the Winding River core indicate that a large time lag may occur between glacier recession and revegetation. From 2,500 to possibly as many as 4,500 yr elapsed between the disappearance of ice at Winding River kettle and the deposition of the fine, black, organic mud of unit 2 (fig. 2). Whether or not the lag recorded between these two events at this site is typical of the region as a whole is unknown.

The accord between the 10,320±200 yr B.P. date for unit 2 of the Winding River core and three other dates from similar settings (two of which were not discussed in the previous section) suggests that the dates from the bottom of organic-rich sediment in bogs and ponds probably mark the time of revegetation and bog formation rather than glacier recession. The other three dates include one of 10,630±250 yr B.P. from the base of Hidden Valley bog (alt. 2,802 m or 9,180 ft), a second of 10,340±285 yr (Stockholm Univ. sample St 3894) from a streak of organic matter in gravel just below peat near Stapp Lakes (site 5, table 1; alt 2,890 m or 9,480 ft), and a third of 10,530±230 yr (Gakushuin Univ. sample GaK–4165) from charcoal-like fragments in mud beneath peat in a kettle on the outermost (early stade) Pinedale lateral moraine, 2 km upvalley from the Winding River site (site 8, fig. 1; alt 2,750 m or

9,025 ft). These dates are interpreted as indicating that revegetation of deglaciated areas had extended to altitudes of at least 2,900 m (9,500 ft) by 11,000–10,000 yr ago.

Radiocarbon dates from peat obtained from a variety of settings (see also table 1) suggest that bogs did not all form at the same time, but kept pace with glacier recession. Those from similar settings, but at successively higher altitudes, tend to be progressively younger. However, as shown in table 1, there are exceptions. Local peculiarities of topography and drainage also influence how soon after deglaciation bogs begin to form. Apparently, the poorer the drainage, the sooner peat began to form. The age difference between the bogs at site 4 (7,690±115 yr B.P.) and site 7 (5,250± 120 yr B.P.) (table 1), which have comparable settings, is attributed to incomplete topographic closure—and, hence, continuing drainage—at site 7. The same explanation is offered for the anomalously youthful date (7,085±100 yr B.P.) at site 6, which lies only about 300 m from another site known to have been free of glacier ice by 9,490±150 yr B.P. (I–4581) (Maher, 1972).

A single radiocarbon date provides an estimate of when Pinedale deglaciation ended. The date, 7,690± 115 yr B.P., for peat from Mitchell bog, a site within 3.6 km of the cirque headwalls, shows that Pinedale ice was nearly, if not entirely, gone from the east slope of the Front Range by 8,000 yr B.P. The time at which peat began to accumulate in Mitchell bog probably postdates the end of Pinedale deglaciation in this area.

The moraines at the key sites have been correlated with either the early or late stade of Pinedale Glaciation of Richmond (1960), Madole (1969), and Madole, Fahnestock, and Meierding (1972). The radiocarbon date from the base of the Winding River core shows that the early stade moraine there is no younger than 13,000 yr B.P. and may be older than 14,600 yr. Likewise, the date from Mitchell bog suggests that the moraine system originally mapped as late Pinedale is no younger than about 7,600 yr B.P. and may be older than 7,800 yr—a distinct probability inasmuch as some lag probably occurred between glacier recession and peat formation. Again, it should be noted that all dates reported here are minimal.

Finally, all the radiocarbon dates reported, but especially those from Winding River kettle and Mitchell bog, which are sites near the lower and upper limits of Pinedale Till, indicate that most of the till mapped as Pinedale was deposited between about 14,600 and 8,000 yr ago. This would help explain the lack of success in using soil studies and weathering to subdivide and correlate stades of Pinedale Glaciation. The times at which soil formation began near the lower and upper limits of till would not be notably different, at least not different enough to override the influence of differences in climate and vegetation.

REFERENCES CITED

Bonde, E. K., 1969, Plant disseminules in wind-blown debris from a glacier in Colorado: Arctic and Alpine Research, v. 1, no. 2, p. 135–139.

Florin, Maj-Britt, and Wright, H. E., Jr., 1969, Diatom evidence for the persistence of stagnant glacial ice in Minnesota: Geol. Soc. America Bull., v. 80, p. 695–704.

Gable, D. J., and Madole, R. F., 1975, Geologic map of the Ward quadrangle, Boulder County, Colorado: U.S. Geol. Survey Geol. Quad. Map GQ–1277. (In press.).

TABLE 1.—*Time of beginning of peat formation with respect to altitude and physiographic setting as determined at bogs in Ward quadrangle, Colorado, listed in order of ascending altitude*

Site No. (fig. 1) and location	Lat N.	Long W.	Approximate altitude		Physiographic setting	Age of basal peat (yr B.P.)
			Metres	Feet		
5. 700 m southeast of the lodge at Stapp Lakes.	40°07′	105°32′	2,883	9,460	Kettle hole 650 m behind outermost Pinedale moraine and about 4–6 km from lower limit of glaciation. Seasonal stream drains through saddle on the encircling moraines.	[1] 8,930±245
5. 775 m west-southwest of the lodge at Stapp Lakes.	40°06′ 52″	105°33′ 34″	2,890	9,480	Peat over fluvial and glaciofluvial gravel in poorly drained, but not closed, area just beyond Pinedale terminal moraines.	[2] 10,340±285
6. 300 m west of Red Rock Lake__	40°04′ 54″	105°32′ 41″	3,104	10,185	Imperfectly drained area on till of Pinedale age near valley wall a little below the midpoint between upper and lower limits of glaciation. Bog is thought to have formed gradually and progressively outward from the base of the valley wall.	[5] 7.085±100
7. 150 m east of Long Lake _____	40°04′ 30″	105°31′ 10″	3,200	10,500	Poorly drained, but not closed, area on till of Pinedale age 4.6 km from the cirque area at the head of South St. Vrain Creek.	[4] 5,250±120
4. Mitchell bog, 500 m east of Mitchell Lake.	40°05′ 13″	105°35′ 18″	3,255	10,680	Closed depression on crest of a Pinedale moraine 3.6 km from cirque area.	[5] 7,690±115

[1] Stockholm Univ. St 3896 [2] Stockholm Univ. St 3894 [3] Stockholm Univ. St 3897 [4] Gakushuin Univ. GaK–3976 [5] Stockholm Univ. St 3898

Madole, R. F., 1969, Pinedale and Bull Lake Glaciation in upper St. Vrain drainage basin, Boulder County, Colorado: Arctic and Alpine Research, v. 1, no. 4, p. 279–287.

Madole, R. F., Bachhuber, F. W., and Larson, E. E., 1973, Geomorphology, palynology, and paleomagnetic record of glacial Lake Devlin, Front Range: Geol. Soc. America Rocky Mtn. Section Ann. Mtg., 26th, Guidebook (Trip 1), 25 p.

Madole, R. F., Fahnestock, R. K., and Meierding, T. C., 1972, Glaciation of the west slope of the Colorado Front Range: Geol. Soc. America Abs. with Programs, v. 4, no. 7, p. 583–584.

Maher, L. J., 1972, Absolute pollen diagram of Redrock Lake, Boulder County, Colorado: Quaternary Research, v. 2, no. 4, p. 531–553.

Porter, S. C., and Carson, R. J., III, 1971, Problems of interpreting radiocarbon dates from dead-ice terrain, with an example from the Puget lowland of Washington: Quaternary Research, v. 1, no. 3, p. 410–414.

Richmond, G. M., 1960, Glaciation of the east slope of Rocky Mountain National Park, Colorado: Geol. Soc. America Bull., v. 71, p. 1371–1382.

Jour. Research U.S. Geol. Survey
Vol. 4, No. 2, Mar.–Apr. 1976, p. 171–180

GEOLOGY OF THE MASSIFS AT THE APOLLO 17 LANDING SITE

By EDWARD W. WOLFE and V. STEPHEN REED,
Flagstaff, Ariz.

Abstract.—The Apollo 17 spacecraft landed in a narrow valley that embays mountainous terrain near the southeastern edge of Mare Serenitatis. Two overlapping basin structures underlie Mare Serenitatis: a larger one to the south and a smaller one to the north. The massifs and sculptured hills in the Taurus-Littrow area and the mountains and knobby terrain in the outer Rook ring (third ring) of the Orientale basin are similar in morphology; the Apollo 17 site lies approximately on the third ring of the southern Serenitatis basin structure. Assuming the third ring represents the approximate rim of the transient cavity of the southern Serenitatis structure, we suggest that ejecta many kilometres thick was deposited in the Taurus-Littrow area by the southern Serenitatis impact. This ejecta is visible in the massifs in the Apollo 17 landing site as discontinuous, irregular lenses of variable lithology. The southern Serenitatis target rocks were predominantly breccias that were invaded by impact-generated melt and redeposited during the southern Serenitatis event.

Apollo 17 landed on the floor of a narrow valley that embays mountainous terrain near the southeastern edge of Mare Serenitatis. Descriptions by the crew during the mission and the returned samples show that the valley is underlain by mare-type basalt and the bordering massifs are underlain by impact-generated feldspathic breccias. Interpretation of the geologic significance of these massif breccias depends upon assessment of (1) the Serenitatis basin structure, (2) its significance in interpreting the geology of the Apollo 17 site, (3) local massif geology, and (4) later modification of the mountain slopes, largely by deposition of basin ejecta and by local impact and mass wasting.

Acknowledgments.—This work was done under NASA contracts T–5874A and W13, 130.

THE SERENITATIS BASIN STRUCTURE

The Serenitatis basin has been interpreted as one of the Moon's older circular basins (Stuart-Alexander and Howard, 1970; Hartmann and Wood, 1971), which are generally considered to have been formed by giant impacts. Wilhelms and McCauley (1971) mapped a Serenitatis basin structure of four rings concentric to a single basin center (fig. 1). They placed the second ring crest in an area slightly west of the Apollo 17 landing site; the overall diameter of their basin structure is about 1,400 km. The outer two rings of their inferred basin structure are difficult to recognize; only the first ring, defined by wrinkle ridges within Mare Serenitatis, and segments of the second ring, defined by the discontinuous mountainous border of Mare Serenitatis, are unequivocally distinct. Hence, Stuart-Alexander and Howard (1970) and Hartmann and Wood (1971) suggested that the second ring, less than 700 km in diameter, might be the basin rim.

Geologic mapping by Scott (1972) suggested that Mare Serenitatis is underlain by two overlapping basins, the smaller one in the north and the major basin to the south. Subsequent interpretation of the Apollo 15 and 17 gravity data by Sjogren, Wollenhaupt, and Wimberly (1974) showed that Mare Serenitatis is underlain by two mascons, one centered near 23° N., 18°

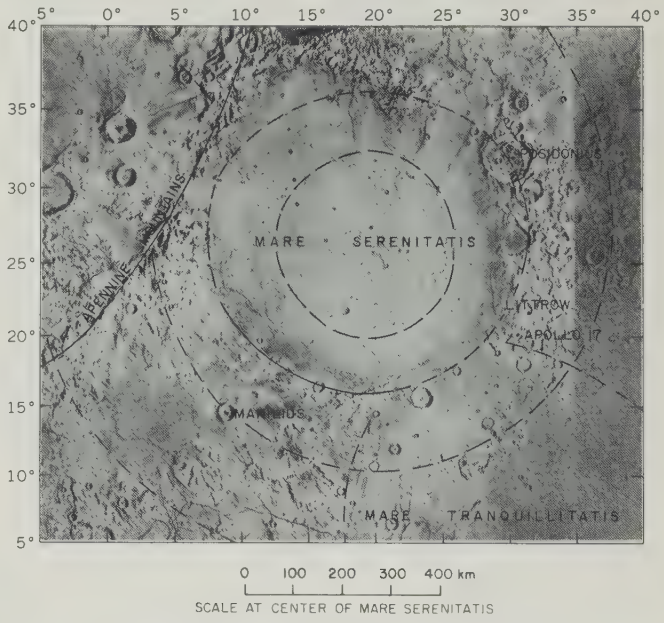

FIGURE 1.—Ring structure of Serenitatis basin as shown by Wilhelms and McCauley (1971).

E., and the other north of a gravity saddle at 27.5° N. In light of these results, Scott (1974) revised the photogeologic interpretation to show a double basin structure with the larger, southern basin centered at approximately 24.5° N., 18° E. (fig. 2).

Using Scott's basin center and modifying the ring structure of Wilhelms and McCauley (1971), one can derive the ring structure shown in figure 2. Comparison of this ring structure with the better preserved structure of the Orientale basin is shown in table 1.

Ring 1 in the southern Serenitatis basin is represented by prominent wrinkle ridges whose distribution approximates a circle 400 km in diameter on the mare surface. Muehlberger (1974) suggested that such a wrinkle ridge ring may form in mare basalt where a drowned ring of the basin structure affects the compressional stress field that produced the ridges. In the Orientale basin (fig. 3) the innermost ring, 320 km in diameter, is marked by a bench surrounding mare material at the basin center (Moore and others, 1974). Such a bench in the southern Serenitatis basin would have been buried under the much more extensive Serenitatis mare fill.

Ring 2 in the southern Serenitatis basin is represented only by the arcuate structure of the Haemus Mountains. Maintaining the 290-km radius measured from the basin center to the Haemus Mountains, we extend this ring eastward beneath mare basalt west of the landing site; it does not connect with the ring (Littrow ring) drawn by Wilhelms and McCauley (1971) through the mountains immediately east of Mare Serenitatis. In the Orientale basin the second ring is about 480 km in diameter (Moore and others, 1974). Head (1974b) described this ring (his inner Rook ring) as formed by isolated peaks or groups of peaks up to 3 km high.

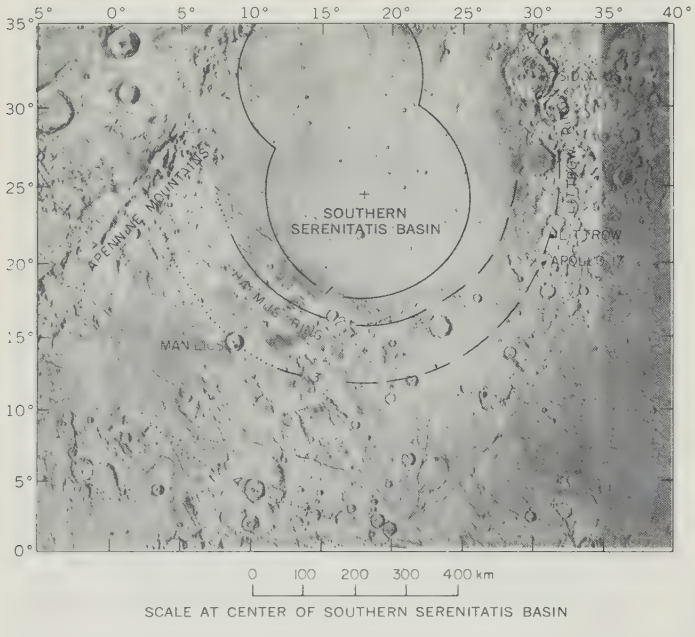

FIGURE 2.—Revised ring structure of Serenitatis basin. Solid-line segments from Scott (1974); dotted-line segments from Wilhelms and McCauley (1971); dashed-line segments, this report. Cross shows approximate center of southern Serenitatis basin. Numbers 1 through 4 identify basin rings discussed in the text.

TABLE 1.—*Comparison of southern Serenitatis and Orientale basin structures*

[Data for Orientale basin, except as indicated, from Moore, Hodges, and Scott (1974)]

	Southern Serenitatis basin structure diameters (kilometres)		Orientale basin structure diameters (kilometres)		Ratio of diameters
Ring 1	400		320		1.25
2	580	(Haemus ring)	480	(inner Rook ring)	1.21
3	750	(Littrow ring)	600	(outer Rook ring)	1.25
4	1,300		900	(Cordillera ring)	1.44
Mascon (Calculated surface disk).	*442		†300		1.5

* Sjogren and Wimberly (1974).
† Scott (1974).

Ring 3 (Littrow ring) in the southern Serenitatis basin (fig. 2) is represented by the part of the second ring of Wilhelms and McCauley (1971) that passes through the crater Posidonius and by the part of their third ring that passes through the crater Manilius. Adjustment so that the Littrow ring passes through the west rim of the crater Littrow and through the landing site preserves concentricity. However, as shown for the Orientale basin in figure 3, perfect circularity and concentricity of rings exist only conceptually.

In the Orientale basin, ring 3, 600 km in diameter, forms the crest of the Rook Mountains. Morphologic similarities suggest that this so-called outer Rook ring (Head, 1974b) and the Littrow ring represent analogous structures in the two basins. Figures 4 and 5 are orbital views at similar scale of the Rook Mountains in the southeastern part of the Orientale basin and the Apollo 17 landing area southeast of Mare Serenitatis. In each area several massifs of similar shape and size are crudely alined along radials to the basin centers. In contrast, the fourth (Cordillera) ring of the Orientale basin is marked by a single, clean-cut mountain crest and basin-facing scarp (fig. 6). In each area, linear grabenlike troughs radial to the basin centers cut through the mountainous third ring. In the Apollo 17 area, mare basalt has flooded such troughs and buried the lower parts of the massifs.

FIGURE 3.—Ring structure of Orientale basin as shown by Scott (1974). Mountains or scarps forming rings shown by solid lines, idealized concentric rings by dashed lines. Numbers 1 to 4 identify rings discussed in text (1, innermost ring; 2, inner Rook ring; 3, outer Rook ring; and 4, Cordillera ring).

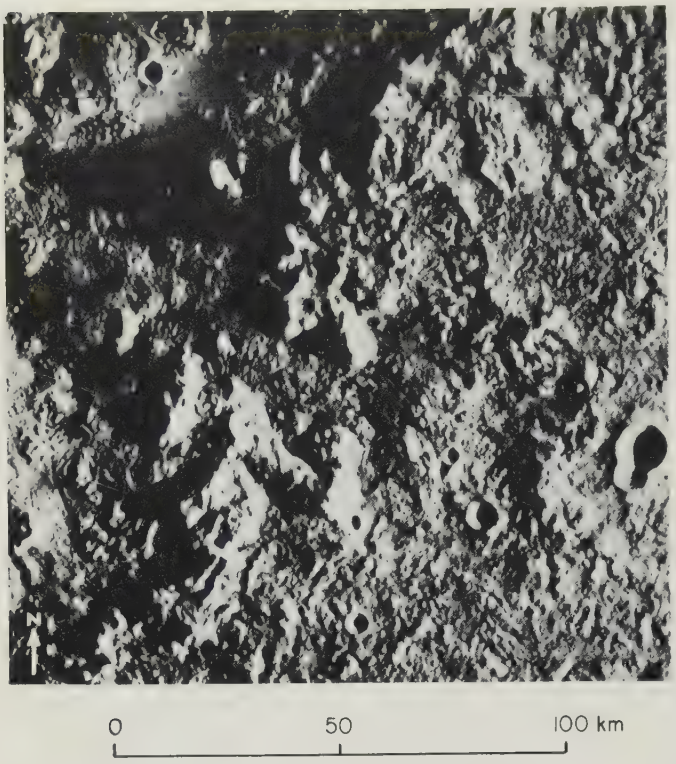

FIGURE 4.—Rook Mountains in the southeastern quadrant of the Orientale basin. Lunar Orbiter IV high-resolution frame 181. Location of this area is shown in figure 6.

FIGURE 5.—Mountainous terrain southeast of Mare Serenitatis in the Apollo 17 region. Cross shows Apollo 17 landing point. Mapping-camera photograph AS17–M–446.

In the Orientale basin, knobby textured terrain (knobby basin material of Moore and others, 1974; domical faces of Head, 1974b) occurs in the graben-like trough that transects the outer Rook ring and extends over most of the surface between the Rook Mountains and the scarp that forms the west face of the Cordillera Mountains. Comparable knobby textured terrain (known informally as the sculptured hills) forms a major part of the highlands adjacent to eastern Mare Serenitatis.

Wilhelms and McCauley (1971) identified a fourth ring with a radius of about 670 km in the highlands southwest of Mare Serenitatis. Their third ring lies about 550 km east of the basin center shown in figure 2. It is difficult to say whether either of these segments represents a basin rim analogous to the fourth ring (Cordillera Mountains) of the Orientale basin or to the outer ring (Apennine Mountains) of the Imbrium basin. Such a ring in the southern Serenitatis basin structure may never have been well developed or may have been largely obliterated by subsequent events.

As summarized in table 1, the southern Serenitatis basin structure consists of rings that we correlate with the four well-defined rings of the Orientale basin structure. The correlation derives particular support from the shape, size, and distribution of massifs near the Apollo 17 site and in the outer Rook ring and also from the spatial relation in both basins of the massifs to the knobby terrain. These results are in agreement with a similar correlation that Head (1974a) made between the Apollo 17 region and the Alpes Mountains and the Alpes Formation of the Imbrium basin.

The southern Serenitatis basin structure is larger than its Orientale counterpart; its rings range in diameter from about 1.2 to 1.4 times the diameters of the equivalent Orientale rings. It is interesting that the surface disk calculated by Sjogren and Wimberly (1974) for the southern Serenitatis mascon is 1.5 times larger in diameter than the surface disk calculated by Scott (1974) for the Orientale mascon. In each basin the diameter of the calculated surface disk approximates the diameter of the inner ring. Apparently a crude linear relation exists from one basin to the other in the relative diameters of analogous features.

SIGNIFICANCE OF THE BASIN STRUCTURE IN INTERPRETING THE GEOLOGY OF THE APOLLO 17 LANDING SITE

Assuming that our correlation of the southern Serenitatis and Orientale basin ring structures is correct,

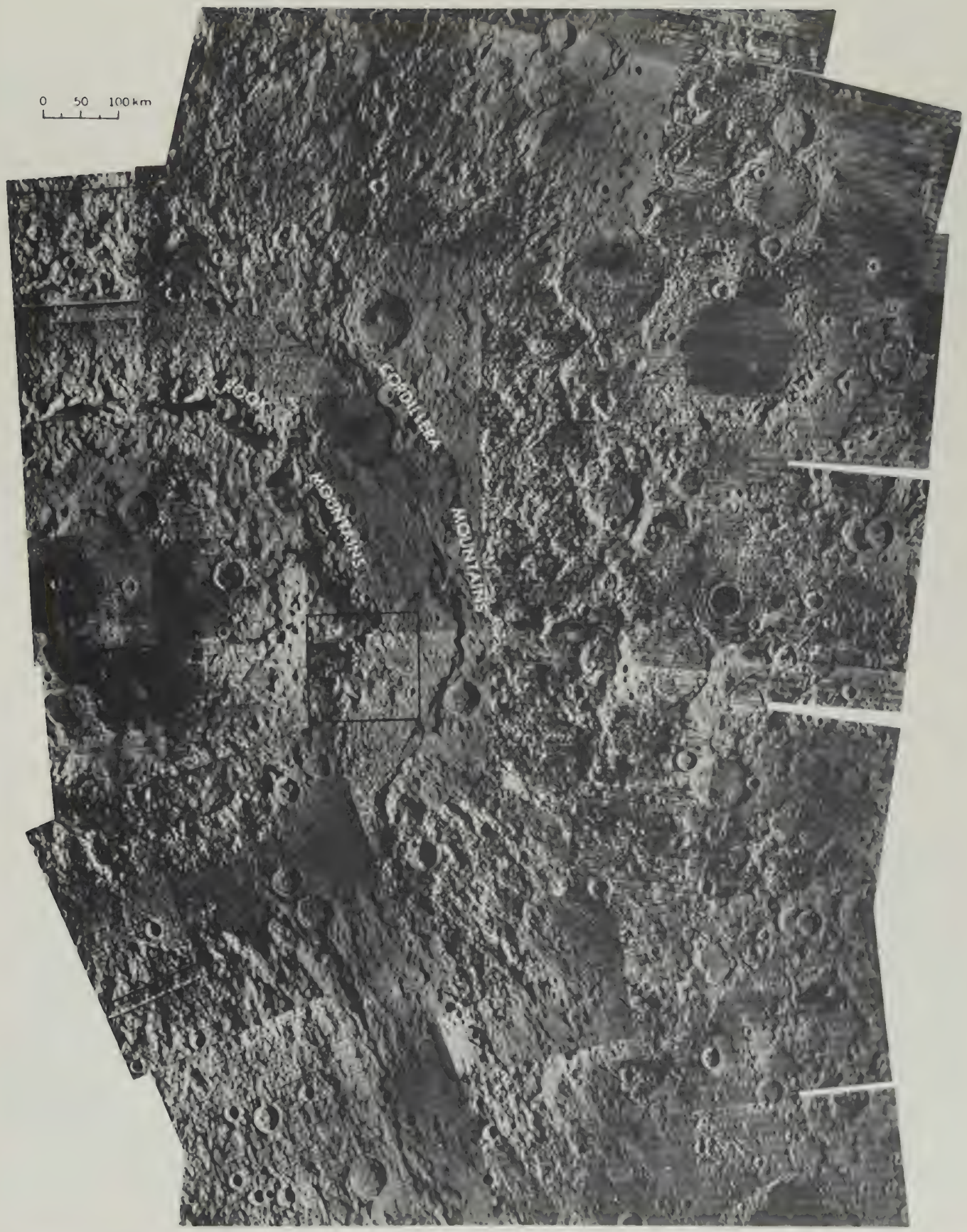

FIGURE 6.—Eastern part of the Orientale basin. Uncontrolled mosaic of Lunar Orbiter IV high-resolution photographs. Rectangle shows area of figure 4.

and that the massifs and sculptured hills at the Apollo 17 landing site are similar in origin to, respectively, the outer Rook Mountain massifs and the associated knobby basin material, we can extrapolate geologic relations and interpretations from the relatively fresh Orientale basin to the Apollo 17 landing area. Howard, Wilhelms, and Scott (1974) summarized recent thought on the origin of ring structure as follows:

> Two main views have been expressed on the origin of the mountain rings (Baldwin, 1974). One is that the rings represent slumping into the impact basin (McCauley, 1968; Hartman and Kuiper, 1962), possibly enhanced by ring dikes (Hartman and Wood, 1971). The other is that the rings represent frozen tsunami-like waves formed by the shock (Baldwin, 1949, 1972, 1974; Van Dorn, 1968, 1969). The observed ring spacing has been incorporated into both models (Van Dorn, 1968; Hartman and Wood, 1971). Upturning or folding of the outer mountain rings is required by the ring-wave model. Evidence for this uplift is provided by the outer (Altai-scarp) ring of the Nectaris basin which tilts sharply up from outside terrain (Baldwin, 1972), and by the broad concentric rises and depressions outside some basins, notably Imbrium (Baldwin, 1949; Hartmann and Kuiper, 1962; Wilhelms, 1964). On the other hand the height of the Cordillera ring is comparable to the thickness of Orientale ejecta * * * and so may be entirely depositional. Possibly both models are correct: rings (or the whole region) were uplifted and then immediately collapsed inward (McCauley, 1968).

It seems probable to us that the rings were formed by a combination of uplift, due to the effect of tsunami-like waves or to some other deformational process, and normal faulting, due to basinward collapse.

Assessment of the geologic significance of the material of the third ring depends not only on the mode of ring formation but on its relation to the transient cavity created by the impact. As Howard, Wilhelms, and Scott (1974) have cautioned, (1) no unequivocal way has been found to determine which, if any, of the rings represents the transient crater, and (2) inner ring diameters may have been shortened from their original lengths in the centripetal motion that occurred during collapse along outer rings. Head (1974b) summarized some previously published estimates that range from about 100 to 600 km for the diameter of the transient cavity for the Orientale basin. Later writers (Baldwin, 1972; McGetchin and others, 1973; Moore and others, 1974; Head, 1974b) have preferred to regard the outer Rook ring (ring 3, fig. 3, approximately 600 km in diameter) as the approximate rim of the transient cavity. The most cogent photogeologic support for this hypothesis has been developed by Head (1974b), who, by analogy to the large crater Hausen (170 km in diameter) and to the Schrodinger basin (320 km in diameter), suggested that the inner Rook ring (ring 2, fig. 3) is a central peak ring and that the outer Rook ring is the approximate rim of the transient cavity.

Moore, Hodges, and Scott (1974), estimating thickness from the calculated depths of buried craters, determined a thickness of 2–4 km of Orientale ejecta at the crest of the Cordillera ring. They found empirically that the ejecta thins away from the basin as predicted by the equation of McGetchin, Settle, and Head (1973) for a transient cavity 600 km across with 12 km of ejecta at its rim and 3.6 km of ejecta at a position equivalent to the crest of the Cordillera ring. The equation is $t=T(r/R)^{-3.0}$, where T is the thickness of ejecta at the initial crater rim, R is the radius of the initial crater, and t is the thickness of ejecta at distance r, measured from the center of the crater. In addition, Moore, Hodges, and Scott (1974) pointed out that the equation of McGetchin, Settle, and Head (1973) for small experimental craters ($T=0.04R$, notation as above) predicts 12 km of ejecta at the rim of a transient crater 600 km in diameter. Using the equation of McGetchin, Settle, and Head (1973) for cumulative volume (Vo) at distances of r and larger ($Vo=2\pi TR^2(R/r)$, notation as above) and using $R=300$, $T=12$ km, Moore, Hodges, and Scott (1974) calculated the total volume of Orientale ejecta beyond the Cordillera rim to be about 4.5×10^6 km^3, a value in reasonable agreement with the 5.3×10^6 km^3 predicted by Scott (1974) from interpretation of gravity data.

Influenced by Head's (1974b) photogeologic interpretation and by the measurements and calculations of Moore, Hodges, and Scott (1974), we believe that the massifs of the outer Rook ring (fig. 4) represent thick Orientale ejecta emplaced near the rim of the transient cavity. Whether or not the 12-km estimate of thickness is correct, the ejecta at the outer Rook ring must be thicker than the 3.6 km predicted at the Cordillera rim.

By extrapolation from Orientale to the slightly larger southern Serenitatis basin, we infer that many kilometres of ejecta was emplaced in the vicinity of the landing site. (The relation, $T=0.04R$, suggests a thickness of 15 km.) Later, but still during the period of basin formation, the ring structure and radial faults that define the massifs were imposed.

Application of Pike's (1972) equations for experimental craters ($a=0.225D^{0.96}$ and $h=0.043D^{0.91}$, where a is the depth of the crater measured from the rim crest, h is the height of the rim above the local surroundings, and D is the diameter of the crater; all variables in kilometres) to an inferred transient cavity 750 km in diameter suggests that the southern Serenitatis impact could have excavated to depths of about 100 km.

THE APOLLO 17 MASSIFS

Massifs at the Apollo 17 site rise more than 2 km above a grabenlike valley floor (figs. 5, 7) that is underlain by at least 1 km of basalt (Duennebier and others, 1974; Talwani and others, 1973; Cooper and Kovach, 1974). Large boulders were sampled at the base of the South Massif at station 2 and at the base of the North Massif at stations 6 and 7 (fig. 7). The station 2 boulders may have rolled from a patch of boulders about two-thirds of the way up the South Massif; the boulders at stations 6 and 7 may have come from the lower one-third of the North Massif (Muehlberger and others, 1973).

A major question about the massifs is whether they are composed of layered sequences or are heterogeneous mixtures of breccias. The problem is complicated by the veneer of regolith, which prevents direct observation of outcrops. Most of the rocks seen on the surface of the massifs are not in place but are blocks ejected by local impacts. The possible exception is a thin band of rocks that forms a ledge high on the western face of the South Massif. Boulders are randomly scattered or clustered on the massif surfaces. Color differences on the South Massif that were recognized both from the surface by the crew and in photographs may be instructive about the fabric of the massifs. Detailed mapping on telephotographs taken from the surface shows that the massif is a patchwork of irregular and discontinuous light and dark units (fig. 8). The patchy color distribution may be explained in two ways: (1) the massifs are not layered but are composed of irregular lenses of differing lithology, or (2) the dark color is caused by dark mantle material irregularly distributed on the surface of the massif as shown on Lucchitta's (1972) geologic map. Both light- and dark-colored rocks are visible in the large patch of boulders presumed to be the source of station 2 boulders (fig. 8). However, dark rocks predominate in this predominantly dark part of the massif, suggesting that the color differences reflect litho-

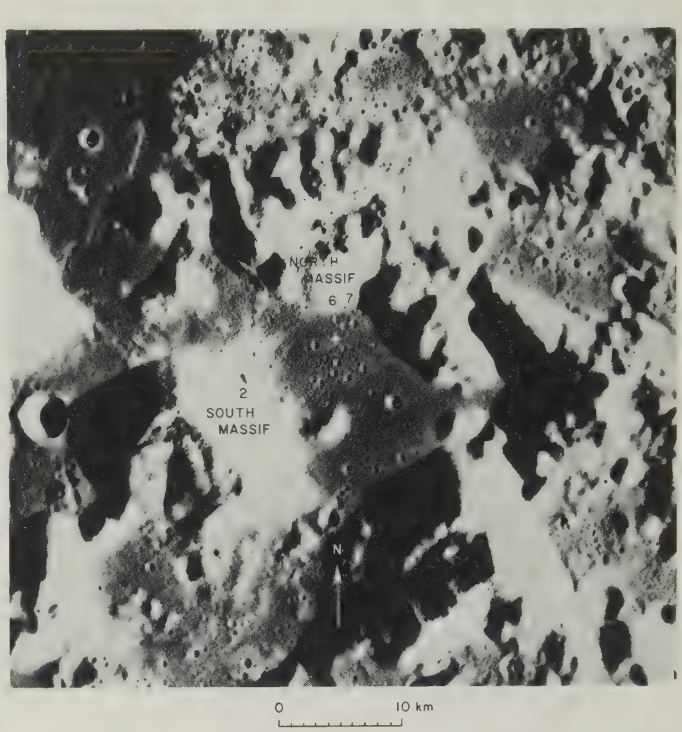

FIGURE 7.—Major physiographic features in the Taurus-Littrow region. Cross shows Apollo 17 landing point. Numbers 2, 6, 7 refer to massif localities sampled by the Apollo 17 crew. Mapping-camera photograph AS17–M–446.

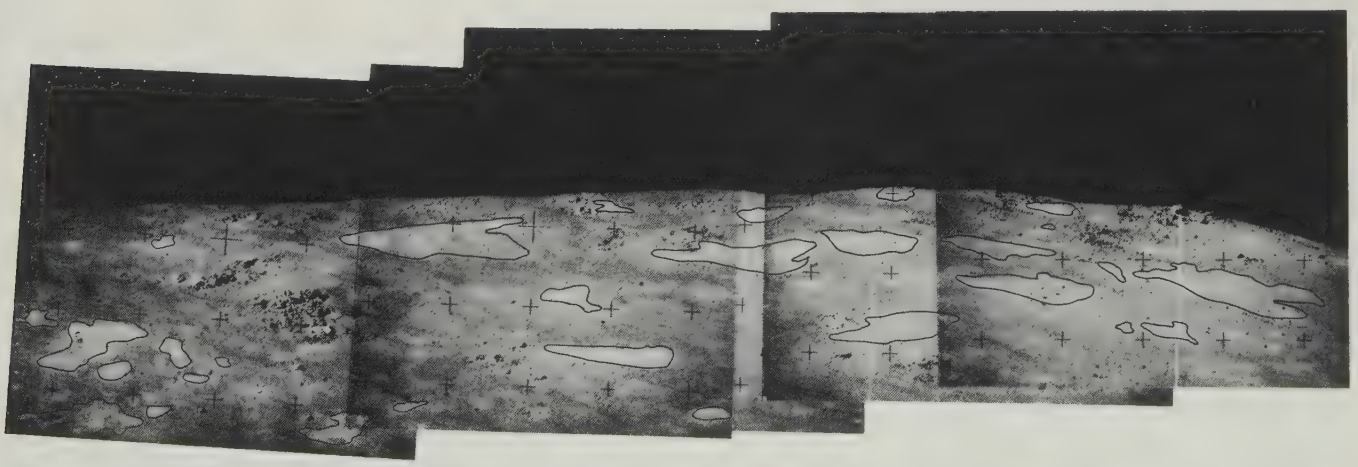

FIGURE 8.—Panorama of 500-mm photographs showing light-colored patches on the South Massif. Large patch of boulders on the left may be the source of the station 2 boulders. Width of view approximately 6 km. Telephotographs AS17–144–22051 to 22057 taken from the lunar surface.

logic variations and not just dark mantle deposits. It is probable that we see both effects.

Four major rock types that were collected from the North and South Massifs are shown in table 2. Only boulder samples are given, but several single rock fragments and rake samples also fall into these lithologic categories. All these rocks are multiple breccias that suggest derivation from multiple impact events.

TABLE 2.—*Major breccia types from the North and South Massifs*

Layered light gray		Blue gray		Green gray		Light gray	
Station	Boulder	Station	Boulder	Station	Boulder	Station	Boulder
2	1	2	3	2	2	--	--
--	--	6	1, 2	6	2, 4, 5	6	1
--	--	7	(1)	7	(1)	7	(1)

[1] Only one boulder sampled at station 7.

Preliminary examination suggests the following lithologic correlations between the South Massif and North Massif boulders (Muehlberger and others, 1973):

1. The green-gray breccias from both massifs are similar except that the vugs are smaller in the South Massif boulders. In addition, green-gray breccias with no cavities are seen in both massifs.
2. Blue-gray breccias appear identical.
3. Light-gray breccias from both massifs are highly variable. The light-gray breccias fall into two major categories—noritic breccias (station 2, boulder 1) and anorthositic gabbros (stations 6 and 7).

These rock types, seen as individual boulders on the South Massif, are all within single boulders on the North Massif. The station 7 boulder (fig. 9) shows the relations particularly well: Light-gray breccia is enclosed by blue-gray breccia, which, in turn, has been incorporated within vuggy greenish-gray breccia. Some of the clasts of blue-gray and light-gray breccia are large. The station 6 boulders are fragments of what was once a single boulder with a blue gray clast about 9 m across. The light-gray breccias are as large as the 2-m boulder 1 at station 2. Another large boulder (about 35 m across) on the slopes of the North Massif shows clasts up to 10 m across (fig. 10). Such large clasts may indicate proximity to the target of a major impact.

We have drawn the following conclusions from these observations:

1. The massifs are not composed of uniformly layered sequences of units of differing lithologies. It appears from both the rock distributions and the patchy nature of color variations that pods and lenses of differing rock types are irregularly distributed in the massifs. The occurrence of coarsely fragmental boulders suggests that the massifs are formed of thick, coarse breccia. If the station 2 boulders originated in the upper third of the South Massif, and the boulders of stations 6 and 7 in the lower third of the North Massif, it is reasonable to suppose that most of the total visi-

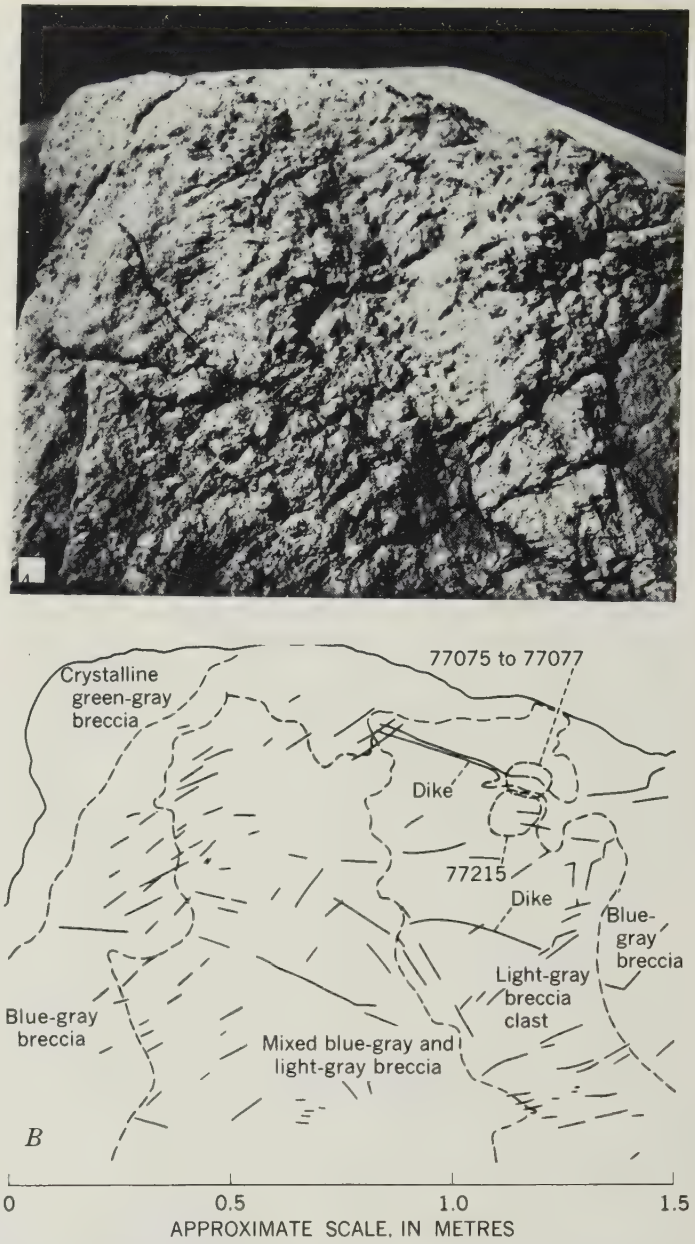

FIGURE 9.—Station 7 boulder. *A*, Closeup view of the boulder. *B*, Sketch map. The light-gray breccia clast is enclosed in blue-gray breccia, which in turn is enclosed in green-gray breccia. Except for labeled dikes and outline of boulder, solid lines indicate traces of fractures. Dashed lines separate rock units. Hasselblad photograph AS17–146–22305.

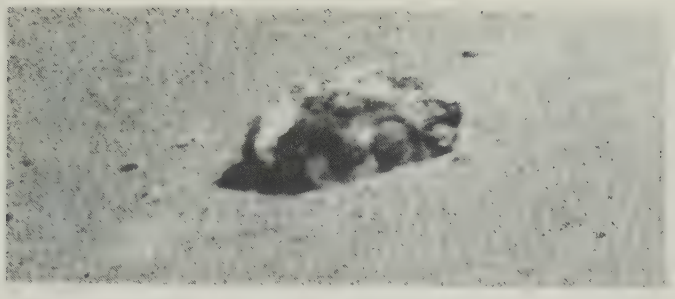

FIGURE 10.—Enlarged photograph showing a breccia boulder 35 m long on the North Massif. Note the large (to 10 m) clasts in this boulder. Hasselblad photograph AS17–139–21256.

ble thickness of these massifs consists of similar materials.

2. We infer from the multiple breccias seen in the boulders that breccia was a major component of the pre-Serenitatis target material. Heterogeneous target material produced heterogeneous ejecta. Hence the massifs are composed of pods and lenses instead of continuous lithologically distinct layers.
3. The light-gray and blue-gray breccias are older breccias that were reexcavated and enclosed by the impact-melted green-gray breccia during creation of the southern Serenitatis basin.

POST-SERENITATIS EVENTS

The landscape in the Apollo 17 area, in approximately its present form except for mare flooding, was created by the southern Serenitatis impact. Subsequent structural modification (Head, 1974a; Muehlberger, 1974) has little bearing on our interpretation of massif samples.

It would be unreasonable to suppose that all the materials in the highlands are Serenitatis ejecta. Moore, Hodges, and Scott (1974) have suggested that the Apollo 17 site lies within the area that may have been blanketed by Imbrium ejecta. Crisium ejecta might also be present in the Apollo 17 area. Scott and Pohn (1972) have mapped lineated terrain north of the crater Littrow as well as still farther north in the vicinity of the Taurus Mountains. They suggested that, in the latter area, the lineated terrain, which is radial to the Imbrium basin and was mapped by Wilhelms and McCauley (1971) as the Fra Mauro Formation, may include Imbrium ejecta. The lineated terrain north of Littrow, which was regarded as pre-Imbrian by Wilhelms and McCauley (1971), is not radial to either Imbrium or Crisium; we assume that it represents basin or large-crater ejecta deposited before the Imbrium impact. Scott and Pohn (1972) recognized no lineated terrain south of Littrow. The preservation of pre-Imbrian lineated terrain north of Littrow and the absence of sculpturing related to Imbrium or Crisium in the Taurus-Littrow area suggest to us that Imbrium and Crisium ejecta, if present, are thin in the Taurus-Littrow area. Parallel evidence is provided by the preservation of the sculptured-hills topography. If our correlation of the Littrow ring and the outer Rook ring is valid, the sculptured-hills terrain is related in origin to the southern Serenitatis impact. Its distinctive topography would not be visible through great thicknesses of Imbrium and Crisium ejecta. This physiographic evidence combined with the extreme coarseness of the massif breccias suggests that the sampled massif boulders represent southern Serenitatis ejecta.

Erosion of the massifs is difficult to assess. Continuing meteoroid bombardment and mass wasting have certainly removed material from their surfaces. If there was a thin deposit of post-Serenitatis ejecta on the massif faces, part or all of it may have been removed.

SUMMARY

The following points are critical in developing the geologic model proposed in this paper:

1. The Apollo 17 landing site lies approximately on the third ring of the southern Serenitatis basin structure, which is slightly greater in diameter than the Orientale basin structure.
2. The third ring is located near the rim of the transient cavity created by the southern Serenitatis impact.
3. Many kilometres of southern Serenitatis basin ejecta were emplaced near the rim of the transient cavity, and the massifs were defined by development of the basin ring structure and radial faults. This ejecta is visible in the massifs as discontinuous lenses of variable lithology.
4. Target rocks for the southern Serenitatis impact included large amounts of breccia; the blue-gray and light-gray breccias are older breccias that were reexcavated from this target and enclosed by impact-melted green-gray breccia during the southern Serenitatis event.
5. Photogeologic evidence suggests that basin ejecta younger than the southern Serenitatis impact is thin or absent.

REFERENCES CITED

Baldwin, R. B., 1949, The face of the Moon: Chicago, Univ. Chicago Press, 239 p.

——— 1972, The tsunami model of the origin of ring structures concentric with large lunar craters: Physics Earth Planetary Interiors, v. 6, p. 327–339.

——— 1974, On the origin of the mare basins, *in* Lunar Sci. Conf., 5th, Proc.: Geochim. et Cosmochim. Acta, Supp. 5, v. 1, p. 1–10.

Cooper, M. R., and Kovach, R. L., 1974, Lunar near-surface structure: Rev. Geophysics and Space Physics, v. 12, no. 3, p. 291–308.

Duennebier, F. K., Watkins, J. S. and Kovach, R. L., 1974, Results from the lunar surface profiling experiment [abs.], *in* Lunar Science V, Abstracts: Houston, Lunar Sci. Inst., p. 183.

Hartmann, W. K., and Kuiper, G. P., 1962, Concentric structures surrounding lunar basins: Arizona Univ., Lunar Planetary Lab. Commun. 1, p. 51–66.

Hartmann, W. K., and Wood, C. A., 1971, Moon—origin and evolution of multi-ring basins: The Moon, v. 3, p. 3–78.

Head, J. W., 1974a, Morphology and structure of the Taurus-Littrow highlands (Apollo 17)—evidence for origin and evolution: The Moon, v. 9, p. 355–395.

——— 1974b, Orientale multi-ringed basin interior and implications for the petrogenesis of lunar highland samples: The Moon, v. 11, p. 327–356.

Howard, K. A., Wilhelms, D. E., and Scott, D. H., 1974, Lunar basin formation and highland stratigraphy: Rev. Geophysics and Space Physics, v. 12, p. 309–327.

Lucchitta, B. K., 1972, *in* Scott, D. H., Lucchitta, B. K., and Carr, M. H., Geologic map of the Taurus-Littrow region of the Moon: U.S. Geol. Survey Misc. Geol. Inv. Map I–800, scale 1:50,000.

McCauley, J. F., 1968, Geologic results from the lunar precursor probes: Am. Inst. Aeronautics Astronautics Jour., v. 6, p. 1991–1996.

McGetchin, T. R., Settle, M., and Head, J. W., 1973, Radial thickness variation in impact crater ejecta—implications for lunar basin deposits: Earth and Planetary Sci. Letters, v. 20, p. 226–236.

Moore, H. J., Hodges, C. A., and Scott, D. H., 1974, Multiringed basins—illustrated by Orientale and associated features, *in* Lunar Sci. Conf., 5th, Proc.: Geochim. et Cosmochim. Acta, Supp. 5, v. 1, p. 71–100.

Muehlberger, W. R., Batson, R. M., Cernan, E. A., Freeman, V. L., Hait, M. H., Holt, H. E., Howard, K. A., Jackson, E. D., Larson, K. B., Reed, V. S., Rennilson, J. J., Schmitt, H. H., Scott, D. H., Sutton, R. L., Stuart-Alexander, D. E., Swann, G. A., Trask, N. J., Ulrich, G. E., Wilshire, H. G., and Wolfe, E. W., 1973, Preliminary geologic investigation of the Apollo 17 landing site: Natl. Aeronautics and Space Admin. Spec. Pub. 330, p. 6–1 to 6–91.

Muehlberger, W. R., 1974, Structural history of southeastern Mare Serenitatis and adjacent highlands, in Lunar Sci. Conf., 5th, Proc.: Geochim. et Cosmochim. Acta, Supp. 5, v. 1, p. 101–110.

Pike, R. J., 1972, Geometric similitude of lunar and terrestrial craters: Internat. Geol. Cong., 24th, Montreal 1972, Proc., sec. 15, Planetology, p. 41–47.

Scott, D. H., 1972, Geologic Map of the Eudoxus quadrangle of the moon: U.S. Geol. Survey Misc. Geol. Inv. Map I–705, scale 1:1,000,000.

——— 1974, The geologic significance of some lunar gravity anomalies, *in* Lunar Sci. Conf., 5th, Proc.: Geochim. et Cosmochim. Acta, Supp. 5, v. 3, p. 3025–3036.

Scott, D. H., and Pohn, H. A., 1972, Geologic map of the Macrobius quadrangle of the moon: U.S. Geol. Survey Misc. Geol. Inv. Map I–799, scale 1:1,000,000.

Sjogren, W. L., and Wimberly, R. N., 1974, Apollo 17 gravity results [abs.], *in* Lunar Science V, Abstracts: Houston, Lunar Sci. Inst., p. 712–714.

Sjogren, W. L., Wollenhaupt, W. R., and Wimberly, R. N., 1974, Lunar gravity—Apollo 17: The Moon, v. 11, p. 41–52.

Stuart-Alexander, D. E., and Howard, K. A., 1970, Lunar maria and circular basins—a review: Icarus, v. 12, p. 440–456.

Talwani, Manik, Thompson, George, Dent, Brian, Kahle, Hans-Gert, and Buck, Sheldon, 1973, Traverse gravimeter experiment: Natl. Aeronautics and Space Admin. Spec. Pub. 330, p. 13–1 to 13–13.

Van Dorn, W. G., 1968, Tsunamis on the Moon: Nature, v. 220, p. 1102–1107.

——— 1969, Lunar maria, structure and evolution: Science, v. 165, p. 693–695.

Wilhelms, D. E., 1964, Major structural features of the Mare Vaporum quadrangle: Astrogeologic Studies Ann. Prog. Rept., July 1963 to July 1964, pt. A, p. 1–16.

Wilhelms, D. E., and McCauley, 1971, Geologic map of the near side of the moon: U.S. Geol. Survey, Geologic Atlas of the Moon, Map I–703, scale 1:5,000,000.

Jour. Research U.S. Geol. Survey
Vol. 4, No. 2, Mar.–Apr. 1976, p. 181–188

RISE OF A VARIABLE-VISCOSITY FLUID IN A STEADILY SPREADING WEDGE-SHAPED CONDUIT WITH ACCRETING WALLS [1]

By ARTHUR H. LACHENBRUCH and MANUEL NATHENSON,
Menlo Park, Calif.

Abstract.—Relatively rigid plates making up the outer 50 to 100 km of the Earth are steadily separating from one another along narrow globe-circling zones of submarine volcanism, the oceanic spreading centers. Continuity requires that the viscous underlying material rise beneath spreading centers and accrete onto the steadily diverging plates. It is likely that during the rise the viscosity changes systematically and that the viscous tractions exerted on the plates contribute to the unique pattern of submarine mountains and earthquake faults observed at spreading centers. The process is modeled by viscous creep in a wedge-shaped conduit (with apex at the sea floor) in which the viscosity varies as r^m where r is distance from the apex and m is a parameter. For these conditions, the governing differential equations take a simple form. The solution for the velocity is independent of r and of the sign of m. As viscous stresses vary as r^{m-1}, the pattern of stress on the conduit wall is sensitive to viscosity variation. For negative m, the viscous pressure along the base of the conduit is quite uniform; for positive m, it falls toward zero in the axial region as the conduit base widens. For small opening angles, viscous forces push the plates apart, and for large ones, they oppose plate separation. Though highly idealized, the solution provides a tool for investigating tectonic processes at spreading centers.

The purpose of this paper is to present mathematical results for a problem in fluid flow that is useful in studies of the dynamics of oceanic spreading centers. There is now extensive evidence that the outer 50 to 100 km of the Earth is broken into a relatively few large "plates" with lateral dimensions of thousands of kilometres (see, for example, McKenzie, 1972; McKenzie and others, 1974; Turcotte and Oxburgh, 1972; Vine, 1971; Oxburgh, 1971). It has been useful to view these plates (collectively called the lithosphere) as rigid objects moving relative to one another over the Earth's surface. The lithosphere is evidently partially decoupled at its base by the relatively fluid asthenosphere, a layer that probably contains a small fraction of molten material. The lateral boundaries of lithosphere plates are the loci of most of the Earth's seismic and volcanic activity. There are three kinematically distinct types of lateral plate boundaries: (1) Those where the plates slide past one another, the transform faults such as the San Andreas fault in California, (2) those where the plates converge and overlap, as beneath the great oceanic trenches, and (3) those where the plates diverge, chiefly at narrow globe-circling zones of submarine volcanic activity, the spreading centers.

At the diverging boundaries, continuity requires that new material be brought up from the viscous asthenosphere and accreted onto the trailing edges of the spreading plates (fig. 1). As the asthenosphere material moves upward in the cleft (or "conduit") between the plates, its effective viscosity probably changes systematically as a result of temperature changes, selective accretion of suspended crystals on the conduit walls (Lachenbruch, 1973a), and partial melting induced by the diminishing pressure (for example, Kay and others, 1970). The upward flow also results in tractions on the adjacent lithosphere that probably control

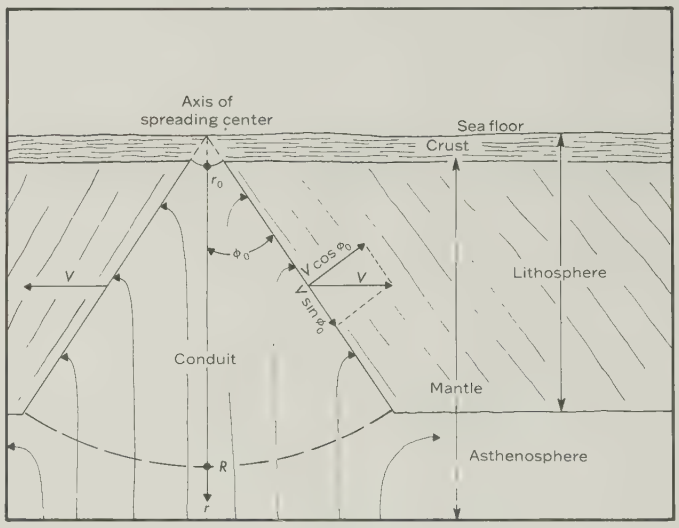

FIGURE 1.—The physical model.

[1] This article was released in 1974 as U.S. Geological Survey open-file report 74–251.

the unique patterns of submarine mountains and earthquake faults observed at oceanic spreading centers (for example, Atwater and Mudie, 1968; Anderson and Noltimier, 1973; Menard and Atwater, 1969). In order to understand better the mechanical origins of these features, we have considered a problem of Newtonian viscous flow in an idealized conduit between diverging rigid plates. The problem and its solution are described below; its geological application (Lachenbruch, 1976) requires several additional considerations not discussed in this brief report.

The walls $r_0<r<R$, $\phi=\pm\phi_0$ of the wedge-shaped conduit region in figure 1 spread symmetrically in the horizontal direction with velocity V, of the order of a few centimetres per year in our application. New material rises slowly across the surface $r=R$, $|\phi|<\phi_0$ to maintain mass balance. Material from the conduit continually accretes on the walls at $\phi=\pm\phi_0$, where it is transformed into rigid lithosphere. As the process is steady, accretion keeps pace with spreading of the walls, and the conduit size and shape remain unchanged. The flux of material through the upper surface $r=r_0$, $|\phi|<\phi_0$ is just adequate to create the spreading crustal layer. The region $r<r_0$ is eliminated from the problem domain for physical and mathematical reasons to be discussed below. Mechanical effects of systematic variations in viscosity are explored by allowing the viscosity η to vary as follows:

$$\eta(r)=\eta_R\left(\frac{r}{R}\right)^m \tag{1}$$

where m may assume any value, and η_R is the effective viscosity of the asthenosphere, possibly of the order of 10^{21} poise. For the special case of uniform viscosity ($m=0$), the problem is a member of the class of corner flows considered by Moffatt (1964), although he did not discuss these boundary conditions. The related problem for a parallel-walled conduit and exponentially varying viscosity has been discussed elsewhere (Lachenbruch, 1973b).

THE MATHEMATICAL PROBLEM

As the Reynolds number for this problem is very small (Lachenbruch, 1973b), we neglect inertial terms in the Navier Stokes equations. With the terms for radial dependence of viscosity retained, the governing differential equations take the form

$$\frac{\partial V_r}{\partial r}+\frac{V_r}{r}+\frac{1}{r}\frac{\partial V_\phi}{\partial \phi}=0, \tag{2}$$

$$\frac{\partial P}{\partial r}=\gamma\cos\phi+\eta\left(\frac{\partial^2 V_r}{\partial r^2}+\frac{1}{r}\frac{\partial V_r}{\partial r}-\frac{V_r}{r^2}+\frac{1}{r^2}\frac{\partial^2 V_r}{\partial \phi^2}-\frac{2}{r^2}\frac{\partial V_\phi}{\partial \phi}\right)+2\frac{\partial \eta}{\partial r}\frac{\partial V_r}{\partial r}, \tag{3}$$

$$\frac{1}{r}\frac{\partial P}{\partial \phi}=-\gamma\sin\phi+\eta\left(\frac{\partial^2 V_\phi}{\partial r^2}+\frac{1}{r}\frac{\partial V_\phi}{\partial r}-\frac{V_\phi}{r^2}+\frac{1}{r^2}\frac{\partial^2 V_\phi}{\partial \phi^2}+\frac{2}{r^2}\frac{\partial V_r}{\partial \phi}\right)+\frac{\partial \eta}{\partial r}\left[\frac{1}{r}\frac{\partial V_r}{\partial \phi}+r\frac{\partial}{\partial r}\left(\frac{V_\phi}{r}\right)\right] \tag{4}$$

where γ represents specific weight and P represents pressure.

Equations 2, 3, and 4 must be solved subject to the following conditions of symmetry and boundary motion:

$$V_\phi(r,\phi)=-V_\phi(r,-\phi), \tag{5}$$

$$V_\phi=\pm V\cos\phi_0,\ \phi=\pm\phi_0, \tag{6}$$

$$V_r(r,\phi)=V_r(r,-\phi), \tag{7}$$

$$V_r=V\sin\phi_0,\ \phi=\pm\phi_0. \tag{8}$$

A uniform increase in density due to phase change at the conduit wall can be accommodated by making the constant V, equations 6 and 8, greater than the speed of rigid motion behind the wall.

As the boundary conditions on velocity, equations 6 and 8, are independent of r, it is anticipated that equations 2, 3, and 4 can be solved subject to conditions 5, 6, 7, and 8 with the simplification

$$\frac{\partial V_r}{\partial r}\equiv 0. \tag{9}$$

Applying equation 9 to equation 2 yields

$$\frac{\partial V_\phi}{\partial \phi}=-V_r. \tag{10}$$

Equations 9, 10, and 6 require

$$\frac{\partial V_\phi}{\partial r}\equiv 0; \tag{11}$$

and hence we are seeking a solution in which both velocity components depend only on the angular coordinate, ϕ. The velocity condition on the lower boundary, $r=R$, is left unspecified. With the aid of equations 9 and 11, equations 3 and 4 can be simplified as follows:

$$\frac{\partial P}{\partial r}=\gamma\cos\phi+\frac{\eta}{r^2}\left(\frac{\mathrm{d}^2 V_r}{\mathrm{d}\phi^2}-2\frac{\mathrm{d}V_\phi}{\mathrm{d}\phi}-V_r\right) \tag{12}$$

$$\frac{\partial P}{\partial \phi}=-r\gamma\sin\phi+\frac{\eta}{r}\left(\frac{\mathrm{d}^2 V_\phi}{\mathrm{d}\phi^2}+2\frac{\mathrm{d}V_r}{\mathrm{d}\phi}-V_\phi\right)+\frac{\mathrm{d}\eta}{\mathrm{d}r}\left(\frac{\mathrm{d}V_r}{\mathrm{d}\phi}-V_\phi\right). \tag{13}$$

We now introduce equation 1, cross differentiate equations 12 and 13, and simplify with equation 10 to obtain

$$\frac{\partial^2 P}{\partial\phi\partial r}=-\gamma\sin\phi-\frac{\eta}{r^2}\left(\frac{\mathrm{d}^4V_\phi}{\mathrm{d}\phi^4}+\frac{\mathrm{d}^2V_\phi}{\mathrm{d}\phi^2}\right) \tag{14}$$

$$\frac{\partial^2 P}{\partial r\partial\phi}=-\gamma\sin\phi-\frac{\eta}{r^2}\left(\frac{\mathrm{d}^2V_\phi}{\mathrm{d}\phi^2}+V_\phi\right)(m^2-1). \tag{15}$$

Equating 14 and 15 yields the general differential equation

$$\frac{\mathrm{d}^4V_\phi}{\mathrm{d}\phi^4}+(2-m^2)\frac{\mathrm{d}^2V_\phi}{\mathrm{d}\phi^2}+(1-m^2)V_\phi=0 \tag{16}$$

which is easily solved by standard analytical methods.

The solution to equation 16 taken with conditions 5–8 yields complete analytic results for the velocity field for any value of m. The pressure can then be determined by integration of equations 12 and 13, adjusting the constants as required by the physical problem. The components of stress are determined from their definitions as follows:

$$\sigma_r=2\eta\frac{\partial V_r}{\partial r}-P, \tag{17a}$$

$$\sigma_\phi=2\eta\left(\frac{1}{r}\frac{\partial V_\phi}{\partial\phi}+\frac{V_r}{r}\right)-P, \tag{17b}$$

$$\tau=\eta\left[r\frac{\partial}{\partial r}\left(\frac{V_\phi}{r}\right)+\frac{1}{r}\frac{\partial V_r}{\partial\phi}\right]. \tag{17c}$$

By applying equations 9 and 10, equations 17 may be simplified as follows:

$$\sigma_r=\sigma_\phi=-P \tag{18}$$

$$\tau=\frac{\eta}{r}\left(\frac{\mathrm{d}V_r}{\mathrm{d}\phi}-V_\phi\right). \tag{19}$$

ANALYTICAL RESULTS

Complete expressions for the velocity and stress fields for all possible values of the parameter m are as follows:

I. $m=0$, homogeneous case:

$$V_\phi=VB(\phi\cos\phi-\cos^2\phi_0\sin\phi) \tag{21a}$$

$$V_r=VB(\phi\sin\phi-\sin^2\phi_0\cos\phi) \tag{21b}$$

$$P_\eta=2B\frac{\eta V}{R}\cos\phi_0\left(\beta^{-1}-\frac{R}{r}\frac{\cos\phi}{\cos\phi_0}\right) \tag{21c}$$

$$\tau=2B\frac{\eta V}{R}\frac{R}{r}\sin\phi \tag{21d}$$

$$B=(\phi_0-\cos\phi_0\sin\phi_0)^{-1}>0 \tag{21e}$$

II. $m^2>1$:

$$V_\phi=\frac{V}{Q}(N\sin\phi-\sinh\sqrt{m^2-1}\,\phi) \tag{22a}$$

$$V_r=\frac{V}{Q}(\sqrt{m^2-1}\cosh\sqrt{m^2-1}\,\phi-N\cos\phi) \tag{22b}$$

$$P_\eta=\frac{m^2\sqrt{m^2-1}}{Q(m-1)}\frac{\eta_R V}{R}\cosh\sqrt{m^2-1}\,\phi_0\times\left[\left(\frac{r}{R}\right)^{m-1}\frac{\cosh\sqrt{m^2-1}\,\phi}{\cosh\sqrt{m^2-1}\,\phi_0}-\beta^{m-1}\right] \tag{22c}$$

$$\tau=\frac{m^2}{Q}\frac{\eta_R V}{R}\left(\frac{r}{R}\right)^{m-1}\sinh\sqrt{m^2-1}\,\phi \tag{22d}$$

$$Q=\sqrt{m^2-1}\sin\phi_0\cosh\sqrt{m^2-1}\,\phi_0-\cos\phi_0\sinh\sqrt{m^2-1}\,\phi_0 \tag{22e}$$

$$N=\sqrt{m^2-1}\cos\phi_0\cosh\sqrt{m^2-1}\,\phi_0+\sin\phi_0\sinh\sqrt{m^2-1}\,\phi_0 \tag{22f}$$

III. $0<m^2<1$:

$$V_\phi=\frac{V}{S}(M\sin\phi-\sin\sqrt{1-m^2}\,\phi) \tag{23a}$$

$$V_r=\frac{V}{S}(\sqrt{1-m^2}\cos\sqrt{1-m^2}\,\phi-M\cos\phi \tag{23b}$$

$$P_\eta=\frac{m^2\sqrt{1-m^2}}{S(1-m)}\frac{\eta_R V}{R}\cos\sqrt{1-m^2}\,\phi_0\times\left[\beta^{m-1}-\left(\frac{R}{r}\right)^{1-m}\frac{\cos\sqrt{1-m^2}\,\phi}{\cos\sqrt{1-m^2}\,\phi_0}\right] \tag{23c}$$

$$\tau=\frac{m^2}{S}\frac{\eta_R V}{R}\left(\frac{r}{R}\right)^{m-1}\sin\sqrt{1-m^2}\,\phi \tag{23d}$$

$$S=\sqrt{1-m^2}\sin\phi_0\cos\sqrt{1-m^2}\,\phi_0-\cos\phi_0\sin\sqrt{1-m^2}\,\phi_0>0 \tag{23e}$$

$$M=\sqrt{1-m^2}\cos\phi_0\cos\sqrt{1-m^2}\,\phi_0+\sin\phi_0\sin\sqrt{1-m^2}\,\phi_0 \tag{23f}$$

IV. $m^2=1$:

$$V_\phi=VA[(\phi_0\sin\phi_0+\cos\phi_0)\sin\phi-\phi] \tag{24a}$$

$$V_r=VA[1-(\phi_0\sin\phi_0+\cos\phi_0)\cos\phi] \tag{24b}$$

$$A=(\sin\phi_0-\phi_0\cos\phi_0)^{-1} \tag{24c}$$

IVa. $m=-1$:

$$P_\eta(r,\phi)=\frac{1}{2}A\frac{\eta_R V}{R}\left[\beta^{-2}-\left(\frac{R}{r}\right)^2\right] \tag{25a}$$

$$\tau=A\frac{\eta_R V}{R}\left(\frac{R}{r}\right)^2\phi \tag{25b}$$

IVb. $m=+1$:

$$P_\eta(r,\phi)=A\frac{\eta_R V}{R}\left[\ln\left(\beta^{-1}\frac{r}{R}\right)+\phi^2-\phi_0^2\right] \tag{26a}$$

$$\tau=A\frac{\eta_R}{R}\mathrm{V}\phi \tag{26b}$$

In equations 21–26, we have used the notation

$$\beta=\frac{r_0}{R}$$

and P_η is used to denote the viscous part of the pressure. The total pressure, P, at any point is obtanied by adding to it the hydrostatic part, as follows:

$$P(r, \phi) = r\,\gamma\cos\phi + P_\eta(r, \phi), \tag{27}$$

It is seen that the radial dependence of the viscous stresses (P_η, τ) is generally as r^{m-1}. Hence for $m<1$, it would not be possible to impose a bounded pressure condition at the top of the conduit if some region $r<r_0$ were not excluded from the problem domain. Physically it is natural to identify $r<r_0$ as the crustal portion of the conduit where the viscous stresses are expected to be very small relative to those in the mantle portion, $r_0<r<R$. Hence in the results above (eq 21–26), we have imposed the condition

$$P_\eta(r_0, \phi_0) = 0. \tag{28}$$

In the applications, the pressure in the crust $r<r_0$ is assumed to be hydrostatic.

It is convenient to normalize the viscous stresses by the viscous pressure $P_\eta(R, \phi_0)$ at the base of the conduit wall. We adopt the following notation:

$$P^*_\eta = P_\eta(R, \phi_0), \tag{29a}$$

$$P'_\eta(r, \phi) = \frac{P_\eta(r, \phi)}{P^*_\eta}, \tag{29b}$$

$$\tau'(r, \phi) = \frac{\tau(r, \phi)}{P^*_\eta}, \tag{29c}$$

where it is understood that in any equation P^*_η and P_η or τ are always evaluated for the same values of the parameters ϕ_0, m. Foregoing results can now be represented as follows:

$$P'_\eta = \frac{\left(\frac{r}{R}\right)^{m-1}\frac{\cosh\sqrt{m^2-1}\,\phi}{\cosh\sqrt{m^2-1}\,\phi_0} - \beta^{m-1}}{1-\beta^{m-1}}, \qquad m\neq 1, \tag{30a}$$

$$= \frac{\ln\left(\beta^{-1}\frac{r}{R}\right) + \phi^2 - \phi_0^2}{\ln(\beta^{-1})}, \qquad m=1, \tag{30b}$$

$$\tau' = \frac{m-1}{\sqrt{m^2-1}}\left(\frac{r}{R}\right)^{m-1}\frac{\sinh\sqrt{m^2-1}\,\phi}{(1-\beta^{m-1})\cosh\sqrt{m^2-1}\,\phi_0}, \qquad |m|\neq 1, \tag{31a}$$

$$= 2\left(\frac{r}{R}\right)^{-2}\frac{\phi}{\beta^{-2}-1}, \qquad m=-1, \tag{31b}$$

$$= \frac{\phi}{\ln(\beta^{-1})} \qquad m=+1. \tag{31c}$$

In these relations $\sqrt{m^2-1}$ is treated as a complex quantity.

DISCUSSION

The selected streamlines and velocity profiles illustrated in figures 2 and 3 show that the flow seems to

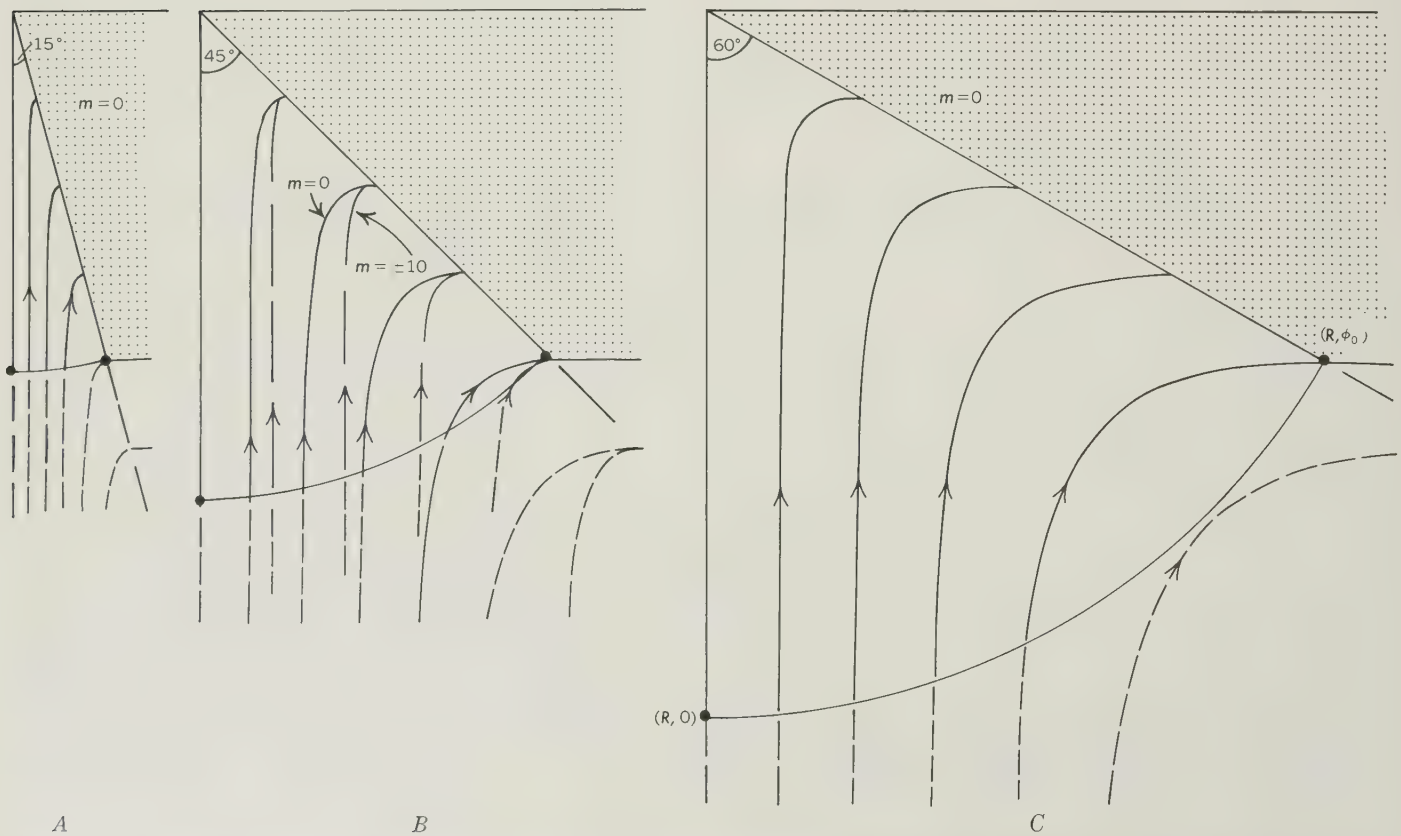

FIGURE 2.—Streamlines for a steadily spreading wedge-shaped conduit ($|\phi|<\phi_0$, $r<R$). *A*, Case $\phi_0=15°$, $m=0$. *B*, Case $\phi_0=45°$, $m=0, \pm 10$. *C*, Case $\phi_0=60°$, $m=0$.

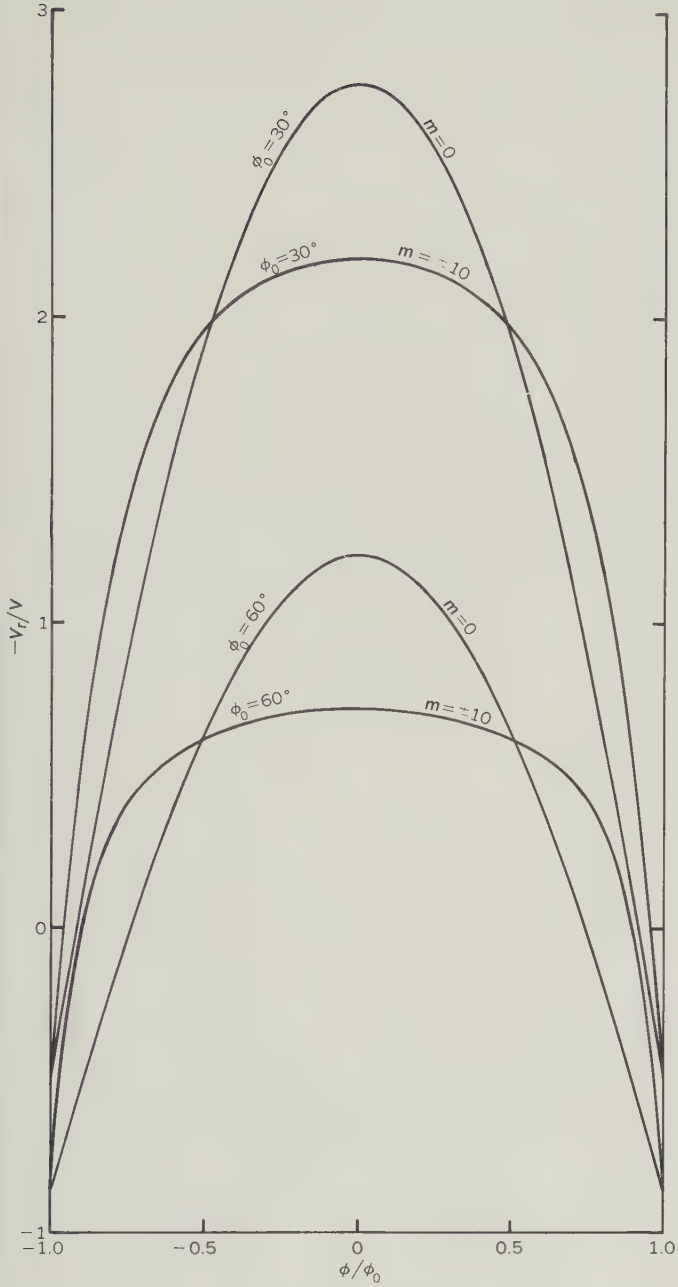

FIGURE 3.—Radial velocity in a wedge-shaped conduit for $\phi_0=30°$ and 60° and $m=0$ and ± 10.

take on a boundary layer character for very large $|m|$. It is surprising that the velocity is independent of the sign of m (eq 21–24); that is, the velocity field is the same whether the viscosity decreases as r^{-2} or increases as r^{+2}. The dynamics of flow, however, are very different in each case.

The normal component P'_η, and tangential component τ', of normalized viscous stress at the conduit wall are shown for selected conditions in figure 4. It has been pointed out that both stresses have a singularity at $r=0$ for $m<1$ (eq 21–25). For $m=+1$ (fig. 4*D*), the shearing stress is independent of r (eq 26b), but the normal stress has a logarithmic singularity (eq 26a). Figure 4 is drawn for the case $\beta=0.1$, corresponding to a crustal thickness ($r_0 \cos \phi_0$) of 5 km and a lithosphere thickness ($R \cos \phi_0$) of 50 km. It is seen that as m increases to large positive values, viscous stress on the wall becomes negligible in the upper part of the conduit, and we can set $\beta=0$ (eqs 22a–f), eliminating the formal distinction between crust and mantle . For $m>+1$ the shearing stress asymptotically approaches limiting values with increasing ϕ_0 (figs. 4*E*, *F*), and for very large m, this limit is the normal stress P_η (r, ϕ_0). The horizontal component of the normal viscous stress at the wall, $P_\eta(r, \phi_0) \cos \phi_0$, acts to push the walls apart, whereas the horizontal component of the tangential stress, $\tau(r, \phi_0) \sin \phi_0$, acts to pull them together. Hence for smaller opening angles, viscous forces in the conduit contribute driving energy to the separating walls, and for larger angles they resist this separation. (In applying these results, effects of gravity forces must, of course, be superimposed.) For m between 0 and 5, the integrated effect of these horizontal tractions changes sign when ϕ_0 is between 50° and 60°. For $m=-1$, the crossover occurs at $\phi_0 \approx 75°$. The vertical component of the viscous traction is, of course, always directed upward. It evidently relates to the uplift-and-collapse topographic features of the sea floor and to the Earth's gravity field near a spreading center. Discussion of these complex features is beyond the purpose of this presentation.

Along any arc of constant r, the viscous pressure increases toward the axis for $m<-1$ and decreases toward the axis for $m>-1$; for the special case $m=-1$, it is uniform (eq 25a). The variation of the viscous pressure along the base of the conduit $r=R$ is indicated by the value at the axis shown in figure 5. This pressure is uniform to terms of higher order for any ϕ_0 at $r=R$ for all $m \leq -1$. As m becomes positive, however, any assumption of uniform basal pressure would be valid only for smaller opening angles ϕ_0. For the larger values of m, viscous forces are negligible in the axial region for intermediate and large opening angles ϕ_0.

The viscous pressure P_η $(r_0, 0)$ at the axis on the upper boundary is shown in figure 6. It is seen that the condition in equation 28 is adequate to assure that the viscous pressure is negligible on $r=r_0$ for $m \gtrsim +2$ and $m=-1$. As the pressure changes rapidly with r near $r=r_0$ for $m \leq +1$ (fig. 4), we can assure negligible viscous pressure along the upper boundary by replacing

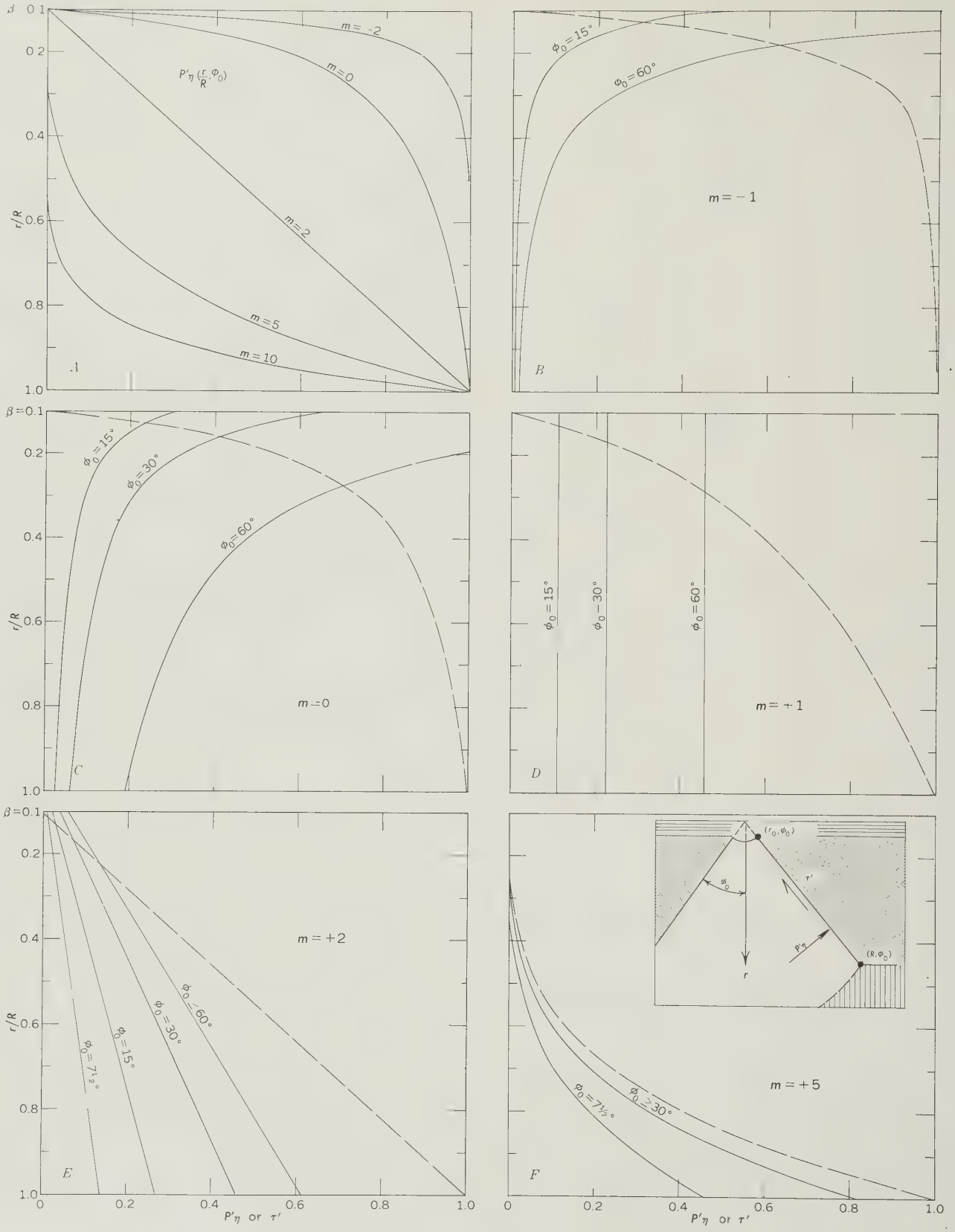

FIGURE 4.—Viscous traction at wall ($\phi=\phi_0$) of a spreading wedge-shaped conduit for various opening angles (ϕ_0) and viscosity distributions (m). P_η' is the normal component, τ' is the tangential component. Both are normalized by the viscous pressure $P_\eta(R,\phi_0)$. In *B*, *C*, *D*, *E*, and *F*, dashed curves represent P_η' and solid curves represent τ'. Case illustrated is $r_0/R=0.1$.

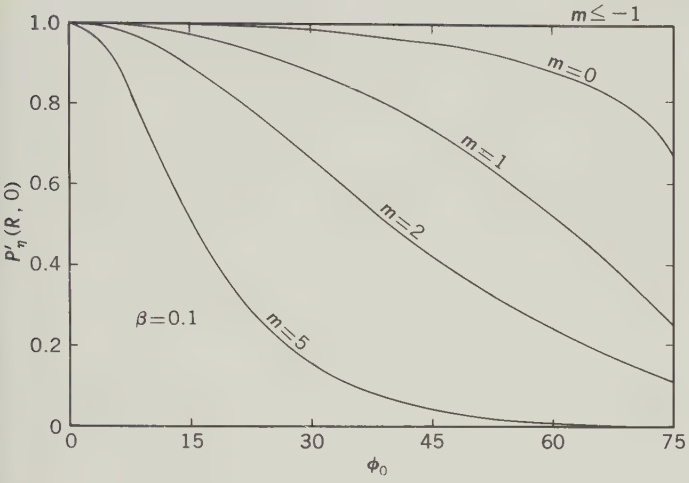

FIGURE 5.—Normalized viscous pressure on the axis ($\phi=0$) at the base ($r=R$) of a wedge-shaped conduit as a function of opening angle (ϕ_0) for various viscosity distributions (m). Case illustrated is $r_0/R=0.1$.

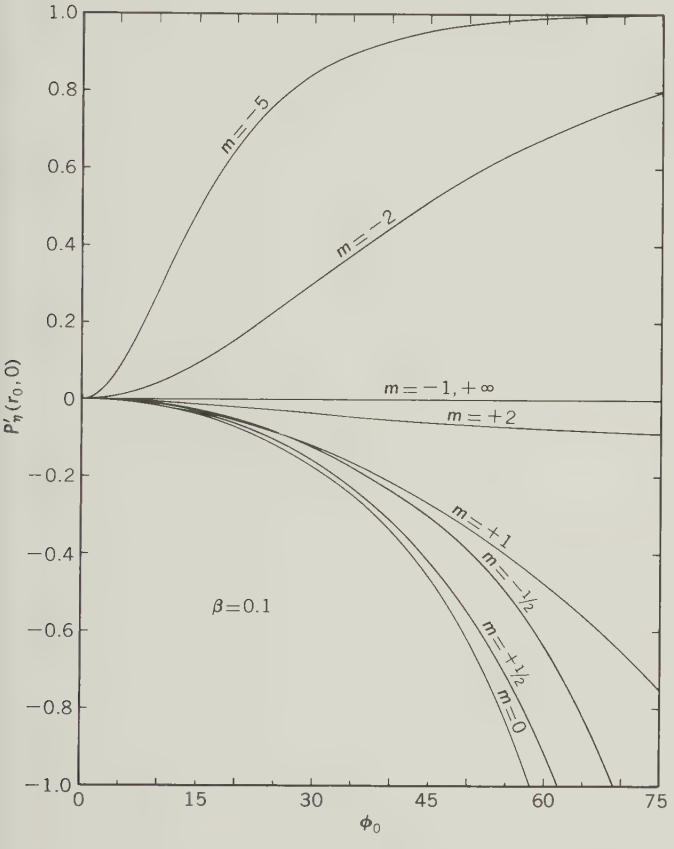

FIGURE 6.—Normalized viscous pressure on the axis ($\phi=0$) at the top ($r=r_0$) of a wedge-shaped conduit as a function of opening angle (ϕ_0) for various viscosity distributions (m). Case illustrated is $r_0/R=0.1$.

the boundary curve $r=r_0$ with an arc through (r_0, $\pm\phi_0$) with somewhat less curvature for $m<-1$, and, provided ϕ_0 is not too great, one with somewhat more curvature for $-1<m\leq+1$. In general, an appreciable tangential stress will persist near the conduit wall on the upper boundary for $m<2$, but its effects on the equilibrium of the conduit and the energetics of the system will not be great (for $\beta=0.1$) as long as ϕ_0 is restricted to values less than 60° to 75°.

The dimensionless function Ψ defined by

$$\Psi(\phi_0, \beta, m) = P^*_\eta \left(\frac{\eta_R V}{H} \right)^{-1} \tag{32}$$

relates the normalizing factor for equations 30 and 31 and figures 4 through 6 to the other parameters of the problem. It is illustrated for $\beta=0.1$ in figure 7. The quantities η_R and H may be considered as constant, though poorly known, properties of the asthenosphere and lithosphere, respectively. If the viscous pressure at the base of the conduit wall, P^*_η, remains constant as the velocity of plate separation V increases from one steady state to another, the conduit opening ϕ_0 must increase according to Ψ to admit the increased flow as required by continuity. For small values of ϕ_0 (not exceeding 10° or 15°), it can be shown that Ψ varies as ϕ_0^{-3} and in fact, that the curves of figure 7 practically coincide with the comparable ones for a narrow vertical-walled conduit having the same mean width and viscosity variation (Lachenbruch, 1973b).

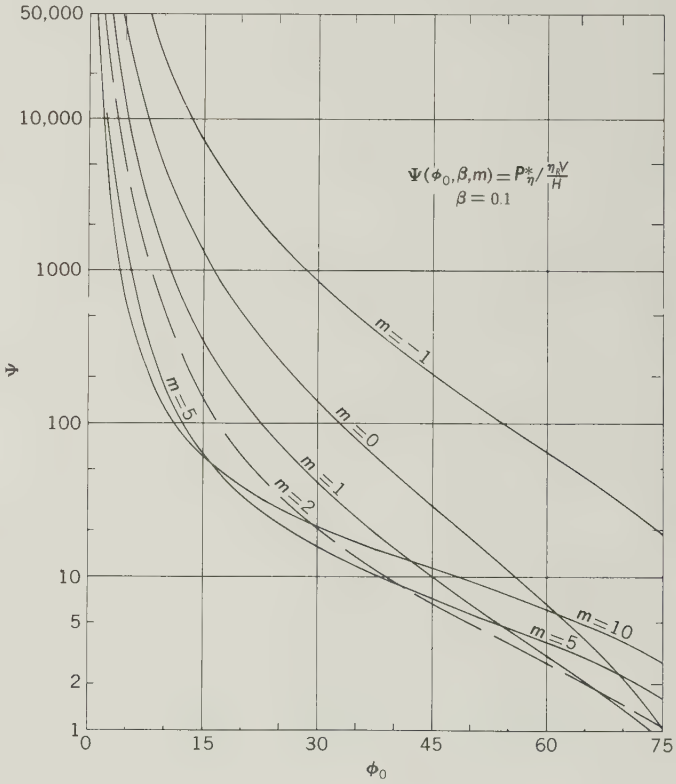

FIGURE 7.—The function Ψ of equation 32 as a function of opening angle (ϕ_0) for various viscosity distributions (m). Case illustrated is $r_0/R=0.1$.

Representing physical processes in the Earth with an idealized model like this one, of course, presents difficulties, but as the model is supported by exact analytical results, these difficulties can be understood. The solution provides a useful point of reference for considerations of the dynamics and energetics of an oceanic spreading center (Lachenbruch, 1976).

REFERENCES CITED

Anderson, R. N., and Noltimier, H. C., 1973, A model for the horst and graben structure of midocean ridge crests based upon spreading velocity and basalt delivery to the oceanic crust: Royal Astron. Soc. Geophys. Jour., v. 34, p. 137–147.

Atwater, T. M., and Mudie, J. D., 1968, Block faulting on the Gorda Rise: Science, v. 159, p. 729–731.

Kay, R., Hubbard, N. J., and Gast, P. W., 1970, Chemical characteristics and origin of oceanic ridge volcanic rocks: Jour. Geophys. Research, v. 75, p. 1585–1613.

Lachenbruch, A. H., 1973a, Differentiation and the gravitational driving force for material rising at an oceanic ridge: Jour. Geophys. Research, v. 78, 825–831.

——— 1973b, A simple mechanical model for oceanic spreading centers: Jour. Geophys. Research, v. 78, p. 3395–3417.

——— 1976, Dynamics of a passive spreading center: Jour. Geophys. Research. (In press.)

McKenzie, D. P., 1972, Plate tectonics, *in* Robertson, E. C., Hays, F. J., and Knopoff, Leon, eds., The nature of the solid earth: New York, McGraw-Hill, Inc., p. 323–360.

McKenzie, D. P., Roberts, J. M., and Weiss, N. O., 1974, Convection in the earth's mantle: towards a numerical simulation: Jour. Fluid Mechanics, v. 62, p. 465–538.

Menard, H. W., and Atwater, Tanya, 1969, Origin of fracture zone topography: Nature, v. 222, p. 1037–1040.

Moffatt, H. K., 1964, Viscous and resistive eddies near a sharp corner: Jour. Fluid Mechanics, v. 18, p. 1–18.

Oxburgh, E. R., 1971, Plate tectonics, *in* Gass, I. G., Smith, P. J., and Wilson, R. C. L., eds., Understanding the earth: Sussex England, The Artemis Press, p. 263–285.

Turcotte, D. L., and Oxburgh, E. R., 1972, Mantle convection and the new global tectonics: Ann. Rev. Fluid Mechanics, v. 4, p. 33–68.

Vine, F. J., 1971, Sea-floor spreading, *in* Gass, I. G., Smith, P. J., and Wilson, R. C. L., eds., Understanding the earth: Sussex, England, The Artemis Press, p. 233–249.

Jour. Research U.S. Geol. Survey
Vol. 4, No. 2, Mar.–Apr. 1976, p. 189–193

THE VOLUMETRIC PROPERTIES OF H_2O— A GRAPHICAL PORTRAYAL

By JAMES R. FISHER, Reston, Va.

Abstract.—A graphical display of the volumetric properties of H_2O is presented as density (0.01 to 1.0 $g \cdot cm^{-3}$) contoured on pressure-temperature coordinates and pressure (1–10,000 bars) contoured on density-temperature coordinates over the temperature range 0–1,000 °C. Data were obtained from sources published during 1964–1969; several minor inconsistencies are observed and attributed to inadequacies in the equations of state used to describe experimental data obtained above 1,000 bars.

To date, the volumetric properties of H_2O have been investigated experimentally from 0 °C to 900 °C and to pressures of 8,200 bars; extensive tables derived from the fitting of equations of state to such data are available (Bain, 1964; Burnham, Holloway, and Davis, 1969; Keenan, Keyes, Hill, and Moore, 1969; the last two are hereafter referred to as "BHD" and "KKHM"). Those whose work requires relatively precise data must consult these tables directly; others, such as those engaged in fluid-inclusion research, may require less precision and can profitably use a graphical portrayal, with its attendant speed and convenience. For these latter workers, the volumetric properties of H_2O are presented in figures 1–4.

Data below 1,000 bars were taken from Bain and KKHM; those above 1,000 bars, from BHD. Figure 1 is a plot of density ($g \cdot cm^{-3}$) versus temperature (°C) contoured in pressure (bars). Isobars from 1 to 50 bars have been omitted for clarity in the single-phase region at low densities, as have the isobars from 1 to 200 bars at high densities adjacent to the two-phase region. The area outlined by the rectangle in figure 1 at high densities and low temperatures is presented in figure 2, where again the 1- to 50-bar isobars in the single-phase region have been omitted. Figure 3 shows isochores contoured on pressure-temperature coordinates. The area in figure 3 outlined by the rectangle at low temperatures and pressures is presented in figure 4. The isochores below 1,000 bars were obtained directly by evaluating the equation of state (of the form $P=f(V,T)$) given by KKHM; those above 1,000 bars (in fig. 3) were calculated using the equations of state given by BHD. The latter are of the form $\rho=g(P,T)$, where ρ is density. In order to determine the exact pressure for a given density and temperature, an initial estimate of P was obtained from their tables, and a density calculated for that P and T. The pressure was then systematically varied, and the equation repeatedly evaluated until the calculated density agreed with that required for the isochore to 1 part in 10,000.

The observant reader will note several oddities in figure 3. The isochores between 0.70 and 0.95 $g \cdot cm^{-3}$ above 1,000 bars (from the BHD equations of state) do not join smoothly with those below 1,000 bars (from the tables of Bain and KKHM). In addition, the BHD isochores are linear along their midsections but concave toward the temperature axis both at high and low pressures. These effects are most likely the result of inadequate constraints on the BHD equations of state (polynomials of high degree) along their boundaries.

These inconsistencies are of little consequence in the present context but probably could be eliminated by fitting a single equation of state to all available volumetric and thermodynamic data on H_2O over the entire P-T range of interest.

Figures 1 through 4 follow "References Cited."

REFERENCES CITED

Bain, R. W., 1964, Steam tables 1964 : Edinburgh, Her Majesty's Stationery Office, 147 p.

Burnham, C. W., Holloway, J. R., and Davis, N. F., 1969, Thermodynamic properties of water to 1,000 °C and 10,000 bars: Geol. Soc. America Spec. Paper 132, 96 p.

Keenan, J. H., Keyes, F. G., Hill, P. G., and Moore, J. G., 1969, Steam tables: New York, John Wiley & Sons, 162 p.

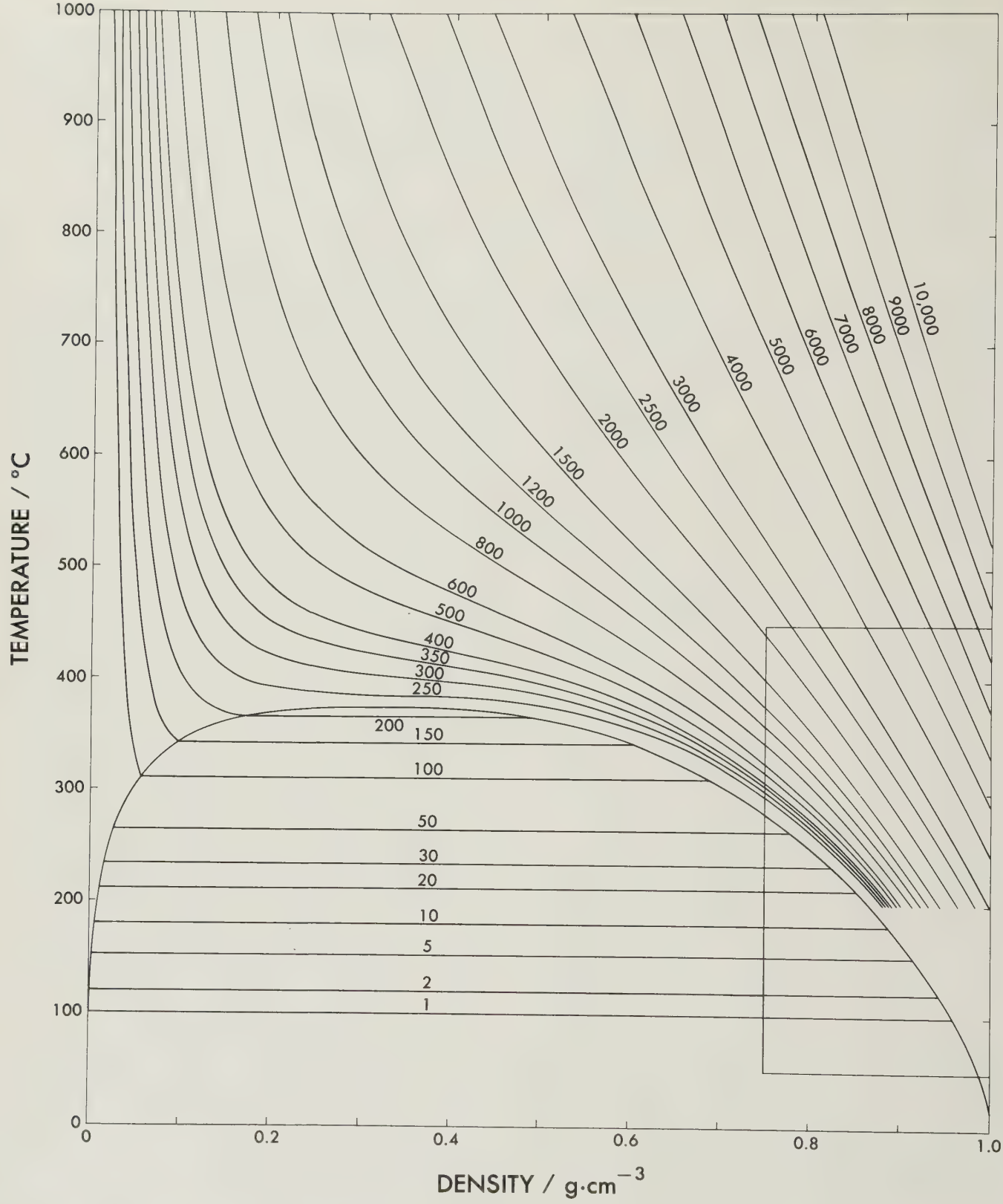

FIGURE 1.—Pressure (bars) contoured on temperature-density coordinates. The dome-shaped curve encloses the two-phase region of liquid-vapor coexistence. The area outlined by the rectangle is expanded in figure 2.

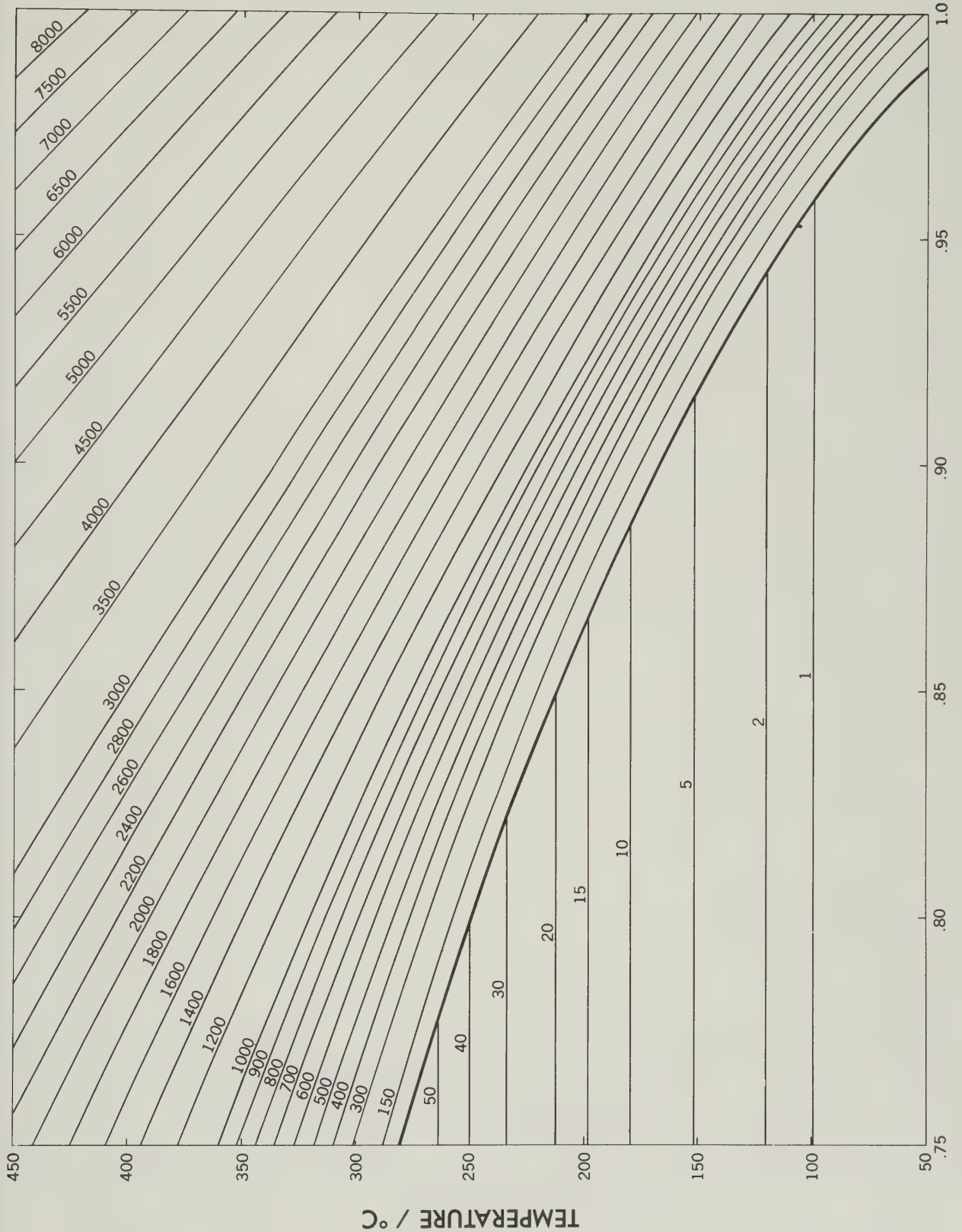

FIGURE 2.—Pressure (bars) contoured on temperature-density coordinates. The curve terminating the horizontal 1–50 bar isobars separates the two-phase liquid-vapor coexistence region from that of the single-phase fluid.

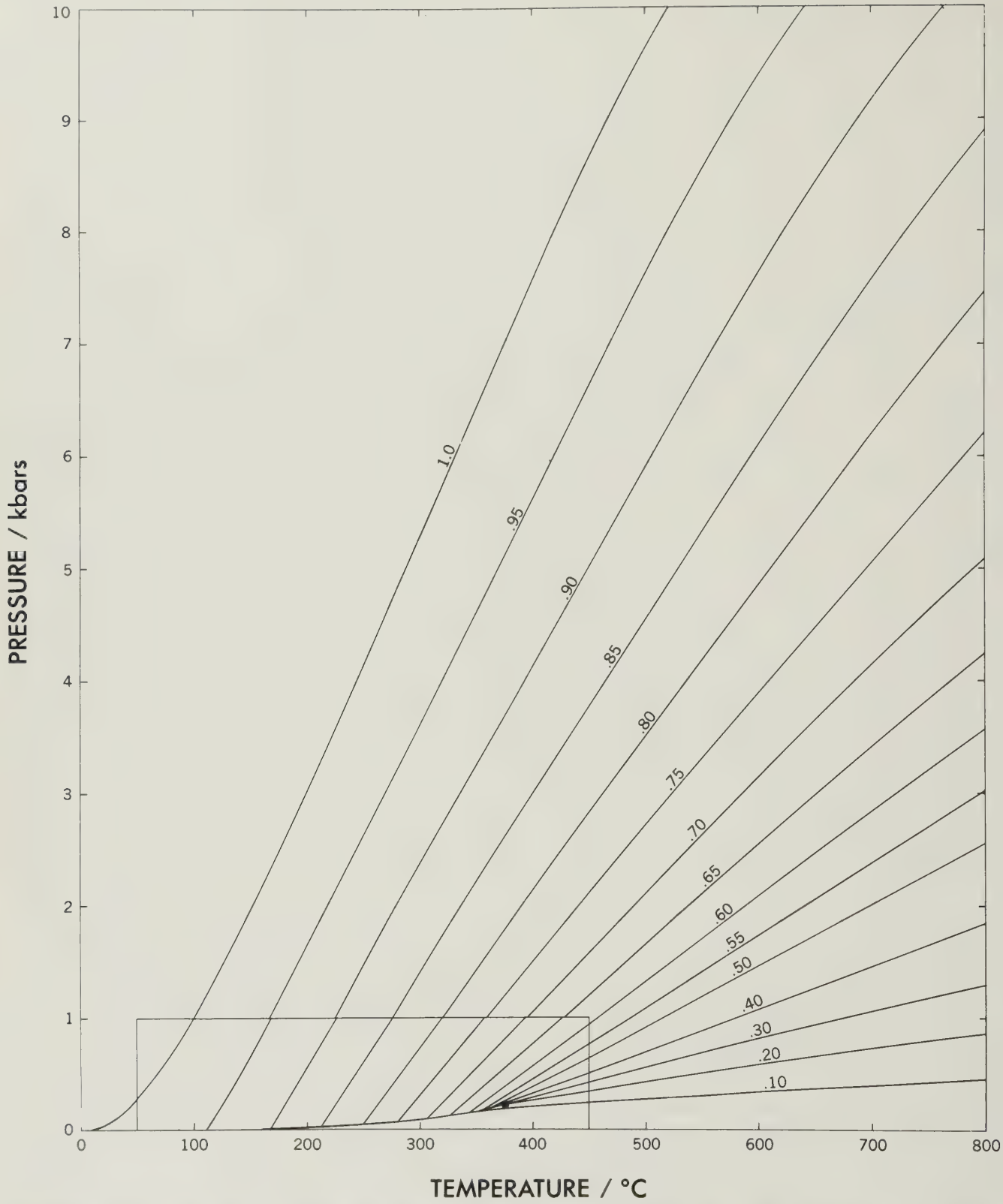

FIGURE 3.—Density contoured on pressure-temperature coordinates. The two-phase liquid-vapor coexistence curve terminates at the critical point. The area outlined by the rectangle is expanded in figure 4.

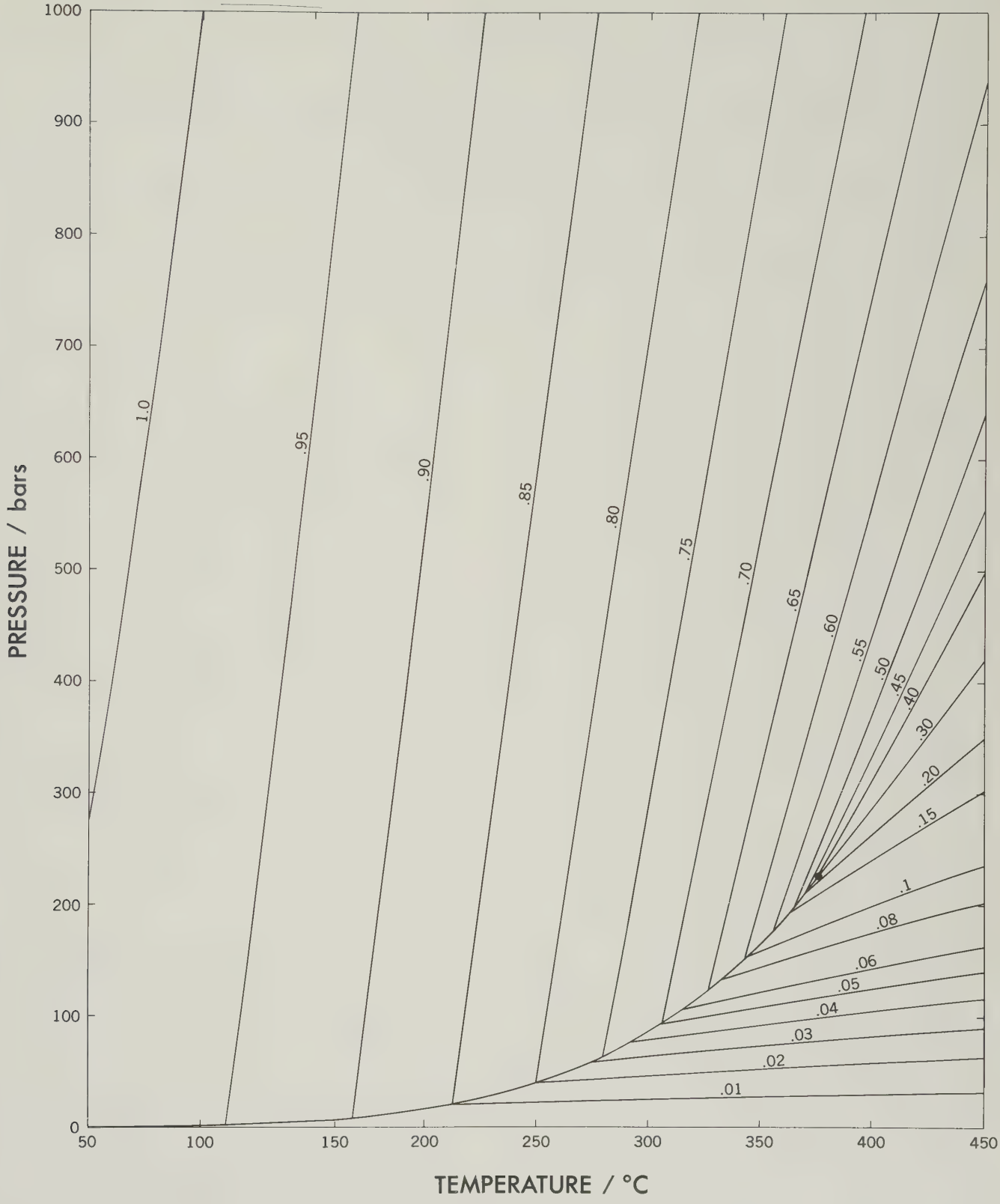

FIGURE 4.—Density contoured on pressure-temperature coordinates. The two-phase liquid-vapor coexistence curve terminates at the critical point.

Jour. Research U.S. Geol. Survey
Vol. 4, No. 2, Mar.–Apr. 1976, p. 195–204

THE HEAT CAPACITIES AT LOW TEMPERATURES AND ENTROPIES AT 298.15 K OF LOW ALBITE, ANALBITE, MICROCLINE, AND HIGH SANIDINE

By RONALD E. OPENSHAW;[1] [2] BRUCE S. HEMINGWAY, RICHARD A. ROBIE;
DAVID R. WALDBAUM;[3] and KENNETH M. KRUPKA,
Princeton, N.J.; Reston, Va.; Princeton, N.J.; Reston, Va.

Abstract.—The heat capacities of low albite and analbite, $NaAlSi_3O_8$, and of microcline and high sanidine, $KAlSi_3O_8$, have been measured from 15 to 375 K using an adiabatic calorimeter. Tables of the thermodynamic functions $C°_p$, $(H°_T-H°_0)/T$, $(G°_T-H°_0)/T$, and $S°_T-S°_0$ are presented for these four feldspars from 0 to 370 K. At 298.15 K (25.0°C) the values for $S°_T-S°_0$ for low albite, analbite, microcline, and high sanidine are 207.4±0.4, 207.7±0.4, 214.2±0.4, and 214.2±0.4 J/(mol·K), respectively.

The effect of the state of Al/Si order upon the heat capacity is quite small. The difference, $\Delta C°_p$, between albite-analbite and microcline-sanidine never exceeds 0.5 percent at temperatures below 400 K.

With the exception of microcline, the heat capacities of these four feldspars follow a smooth S-shaped curve between 15 and 375 K, with no indication of transitions or anomalous behavior. Above 250 K, the heat capacity of microcline shows a form of thermal hysteresis. In the temperature range 250 to 375 K, the heat capacity of microcline is dependent upon its past thermal history. At 375 K, microcline which had been cooled to 230 K before the measurement of $C°_p$ has a heat capacity greater by approximately 1.2 percent than microcline which had not been previously cooled below 295 K. After a day of annealing at about 300 K, $C°_p$ of the previously cooled microcline decreases to essentially the same value as the microcline which had never been at a temperature below 300 K.

The polymorphic modifications of $NaAlSi_3O_8$ and $KAlSi_3O_8$, the alkali feldspars, occur in a wide range of geologic environments and constitute one of the most important groups of rock-forming minerals. Accurate thermodynamic data for these important minerals is desirable as an aid to understanding chemical equilibrium in many rock-forming processes and for delineating more exactly the stable phase relations within the alkali feldspar group. To this purpose, we have measured the heat capacities, $C°_p$, for low albite, analbite, microcline, and high sanidine between 15 and 375 K in order to obtain their standard entropies, $S°_{298.15}$, from the third law of thermodynamics. In particular we were interested in the effect of the state of the Al/Si order on the low-temperature vibrational properties of the alkali feldspar framework.

In this report, we shall use the phase names low albite and microcline to refer to the triclinic modifications of $NaAlSi_3O_8$ and $KAlSi_3O_8$, space group $C\bar{1}(2)$, in which the aluminum occupies the $T_1(0)$ position exclusively and the three silicon atoms occupy the $T_1(m)$, $T_2(0)$, and $T_2(m)$ positions (Megaw, 1956). Conversely, we will use the names analbite and high sanidine to mean $NaAlSi_3O_8$ and $KAlSi_3O_8$, in which the aluminum and three silicon atoms are randomly distributed over the $T_1(0)$, $T_1(m)$, $T_2(0)$, and $T_2(m)$ sites. Analbite is triclinic, space group $C\bar{1}(2)$, and high sanidine is monoclinic, space group $C2/m(12)$. Phases for which the Al/Si distribution is partially ordered will not be considered in this report.

Previous measurements of the heat capacities of the alkali feldspars have been reported for low albite, adularia, and ferriferous orthoclase over the range 50 to 300 K by Kelley and others (1953). These authors also reported values of $H°_T-H°_{298}$ for low albite for temperatures as high as 1,271 K. White (1919) determined the relative enthalpies, $(H°_T-H°_{273})$, for low albite, $NaAlSi_3O_8$ glass, "microcline," and $KAlSi_3O_8$ glass at intervals of 200 K to as high as 1,373 K. Holm and Kleppa (1968) have reported a single value for $(H°_{971}-H°_{289})$ for low albite and analbite.

Acknowledgments.—The studies presented in this report were made possible by the support of the Advanced Research Projects Agency, U.S. Department of Defense (A.R.P.A. Order 1813), to whom we are most grateful. The views and conclusions contained in this report are those of the authors and should not be interpreted as necessarily representing the official policies, either expressed or implied, of the Defense Advanced

[1] Department of Geology, Princeton University, Princeton, N.J. 08540.
[2] Present address: Centre de Recherches Petrographiques et Geochimiques, C.O. No. 1, 54500 Vandoeuvre-les-Nancy, France.
[3] Deceased.

Research Projects Agency. We thank W. H. Wilson for help with the data reduction and Maria Borscik, Princeton University, for the atomic absorption chemical analyses. R. E. Openshaw and D. R. Waldbaum wish to thank the National Science Foundation for support under grant GA–31136.

APPARATUS AND PROCEDURES

The adiabatically shielded low-temperature heat capacity calorimeter and the methods of data reduction used in this investigation have been described by Robie and Hemingway (1972). The platinum resistance thermometer used with our calorimeter was calibrated in terms of the International Practical Scale of Temperature of 1968 (Comité International des Poids et Mesures, 1969). It had an ice point resistance, R_0 of 34.94 ohms and the temperature derivative of the resistance at 0°C was 0.14 ohm deg^{-1}. The atomic weights for 1969 (Commission on Atomic Weights, 1970) were used to calculate the gram-formula weights for $NaAlSi_3O_8$ =262.224 and $KAlSi_3O_8$=278.337. The densities used to correct the sample weights for bouyancy were 2.620, 2.611, 2.560, and 2.552 g cm^{-3} for low albite, analbite, microcline, and high sanidine, respectively. The weights (in vacuo), of the samples used in the measurements were 77.026, 60.335, 53.510, and 59.925 g for low albite, analbite, microcline, and high sanidine, respectively. The contribution of the calorimeter to the total observed heat capacity, (sample+calorimeter), was about 60 percent from 20 K to 370 K. The observed heat capacities were corrected for slight differences in the quantity of helium, solder, and Teflon tape between the measurements on the empty and filled calorimeter. The results are reported in S.I. units (Page and Vigoureux, 1974).

MATERIALS

Low albite was obtained as crystal-clear cleavage fragments of albite crystals from the Rutherford mine, Amelia County, Va. The crystal fragments, +70 mesh, were handpicked free of impurities. Microcline was obtained by ion-exchange of the Amelia albite starting material, −150 mesh, in fused KCl (9 g KCl/gram $NaAlSi_3O_8$) at 1,083 K for 35 to 40 hours followed by ion-exchange of this product in fused KCl (2 g KCl/gram $KAlSi_3O_8$) at 1,113 K for 16 hours. The analbite used in the heat-capacity measurements (7001 in table 2) was prepared by heating a portion of the low albite sample at 1,325±10 K for 755 hours. A second analbite (7015 in table 2) was prepared by heating another portion of the low albite sample at 1,325±10 K for 710 hours. High sanidine was prepared by ion-exchanging the second analbite in fused KCl (6–9 g KCl/gram $NaAlSi_3O_8$) at 1,138 ± 10 K for 31 to 40 hours. Four separate exchanges were performed, and the products (71105, 71106, 71107, and 71108 in table 2) were mechanically mixed to obtain the calorimetric sample. Both the microcline and the sanidine occurred as a fine powder as a result of the fused KCl ion-exchange. Analytical data for the samples used in our calorimetric studies are listed in table 1. X-ray unit cell parameters for these samples are given in table 2.

TABLE 1.—*Atomic absorption analyses of alkali feldspar heat-capacity samples*

[The fifth analysis listed for low albite was obtained by H. W. Kruger, Geochron Laboratories, by flame photometry. All other analyses were made by Maria Borcsik, Department of Geological and Geophysical Sciences, Princeton University, by atomic absorption. N.d., not determined]

Sample	Chemical analyses (ppm)			Mole percent (An-Ab-Or tenary)		
	Ca	Na	K	An	Ab	Or
Analbite	468	80,256	1,706	0.33	98.44	1.23
	465	80,316	1,710	.33	98.44	1.23
	668	79,341	1,355	.48	98.54	.99
	N.d.	79,540	1,977	(*)	98.56	1.44
Average	534	79,863	1,687	.38	98.40	1.22
Low albite	832	81,467	1,413	0.58	98.42	1.00
	430	82,533	1,367	.30	98.74	.96
	666	82,149	1,342	.46	98.60	.95
	N.d.	78,290	2,158	(*)	98.40	1.60
	N.d.	80,500	1,650	(*)	98.81	1.19
Average	643	80,988	1,586	.45	98.42	1.13
Microcline	426	168	116,462	0.36	0.24	99.40
	277	139	126,468	.21	.19	99.60
	N.d.	498	126,942	(*)	.66	99.34
Average	351	268	123,291	.28	.37	99.36
High sanidine	288	434	127,101	0.22	0.58	99.20
	342	402	127,388	.26	.53	99.21
	†N.d.	†991	†126,780	(*)	†1.31	†98.69
Average	315	418	127,245	.24	.554	99.206

* Mole percent calculated for Ab-Or binary.
† Not a composite sample and not included in average.

To correct the heat-capacity measurements for deviations of the samples from the exact compositions $NaAlSi_3O_8$ and $KAlSi_3O_8$, we assumed that the samples are within the ternary system $KAlSi_3O_8$–$NaAlSi_3O_8$–$CaAl_2Si_2O_8$, and on the basis of the analytical data in table 1, we have used $(Na_{.984}K_{.011}Ca_{.003})AlSi_3O_8$; $(Na_{.984}K_{.012}Ca_{.002})AlSi_3O_8$; $(K_{.994}Na_{.004}Ca_{.001})AlSi_3O_8$; and $(K_{.992}Na_{.006}Ca_{.001})AlSi_3O_8$ as the chemical formulas for our low albite, analbite, microcline, and high sanidine respectively.

Furthermore, we assumed that the heat capacity of a ternary feldspar is an additive function of the heat capacities of $NaAlSi_3O_8$, $KAlSi_3O_8$, and $CaAl_2Si_2O_8$ for small deviations from end-member compositions.

Inasmuch as all four samples had a composition of >0.98 with respect to the ideal components $KAlSi_3O_8$ or $NaAlSi_3O_8$ (within the ternary) and the heat ca-

TABLE 2.—*X-ray unit cell parameters of feldspar calorimetric samples*

[Cell parameters obtained for Amelia, Va., albite and microcline 6452 are included for comparison with results of other investigators. A, angstroms]

	Sample	a (A)	b (A)	c (A)	α (deg)	β (deg)	γ (deg)	Unit cell volume A^3	Number of lines
High sanidine	71105	8.606 ±.002	13.025 ±.001	7.180 ±.001	90.0	115.99 ±.01	90.0	723.4 ±.3	35
	71106	8.606 ±.001	13.030 ±.001	7.183 ±.001	90.0	116.02 ±.01	90.0	723.8 ±.2	66
	71107	8.606 ±.001	13.023 ±.001	7.181 ±.001	90.0	116.01 ±.01	90.0	723.3 ±.2	36
	77108	8.605 ±.001	13.025 ±.001	7.181 ±.001	90.0	116.00 ±.01	90.0	723.4 ±.3	37
Analbite	7001	8.177 ±.005	12.869 ±.003	7.112 ±.003	93.46 ±.03	116.51 ±.02	90.26 ±.04	668.1 ±.7	36
	7015	8.156 ±.003	12.872 ±.002	7.108 ±.002	93.42 ±.02	116.42 ±.02	90.30 ±.20	666.8 ±.4	39
Low albite	7010	8.143 ±.002	12.787 ±.001	7.160 ±.001	94.21 ±.02	116.61 ±.01	87.67 ±.01	664.7 ±.3	42
	Amelia	8.144 ±.002	12,788 ±.002	7.162 ±.001	94.22 ±.02	116.61 ±.01	87.65 ±.02	665.1 ±.3	36
	Amelia	8.143 ±.006	12,788 ±.004	7.161 ±.002	94.23 ±.04	116.59 ±.03	87.80 ±.05	665.0 ±.7	22
Microcline	71104	8.587 ±.002	12.966 ±.002	7.220 ±.001	90.62 ±.01	115.93 ±.01	87.66 ±.01	722.3 ±.3	32
	6452	8.582 ±.003	12.961 ±.003	7.219 ±.001	90.59 ±.02	115.91 ±.01	87.69 ±.02	721.7 ±.3	34

pacities per gram of the four phases were always within 5 percent or less of one another above 30 K, the magnitude of the impurity correction never exceeds 1.0 percent, and this method of correction should not introduce any further uncertainty beyond that of the experimental scatter of the raw heat-capacity data, that is about 0.1 percent. The correction for the $CaAl_2Si_2O_8$ component was made using the heat capacity data of King (1957).

HEAT CAPACITIES OF THE ALKALI FELDSPARS BETWEEN 15 AND 375 K

The experimental heat-capacity measurements for low albite, analbite, microcline, and high sanidine, corrected for curvature but not corrected for the small deviations from the ideal end-member formulas, as described above, are listed in tables 3 through 6 in their chronological order of measurement.

The heat capacities of low albite, analbite, and high sanidine behaved normally, displaying a continuous sigmoidal curve between 15 and 375 K and no indication of a transition or anomalous behavior. The data for low albite are shown in figure 1. The results of Kelley and others (1953) on a sample of low albite from Varutrask, Sweden, are in excellent agreement with our results for low albite.

In figure 2, the difference between the smoothed values, C_p° (analbite) minus C_p° (low albite), is plotted at integral temperatures. As can be seen from the figure, the difference in the heat capacities of analbite and low albite is always less than 0.3 percent between 40 and

TABLE 3.—*Experimental heat capacities of low albite uncorrected for* $KAlSi_3O_8$ *and* $CaAl_2Si_2O_8$ *in solid solution*

[Asterisk indicates data not used in calculating thermodynamic functions]

Temperature in K	Heat capacity in J/(g·K)	Temperature in K	Heat capacity in J/(g·K)	Temperature in K	Heat capacity in J/(g·K)
SERIES 3		SERIES 6,7,8		SERIES 15	
71.84	.20892	271.28	.73650	15.82	.00942
76.04	.22480	276.37	.74450	17.09	.01179
80.63	.24197	281.47	.75334	18.55	.01500
85.67	.26050	286.77	.76375	19.90	.01850
91.25	.28055	292.31	.77238	21.54	.02279
97.34	.30211	298.29	.78135	23.77	.02922
103.86	.32451	304.70	.79213	26.42	.03738
110.58	.34700	311.46	.80290	29.46	.04739
117.06	.36818			32.65	.05857
123.18	.38773	SERIES 9		35.79	.07004
129.15	.40634	298.44	.78147	39.17	.08267
135.06	.42404	305.28	.79231	42.84	.09668
140.94	.44140	312.77	.80425	46.85	.11268
146.78	.45816	320.93	.81704	51.25	.13320*
152.61	.47449	329.60	.83009	56.00	.14878
158.44	.49047			61.08	.16814
164.20	.50599	SERIES 10		66.39	.18843
169.91	.52072	328.97	.82995		
175.57	.53534	337.71	.84305	SERIES 16	
		346.51	.85457	63.27	.17645
SERIES 4		355.37	.86556	68.44	.19616
169.13	.51870	364.28	.87678	73.88	.21676
174.81	.53334	373.26	.88953	79.51	.23785
180.45	.54730			85.28	.25903
186.06	.56111	SERIES 12		91.04	.27981
191.58	.57446	31.41	.05414	96.84	.30027
197.08	.58755	34.32	.06464	102.69	.32042
202.62	.60003	37.17	.07514	108.55	.34021
213.82	.62445	40.31	.08697	114.37	.35938
219.49	.63690	43.79	.10037	120.10	.37782
		47.65	.11598	125.76	.39561
SERIES 5		56.59	.15109	131.30	.41275
225.22	.64897	61.59	.17017	136.75	.42894
230.94	.66019	66.85	.19025	142.19	.44488
236.71	.67167				
242.52	.68357	SERIES 13,14		SERIES 17	
248.33	.69461	288.12	.76514	153.00	.47543
254.13	.70549	293.19	.77385	158.32	.48994
259.93	.71639	299.75	.78429	163.65	.50429
265.79	.72747			169.00	.51838
271.70	.73912			174.37	.53217
277.28	.74727				

340 K, which indicates that the Al/Si distribution has very little effect upon the heat capacities below 340 K. This is not unexpected, inasmuch as their molar volumes differ by only 0.3 percent.

Our results for high sanidine and those of Kelley and others (1953) for adularia from St. Gothard, Switzerland, are shown in figure 3. In figure 4, the difference in the heat capacities, C_p° (sanidine) $- C_p^\circ$ (microcline), is shown at integral temperatures, and again, ΔC_p° is less than about 0.3 percent over most of the temperature range.

In contrast to the other feldspars studied, the heat capacity of microcline behaves anomalously at temperatures above 250 K. The heat capacity in this temperature range apparently depends upon the immediate prior thermal history of the sample—to how low a temperature it has been cooled and the length of time it has remained at a temperature above 250 K. Some of

TABLE 4.—*Experimental heat capacities of analbite uncorrected for* $KAlSi_3O_8$ *and* $CaAl_2Si_2O_8$ *in solid solution*

[Asterisk indicates data not used in calculating thermodynamic functions]

Temperature in K	Heat capacity in J/(g·K)	Temperature in K	Heat capacity in J/(g·K)	Temperature in K	Heat capacity in J/(g·K)
SERIES 1-2		SERIES 5		SERIES 9	
304.64	.78981	154.75	.47963	315.33	.80746
311.43	.80068	159.91	.49360	321.04	.81676
318.57	.81210	165.12	.50764	326.72	.82531
326.09	.82370	170.36	.52112	332.43	.83392
333.93	.83519	175.64	.53463		
341.94	.84608	180.89	.54784	SERIES 10	
		186.20	.56080	15.65	.01097
SERIES 3		191.62	.57375	16.64	.01233
350.03	.85489	197.09	.58679	17.74	.01495
358.24	.86541	202.61	.59911	18.99	.01763
366.44	.87829	208.19	.61140	20.55	.02320*
374.64	.88585	213.76	.62342		
		219.32	.63539	SERIES 11	
SERIES 4		224.94	.64710	22.69	.02729
60.24	.16540			24.88	.03370
65.62	.18612	SERIES 6		27.51	.04187
70.98	.20649	219.02	.63401	30.43	.05154
76.45	.22713	224.53	.64628	33.69	.06306
82.08	.24793	230.09	.65762	37.19	.07585
87.72	.26847	235.72	.66876	40.74	.08914
93.33	.28840			44.48	.10342
98.94	.30797	SERIES 7		48.49	.11904
104.49	.32681	245.60	.68828		
109.95	.34512	251.32	.69862	SERIES 12	
115.35	.36288	257.05	.70926	52.94	.13672
120.76	.38	262.79	.72014	56.89	.15224
126.21	.39695	268.53	.73106	60.87	.16782
131.64	.41379	274.21	.74144	65.22	.18451
137.06	.42962	279.92	.74980	70.03	.20291
142.41	.44523	285.63	.76002	75.12	.22209
147.70	.46009	291.30	.76989		
153.01	.47501	269.99	.77845	SERIES 13	
158.34	.48943	302.69	.78745	227.70	.65220
		308.35	.79618	233.27	.66355
				238.73	.67451
				244.20	.68505
				249.76	.69553
				255.33	.70575
				260.92	.71609

TABLE 5.—*Experimental heat capacities of microline uncorrected for* $NaAlSi_3O_8$ *and* $CaAl_2Si_2O_8$ *in solid solution*

[Asterisk indicates data not used in calculating thermodynamic functions]

Temperature in K	Heat capacity in J/(g·K)	Temperature in K	Heat capacity in J/(g·K)	Temperature in K	Heat capacity in J/(g·K)
SERIES 1-2		SERIES 9-10		SERIES 19*	
304.89	.73860	244.78	.65058	266.86	.6835
		250.52	.66063	272.80	.6938
313.73	.74822	256.18	.67098	278.64	.7032
321.59	.76086			284.43	.7125
329.49	.77302	261.73	.68001	290.17	.7219
337.66	.78391	267.45	.69081	295.87	.7298
346.02	.79384	273.12	.70103	301.52	.7381
354.43	.80420	278.82	.70777		
362.80	.81415	284.61	.71763	SERIES 20-21*	
371.13	.82462	209.41	.72701	300.94	.7339
SERIES 3,4,5		SERIES 12		304.72	.7390
15.84	.00892	287.34	.72226	310.36	.7475
		293.01	.73083	315.9	.7556
17.33	.01150	298.70	.73876	321.5	.7635
18.69	.01443	304.41	.74776		
20.60	.01918			SERIES 22-23	
22.96	.02606	SERIES 13-14		305.11	.73786
		234.06	.63104	310.83	.74663
25.65	.03503	239.75	.64120	316.45	.75527
28.67	.04590	245.39	.65086	322.00	.76379
		251.03	.66031	327.50	.77201
SERIES 6		256.70	.67030		
32.44	.06055	262.38	.68100	327.88	.77138
35.72	.07391	268.09	.69115	333.37	.77881
39.34	.08873	273.81	.70140		
43.47	.10549	279.55	.70833	SERIES 24*	
48.01	.12399			251.10	.7704
52.90	.14365	285.07	.71630	256.83	.6698
58.11	.16394	290.74	.72647	262.50	.6793
63.55	.18431	296.40	.73310	268.13	.6886
69.04	.20432	302.09	.74166		
		307.81	.74984	SERIES 25*	
SERIES 7				273.23	.6976
68.77	.20340	SERIES 15		278.77	.7061
74.11	.22245	302.11	.73182	284.27	.7145
79.71	.24202	309.13	.74311		
85.50	.26172	316.29	.75478	SERIES 26	
91.42	.28126	323.52	.76592	288.50	.72120
97.40	.30014	330.71	.77616	293.93	.73107
103.31	.31862			299.32	.73814
109.19	.33652	SERIES 16-17		304.69	.74613
115.06	.35393	339.11	.78520	310.01	.75393
120.86	.37076				
126.70	.38743	347.14	.79484	SERIES 27	
132.58	.40367	355.74	.80614	280.58	.70796
138.37	.41921	364.48	.81606	285.44	.71682
144.09	.43418	373.06	.82651	289.15	.72314
149.82	.44909			291.77	.72786
155.50	.46339	SERIES 18		293.86	.73116
161.27	.47771	260.33	.67730	295.94	.73396
167.21	.49226	265.99	.68754	298.02	.73602
173.11	.50585	271.61	.69797	300.62	.74014
178.91	.51923	277.33	.70484	304.25	.74468
		283.16	.71435		
SERIES 8		289.01	.72400	SERIES 28	
177.85	.51729	294.81	.73244	291.35	.72454
183.65	.53030	300.65	.73998	295.68	.73205
189.49	.54354	306.52	.74947	299.99	.73855
195.39	.55626	312.34	.75789	304.27	.74497
201.27	.56860	318.06	.76632	308.53	.75142
207.14	.58051	323.60	.77405		
213.01	.59262	329.04	.78133		
218.80	.60431	334.44	.78890		
244.52	.61502	339.80	.79580		
230.24	.62479	345.13	.80183		
235.98	.63569	351.77	.80941		
241.64	.64671	359.86	.81884		
247.31	.65638	368.29	.83063		

our heat-capacity measurements on microcline in the temperature interval 230 to 375 K are shown in figure 5.

Although our heat-capacity data are insufficient to resolve the exact nature of the transition in microcline (see for example Pippard, 1957, p. 137), they do limit the temperature of transition to the range 250 to 300 K (see particularly series 19, table 5).

New measurements of $C°_p$ for this sample of microcline after a much longer annealing time at temperatures between 270 and 300 K are clearly desirable, as would be heat-capacity studies on a different sample of microcline in order to prove that the observed behavior of $C°_p$ is not unique to this sample. A detailed structural refinement of the microcline in both the annealed state, that is after several days at 300 K or above, and after rapid cooling to below 230 K but without heating above 290 K would be most useful.

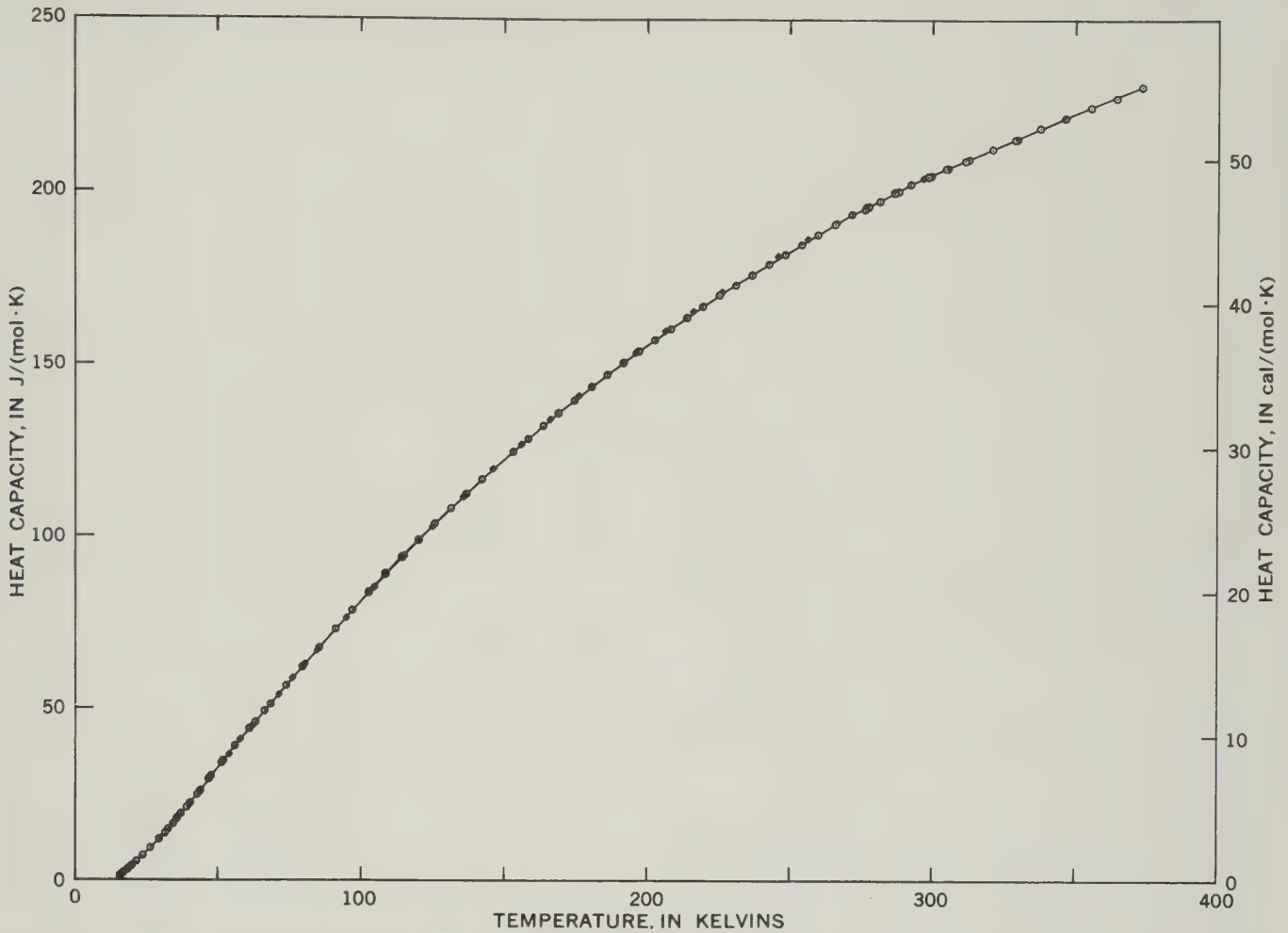

FIGURE 1.—Experimental molar heat capacities between 15 and 375 K for low albite ($NaAlSi_3O_8$) not corrected for $KAlSi_3O_8$ and $CaAl_2Si_2O_8$ in solid solution. Open circles, this investigation. Solid diamonds are the measurements of Kelley and others (1953) on low albite from Varutrask, Sweden. Solid line is the least-squares fit to the data of this investigation.

The heat capacity below 15 K for each phase was estimated by plotting the data below 45 K in the form C_p°/T versus T^2 (Pitzer and Brewer, 1961, p. 123) and extrapolating this function smoothly to 0 K; then all the data were analytically smoothed, as described by Robie and Hemingway (1972). The entropy change, $S_T^\circ - S_0^\circ$, is obtained from the experimental heat-capacity data using the relation

$$S_T^\circ - S_0^\circ = \int_0^T C_p^\circ/T \, dT \qquad (1)$$

For each of the feldspar phases, the extrapolation of C_p° below 15 K involved a contribution to $S_{298.15}^\circ - S_0^\circ$ of less than 0.8 J/(mol·K), or about 0.3 percent. By comparison, the measurements of Kelley and others (1953) required an extrapolation of C_p° below 51 K, which contributed about 21 J/(mol·K) to $S_{298.15}^\circ$, or about 10 percent.

The values of $S_{298.15}^\circ - S_0^\circ$ obtained in this study for low albite and sanidine differ from the values reported by Kelley and others (1953) for the Varutrask low albite and the St. Gothard adularia by 2.6 and 5.4 J/(mol·K), respectively. $S_{298.15}^\circ - S_{51}^\circ$ obtained in the two studies differs by only 0.4 J/(mol·K) for both the Na and K feldspars, whereas $S_{51}^\circ - S_0^\circ$, the extrapolated part of Kelley and others' (1953) measurements, differs by 3.3 and 6.2 J/(mol·K) for the Na and K feldspars, respectively. The extrapolation from 51 K introduces significant errors into the value of the calorimetric entropy at 298.15 K.

After the measurements of the feldspars had been completed, the heat capacity of the empty calorimeter was redetermined over the range 15 to 380 K. These new measurements agreed to within ±0.1 percent with results obtained 6 years previously on this same calori-

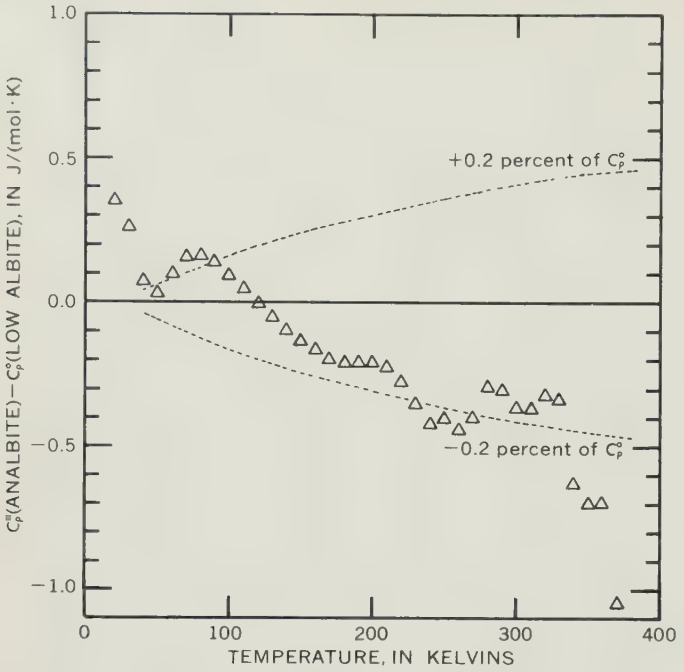

FIGURE 2.—Difference between the smoothed values of C°_p for analbite minus C°_p for low albite versus temperature.

meter. This result eliminates the possibility that the anomalous thermal behavior of microcline was an artifact of the sample container.

Because the original calibration by the National Bureau of Standards of the platinum thermometer (Meyers 322) used for the feldspar measurements was made 13 years previously and because we had recently acquired a new miniature platinum thermometer (Minco 68), which also had been calibrated by the Bureau in 1972, we decided to check the calibration of the Meyers thermometer against the Minco thermometer to see if any change had taken place. Minco 68 thermometer, Meyers 322 thermometer, and a second uncalibrated Minco thermometer (No. 84) were mounted in a cylindrical copper calibration block weighing 369 g.

The three thermometers were connected in series, and the calibration block was mounted within the cryostat in the position normally occupied by the calorimeter. The calibration block has an electrical heater wound on its outer surface and a differential thermocouple is connected between the block and the adiabatic shield. The voltage drop across each of the three thermometers and an NBS calibrated 100-ohm standard resistor were measured alternately for a period of 30 minutes while the block was maintained at a constant temperature. Measurements were made at 71 temperatures between 14.1 and 381.4 K.

The original calibration of the Meyers 322 thermometer gave a resistance of 0.05421 ohms at 14 K, whereas the U.S. Geological Survey calibration of May 1973 gave 0.05412 ohms; ΔT, then, is 0.0036 K.

On the basis of our recalibration, we conclude that Meyers 322 thermometer has changed by less than 0.004 K at 14 K and 0.009 K at 300 K in the 13 yr since it was initially calibrated.

TABLE 6.—*Experimental heat capacities of high sanidine uncorrected for* $NaAlSi_2O_8$ *and* $CaAl_2Si_2O_8$ *in solid solution*

[Asterisk indicates data not used in calculating thermodynamic functions]

Temperature in K	Heat capacity in J/(g·K)	Temperature in K	Heat capacity in J/(g·K)	Temperature in K	Heat capacity in J/(g·K)
SERIES 1		SERIES 6		SERIES 10	
303.20	.74092	105.91	.32627	319.50	.76387
308.70	.74955	111.24	.34223	325.70	.77307
314.19	.75774	116.75	.35846	332.25	.78216
319.64	.76536	122.36	.37449	339.16	.79075
325.01	.77278	128.01	.39030	346.47	.79941
330.48	.78000	133.71	.40601	353.98	.80775
336.04	.78742	139.40	.42140	361.47	.81626
341.69	.79448	145.02	.43589	368.88	.82857
347.63	.80144	150.71	.45044		
354.18	.80931	156.43	.46470	SERIES 11,12	
361.32	.81795	162.02	.47850	15.87	.00841
368.58	.82755	167.65	.49178	17.27	.01077
375.76	.83022			18.94	.01542
		SERIES 7,8			
SERIES 2		173.35	.50522	35.70	.07522
219.53	.72539	179.06	.51874	39.34	.09020
295.56	.73193	184.73	.53149	43.59	.10742
299.55	.73782	190.46	.54397	48.10	.12561
303.58	.74387	196.16	.55594	52.84	.14456
		201.79	.56776	57.93	.16432
SERIES 3				63.27	.18417
273.70	.69583	204.93	.57414		
278.98	.70495	210.52	.58565	SERIES 13,14	
284.18	.71352	216.16	.59652	21.30	.02636*
289.35	.72208	221.86	.60718	24.26	.03260*
294.48	.72950	227.55	.61823		
		233.18	.62776	27.38	.04208
SERIES 4				30.19	.05286
87.96	.27001	SERIES 9		33.33	.06553
92.97	.28621	243.82	.64461	36.59	.07852
97.88	.30159	249.29	.65479	40.18	.09361
		254.89	.66419	44.27	.11022
SERIES 5		260.59	.67492	48.78	.12828
62.02	.17998	266.23	.68504	53.63	.14767
66.99	.19796	271.96	.69482	58.72	.16720
72.02	.21591	277.79	.70334	64.06	.18685
77.24	.23406	283.57	.71258	69.66	.20696
82.67	.25247	289.31	.72113	75.09	.22613
87.98	.27012	295.14	.72906		
93.22	.28719	301.08	.73864	SERIES 15,16	
98.58	.30405	306.96	.74687	297.96	.73471
103.99	.32058	312.80	.75458	303.18	.74289
				298.69	.73660
				304.03	.74481

THERMODYNAMIC PROPERTIES OF $NaAlSi_3O_8$ AND $KAlSi_3O_8$

The smoothed values for C°_p and the functions derived therefrom, $(H^\circ_T - H^\circ_0)/T$, $(G^\circ_T - H^\circ_0)/T$, and $S^\circ_T - S^\circ_0$ for the alkali feldspars are listed at integral temperatures from 0 to 370 K in tables 7 through 10 for

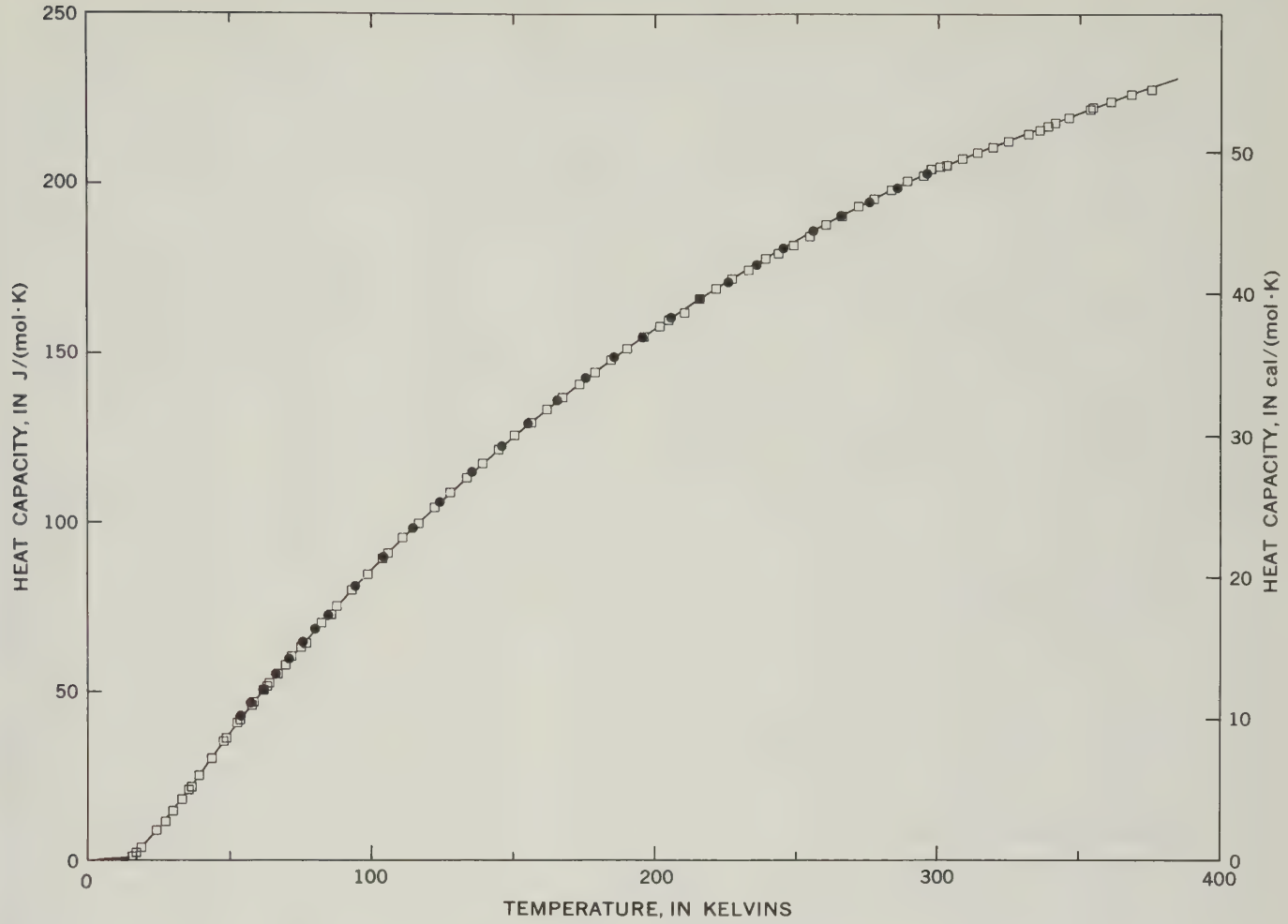

FIGURE 3.—Experimental molar heat capacities of high sanidine ($KAlSi_3O_8$) from 15 to 375 K not corrected for $CaAl_2Si_2O_8$ and $NaAlSi_3O_8$ in solid solution. Open squares, this investigation. Filled circles are the measurements of Kelley and others (1953) for adularia from St. Gothard, Switzerland.

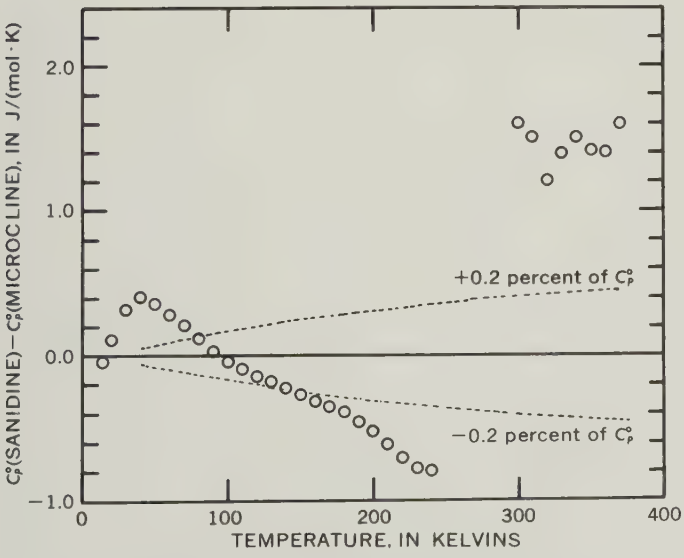

FIGURE 4.—Difference between the smoothed values of $C°_p$ for high sanidine minus $C°_p$ for microcline versus temperature.

low albite, analbite, microcline, and high sanidine, respectively.

In the ideal low albite and microcline structures, the aluminum atoms are entirely on the $T_1(0)$ sites, and the three silicon atoms are on $T_1(m)$, $T_2(0)$, and $T_2(m)$ sites. Consequently, there is no configurational contribution to the entropy; that is, $S°_0$ is zero for these phases, and accordingly the values for the entropies, $S°_{298.15}$, to be used in thermodynamic calculations are, 207.4±0.4, and 214.2±0.4 J/(mol·K) for low albite and microcline, respectively.[4]

On the other hand, in the structures of ideal analbite and high sanidine, the (Al+3Si) are randomly distributed over the four tetrahedral sites. This distribu-

[4] Although there is some evidence (Stewart and Ribbe, 1969; Stewart and Wright, 1974) that Amelia albite is not completely ordered with respect to the (Al+3Si) distribution within the four tetrahedral sites, the very close numerical agreement between the heat capacities of low albite and analbite below 350 K indicates that the vibrational part of the heat capacity is relatively insensitive to the Al/Si distribution and therefore does not effect the values for $S°_{298.15}-S°_0$ for ideal low albite and analbite reported in tables 7 and 8.

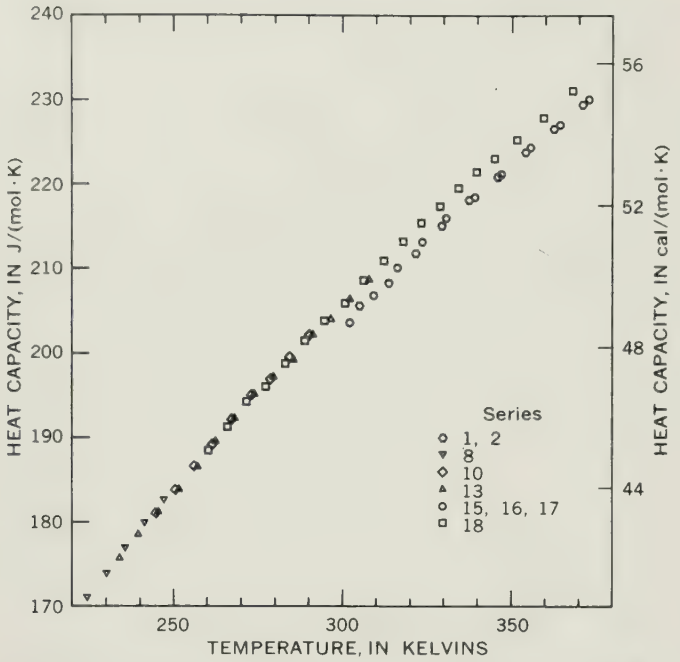

FIGURE 5.—Heat capacity of microcline between 230 and 375 K.

tion is apparently "frozen in" at low temperatures, and therefore S°_0 is not zero for these two phases. Holm and Kleppa (1968) have shown that the difference in the entropies of ideal low albite and analbite, that is, the configurational term arising from Al/Si disorder in analbite, is $4R(0.75 \ln 0.75 + 0.25 \ln 0.25) = -18.70$ J/(mol·K), where R is the gas constant and has the value 8.31434 ± 0.00070 J/(mol·K) (U.S. National Bureau of Standards, 1971). Thus to the values of $S^\circ_{298} - S^\circ_0$ listed in tables 8 and 10, we must add 18.70 J/(mol·K) to obtain the correct entropies for use in thermodynamic calculations. The correct values for S°_{298} for analbite and high sanidine are therefore $207.7 + 18.70 = 226.4 \pm 0.4$, and $214.2 + 18.70 = 232.9 \pm 0.4$ J/(mol·K), respectively.

TABLE 7.—*Molar thermodynamic properties of low albite,* $NaAlSi_3O_8$

Temperature, T, in kelvins	Heat capacity, C°_p, in J/(mol·K)	Entropy $(S^\circ_T - S^\circ_0)$, in J/(mol·K)	Enthalpy function $(H^\circ_T - H^\circ_0)/T$, in J/(mol·K)	Gibbs energy function $-(G^\circ_T - H^\circ_0)/T$, in J/(mol·K)
5	0.080	0.026	0.019	0.007
10	0.632	0.207	0.155	0.052
15	2.118	0.705	0.529	0.176
20	4.905	1.656	1.239	0.417
25	8.695	3.146	2.341	0.806
30	12.97	5.101	3.748	1.353
35	17.64	7.446	5.394	2.052
40	22.50	10.12	7.226	2.890
45	27.60	13.06	9.205	3.854
50	32.82	16.23	11.30	4.932
60	43.02	23.11	15.73	7.378
70	53.06	30.50	20.35	10.15
80	62.86	38.23	25.06	13.17
90	72.41	46.19	29.79	16.40
100	81.66	54.30	34.52	19.78
110	90.57	62.50	39.21	23.29
120	99.10	70.75	43.85	26.90
130	107.3	79.01	48.41	30.59
140	115.1	87.24	52.90	34.35
150	122.6	95.44	57.30	38.15
160	129.8	103.6	61.60	41.98
170	136.7	111.7	65.82	45.84
180	143.4	119.7	69.95	49.72
190	149.8	127.6	73.98	53.61
200	155.9	135.4	77.92	57.51
210	161.7	143.2	81.78	61.40
220	167.4	150.8	85.54	65.30
230	172.8	158.4	89.22	69.18
240	178.1	165.9	92.81	73.05
250	183.1	173.2	96.32	76.91
260	188.1	180.5	99.76	80.76
270	192.8	187.7	103.1	84.59
280	197.3	194.8	106.4	88.40
290	201.7	201.8	109.6	92.19
300	205.9	208.7	112.8	95.95
310	210.0	215.5	115.8	99.70
320	214.1	222.3	118.8	103.4
330	218.2	228.9	121.8	107.1
340	222.0	235.5	124.7	110.8
350	225.5	242.0	127.5	114.5
360	228.7	248.4	130.3	118.1
370	232.2	254.7	133.0	121.7
273.15	194.2	189.9	104.2	85.79
298.15	205.1	207.4	112.2	95.26

REFERENCES CITED

Bearden, J. A., 1967, X-ray wavelengths and X-ray atomic energy levels: U.S. Natl. Bur. Standards Natl. Standard Reference Data Ser. NSRDS–NBS 14, 38 p.

Comite International des Poids et Mesures, 1969, The International Practical Temperature Scale of 1968: Metrologia, v. 5, p. 35–44.

Commission on Atomic Weights, 1970, Atomic weights for 1969: Pure and Applied Chemistry, v. 21, p. 95–108.

Holm, J. L., and Kleppa, O. J., 1968, Thermodynamics of the disordering process in albite: Am. Mineralogist, v. 53, p. 123–133.

Kelley, K. K., Todd, S. S., Orr, R. L., King, E. G., and Bonnickson, K. R., 1953, Thermodynamic properties of sodium-aluminum and potassium-aluminum silicates: U.S. Bur. Mines Rept. Inv. 4955, 21 p.

King, E. G., 1957, Low temperature heat capacities and entropies at 298.15 K of some crystalline silicates containing calcium: Am. Chem. Soc. Jour., v. 79, p. 5437–5438.

Megaw, H. D., 1956, Notation for feldspar structures: Acta Cryst., v. 9, p. 56–60.

Page, C. H., and Vigoureux, Paul, eds., 1974, The international system of units (SI): U.S. Natl. Bur. Standards Spec. Pub. 330, 43 p.

Pippard, A. B., 1957, Elements of classical thermodynamics for advanced students of physics: Cambridge, England, Univ. Press, 165 p.

Pitzer, K., and Brewer, Leo, 1961, Thermodynamics: New York, McGraw-Hill Book Co., 723 p.

Robie, R. A., and Hemingway, B. S., 1972, Calorimeters for heat of solution and low-temperature heat capacity measurements: U.S. Geol. Survey Prof. Paper 755, 32 p.

Stewart, D. B., and Ribbe, P. H., 1969, Structural explanation for variations in cell parameters of alkali feldspar with Al/Si ordering: Am. Jour. Sci., v. 267A (Schairer vol.), p. 444–462.

Stewart, D. B., and Wright, T. C., 1974, Al/Si order and symmetry of natural potassic feldspars and the relationship of strained cell parameters to bulk composition: Colloque Internat. du C.N.R.S., Solutions solides en mineralogie, p. 500–540.

U.S. National Bureau of Standards, 1971, Revised list of physical constants: U.S. Natl. Bur. Standards Tech. News Bull., v. 55(3), p. 71–72.

White, W. P., 1919, Silicate specific heats—Second series: Am. Jour. Sci., 4th ser., v. 47, p. 1–43.

TABLE 8.—*Molar thermodynamic properties of analbite,* $NaAlSi_3O_8$

[A zero point entropy of 18.70 J/(mol·K) has been included in the Gibbs energy function]

Temperature, T, in kelvins	Heat capacity, C_p°, in J/(mol·K)	Entropy $(S_T^\circ - S_0^\circ)$, in J/(mol·K)	Enthalpy function $(H_T^\circ - H_0^\circ)/T$, in J/(mol·K)	Gibbs energy function $-(G_T^\circ - H_0^\circ)/T$, in J/(mol·K)
5	0.101	0.033	0.024	18.71
10	0.741	0.251	0.186	18.77
15	2.401	0.823	0.612	18.91
20	5.289	1.884	1.398	19.19
25	8.939	3.443	2.529	19.61
30	13.14	5.435	3.939	20.20
35	17.78	7.804	5.580	20.92
40	22.63	10.49	7.407	21.79
45	27.63	13.45	9.374	22.77
50	32.82	16.62	11.45	23.87
60	43.11	23.51	15.87	26.34
70	53.21	30.92	20.49	29.14
80	63.03	38.67	25.19	32.18
90	72.55	46.65	29.93	35.42
100	81.76	54.77	34.65	38.82
110	90.61	62.98	39.34	42.34
120	99.09	71.23	43.97	45.96
130	107.2	79.48	48.52	49.66
140	115.0	87.72	53.00	53.42
150	122.5	95.91	57.38	57.23
160	129.6	104.0	61.67	61.07
170	136.5	112.1	65.87	64.93
180	143.2	120.1	69.99	68.82
190	149.6	128.0	74.01	72.71
200	155.7	135.8	77.94	76.60
210	161.5	143.6	81.78	80.50
220	167.1	151.2	85.53	84.39
230	172.5	158.8	89.20	88.27
240	177.6	166.2	92.77	92.15
250	182.7	173.6	96.27	96.00
260	187.6	180.8	99.69	99.85
270	192.4	188.0	103.0	103.7
280	197.0	195.1	106.3	107.5
290	201.4	202.1	109.5	111.3
300	205.5	209.0	112.6	115.0
310	209.6	215.8	115.7	118.8
320	213.8	222.5	118.7	122.5
330	217.9	229.1	121.7	126.2
340	221.4	235.7	124.5	129.9
350	224.4	242.2	127.3	133.5
360	227.8	248.5	130.1	137.1
370	231.9	254.8	132.8	140.7
273.15	193.9	190.3	104.1	104.9
298.15	204.8	207.7	112.1	114.3

TABLE 9.—*Molar thermodynamic properties of microcline,* $KAlSi_3O_8$

Temperature, T, in kelvins	Heat capacity, C_p°, in J/(mol·K)	Entropy $(S_T^\circ - S_0^\circ)$, in J/(mol·K)	Enthalpy function $(H_T^\circ - H_0^\circ)/T$, in J/(mol·K)	Gibbs energy function $-(G_T^\circ - H_0^\circ)/T$, in J/(mol·K)
5	0.080	0.026	0.019	0.007
10	0.632	0.207	0.155	0.052
15	2.117	0.705	0.529	0.176
20	4.905	1.656	1.239	0.417
25	9.117	3.176	2.369	0.807
30	14.24	5.281	3.911	1.370
35	19.69	7.882	5.773	2.110
40	25.47	10.90	7.880	3.016
45	31.11	14.22	10.15	4.074
50	36.78	17.80	12.53	5.266
60	47.63	25.47	17.48	7.990
70	57.90	33.59	22.53	11.06
80	67.67	41.97	27.57	14.40
90	76.98	50.48	32.54	17.94
100	85.87	59.05	37.44	21.62
110	94.37	67.64	42.23	25.41
120	102.5	76.20	46.91	29.29
130	110.4	84.72	51.50	33.23
140	117.9	93.18	55.97	37.21
150	125.1	101.6	60.34	41.22
160	132.1	109.9	64.61	45.25
170	138.8	118.1	68.78	49.29
180	145.3	126.2	72.85	53.34
190	151.5	134.2	76.82	57.38
200	157.5	142.1	80.71	61.42
210	163.3	150.0	84.51	65.45
220	168.7	157.7	88.21	69.47
230	173.8	165.3	91.82	73.47
240	178.7	172.8	95.34	77.45
250	183.3	180.2	98.77	81.42
260	187.7	187.5	102.1	85.36
270	191.8	194.6	105.3	89.27
280	195.6	201.7	108.5	93.16
290	199.3	208.6	111.6	97.02
300	203.1	215.4	114.6	100.9
310	207.1	222.1	117.5	104.7
320	211.3	228.8	120.3	108.4
330	215.4	235.3	123.2	112.2
340	218.9	241.8	125.9	115.9
350	222.2	248.2	128.6	119.6
360	225.6	254.5	131.3	123.2
370	228.9	260.8	133.9	126.9
273.15	193.0	196.8	106.4	90.50
298.15	202.4	214.2	114.0	100.1

TABLE 10.—*Molar thermodynamic properties of high sanidine,* $KAlSi_3O_8$

[A zero point entropy of 18.70 J/(mol·K) has been included in the Gibbs energy function]

Temperature, T, in kelvins	Heat capacity, C_p°, in J/(mol·K)	Entropy $(S_T^\circ - S_0^\circ)$, in J/(mol·K)	Enthalpy function $(H_T^\circ - H_0^\circ)/T$, in J/(mol·K)	Gibbs energy function $-(G_T^\circ - H_0^\circ)/T$, in J/(mol·K)
5	0.075	0.024	0.018	18.71
10	0.601	0.197	0.148	18.75
15	2.045	0.667	0.499	18.87
20	4.862	1.601	1.203	19.10
25	9.256	3.130	2.349	19.48
30	14.54	5.277	3.933	20.04
35	20.12	7.933	5.842	20.79
40	25.86	10.99	7.985	21.71
45	31.50	14.37	10.29	22.78
50	37.15	17.98	12.69	23.99
60	47.90	25.71	17.67	26.74
70	58.10	33.87	22.72	29.84
80	67.79	42.27	27.76	33.21
90	77.02	50.79	32.72	36.77
100	85.83	59.36	37.60	40.47
110	94.27	67.94	42.37	44.27
120	102.4	76.49	47.03	48.16
130	110.2	85.00	51.59	52.11
140	117.7	93.44	56.04	56.09
150	124.9	101.8	60.39	60.11
160	131.8	110.1	64.64	64.14
170	138.4	118.3	68.79	68.19
180	144.9	126.4	72.83	72.23
190	151.1	134.4	76.79	76.28
200	157.0	142.3	80.65	80.31
210	162.7	150.1	84.43	84.34
220	168.0	157.8	88.10	88.35
230	173.0	165.3	91.69	92.35
240	177.9	172.8	95.18	96.33
250	182.6	180.2	98.58	100.28
260	187.3	187.4	101.9	104.2
270	192.1	194.6	105.2	108.1
280	196.7	201.6	108.3	112.0
290	201.1	208.6	111.5	115.9
300	205.2	215.5	114.5	119.7
310	209.1	222.3	117.5	123.5
320	212.9	229.0	120.4	127.3
330	216.8	235.6	123.3	131.0
340	220.4	242.1	126.1	134.7
350	223.6	248.6	128.8	138.4
360	226.9	254.9	131.5	142.1
370	230.8	261.2	134.2	145.7
273.15	193.6	196.8	106.2	109.3
298.15	204.5	214.2	114.0	119.0

Jour. Research U.S. Geol. Survey
Vol. 4, No. 2, Mar.–Apr. 1976, p. 205–212

DEFINITIVE X-RAY POWDER DATA FOR COVELLITE, ANILITE, DJURLEITE, AND CHALCOCITE

By ROBERT W. POTTER II and HOWARD T. EVANS, Jr.,
Menlo Park, Calif., Reston, Va.

Abstract.—**By using the Guinier-Hägg focusing X-ray powder camera with Cr$K\alpha_1$ and Cu$K\alpha_1$ radiations, new powder data for covellite (CuS), anilite (Cu_7S_4), djurleite ($Cu_{1.934}S$), and low chalcocite (Cu_2S) have been obtained from synthetic and natural materials. The powder data were treated by least-squares analysis to obtain the best unit-cell parameters consistent with the data. These powder data are intended to replace inferior and incomplete data previously published and to serve as standards for the study of copper sulfide minerals.**

During an electrochemical investigation of the equilibrium relationships and thermodynamic properties of the copper sulfides, it was found necessary to confirm the identity of the phases composing the sulfide electrodes by X-ray powder diffraction as well as by reflected light microscopy. X-ray powder data were obtained for powdered electrodes by using a modified Guinier-Hägg powder camera (fig. 1) and compared with those listed in the Powder Diffraction File (PDF) of the Joint Committee on Powder Diffraction Standards. The Guinier-Hägg films contained many more lines than were reported in the PDF for the copper sulfide phases of which the sulfide electrodes were presumed to have been composed. Much time was wasted in trying to identify "new phases" until indexing showed that all the extra lines could be accounted for by the appropriate Cu-S phases. To avoid such confusion in the future, the powder data for the Cu-S phases stable at 25°C and 1 atm have been measured with the sensitivity and precision afforded by the most recent Guinier-Hägg techniques and are here reported.

A well-known and valuable compilation of powder data for mineral sulfides is in the atlas of Berry and Thompson (1962). Our understanding of the Cu-S system, as well as the X-ray powder techniques we use, have advanced somewhat beyond what was available to those authors. In particular, the important minerals djurleite and anilite were not known to exist at that time.

EXPERIMENTAL METHODS

The copper sulfides were synthesized from high-purity copper wire (99.975 percent) and sulfur (99.999 percent). Spectrographic analysis of the copper wire by the U.S. Geological Survey showed only the presence of iron (100 ppm), nickel (100 ppm), magnesium (10 ppm), and barium (10 ppm) above the limits of detection. The copper wire was cleaned by using hydrochloric acid, washed in distilled water, dried, and weighed to ±0.01 mg. Crystalline fragments of sulfur were weighed (to ±0.01 mg) and sealed with the copper in an evacuated silica tube. The charge was heated to 450° ± 5°C for 24 to 120 h and then rapidly quenched in cold water.

The grinding of certain copper sulfides is known to produce phase transitions (Morimoto and others, 1969). In order to guard against this difficulty, samples were gently crushed or annealed at temperatures as high as 84°C (low chalcocite decomposes at 103°, djurleite at 93°, and anilite at 75°C). Except for the time during which they were exposed to X-rays, the samples were stored in evacuated sealed Pyrex tubes.

Finely powdered and annealed CaF_2 was intimately mixed with each copper sulfide powder to serve as an internal standard. For this purpose, the lattice constant $a = 5.4638(4)$ A[1] (Robie and others, 1967) was used as a reference datum. (The best recorded value measured from single crystals of synthetic CaF_2 by Batchelder and Simmons (1965) is $a = 5.46375(7)$ A.) NaCl and MgO were also used in the study of covellite and anilite; the lattice constants were given by Robie, Bethke, and Beardsley (1967). The sample was mounted in a standard aluminum planchet on matte-surface transparent tape, and strictly monochromatic Cu$K\alpha_1$ ($\lambda = 1.54050$ A) and Cr$K\alpha_1$ ($\lambda = 2.28962$ A) radiations were used (Bragg, 1947); exposure times ranged

[1] In this paper, standard errors are indicated in terms of the last significant figure in parentheses.

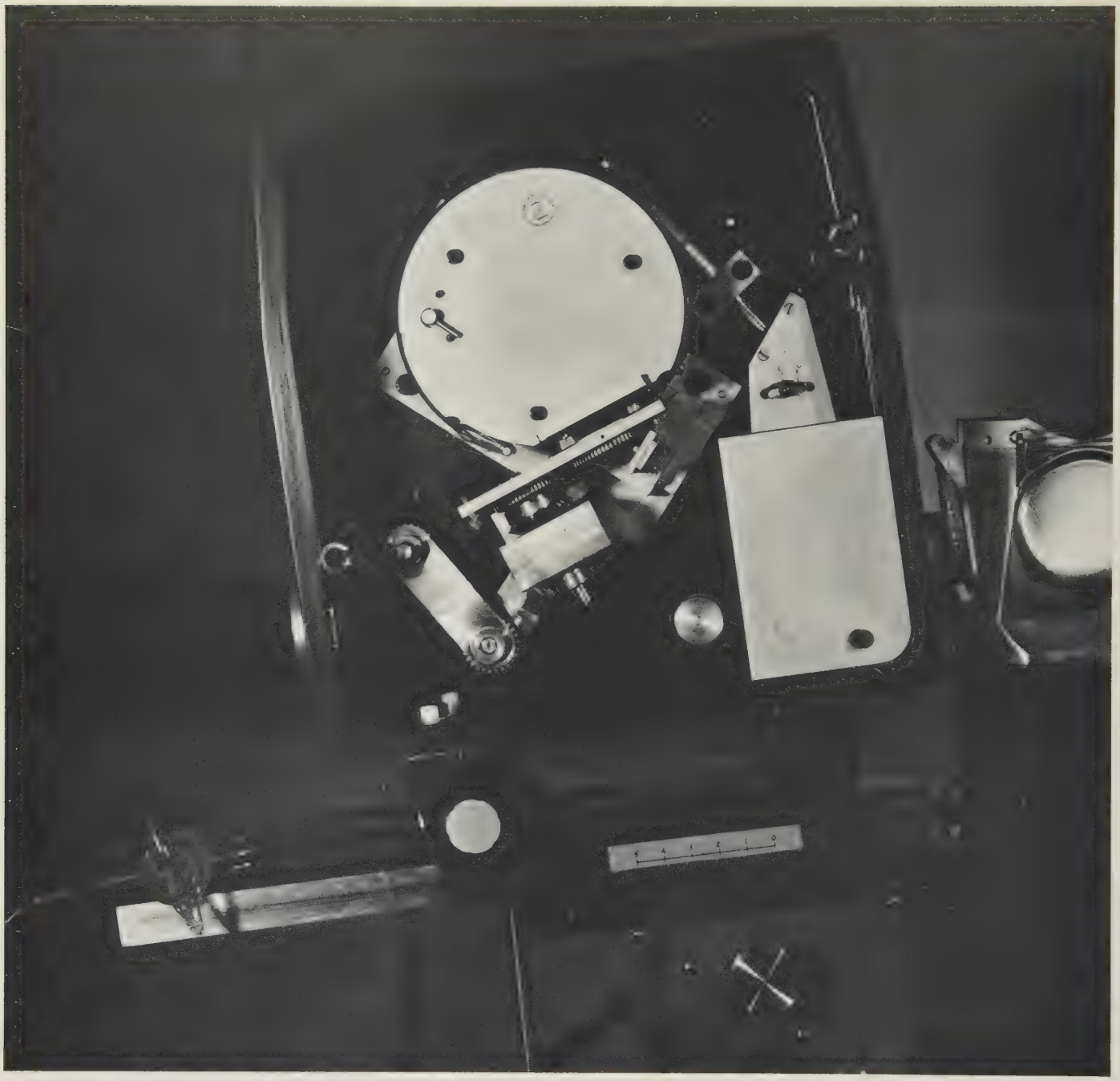

FIGURE 1.—The new model Guinier-Hägg focusing X-ray powder camera with cover removed to show modification of the sample drive. The circular film holder is 100 mm in diameter. The flat powder sample in a planchet is rotated in its plane immediately below the film holder through a gear-and-chain linkage by the motor, which is mounted outside the vacuum chamber behind the shaft at the left.

from 4 to 48 h. The processed films were measured in a microfilm reader (magnification, × 20) and also a standard powder film reader. The line positions were taken from a millimetre scale (graduated in tenths) exposed on the film prior to exposure to X-rays and were measured to ±0.02 mm (0.01° 2θ). As a test of the accuracy of the method, the powder pattern of pure silicon was measured in the same fashion by comparison with CaF_2. The measured cell edge was 5.4303(3) A, in close agreement with the value of 5.4305(3) A given by Robie, Bethke, and Beardsley (1967). (The best recorded value measured from single crystals of zone-purified silicon by Bond (1960) is $a=5.43072(2)$ A.) The relative intensities for each powder pattern

were obtained by one or a combination of three methods, depending on the complexity of the powder pattern, as follows: (1) Densitometer, (2) counter diffractometer (major reflections only), and (3) visual comparison with a calibrated film strip.

The powder data were indexed and the unit-cell parameters refined by using a computer program written by Appleman and Evans (1973) for the indexing and least-squares refinement of powder data. Wherever possible, indexing was verified by reference to single-crystal intensity data.

The X-ray powder diffraction patterns were made using the new version of the Guinier-Hägg focusing camera (Hägg and Ersson, 1969). This instrument has been found to provide high resolution (approx 0.08° 2θ), precision (approx 0.01° 2θ), and great sensitivity (recording of weak lines), all with comparative ease and speed of operation. One difficulty was encountered in the instrument as supplied; namely, the sample holder was heated as much as 10°–15°C above room temperature by the operation of the motor that rotates the sample which is mounted on the same metal block. This problem was eliminated in our instrument by mounting the motor outside the case and driving the sample holder through a chain-and-gear linkage. The linkage, which is shown in figure 1, is arranged so that the camera block can be shifted from the Cu$K\alpha_1$ to the Cr$K\alpha_1$ position, and also moved aside to permit initial alinement of the camera on the track, without being disconnected. By using this arrangement, heating of the specimen is negligible, and changes in the X-ray pattern caused by thermal expansion are eliminated. During this investigation, the ambient room temperature varied from 23° to 26°C.

RESULTS

According to the best and most recent studies, four compounds are stable in the Cu-S system at room temperature and pressure (Djurle, 1958; Roseboom, 1966; Morimoto and Koto, 1970; Cook, 1971, 1972; Potter, 1974): low chalcocite ($Cu_{1.993-2.000(2)}S$), djurleite ($Cu_{1.934-1.965(2)}S$), anilite ($Cu_{1.750(3)}S$), and covellite ($Cu_{1.0000(5)}S$). Low digenite ($Cu_{1.765-1.8000}S$) has been shown to be a metastable phase in the pure Cu-S system (Potter, 1974) and does not occur in nature without an appreciable amount of iron present to stabilize the phase (Morimoto and Koto, 1970). Because of the sensitivity it shows to compositional variations, we have not included it here. Our results are shown in tables 1–4, in which all d spacings are in angstroms and all intensities are scaled to 100 for the strongest reflection.

COVELLITE

We have measured and indexed 48 lines for this compound on a pattern made by using Cu$K\alpha_1$ radiation (table 1), whereas Swanson, Fuyat, and Ugrinic (1955), in their diffractometer study of synthetic material, reported 26 (PDF card 6–464) and Berry and Thompson (1962) listed 17. The agreement between our spacing and intensity measurements and those of Swanson, Fuyat, and Ugrinic, as shown in table 1, is excellent. By least-squares analysis, we find hexagonal unit-cell parameters that are in full agreement with previously reported values, but are considerably more accurate, as shown below (a and c in angstroms):

	a	c
This work	3.7938(5)	16.341(1)
Swanson, Fuyat, and Ugrinic (1955)	3.792	16.344
Djurle (1958)	3.794(2)	16.332(10)

TABLE 1.—*X-ray powder data for synthetic covellite*

[Guinier-Hägg method; Cu$K\alpha_1$ radation (λ=1.54050 A); CaF_2 as internal standard; *, least-squares analysis]

Calculated		This work		Swanson and others (1955)	
hkl	*d*(calc)	*d*(obs)	*I*(obs)	*d*(obs)	*I*(obs)
002	8.171	*8.162	7	8.18	7
004	4.085	4.078	4	----	---
100	3.286	*3.284	15	3.285	14
101	3.221	*3.220	27	3.220	28
102	3.048	*3.047	62	3.048	67
103	2.813	*2.813	100	2.813	100
006	2.724	*2.735	58	2.724	56
104	2.560	*2.559	10	----	---
105	2.317	*2.316	24	2.317	10
106	2.097	*2.097	6	2.097	6
008	2.043	*2.043	7	2.043	7
107	1.9030	*1.9020	25	1.902	25
110	1.8969	*1.8971	75	1.896	75
112	1.8477	*1.8474	3	----	---
108	1.7347	*1.7345	34	1.735	34
114	1.7205	*1.7208	7	----	---
200	1.6428	*1.6423	3	----	---
201	1.6345	1.6349	5	1.634	3
202	1.6105	*1.6108	6	1.609	8
109	1.5892	*1.5886	8	----	---
203	1.5728	*1.5733	15	1.572	15
116	1.5566	*1.5564	37	1.556	37
204	1.5242	*1.5244	7	----	---
205	1.4678	*1.4684	3	1.463	5
1.0.10	1.4632	*1.4637	3		
206	1.4067	*1.4073	6	----	---
118	1.3899	*1.3905	9	1.390	6
0.0.12	1.3618	*1.3615	3	----	---
1.0.11	1.3536	*1.3536	9	1.354	7
207	1.3435	*1.3434	5	1.343	5
208	1.2801	*1.2796	9	1.280	9
1.0.12	1.2580	*1.2577	3	----	---
210	1.2418	*1.2417	4	----	---
211	1.2382	1.2378	1	----	---
212	1.2277	*1.2278	5	1.227	5
209	1.2182	*1.2183	2	----	---
213	1.2108	*1.2106	9	1.210	9
214	1.1881	*1.1884	2	----	---
1.0.13	1.1740	*1.1742	4	----	---
0.0.14	1.1672	*1.1675	3	----	---
215	1.1608	1.1600	3	----	---
216	1.1299	*1.1298	4	----	---
1.1.12	1.1069	*1.1063	2	----	---
2.0.11	1.1019	1.1014	8	----	---
1.0.14	1.0999	*1.0998	3	1.0998	8
217	1.0964	*1.0962	10	----	---
300	1.0952	1.0952	3	1.0946	10
301	1.0927	1.0927	2	----	---

TABLE 2.—*X-ray powder data for synthetic anilite*

[Guinier-Hägg method; Cu$K\alpha_1$ radation (λ=1.54050 A); CaF_2 as internal standard; *, least-squares analysis]

Calculated		This work		D. K. Smith (unpub. data, 1973)	Morimoto and others (1969)	
hkl	*d*(calc)	*d*(obs)	*I*(obs)	*I*(calc)	*d*(obs)	*I*(obs)
011	6.390	*6.395	1	3	----	---
112	3.924	*3.928	5	14	----	---
211	3.362	*3.357	25	47	3.36	20
103	3.346	3.343	25	22	3.32	17
121	3.342			25		
013	3.339	*3.340	10	14		
202	3.218	*3.218	40	38	3.20	57
022	3.195	*3.198	9	11	----	---
113	3.076	*3.076	3	3	----	---
220	2.780	*2.780	55	59	2.77	65
004	2.770	*2.769	15	22	2.75	21
203	2.699	*2.699	6	11	2.69	14
221	2.697	*2.697	25	41		
104	2.614	2.619	20	29	2.59	20
301	2.564	*2.565	3	4	----	---
031	2.538	*2.538	25	31	2.54	31
131	2.417	*2.418	2	3	----	---
302	2.380	*2.380	30	22	2.39	10
124	2.173	*2.173	35	49	2.16	39
321	2.144	*2.145	10	18	2.13	15
231	2.136	2.140	6	7	----	---
015	2.132	*2.132	2	3	----	---
313	2.069	*2.068	11	10	2.05	5
133	2.057	*2.056	20	25	----	---
400	1.977	*1.977	25	21	----	---
224	1.962	*1.962	100	100	1.965	100
040	1.956	1.953	40	38		
304	1.909	*1.909	15	16	----	---
323	1.8809	*1.8813	10	10	1.873	10
006	1.8464	------	---	---	1.847	3
134	1.8460	------	---	2		
412	1.8111	*1.8108	2	2	----	---
142	1.7958	*1.7960	15	12	----	---
240	1.7528	*1.7526	5	6	----	---
225	1.7328	*1.7328	1	1	----	---
305	1.6960	*1.6965	2	2	----	---
422	1.6809	1.6784	15	16	1.677	35
206	1.6729			16		
026	1.6697	*1.6698	10	11	----	---
135	1.6512	*1.6512	2	2	----	---
126	1.6335	*1.6336	1	1	----	---
423	1.5918	*1.5918	2	2	----	---
431	1.5595	*1.5590	10	14	----	---
325	1.5560	*1.5565	10	10	----	---
051	1.5491	*1.5492	1	1	----	---
433	1.4489	*1.4491	5	4	----	---
343	1.4452	*1.4454	2	1	----	---
440	1.3902	*1.3900	5	4	----	---
108	1.3640	*1.3638	2	3	----	---
317	1.3368	*1.3370	1	1	----	---
505	1.2871	*1.2872	1	1	----	---
345	1.2813	*1.2808	1	1	----	---

TABLE 3.—*X-ray powder data for synthetic djurleite*

[Guinier-Hägg method; Cr$K\alpha_1$ and Cu$K\alpha_1$ radiations; CaF_2 as internal standard; *, least-squares analysis; W, weak; M, medium; S, strong. Composition Cu_xS; x=1.934 for this work, x=1.96 for Djurle]

Calculated		This work		Djurle (1958)	
hkl	*d*(calc)	*d*(obs)	*I*(obs)	*d*	*I*
120	7.54	7.53	2	------	--
220	6.778	6.76	2	------	--
002	6.768				
121	6.582	6.60	3	------	--
012	6.215	6.17	15	------	--
410	6.181				
112	6.055	6.05	4	------	--
202	6.045				

TABLE 3.—*X-ray powder data for synthetic djurleite*—Con.

Calculated		This work		Djurle (1958)	
hkl	*d*(calc)	*d*(obs)	*I*(obs)	*d*	*I*
130	5.135	5.13	8	------	--
022	5.125				
421	4.777	4.77	2	------	--
402	4.770				
231	4.587	4.59	2	------	--
600	3.483	4.48	4	------	--
331	4.286	*4.284	5	*4.286	W
430	4.129	4.127	3	------	--
213	4.127				
132	4.091	*4.095	5	------	--
232	3.956	*3.957	2	------	--
313	3.904	*3.903	9	3.890	W
332	3.758	*3.758	20	*3.750	M
602	3.737	3.733	1	------	--
141	3.732				
710	3.732				
413	3.644	*3.646	2	------	--
241	3.629	*3.627	4	------	--
711	3.598	3.596	4	------	--
340	3.594				
323	3.585	*3.586	5	*3.584	W
432	3.525	*3.524	6	------	--
341	3.474	*3.472	5	------	--
503	3.457	*3.457	2	------	--
042	3.394	3.385	3	3.381	W
133	3.389				
440	3.389				
004	3.384				
423	3.381				
800	3.362	*3.362	3	------	--
721	3.344	3.344	5	------	--
702	3.341				
233	3.311	*3.310	2	------	--
242	3.291	*3.291	8	------	--
810	3.287	------	--	------	--
114	3.283	3.283	15	3.275	W
204	3.282	------	--	------	--
214	3.212	3.219	3	------	--
811	3.195	3.194	18	3.190	W
333	3.193				
523	3.162	*3.161	5	------	--
314	3.103	*3.104	3	3.101	W
433	3.046	*3.044	15	3.035	W
632	3.041	3.041	1	------	--
151	3.038				
442	3.030	3.031	1	------	--
821	3.013	3.013	19	3.001	W
802	3.011				
251	2.982	*2.982	2	------	--
414	2.968	*2.970	9	*2.963	W
623	2.947	2.947	2	------	--
143	2.943				
324	2.936	2.938	3	2.939	W
910	2.936				
901	2.918	*2.916	2	------	--
351	2.894	*2.895	15	*2.891	W
641	2.885	2.885	3	2.883	W
533	2.884				
542	2.871	2.869	13	2.865	W
411	2.869				
152	2.832	*2.833	2	*2.831	W
424	2.821	2.818	10	2.813	W
514	2.818				
343	2.811	2.812	5		
822	2.811				
252	2.786	2.785	3	2.785	W
451	2.783				
234	2.780	*2.779	10	------	--
921	2.735	2.733	1	------	--
902	2.734				
352	2.714	*2.713	1	------	--
604	2.701	*2,701	2	------	--
		2.691	4	2.688	W
		2.654	20	2.653	W
		2.629	10	------	--

TABLE 3.—*X-ray powder data for synthetic djurleite*—Con.

Calculated		This work		Djurle (1958)	
hkl	*d* (calc)	*d* (obs)	*I* (obs)	*d*	*I*
		2.620	2	------	--
		2.608	6	2.599	W
		2.593	2	------	--
		2.557	8	2.559	W
		2.530--	8	------	--
		2.517	8	2.518	W
		2.477	10	2.476	W
		2.469	10	------	--
		2.440	1	------	--
		2.432	5	------	--
		2.417	17	2.415	W
		2.396	3	------	--
842	2.3886	*2.389	85	2.388	S
		2.385	5	------	--
		2.378	1	------	--
		2.354	5	------	--
		2.336	6	------	--
		2.318	2	------	--
		2.312	6	2.316	W
		2.300	2	------	--
		2.288	5	2.290	W
		2.263	5	------	--
		2.250	1	------	--
		2.234	4	------	--
		2.219	6	------	--
		2.202	1	------	--
		2.188	5	------	--
		2.177	1	------	--
		2.166	1	------	--
		2.148	6	2.143	W
		2.140	2	------	--
		2.107	5	2.107	W
		2.062	4	2.070	W
		2.052	3	------	--
		2.046	5	2.047	W
		2.038	2	------	--
		2.028	4	------	--
		2.017	3	------	--
		2.004	3	------	--
		1.9886	7	------	--
080	1.9630	*1.9626	50	*1.9634	S
046	1.9557	*1.9556	100	*1.9564	S
		1.9455	1	------	--
		1.9328	5	------	--
		1.9195	8	------	--
		1.9007	4	------	--
		1.8871	3	------	--
12.4.2	1.8704	*1.8710	95	*1.8698	S
		1.8689	2	------	--
		1.8360	2	------	--
		1.8275	2	1.8303	W
		1.8208	1	------	--
		1.8180	3	------	--
		1.8132	2	------	--
		1.7931	2	------	--
		1.7773	2	------	--
		1.7649	2	------	--
		1.7504	3	------	--
		1.7320	1	------	--
		1.7229	2	------	--
		1.7120	1	------	--
		1.6950	15	------	--
		1.6905	20	1.6901	M
		1.6807	4	------	--
		1.6790	15	1.6800	W
		1.6634	4	------	--
		1.6412	15	------	--
		1.6319	2	------	--
		1.6267	5	------	--
		1.6240	2	------	--
		1.6154	3	------	--
		1.6067	2	------	--
		1.5921	3	------	--
		1.5843	4	------	--

TABLE 3.—*X-ray powder data for synthetic djurleite*—Con.

Calculated		This work		Djurle (1958)	
hkl	*d* (calc)	*d* (obs)	*I* (obs)	*d*	*I*
		1.5811	2	------	--
		1.5740	1	------	--
		1.5622	2	------	--
		1.5420	2	------	--
		1.5157	8	1.5132	W
		1.5054	2	------	--
		1.4942	2	------	--
		1.4650	3	------	--
		1.4093	2	------	--
		1.3912	2	------	--
		1.3507	1	------	--
		1.3321	1	------	--
		1.3275	1	------	--
		1.2954	2	------	--
		1.2848	12	1.2734	M
		1.2752	2	------	--
		1.2700	1	------	--
		1.2615	4	------	--
		1.2483	2	------	--
		1.2430	1	------	--
		1.2280	3	------	--
		1.2159	2	------	--
		1.2105	2	------	--
		1.1965	2	------	--
		1.1693	2	------	--
		1.1359	3	------	--
		1.1297	4	------	--
		1.1193	5	1.1197	W
		1.1121	5	------	--

TABLE 4.—*X-ray powder data for low chalcocite from Bristol, Conn.*

[Guinier-Hägg method; Cr$K\alpha_1$ radiation (λ=2.28962 A); CaF_2, internal standard; *, least-squares analysis; Vw, every weak; W, weak; M, medium; S, strong. *I* (xl), from single-crystal measurements; Dj, from Djurle (1958)]

hkl (monoclinic)	*I* (xl)	*d* (calc)	*d* (obs)	*I* (obs)	*d* (Dj)	*I* (Dj)	*h'k'l'* (orthorhombic)
011	--	8.480	8.485	2	8.514	Vw	111
$\bar{1}11$	--	8.478					
111	--	6.374	6.379	3	6.413	W	131
$\bar{2}11$	--	6.372					
211	1	4.660	4.668	2	4.661	W	151
$\bar{3}11$	1	4.659					
220	1	4.483	------	--	4.500	Vw	240
					4.409	Vw	---
022	3	4.240	4.239	4	4.245	W	222
$\bar{2}22$	2	4.239					
221	2	3.855	3.855	3	3.857	W	251
$\bar{3}21$	1	3.855					
013	1	3.820	3.817	3	3.820	Vw	133
$\bar{3}13$	1	3.819					
202	1	3.776	3.779	2	3.776	W	062
$\bar{4}02$	1	3.774					
122	15	3.735	3.735	25	3.736	M	242
$\bar{3}22$	8	3.734					
212	11	3.598	3.599	13	3.599	M	162
$\bar{4}12$	6	3.597					
$\bar{3}11$	1	3.576	3.577	2	-----	---	171
$\bar{4}11$	0	3.576	------	--	-----	---	
$\bar{1}23$	0	3.556	------	--	-----	---	213
$\bar{2}23$	1	3.556	3.558	2	-----	---	
					3.482	Vw	---
400	1	3.416	------	--	3.418	Vw	080
$\bar{2}04$	1	3.374	*3.373	3	-----	---	004
113	3	3.334	3.336	6	3.336	W	153
$\bar{4}13$	2	3.333					
032	13	3.314	3.315	18	3.316	M	322
$\bar{2}32$	8	3.314					

TABLE 4.—*X-ray powder data for low chalcocite from Bristol, Conn.*—Continued

hkl (monoclinic)	*I*(xl)	*d*(calc)	*d*(obs)	*I*(obs)	*d*(Dj)	*I*(Dj)	*h'k'l'* (orthorhombic)
$\bar{1}04$	12	3.276	3.276	35	3.275	M	024
$\bar{3}04$	10	3.275					
222	17	3.187	3.188	18	3.187	M	262
$\bar{4}22$	10	3.186					
321	2	3.172	3.171	2	-----	---	241
$\bar{4}21$	3	3.171					
$\bar{1}14$	13	3.158	3.158	25	-----	---	124
$\bar{3}14$	10	3.157					
231	1	3.121	3.121	2	3.121	Vw	351
$\bar{3}31$	2	3.120					
132	8	3.056	3.054	13	3.057	M	342
$\bar{3}32$	4	3.055					
420	1	2.9613	------	--	2.9619	W	280
312	18	2.9524	2.9516	18	2.9530	M	182
$\bar{5}12$	11	2.9514					
014	6	2.9321	2.9328	13	2.9326	M	144
$\bar{4}14$	4	2.9311					
041	7	2.8855	2.8860	6	2.8857	M	411
$\bar{1}41$	3	2.8854					
$\bar{1}24$	2	2.8688	2.8686	4	-----	---	224
$\bar{3}24$	2	2.8683					
213	1	2.8622	2.8628	3	-----	---	173
$\bar{5}13$	1	2.8609					
033	3	2.8266	*2.8267	2	2.8246	W	333
$\bar{3}33$	0	2.8260	------	--	-----	---	
141	12	2.7648	*2.7648	13	2.7655	M	431
$\bar{2}41$	3	2.7647	------	--	-----	---	
232	9	2.7332	2.7318	9	2.7331	M	362
$\bar{4}32$	6	2.7325					
240	31	2.7246	*2.7256	35	2.7246	M	440
024	1	2.6962	2.6973	2	2.6979	W	244
$\bar{4}24$	1	2.6954					
042	13	2.6670	2.6675	18	2.6657	M	422
$\bar{2}42$	7	2.6668					
421	4	2.6512	*2.6504	3	-----	---	291
$\bar{5}21$	1	2.6508	------	--	-----	---	
114	3	2.6537	2.6432	4	2.6429	W	164
$\bar{5}14$	3	2.6422					
$\bar{2}15$	1	2.6201	------	--	-----	---	115
$\bar{3}15$	11	2.6198	*2.6204	18	2.6200	M	
133	4	2.6109	*2.6110	2	-----	---	353
$\bar{4}33$	1	2.6103	------	--	-----	---	
241	9	2.5629	*2.5621	6	2.5630	W	451
$\bar{3}41$	2	2.5627	------	--	-----	---	
402	10	2.5331	2.5329	13	2.5324	M	0.10.2
$\bar{6}02$	7	2.5323					
142	10	2.5266	*2.5273	18	2.5272	M	442
$\bar{3}42$	4	2.5263	------	--	-----	---	
412	15	2.4775	2.4772	18	2.4771	M	1.10.2
$\bar{6}12$	12	2.4767					
$\bar{1}43$	0	2.4691	------	--	-----	---	413
$\bar{2}43$	11	2.4690	*2.4698	4	2.4684	M	
313	6	2.4625	*2.4616	2	-----	---	193
$\bar{6}13$	2	2.4615	------	--	-----	---	
$\bar{2}25$	1	2.4477	*2.4490	2	2.4458	W	215
$\bar{3}25$	0	2.4475	------	--	-----	---	
034	30	2.4045	2.4074	50	-----	---	344
$\bar{4}34$	22	2.4040					
204	28	2.4009	2.4030	70	2.4035	S	084
$\bar{6}04$	16	2.3998	*2.3996	35	2.3993	S	
043	3	2.3923	------	--	2.3924	W	433
$\bar{3}43$	2	2.3920					
$\bar{1}25$	1	2.3729	2.3725	4	2.3697	W	235
$\bar{4}25$	0	2.3724					
431	1	2.3724					391
$\bar{5}31$	1	2.3721					
233	0	2.3655	------	--	-----	---	373
$\bar{5}33$	2	2.3648	*2.3666	3	-----	---	
422	10	2.3302	2.3303	25	2.3292	M	2.10.2
$\bar{6}22$	8	2.3296					
$\bar{3}41$	1	2.3289					471
$\bar{4}41$	12	2.3286					
$\bar{1}52$	13	2.2419	*2.2424	13	2.2420	M	502

TABLE 4.—*X-ray powder data for low chalcocite from Bristol, Conn.*—Continued

hkl (monoclinic)	*I*(xl)	*d*(calc)	*d*(obs)	*I*(obs)	*d*(Dj)	*I*(Dj)	*h'k'l'* (orthorhombic)
440	5	2.2417	------	--	-----	---	480
$\bar{2}44$	1	2.2298	------	--	2.2301	Vw	404
$\bar{2}06$	2	2.2196	2.2183	3	2.2183	Vw	026
$\bar{4}06$	2	2.2192					
052	4	2.2124	2.2122	4	-----	---	522
$\bar{2}52$	3	2.2123					
$\bar{3}16$	23	2.2100	*2.2097	35	2.2088	M	106
$\bar{2}16$	2	2.1818	2.1821	6	2.1814	W	126
$\bar{4}16$	2	2.1815					
413	5	2.1395	2.1375	3	2.1369	Vw	1.11.3
$\bar{7}13$	0	2.1386	------	--	-----	---	
620	1	2.1263	2.1261	3	-----	---	2.12.0
044	7	2.1199	2.1197	9	2.1186	W	444
$\bar{4}44$	4	2.1196					
441	6	2.0978	*2.0969	3	-----	---	491
$\bar{5}41$	1	2.0976	------	--	-----	---	
243	1	2.0930	2.0930	2	-----	---	473
$\bar{5}43$	2	2.0926					
053	4	2.0479	*2.0470	3	2.0467	Vw	533
$\bar{3}53$	1	2.0477	------	--	-----	---	
522	4	2.0283	2.0277	6	2.0277	W	2.12.2
$\bar{7}22$	3	2.0278					
$\bar{1}26$	6	2.0107	2.0108	9	2.0105	W	246
$\bar{5}26$	3	2.0102					
144	5	2.0029	*2.0025	4	2.0022	W	464
$\bar{5}44$	2	2.0024	------	--	-----	---	
$\bar{2}45$	5	1.9926	*1.9920	3	1.9919	Vw	415
$\bar{3}45$	0	1.9922	------	--	-----	---	
016	5	1.9883	1.9886	4	1.9877	Vw	166
$\bar{6}16$	3	1.9879					
060	31	1.9808	*1.9812	9	1.9805	M	600
630	57	1.9742	*1.9746	70	1.9740	S	3.12.0
621	1	1.9607	------	--	-----	---	2.13.1
$\bar{7}21$	5	1.9605	*1.9610	4	1.9604	Vw	
450	17	1.9510	*1.9513	13	1.9513	M	580
343	1	1.9206	------	--	-----	---	493
$\bar{6}43$	3	1.9201	1.9211	2	-----	---	
161	4	1.9160	------	--	1.9171	Vw	631
$\bar{2}61$	0	1.9159	------	--	-----	---	
026	7	1.9098	*1.9110	6	1.9099	W	266
$\bar{6}26$	5	1.9094	*1.9088	6			
532	4	1.8950	1.8942	4	1.8955	W	3.12.2
$\bar{7}32$	4	1.8946					
$\bar{1}36$	36	1.8806	1.8811	70	-----	---	346
$\bar{5}36$	27	1.8802			1.8799	S	
106	17	1.8789	1.8800	100	-----	---	086
$\bar{7}06$	11	1.8781					
045	3	1.8766	*1.8770	9	-----	---	455
$\bar{5}45$	0	1.8762	------	--	-----	---	
602	4	1.8752	1.8745	9	1.8748	---	0.14.2
$\bar{8}02$	4	1.8747					
352	7	1.8744					582
$\bar{5}52$	5	1.8741					
$\bar{2}17$	2	1.8630	1.8627	2	1.8626	Vw	137
$\bar{5}17$	2	1.8627					
451	2	1.8539	1.8547	2	-----	---	591
$\bar{5}51$	1	1.8538					
261	2	1.8448	1.8454	2	1.8444	Vw	651
$\bar{3}61$	2	1.8447					
$\bar{1}63$	1	1.8089	1.8087	3	-----	---	613
$\bar{2}63$	2	1.8088					
424	4	1.7992	1.7994	6	-----	---	2.12.4
$\bar{8}24$	3	1.7985					
036	3	1.7975	1.7980	4	1.7980	W	366
$\bar{6}36$	3	1.7970					
622	4	1.7882	1.7882	6	1.7879	W	2.14.2
$\bar{8}22$	2	1.7878					
154	4	1.7874					564
$\bar{5}54$	2	1.7871					
$\bar{2}55$	0	1.7801	------	--	-----	---	515
$\bar{3}55$	2	1.7800	*1.7794	3	1.7805	W	
443	3	1.7550	*1.7544	2	-----	---	4.11.3
$\bar{7}43$	1	1.7446	------	--	-----	---	

TABLE 4.—*X-ray powder data for low chalcocite from Bristol, Conn.*—Continued

hkl (monoclinic)	*I*(xl)	*d*(calc)	*d*(obs)	*I*(obs)	*d*(Dj)	*I*(Dj)	*h'k'l'* (orthorhombic)
206	1	1.7370	1.7379	2	-----	---	0.10.6
$\bar{8}06$	1	1.7362					
353	3	1.7282	1.7284	3	-----	---	593
$\bar{6}53$	0	1.7279					
344	2	1.7278					4.10.4
$\bar{7}44$	1	1.7274					
$\bar{2}64$	15	1.7082	*1.7085	9	-----	---	604
434	12	1.7042	*1.7041	13	-----	---	3.12.4
$\bar{8}34$	8	1.7034	*1.7033	2	-----	---	
055	0	1.6959	1.6956	3	-----	---	555
$\bar{5}55$	2	1.6956					
$\bar{1}64$	2	1.6950					624
$\bar{3}64$	2	1.6949					
408	12	1.6869	*1.6869	13	-----	---	008
514	2	1.6730	1.6718	3	-----	---	1.14.4
$\bar{9}14$	2	1.6723					

The powder data are consistent with the established space group $P6_3/mmc$ (Berry, 1954) and also are practically identical with those obtained from natural specimens.

ANILITE

The 49 measured powder lines obtained from synthetic anilite by using Cu$K\alpha_1$ radiation are compared in table 2 with a calculated powder pattern (D. K. Smith, unpub. data, 1973) based on the structure refinement data of Koto and Morimoto (1970) (see PDF card 24–58); they are also compared with the original powder data given by Morimoto, Koto, and Shimazaki (1969) (PDF card 22–250). The data listed were compiled from patterns made by using samples that were slightly richer or poorer in copper than the ideal Cu_7S_4 composition of anilite, and the few contaminating lines of djurleite or covellite, respectively, were eliminated. The relative intensities of the measured patterns were determined by using all three methods described earlier, and agreement is good between observed and calculated intensities (table 2). The powder data of anilite are consistent with the space group *Pnma* as found by Morimoto, Koto, and Shimazaki (1969). The cell-constants derived by least-squares analysis of the measured data are as follows (*a*, *b*, and *c* in angstroms):

	a	*b*	*c*
This work	7.9065(8)	7.8223(8)	11.078(1)
Morimoto, Koto, and Shimazaki (1969)	7.89(2)	7.84(2)	11.01(2)

DJURLEITE

The composition of djurleite varies from a copper-to-sulfur ratio of 1.934(2) to 1.965(2) (Potter, 1974). The powder data in table 3 were measured from patterns made by using a synthetic sample having a composition ratio of 1.934(1). The measurements were taken mainly from a pattern made by using Cr$K\alpha_1$ radiation, but some, especially at smaller *d* values ($d<1.62$ A), were taken from a Cu$K\alpha_1$ pattern. The weak low-angle lines ($d>4.5$ A) may be seen only on carefully prepared annealed samples.

For a synthetic sample of composition $Cu_{1.96}S$, Djurle (1958) gave 42 unindexed powder lines which are closely consistent with our data. Takeda, Donnay, Roseboom, and Appleman (1967) measured 45 lines and attempted to index them on the basis of their single-crystal studies, having many extensive ambiguities. Cook (1971) gave 38 lines (PDF card 23–960) and indexed them using an orthorhombic unit cell twice the size of that found by Takeda, Donnay, Roseboom, and Appleman. We have listed 159 lines, but indexing beyond $d=2.70$ A is not feasible without more single-crystal intensity data than we have at this time. Four intense lines at higher angles can be indexed conclusively as belonging to the strong sublattice (842, 080, 046, 12.4.2; Takeda and others, 1967) and they have been used to strengthen the unit-cell refinement. As far as we can tell, the powder data are consistent with the unit cell and space group (*Pmnm*) suggested by Takeda, Donnay, Roseboom, and Appleman. The unit-cell parameters obtained by least-squares analyses of the data indicated by asterisks in table 3 are as follows (*a*, *b*, and *c* in angstroms):

	x in Cu_xS	*a*	*b*	*c*
This work	1.934	26.896(6)	15.694(3)	13.536(3)
Djurle (1958)	1.96	26.861(17)	15.700(6)	13.528(6)
Takeda, Donnay, Roseboom, and Appleman (1967)	1.97	26.92(5)	15.71(3)	13.56(3)

LOW CHALCOCITE

The first valid set of X-ray powder data for low chalcocite was reported for synthetic material by Djurle (1958), who listed 83 lines which he indexed using the orthorhombic unit cell of Buerger and Buerger (1944). Cook (1971) has reported a set of 38 lines which are given on PDF card 23–961. The pattern shown by Berry and Thompson (1962) is actually that of djurleite, and the data listed by them are also those of djurleite plus a few lines of anilite. Our pattern of material from Bristol, Conn., made by using Cr$K\alpha_1$ radiation (Cr$K\alpha_1$ was also used by Djurle), yielded 93 lines, which are shown in table 4 compared with those of Djurle (1958). Clearly, his measurements are as good as ours, and measurements made from synthetic material showed no significant differences or improvement. After the discovery that low chalcocite has a

monoclinic crystal structure (Evans, 1971), we are now able to provide a more accurate indexing, which is shown in table 4 with the pseudo-orthorhombic indexing used by Djurle. The transformation from monoclinic to orthorhombic is accomplished with the matrix 010/201/001.

The availability of a complete set of three-dimensional, single-crystal intensity data has made is possible to assign indices to many of the large number of observed lines that are ambiguous pairs resulting from the nearly exact orthogonality of the pseudo-orthorhombic lattice. These intensities converted to expected powder-diffraction intensities are also shown in table 4. The least-squares analysis of 34 lines, indexed on the basis of the single-crystal data (indicated by asterisks in table 5), was carried out for the monoclinic unit cell found by Evans (1971) in his structure determination. The results are as follows (a, b, and c in angstroms and β in degrees):

	a	b	c	β	
This work	15.235(3)	11.885(2)	13.496(2)	116.26(1)	
Pseudo-orthorhombic cell	11.885(2)	27.325(4)	13.496(2)	90.027(8)	(α)
Djurle (1958)	11.881(4)	27.323(8)	13.491(4)	90	

REFERENCES CITED

Appleman, D. E., and Evans, H. T., Jr., 1973, Indexing and least-squares refinement of powder diffraction data: U.S. Dept. Commerce, Natl. Tech. Inf. Service, no. PB–216–188, 67 p.

Batchelder, D. N., and Simmons, R. O., 1965 X-ray lattice constants of crystals by a rotating-camera method: Al, Ar, Au, CaF_2, Cu, Ge, Ne, Si: Jour. Appl. Physics, v. 36, no. 9, p. 2864–2868.

Berry L. G., 1954, The crystal structure of covellite, CuS, and klockmannite, CuSe: Am. Mineralogist, v. 39, no. 5–6, p. 504–509.

Berry, L. G., and Thompson, R. M., 1962, X-ray powder data for ore minerals—the Peacock atlas: Geol. Soc. America Mem. 85, 281 p.

Bond, W. L., 1960, Precision lattice constant determination: Acta Cryst., v. 13, pt. 10, 814–818.

Bragg, W. L., 1947, The conversion factor for kX units to Angstrom units: Jour. Sci. Instruments, v. 24, no. 1, p. 27.

Buerger, M. J., and Buerger, N. W., 1944, Low-chalcocite and high-chalcocite: Am Mineralogist, v. 29, nos. 1–2, p. 55–65.

Cook, W. R., Jr., 1971, The copper-sulfur phase diagram: Cleveland, Ohio, Case Western Reserve Univ. Ph.D. thesis, 138 p.; Dissert. Abs., v. B32, no. 6, p. 3434.

——— 1972, Phase changes in Cu_2S as a function of temperature, *in* Roth, R. S., and Schneider, S. J., Jr., eds., Solid state chemistry: U. S. Natl. Bur Standards Spec. Pub 364, p. 703–712.

Djurle, Seved, 1958, An X-ray study on the system Cu-S: Acta Chemica Scandinavica, v. 12, no. 7, p. 1415–1426.

Evans, N. T., Jr., 1971, Crystal structure of low chalcocite: Nature; Phys. Sci., v. 232, no. 29, p. 69–70.

Hägg, Gunnar, and Ersson, N.–O., 1969, An easily adjustable Guinier camera of highest precision [abs.]: Acta Cryst., v. A25 Suppl., pt. S3, p. S64.

Koto, Kichiro, and Morimoto, Nobuo, 1970, The crystal structure of anilite: Acta Cryst., v. 26, sec. B, pt. 7, p. 915–924.

Morimoto, Nobuo, Koto, Kichiro, and Shimazaki, Yoshihiko, 1969, Anilite, Cu_7S_4, a new mineral: Am. Mineralogist, v. 54, no. 9–10, p. 1256–1268.

Morimoto, Nobuo, and Koto, Kichiro, 1970, Phase relations of the Cu-S system at low temperatures—stability of anilite: Am. Mineralogist, v. 55, nos., 1–2, p. 106–117.

Potter, R. W., II, 1974, The low temperature phase relations in the system Cu-S derived from an electrochemical investigation: Geol. Soc. America Abs. with Programs, Ann. Meetings, 1974, v. 6, no. 7, p. 915–916.

Robie, R. S., Bethke, P. M., and Beardsley, K. M., 1967, Selected X-ray crystallographic data, molar volumes, and densities of minerals and related substances: U.S. Geol. Survey Bull. 1248, 87 p.

Roseboom, E. H., Jr., 1966, An investigation of the system Cu-S and some natural copper sulfides between 25° and 700°C: Econ. Geology, v. 61, no. 4, p. 641–672.

Swanson, H. E., Fuyat, R. K., and Ugrinic, G. M., 1955, Standard X-ray diffraction powder patterns: U.S. Natl. Bur. Standards Circ. 539, v. 4, p. 13–14.

Takeda, Hiroshi, Donnay, J. D. H., Roseboom, E. H., Jr., and Appleman, D. E., 1967, The crystallography of djurleite, $Cu_{1.97}S$: Zeitschr. Kristallographie, v. 125, p. 404–413.

Jour. Research U.S. Geol. Survey
Vol. 4, No. 2, Mar.–Apr. 1976, p. 213–216

A REVIEW OF THE MINERALS OF THE ALUNITE-JAROSITE, BEUDANTITE, AND PLUMBOGUMMITE GROUPS

By THEODORE BOTINELLY, Denver, Colo.

Abstract.—Minerals of the alunite-jarosite, beudantite, and plumbogummite groups can be divided on the basis of iron or aluminum content into two groups which are consistent in optical and X-ray characteristics. Both chemical and X-ray data are needed for identification.

An investigation of the secondary minerals associated with lead-zinc vein deposits of the Montezuma district of central Colorado disclosed several minerals belonging to the alunite-jarosite, beudantite, and plumbogummite groups. Comparison of the X-ray powder patterns of these minerals with the standard patterns in the file of the Joint Committee on Powder Diffraction Standards (JCPDS) did not lead to definite identification, and it was decided that part of the difficulty was related to the standard patterns. A survey was made of the pertinent patterns in the JCPDS file and of a number of patterns in the literature. This paper comments on some of the problems met in the identification of these mineral groups by X-ray diffraction methods.

The minerals of these groups are isostructural and in Dana's System of Mineralogy (Palache and others, 1951) are separated into groups according to the nature of the anion. The alunite-jarosite group minerals are sulfates, the beudantite group minerals are phosphate-sulfates and arsenate-sulfates, and the plumbogummite group minerals are phosphates and arsenates. (Other groups and classifications have been used by various mineralogists.) The groups include about 30 minerals, of which some are rare but many are widespread and abundant. They usually occur as fine-grained masses mixed with other minerals, and many resemble the hydrous iron oxides. Some X-ray, optical, and chemical data for the minerals of these groups are summarized in table 1.

All the minerals of these groups probably formed at low temperature, under oxidizing conditions, and in a slightly acid environment. Some have been stated to be primary; others occur commonly and abundantly as products of the oxidation of sulfide minerals. A few have been reported in soils treated with phosphate fertilizers.

Acknowledgments.—The author is grateful to P. L. Hauff for running the least-squares computer program for unit-cell dimensions for several of these minerals and to A. L. Sutton for computer solutions of the simultaneous equations for the treatment of Duncan McKie's data.

COMPOSITION

The general formula for the minerals of these groups is $AB_3(XO_4)_2 \cdot (OH)_6$. The A position may be filled by one-, two-, or three-valent ions such as Na, K, H_3O, Ca, Pb, Sr, or Ce. The B position is usually filled dominantly by Al or Fe; in some minerals this position contains some Cu. Usually (XO_4) is (SO_4), (PO_4), (AsO_4), (AsO_4SO_4), or (PO_4SO_4), but some analyses indicate CO_3 or SiO_4 substituting in this position. A few analyses report halogens which substitute in part for $(OH)_6$.

Most analyses of these minerals, at best, lead to approximations of the type formula. Many of the analyses are old and were done on very impure material. Some of the modern analyses were done on very small quantities of material, and some of the more recently named members were analyzed only qualitatively and the composition established by analogy with other members of the groups. Synthetic analogs of these minerals have been prepared by numerous workers, but the products of the synthesis are usually fine grained and may contain unreacted amorphous components. Thus, the composition of many of these naturally occurring minerals is still not adequately known.

The formulas recalculated from some of the published analyses of these minerals suggest that many of the minerals are mixtures of end members, and, as pointed out by Förtsch (1967) for plumbogummite, components originally considered as an impurity may actually be part of the mineral. In general, most analyses show a deficiency (small or large) in the A position

TABLE 1.—*Selected X-ray, optical, and chemical data for minerals of the alunite-jarosite (A), beudantite (B), and plumbogummite (P) groups*

		JCPDS card	a_0	c_0	Index mean or average	A	XO_4	OH	Remarks
	Aluminum-bearing members, optically positive except as noted								
1	Alunite A	4–865	6.97	17.38	1.579	K, Na	SO_4	OH	
2	Alunite A	14–136	6.982	17.32	----	K, Na	SO_4	OH	
3	Crandallite P	(1)	6.989	16.159	1.61±	Ca	PO_4	$OH \cdot H_2O$	
4	Eyelettersite P	(2)	6.98	16.7	----	Th, Pb, and so forth.	$PO_4SiO_4CO_3$	--------	Optic sign?
5	Florencite P	8–143	6.96	16.33	1.698	Ce	PO_4	OH	
6	Florencite P	15–320	6.971	16.42	----	Ce, Sr, Ca	PO_4	OH, F, H_2O	$(SO_4)_{(0.10)}$
7	Gorceixite P	19–535	7.02	16.87	1.625	Ba, Ca, Sr	PO_4	OH, H_2O	
8	Goyazite P	11–194	6.981	16.487	1.632	Sr	PO_4	OH, H_2O	
9	Hidalgoite B	6–380	7.04	16.99	1.709	Pb	AsO_4, SO_4	OH	
10	Hinsdalite B	14–185	6.97	16.8	1.677	Pb, Sr	PO_4, SO_4	OH	
11	Kemmlitzite–(RE) B	22–1248	7.027	16.51	1.703	Sr, RE	AsO_4, SO_4	OH	
12	Natroalunite A	14–130	6.977	16.74	----	Na, K	SO_4	OH	Optic sign?
13	Osarizawaite A	15–178	7.05	[3] 17.25	1.746	Pb	SO_4	OH	
14	Plumbogummite P	20–841	7.018	16.784	1.686	Pb	PO_4, CO_3	OH	
15	Svanbergite B	4–661	6.96	16.8	1.636	Sr	PO_4, SO_4	OH	
16	Svanbergite B	5–737	6.973	16.549	----	Sr, Ca	PO_4, SO_4	OH	
17	Waylandite P	(4)	6.96	16.26	----	Ca, Bi	PO_4 SiO_4	OH	Optic sign(−).
18	Weilerite B	19–1419	7.05	17.16	1.690	Ba	AsO_4, SO_4	OH	
19	Woodhouseite B	4–670	6.975	16.30	1.640	Ca	PO_4, SO_4	OH	
	Iron-bearing members, optically negative								
20	Ammoniojarosite A	17–753	7.3	17.1	1.783	NH_4	SO_4	OH	
21	Argentojarosite A	(5)	7.347	16.580	1.850	Ag	SO_4	OH	
22	Beaverite A	17–476	7.20	16.94	1.85±	Pb	SO_4	OH	(6).
23	Beudantite B	19–689	7.32	17.02	1.952	Pb	AsO_4, SO_4	OH	
24	Corkite B	17–471	7.22	16.66	1.945	Pb	PO_4, SO_4	OH	(7).
25	Dussertite P	19–112	7.40	17.48	1.83	Ba	AsO_4	$OH \cdot H_2O$	
26	Hydronium-jarosite A	21–932	7.3559	17.0097	1.787	H_3O	SO_4	OH	(8).
27	Jarosite A	22–827	7.29	17.16	1.785	K	SO_4	OH	
28	Lusungite P	14–58	7.04	16.80	1.812	Sr, Pb	PO_4	$OH \cdot H_2O$	Optic sign(+)?
29	Natrojarosite A	11–302	7.34	16.72	1.805	Na	SO_4	OH	
30	Plumbojarosite A	18–698	7.315	33.788	1.845	Pb	SO_4	OH	Plotted at $\frac{1}{2}c_0$.

[1] Slade (1974); synthetic. JCPDS card 16–682, crandallite, is triclinic dimorph. Could not be confirmed as either triclinic or hexagonal by least-squares program.
[2] van Wambeke (1972).
[3] From Morris (1963) where value of c_0 is corrected from Morris (1962). B position is filled by (Cu Al).
[4] von Knorring and Mrose (1963).
[5] May, Sjoberg, and Baglin (1973); synthetic.
[6] B position is filled by (Cu, Fe, Al).
[7] Analysis shows some Cu, possibly in B position.
[8] $Fe_3(SO_4)_2(OH)_5 \cdot 2H_2O$, rewritten to show hydronium substitution in A positions.

and also excess water. These discrepancies could be due to hydronium substitution, but the data are inadequate to confirm this. Minor substitutions in the B and (XO_4) positions may occur, but most analyses were done on such impure material that this cannot be proved.

X-RAY DATA

The structure of alunite and the jarosites was determined by Hendricks (1937) to be hexagonal rhombohedral; presumably all the members of the three groups have the same structure. Lattice parameters in the literature have been derived from Debye-Scherrer patterns, from Guinier patterns, from diffractometer patterns, and from single crystal studies. Thus, the unit-cell parameters and the powder patterns vary greatly in quality, and many are not linked to material of known composition.

Because the quality of the data varies so greatly, some of the powder patterns and lattice parameters were checked using the computer program of Evans, Appleman, and Handwerker (1963); others were checked by calculation of d values from the given unit-cell parameters. Generally, values of a_0 checked quite closely, but many values for c_0 showed large discrepancies.

COMPARISON OF UNIT-CELL PARAMETERS AND COMPOSITIONS

Despite the imprecision in analytical and X-ray data, a plot (fig. 1) of a_0 against c_0 shows some consistent variation of unit-cell parameters with composition. With the exception of lusungite, $[(Sr,Pb)Fe_3(PO_4)_2(OH)_5 \cdot H_2O]$ (No. 28, fig. 1, table 1), those minerals with iron in the B position have a_0 greater than 7.20 Å (angstroms) and those with aluminum in the B position have a_0 less than 7.05 Å. The aluminum-bearing

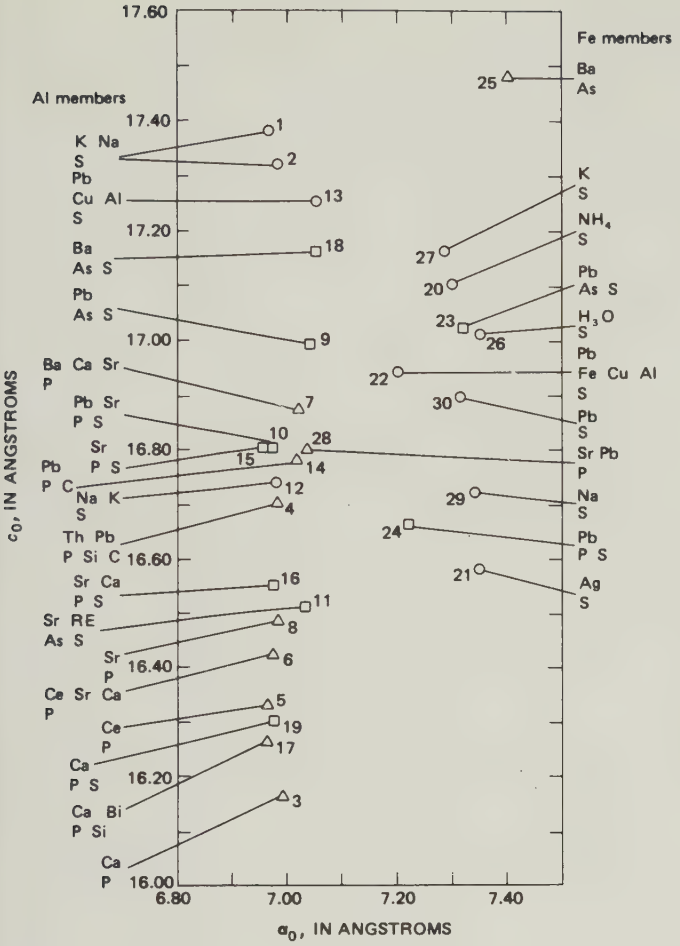

FIGURE 1.—Unit-cell dimensions of minerals of the alunite-jarosite (○), beudantite (□), and plumbogummite (△) groups. Numbers refer to table 1. Chemical symbols indicate composition.

minerals fall into three poorly defined clusters, based on the length of c_0. Those minerals with iron in the B position fall into a somewhat more regular sequence, with the exception of beaverite (No. 22, fig. 1, table 1) and corkite (No. 24, fig. 1, table 1). (These two minerals may each contain copper as well as iron in the B position.)

The aluminum minerals with c_0 ranging from 16.15 to 16.55 Å have strontium, calcium, or rare earths in the A position; the anions are mostly phosphate or phosphate-sulfate with one arsenate-sulfate, kemmlitzite, and one phosphate-silicate, waylandite. Strontium, barium, lead, calcium, and sodium occupy the A position in the aluminum minerals with c_0 ranging from 16.70 to 17.00 Å; the anions are phosphate, phosphate-silicate, phosphate-carbonate, phosphate-sulfate, sulfate, and arsenate-sulfate. Barium, lead and potassium fill the A position in the minerals with c_0 from 17.15 to 17.40 Å; the anions are sulfate with one arsenate-sulfate, weilerite.

The iron members (except for lusungite) are optically negative and have a mean index greater than 1.78. The aluminum members (except for waylandite) are optically positive and have a mean index less than 1.75. Certain members of these groups are in part anomalously biaxial; this anomaly does not seem to be related to composition or unit-cell parameters.

The length of c_0 for the various minerals corresponds only very roughly to the size (table 2) of the ions in the A and XO_4 positions. The lack of a better correlation may be due partly to the imprecision in the determination of c_0 and in the chemical data. McKie (1962, table V) determined lattice parameters and chemical compositions for six naturally occurring solid solutions of crandallite, florencite, gorceixite, and goyazite, and expressed compositions as percentage of end-members. Simultaneous equations were set up from his data and solved for a_0 and c_0 for each end-member.

The results did not agree with a_0 and c_0 in the literature for the various minerals and suggest that a_0 and especially c_0 are not simply related to composition even in minerals that differ only in cation composition. This probably reflects the "looseness" of the structure which can accommodate cations with a large difference in size (table 2).

TABLE 2.—*Radii of certain ions*

[Data, in angstroms, from Weast (1966), p. F–124, except for H_3O^+ from Kubisz (1964, p. 32)]

A		B	
Bi^{3+}	0.96	Al^{3+}	0.51
Na^+	0.97	Fe^{3+}	0.64
Ca^{2+}	0.99	Cu^{2+}	0.72
Ce^{3+}	1.03		
Sr^{2+}	1.12		
Pb^{2+}	1.20		
H_3O^+	1.24	(XO_4)	
Ag^+	1.26	S^{6+}	0.30
K^+	1.33	P^{5+}	0.35
Ba^{2+}	1.34	Si^{4+}	0.42
NH_4^+	1.43	As^{5+}	0.46

CONCLUSIONS

The data from the literature suggest that the minerals of the alunite-jarosite, beudantite, and plumbogummite groups would better be divided into two groups—the alunite and jarosite groups—on the basis of iron or aluminum content as was suggested by McConnell (1942) or be combined into one group with aluminum and iron members (Larsen and Berman, 1934).

Certain mineral names in these groups are superfluous, the compounds being combinations of several end-members. McKie (1962) described complex mixtures of crandallite, florencite, gorceixite, and goyazite by using percentages of end-member molecules, as is commonly

done for feldspars. The use of such a system is more informative than present usage and might avoid further proliferation of names.

X-ray powder patterns usually will not give precise identifications of minerals in these groups. The length of a_0 should indicate whether one is dealing with an iron or aluminum member and should give some indication of the optical properties. The length of c_0 gives an approximate idea of elements in the A and XO_4 positions but chemical data are required for identifications.

Inasmuch as most of these minerals occur as fine-grained masses which are usually impure and also variable in composition, especial care should be taken to insure that optical, X-ray, and chemical data actually come from the same mineral. Data that conflict with the common characteristics of the members of each group should be fully validated.

REFERENCES CITED

Evans, H. T., Jr., Appleman, D. E., and Handwerker, D. S., 1963, The least-squares refinement of crystal unit cells with powder diffraction by automatic computer indexing method [abs. E–10]: Cambridge, Mass., Am. Crystall. Assoc. Meeting, Program and Abs., p. 42–43.

Förtsch, E. B., 1967, "Plumbogummite" from Roughten Gill, Cumberland: Mineralog. Mag., v. 36, p. 530–538.

Hendricks, S. B., 1937, The crystal structure of alunite and the jarosites: Am. Mineralogist, v. 22, p. 773–784.

Kubisz, Jan, 1964, A study on minerals of the alunite-jarosite group [In Polish with English summary]: Polska Akad. Nauk Kom. Nauk Geol. Prace Geol., no. 22, 96 p.

Larsen, E. S., Jr., and Berman, Harry, 1934, The microscopic determination of the nonopaque minerals [2d ed.]: U.S. Geol. Survey Bull. 848, 266 p.

May, Alexander, Sjoberg, J. J., and Baglin, E. J., 1973, Synthetic argentojarosite—Physical properties and thermal behavior: Am. Mineralogist, v. 58, p. 936–941.

McConnell, Duncan, 1942. X-ray data on several phosphate minerals: Am. Jour. Sci., v. 240, p. 649–657.

McKie, Duncan, 1962, Goyazite and florencite from two African carbonatites: Mineralog. Mag., no. 33, p. 281–297.

Morris, R. C., 1962, Osarizawaite from western Australia: Am. Mineralogist, v. 47, p. 1080–1093.

——— 1963, Osarizawaite from western Australia—a correction: Am. Mineralogist, v. 48, p. 97.

Palache, Charles, Berman, Harry, and Frondel, Clifford, 1951, Dana's system of mineralogy [7th ed.]: New York, John Wiley and Sons, Inc., v. 2, 1124 p.

Slade, P. G., 1974, The synthesis of crandallite $CaAl_3H[OH)_6/(PO_4)]$: Neues Jahrb. Mineralogie Monatsh., p. 22–27.

van Wambeke, L., 1972, Eyelettersite, un nouveau phosphate de thorium appartenant a la serie de la crandallite: Soc. Française Mineralogie et Cristallographie Bull., v. 95, p. 98–105.

von Knorring, Oleg, and Mrose, M. E., 1963, Westgrenite and waylandite, two new bismuth minerals from Uganda, *in* Abstracts for 1962: Geol. Soc. America Spec. Paper 73, p. 256–257.

Weast, R. C., ed., 1966, Handbook of chemistry and physics [47th ed.]: The Chemical Rubber Co., Cleveland Ohio, p. F–124.

Jour. Research U.S. Geol. Survey
Vol. 4, No. 2, Mar.–Apr. 1976, p. 217–220

FLAMELESS ATOMIC ABSORPTION DETERMINATION OF BISMUTH IN SOILS AND ROCKS

By W. H. FICKLIN and F. N. WARD, Denver, Colo.

Abstract.—Recent advances in flameless atomic absorption allow determinations of bismuth in concentrations as small as 50 ppb in 0.2 g of rock or soil sample. The sample is fused with sodium bisulfate and the fusion product is leached with hot 2 *M* hydrochloric acid and treated with ammonium citrate, (ethylenedinitrilo)tetraacetic acid disodium salt, and finally with ammonium 1-pyrrolidinedithiocarbamate to form a complex which is extracted into methyl isobutyl ketone. Aliquots of the latter are pipetted into a graphite furnace and then subjected to an established and automated program of drying, charring, and atomizing. Recorded peak heights provide a measure of the amount of bismuth present.

Small amounts of bismuth are often associated with gold and silver in minerals such as sylvanite and with tellurium in tetradymite in high-temperature hydrothermal deposits. Trace amounts of bismuth also occur in galenas, the amount varying with the temperature of deposition in a manner that suggests a quantitative indication of the formation temperatures (Goldschmidt, 1954). In mull ash, bismuth is strongly associated with copper and gold and is to a lesser extent associated with zinc and molybdenum (Curtin and others, 1971).

These associations are significant because small enrichments to levels above the crustal abundance, which is about 100–200 ppb (Taylor, 1964; Vinogradov, 1959, p. 174), may serve to identify areas of lead, copper, gold, zinc, or molybdenum mineralization of possible economic importance. A method for determining these small enrichments of bismuth in soils and rocks is of great importance in the U.S. Geological Survey's expanding effort to test and demonstrate new ways of geochemical exploration for mineral deposits.

Although the Geological Survey has published two different analytical methods for determining trace amounts of bismuth in soils and rocks (Ward and Crowe, 1956; Ward and Nakagawa, 1967) and both methods filled a short-term need, neither procedure had enough sensitivity to measure the small enrichments near and slightly greater than the crustal abundance. The proposed procedure has sufficient sensitivity to measure these enrichments and is therefore applicable to the delineation of dispersion products produced during weathering of concealed ore deposits.

Recent advances in flameless atomic absorption techniques have increased the sensitivity for many elements beyond that heretofore achieved by conventional atomic absorption (Slavin and others, 1972; Ediger and others, 1974). Bismuth is an example of such an element and several workers have developed methods for determining extremely small amounts—1×10^{-8} g per gram of sample—in nickel and iron alloys using selective extraction to enrich the level before measurement.

Headridge and Richardson (1970) developed an atomic absorption method for determining bismuth in iron alloys. They were able to extract into MIBK 2–130 μg of bismuth quantitatively from a solution 2.3 *M* in hydrochloric acid, 0.09 *M* in ascorbic acid, and 0.2 *M* in potassium iodide. The use of a flameless attachment allows one to decrease the lower amount of bismuth to 0.1 μg per millilitre of ketone.

Burke (1972) reported that bismuth as well as antimony, lead, and tin could be extracted into MIBK from a solution of a nickel base alloy containing 10 percent hydrochloric acid, 6 percent potassium iodide, and 2 percent ascorbic acid. The extraction is achieved with a 5-percent solution of trioctylphosphine oxide dissolved in MIBK. The practical limit of the amount of bismuth extracted in Burke's procedure is about 0.1 μg per millilitre of ketone.

Following the practice of others, especially in use of ammonium 1-pyrrolidinedithiocarbamate (APDC), Lau, Droll, and Lott (1971) studied the extraction of the bismuth complex into MIBK. With (ethylenedinitrilo) tetraacetic acid disodium salt (EDTA) and an ammonium citrate buffer, only copper, silver, gold, osmium, thallium, and bismuth are extracted into MIBK. With the addition of potassium cyanide, only bismuth and thallium are extracted. Thus, under basic conditions resulting from the addition of cyanide, bismuth is selectively extracted as the carbamate into MIBK; gold, silver, osmium, and thallium have no

adverse effect. In the absence of cyanide as much as 10 ppm of copper and (or) 10 ppm of thallium do not interfere.

Hofton and Hubbard (1972) applied this method to the analysis of bismuth in steels. We have adapted the extraction step to soils and rocks and finally measured the bismuth using a flameless technique and a graphite furnace to achieve levels as low as 50 ppb in the soil or rock sample or 0.01 μg of bismuth per millilitre of ketone.

REAGENTS AND APPARATUS

Ammonium citrate–(ethylenedinitrilo) tetraacetic acid buffer (EDTA buffer). Prepare by dissolving 294 g of sodium citrate dihydrate, 50 g of (ethylenedinitrilo) tetraacetic acid disodium salt, and 267 ml of concentrated ammonium hydroxide in water and finally add water to make 1 litre of solution.

Ammonium hydroxide, concentrated, reagent grade.

Ammonium 1-pyrrolidinedithiocarbamate (APDC). Prepare by dissolving 1 g of reagent in 100 ml of demineralized water.

Bismuth standard solution A, 1,000 μg/ml, Fisher preparation used.

Bismuth standard solution B, 10 μg/ml. Prepare weekly by diluting 1 ml of 1,000 μg per millilitre of standard solution to 100 ml with water, acidified with 1 ml of concentrated nitric acid.

Bismuth standard solution C, 0.1 μg/ml. Prepare daily by diluting 1 ml of 10 μg/ml standard solution to 100 ml with water.

Bismuth standard solution D, 0.01 μg/ml. Prepare daily by diluting 10 ml of 0.1 μg/ml standard solution to 100 ml with water.

Hydrochloric acid, concentrated, reagent grade.

4-methyl-2-pentanone (methyl isobutyl ketone) (MIBK), reagent grade.

Sodium bisulfate, fused.

Centrifuge.

Culture tubes, borosilicate glass, 18×150 mm.

Culture tubes, borosilicate glass, screwcap, 16×150 mm.

Mechanical shaker.

Pipets, Eppendorff or similar style.

EQUIPMENT

A Perkin-Elmer model 306 atomic absorption spectrophotometer with a Perkin-Elmer HGA–2100 graphite atomizer is used for the analyses. For each bismuth determination a 10-μl sample is introduced into the atomizer with an Eppendorff pipet. A deuterium background corrector is also used.

The instrumental parameters are as follows:

Wavelength	223.7 nm
Slit width	0.2 nm
Source	Perkin-Elmer intensitron bismuth hollow-cathode lamp

The HGA–2100 program is:

Drying	10 s at	125°C
Charring	20 s at	400°C
Atomizing	8 s at	2,000°C

Argon is used as purge gas and the flow rate is 40 cm^3/min with the interruption device on.

Scale expansion of 3× can be used, but generally no scale expansion is necessary.

Peak-height readings are taken from the Perkin-Elmer model 56 strip-chart recorder. Peak heights are compared to those of standards.

PROCEDURE

1. Weigh 0.2 g of finely powdered sample into an 18×150 mm borosilicate glass culture tube.
2. Add 1.0 g of fused sodium bisulfate and fuse sample with bisulfate for 2 or 3 min until dense white fumes evolve from tube.
3. Allow fused material to cool; add 1 ml of concentrated hydrochloric acid and 5 ml of demineralized water. Heat mixture gently until fused material breaks down.
4. Filter solution through No. 41 paper (9-cm diameter) and collect filtrate in a 16×150 mm screwcap culture tube. Rinse residue with 2 ml of hot demineralized water and decant through filter.
5. Add 5 ml EDTA buffer followed by 1 ml of concentrated ammonium hydroxide, 1 ml of APDC reagent, and finally 1 ml of MIBK. Mix after each addition of reagents.
6. Screw cap on culture tube and shake tube on mechanical shaker for 5 min. Then, centrifuge tubes for 1 to 2 min to assist in separating MIBK from aqueous layer.
7. Pipet a suitable aliquot—preferably 10 μl—into graphite tube and initiate automated program of drying, charring, and atomizing.
8. Using a series of working standard solutions prepared according to the following scheme, refer to peak heights to determine bismuth content of aliquot.

Generate a series of working standard solutions according to the following scheme:

Bismuth content of working standard solution (ng/ml of MIBK)	*Volume of suitable bismuth standard solution (ml)*
5	0.5 of D
10	1.0 of D
20	2.0 of D
50	0.5 of C
100	1.0 of C
300	3.0 of C
500	5.0 of C
700	7.0 of C
1000	10.0 of C

Add amounts of appropriate bismuth standard solution to screwcap 16×150 mm culture tubes each containing 1 ml of concentrated hydrochloric acid. If necessary, add water to bring the volume to 10 ml; then add the following reagents sequentially: 5 ml of EDTA buffer, 1 ml of concentrated ammonium hydroxide, 1 ml of APDC reagent, and 1 ml of MIBK. Mix after each addition and shake tubes in mechanical shaker as directed in procedure for samples. Centrifuge. Pipet 10 μl aliquots into graphite furnace and treat as in step 7 of procedure for samples.

Absorbance values obtained for calibration of the instrument with no scale expansion and with 3× scale expansion are listed in table 1.

TABLE 1.—*Calibration of HGA–2100 atomizer for bismuth determination*

Standard concentration (ng/ml of solvent)	Peak height (chart units)
No scale expansion	
50	8
100	16
200	28
300	37
400	48
500	58
600	67
700	77
800	88
900	95
3× scale expansion	
5	5
10	7
20	11
50	23
100	43

Following is an example of the calculation of an unknown sample concentration. If an unknown were to display an absorbance of seven chart units on the 3× scale, then the concentration of bismuth in MIBK is 10 ng/ml. To convert this to parts per billion or nanograms of bismuth per gram of sample, the 10 ng/ml is divided by 0.2 g (the sample size) to give 50 ppb of bismuth.

RESULTS

Shown in table 2 is the range of values in assorted samples of various rock types and soil types analyzed by the EDTA buffer method.

Using the earlier procedure of Headridge and Richardson, we also analyzed five of the standard reference materials, as given in table 2. These are the same materials selected for use in evaluating methods of analysis useful in geochemical exploration (Allcott and Lakin, 1974). Samples GX1 and GX4 contained 1,700 and 9 ppm bismuth, respectively; the relative standard deviations calculated from repeat determinations are 8.5 and 13.2 percent. Samples GX2, 5 and 6 contained less than 500 ppb bismuth.

TABLE 2.—*Values obtained for bismuth by EDTA buffer and APDC extraction*

[Bi content in parts per billion except where noted]

Sample	Type	Bi (mean)	Standard deviation	Relative standard deviation (percent)
GX1 ----	Jasperoid rock, Drum Mountains, Utah.	>100 ppm	----	---
GX2 ----	Soil, Park City, Utah.	360	90	25
GX4 ----	Mill head, Utah	22 ppm	3.3	15
GX5 ----	Soil (B zone), Somerset County, Maine.	349	38	10
GX6 ----	Soil (B zone), Davidson County, N.C.	212	37	17.5
RS1 ----	Ultramafic rock [1]	507	96	19
RS2 ----	Ultramafic rock [1]	1,200	285	24
RS4 ----	Ultramafic rock [1]	588	124	21
G2 ------	USGS analyzed granite. [2]	51	8.5	17

[1] Sample furnished by Geological Survey of Canada.
[2] Recommended value 43 ppb Bi (Flanagan, 1973).

DISCUSSION

Several methods were attempted to extract bismuth from rocks and soils for analysis by flameless atomic absorption. Of these, the procedure which resulted in the best extraction is that based on the work of Lau, Droll, and Lott (1971), who used APDC to form an extractable complex with bismuth. With such an extraction, bismuth is detectable to about 50 ppb in geologic materials. This detection limit is adequate to measure small bismuth enrichments in the Earth's crust that may provide clues to mineral deposits of economic importance.

REFERENCES CITED

Allcott, G. H., and Lakin, H. W., 1974, Statistical summary of geochemical data furnished by 85 laboratories for six geochemical exploration reference samples: U.S. Geol. Survey open-file rept., 5 p., 33 tables.

Burke, K. E., 1972, Determination of microgram amounts of antimony, bismuth, lead, and tin in aluminum, iron and nickel-base alloys by non-aqueous atomic-absorption spectroscopy: Analyst, v. 97, p. 19–28.

Curtin, G. C., Lakin, H. W., Hubert, A. E., Mosier, E. L., and Watts, K. C., 1971, Utilization of mull (forest humus layer) in geochemical exploration in the Empire district, Clear Creek County, Colorado: U.S. Geol. Survey Bull. 1278–B, 39 p.

Ediger, R. D., Peterson, G. E., and Kerber, J. D., 1974, Application of the graphite furnace to saline water analyses: Atomic Absorption Newsletter, v. 13, p. 61–64.

Flanagan, F. J. 1973, 1972 values for international geochemical reference samples: Geochim. et Cosmochim. Acta, v. 37, p. 1189–1200.

Goldschmidt, V. M., 1954, Geochemistry: London, Oxford Univ. Press, 730 p.

Headridge, J. B., and Richardson, J., 1970, Determination of trace amounts of bismuth in ferrous alloys by solvent extraction followed by atomic absorption spectroscopy: Analyst, v. 95, p. 930–934.

Hofton, M. E., and Hubbard, D. P., 1972, The determination of trace amounts of bismuth in steels by solvent extraction and atomic absorption or atomic fluorescence spectrometry: Anal. Chim. Acta, v. 62, p. 311–316.

Lau, H. K. Y., Droll, H. A. and Lott, P. F., 1971, Ammonium 1-pyrrolidinedithiocarbamate as a reagent for bismuth: Anal. Chim. Acta, v. 56, p. 7–16.

Slavin, Sabina, Barnett, W. B., and Kahn, H. L., 1972, The determination of atomic absorption detection limits by direct measurement: Atomic Absorption Newsletter, v. 11, p. 37–41.

Taylor, S. R., 1964, Abundance of chemical elements in the continental crust—A new table: Geochim. et Cosmochim. Acta, v. 28, p. 1273–1285.

Vinogradov, A. P., 1959, The geochemistry of rare and dispersed chemical elements in soils [2d ed.]: New York, Consultants Bureau, Inc. (translators), 209 p.

Ward, F. N., and Crowe, H. E., 1956, Colorimetric determination of traces of bismuth in rocks: U.S. Geol. Survey Bull. 1036–I, p. 173–179.

Ward, F. N., and Nakagawa, H. M., 1967, Atomic absorption determination of bismuth in altered rocks, *in* Geological Survey research 1967: U.S. Geol. Survey Prof. Paper 575–D, p. D239–D241.

Jour. Research U.S. Geol. Survey
Vol. 4, No. 2, Mar.–Apr. 1976, p. 221–222

INTERSTATION CORRELATION OF PEAK-FLOW ESTIMATES

By CLAYTON H. HARDISON, Reston, Va.

Abstract.—Equations are given for using the correlation coefficient between annual peaks at a pair of stream gaging stations to estimate the interstation correlation coefficient of estimated T-year peaks, computed standard deviations, and computed skew coefficients at the same pair of stations. The equations are based on statistics computed from samples of annual peaks simulated from normal distributions with built-in interstation correlation. The interstation correlation of 50-year peaks was found to be about equal to the square of the interstation correlation coefficient of the annual peaks.

The accuracy of flood frequency results obtained by statistical analysis of annual peak discharge at groups of stream gaging stations depends in part on the interstation correlation of the statistics used in the analyses. Hardison (1971), for example, shows that the standard error of prediction of an estimate from a regression of computed T-year peaks against basin characteristics depends in part on the interstation correlation of the T-year peaks. Similarly, the standard error of the mean skew coefficient computed as the average skew of a group of stations depends in part on the interstation correlation of the computed skew coefficients. Unless there is some degree of independence between the statistics computed from the annual peaks observed at a group of stations, a flood frequency result based on the data at all the stations is no more accurate than a result based on the data at a single station.

At most stream gaging stations the lengths of concurrent record are too short to permit the interstation correlation of T-year peaks or of other statistics of the annual peaks to be appraised directly by analysis of data from the sample. It is usually feasible, however, to estimate the interstation correlation between annual peaks at pairs of stations during a concurrent period. This paper uses synthesized records to relate the cross correlation of annual peaks to the cross correlation of flood-frequency statistics based on the annual peaks. These relations provide a means of estimating the cross correlation of flood-frequency statistics computed from streamflow records. Although the relations were developed from samples from normal distributions, the results are applicable to samples from log-normal distributions when the statistics used are those of the logs of the annual peaks.

The computer program used in this study generated correlated random normal numbers from two populations each with a mean of zero and a standard deviation of 0.5 using cross correlation coefficients ranging from 0.1 to 0.9 by steps of 0.1. Each number in one series was obtained by a random normal number generating subroutine. The corresponding numbers in the other series were generated by

$$Y_i = \rho X_i + (\sqrt{1-\rho^2})\,0.5\varepsilon_i \qquad (1)$$

in which X_i is the value in the first series, ρ is the given cross correlation coefficient, Y_i is the corresponding value in the second series, and ε_i is a random number from a normal population with a mean of zero and a standard deviation of 1.0.

Samples of size 10, 25, and 50 from the correlated random numbers were used to compute the mean, standard deviation, and skew coefficient for each sample from each series. The means and standard deviations were then used to compute the 10-, 25-, 50-, and 100-year peaks for each sample by the equation

$$X_T = \bar{X} + K_T S \qquad (2)$$

in which $\bar{X}$ and S are the sample mean and standard deviation, respectively, K_T is the standard normal deviate for recurrence interval T, and X_T is the computed estimate of the T-year peak.

The T-year peaks thus computed from many pairs of concurrent samples from the two series were used to compute a cross correlation coefficient. Values of 50-year peaks computed from 100 samples of size 25 from one series, for example, were correlated with the 100 values of 50-year peaks computed from the corresponding annual peaks in another series that was generated with $\rho = 0.6$ to obtain 0.342 as an estimate of the cross correlation between 50-year peaks at pairs of stations for which the cross correlation coefficient of annual peaks is 0.6. This value of 0.342 is plotted as an "×" on the ρ_a equals 0.6 line of figure 1.

The process was repeated using 100 samples of size 50 and 500 samples of size 10, and then these three

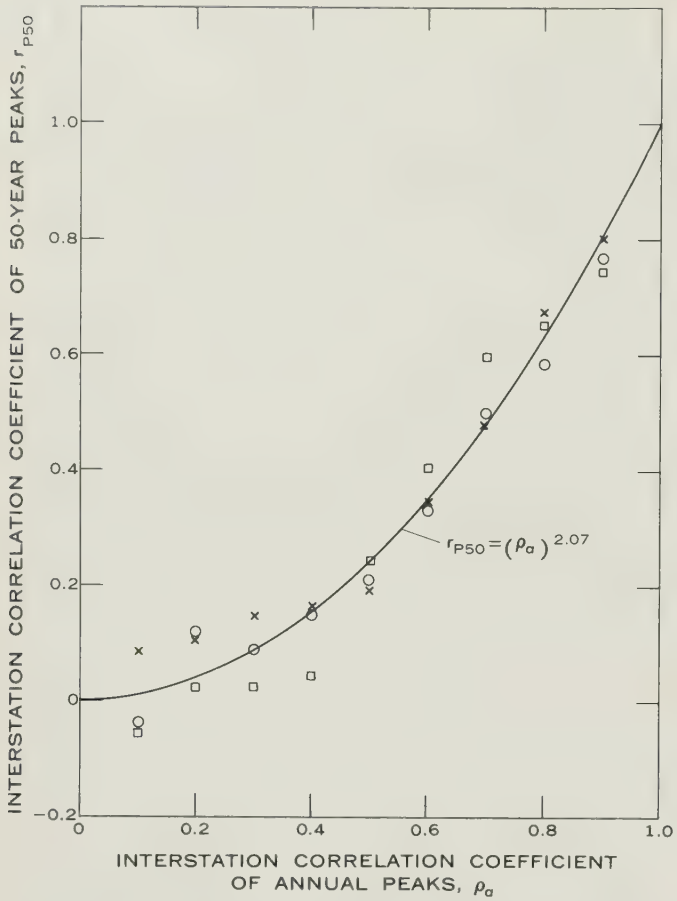

FIGURE 1.—Relation of interstation correlation of 50-year peaks to that of annual peaks. ○, ×, and □ are for sample sizes of 10, 25, and 50, respectively.

runs were repeated using eight other given values of cross correlation coefficients between 0.1 and 0.9. The average cross correlation coefficient for 50-year peaks given by each of these runs is plotted against the cross correlation coefficient of the annual peaks in figure 1. A curve with the equation

$$r_{P50}=(\rho_a)^{2.07} \tag{3}$$

appears to average the points fairly well considering that only 100 samples were used for sample sizes of 25 and 50.

Cross correlation coefficients for peaks with other recurrence intervals were obtained as described for P50. The results are given in equations 4–7.

$$r_{P10}=(\rho_a)^{1.4} \tag{4}$$
$$r_{P25}=(\rho_a)^{1.8} \tag{5}$$
$$r_{P50}=(\rho_a)^{2.07} \tag{6}$$
$$r_{P100}=(\rho_a)^{2.2} \tag{7}$$
$$r_S=(\rho_a)^2-0.04;\ r_S=0.0 \text{ for } \rho_a<0.2 \tag{8}$$
$$r_{CS}=(\rho_a)^2-0.16;\ r_{CS}=0.0 \text{ for } \rho_a<0.4 \tag{9}$$
$$r_{\bar{X}}=\rho_a \tag{10}$$

The cross correlation coefficients between sample standard deviations, r_S, and between the sample skew coefficients, r_{CS}, shown by equations 8 and 9 were determined in the same way as those for the T-year peaks by plotting the cross correlation coefficients of the sample standard deviations and of the sample skew coefficients against the cross correlation coefficient of the populations of annual peaks from which the samples were drawn. Although both populations are normal (skew equal to zero), the skew coefficient of a sample will seldom be zero. Moreover, if the two populations of annual peaks are highly correlated and the skew coefficient of the sample from one of the populations happens to be highly positive, the skew coefficient of the corresponding sample from the other population will also tend to be highly positive. It is this tendency for values of r_{CS} computed from samples taken from correlated populations to be correlated with each other that is evaluated by equation 9.

The cross correlation between sample means will tend to average the same as the cross correlation of annual peaks as indicated in equation 10. This equation was not tested by the random number experiments described here.

Use of equations 4–10 requires that ρ_a, the correlation coefficient between the populations of annual peaks, be estimated as r_a, the correlation coefficient between annual peak flows observed at a pair of stream gaging stations during a concurrent period of record, from a generalization of r_a, or from a Bayesian weighting of the two estimates (Conover, 1971, eq 27). The more accurate the estimate of ρ_a, the more accurate will be the r values given by the equations.

Although equations 4–10 are applicable only to samples from normal or log-normal distributions, they are proposed for interim use in the analysis of flood frequency provided Pearson Type III distributions are fitted to the logarithms of the annual peak discharge. The fact that logarithmic skew coefficients of annual peaks in various regions of the United States are in the range −0.4 to 0.7 should not greatly affect the results. Further analysis with larger samples and with samples from skewed populations would refine the results presented here.

REFERENCES CITED

Conover, W. J., 1971, Introduction to Bayesian methods using the Thomas-Fiering model: Water Resources Research, v. 7, no. 2, p. 406–409.

Hardison, C. H., 1971, Prediction error of regression estimates of streamflow characteristics at ungaged sites, *in* Geological Survey research 1971: U.S. Geol. Survey Prof. Paper 750–C, p. C228–C236.

Jour. Research U.S. Geol. Survey
Vol. 4, No. 2, Mar.–Apr. 1976, p. 223–226

REASSESSMENT OF MERCURY IN SURFACE WATER IN THE ADIRONDACK REGION, NEW YORK

By WILLIAM BULLER, Ithaca, N.Y.

Work done in cooperation with the New York State Department of Health and the New York State Department of Environmental Conservation

Abstract.—A study in 1970 established a natural background concentration of mercury in surface water in the Adirondack region of New York. In 1974, new methods of sample preservation and analysis were used in determining concentrations of mercury of samples of water from the same surface-water sites sampled in 1970–71. Concentrations of mercury for all sites in the 1974 study were virtually the same as those obtained in 1970–71, less than 0.5 microgram per litre, which is the detection limit of the methods.

The results of a study of mercury concentrations in surface water of the Adirondack region of New York were reported by Buller (1972). The purpose of that study was to determine the natural background concentration of mercury in surface water by investigating an area relatively free of artificial sources of mercury. Since that study, new methods of sample preservation and analytical methods for determining concentration of mercury in water have evolved. To obtain a more accurate definition of the background concentration of mercury, the sampling sites of the previous study were resampled in 1974, and the new methods were used to determine the mercury concentrations of the samples.

LITERATURE REVIEW

One of the major problems in studies of mercury in water supplies is the rapid loss of dissolved mercury in water samples. This problem is most pronounced in water samples having low mercury concentrations; for example, natural water. Dokiya, Yamazaki, and Fuwa (1974) found that loss of mercury in 0.1 mg/l aqueous solutions of mercury was as much as 50 percent after 15 days but that mercury in 1 mg/l aqueous solutions of mercury remained stable for 15 days. Much of the loss is due to vaporization of mercury; gaseous mercury may diffuse through the walls of polyethylene containers (Peter Avotins and E. A. Jenne, written commun., November 1974). Bacteria may expedite this process by converting organic mercury to compounds of methylmercury (Wood and others, 1968), or, as indicated by Furukawa, Suzuki, and Tomomura (1969), bacteria may reduce various mercury compounds to metallic mercury. Some compounds of methylmercury have a volatility similar to that of metallic mercury, which has a vapor pressure of 1.2 to 3.4×10^{-3} mm of mercury (Phillips and others, 1959). Loss of mercury may also occur owing to uptake by bacteria adsorbed on container walls (Peter Avotins and E. A. Jenne, written commun., November 1974). Avotins and Jenne use strong oxidizing agents as preservatives. They obtained best results by preserving water samples with a nonacidified 0.05-percent potassium permanganate solution. This treatment method resulted in 90-percent recovery of mercury in an 0.8-μg/l solution after 13 days. A 7.5-percent solution of nitric acid resulted in 60-percent loss of mercury in a 0.5-μg/l solution after 10 days.

The current method of analysis for total mercury (mercury adsorbed on suspended sediment as well as dissolved mercury) is a modification of the method outlined by Hatch and Ott (1968), which was used to determine the total mercury concentrations reported by Buller (1972). The quantities of oxidants used in digesting organomercury compounds in water samples are greater in the current method (American Society for Testing and Materials, 1974, p. 349–350) than in the method of Hatch and Ott (1968). In addition, a heating step (95°C or 203°F, for 2 hours) is used in the current method. The American Society for Testing and Materials (1974) method of digestion is more thorough than that of the previous method. B. A. Malo (oral commun., December 1974) noted that in some

water samples recovery of mercury is several orders of magnitude times the recovery obtained by the previous method.

GEOGRAPHIC, CLIMATIC, AND GEOLOGIC SETTING

The Adirondack region is primarily a rural area, where most communities have a population of less than 2,000, and industry consists of a few papermills and mines (Thomas Lang, oral commun., 1971). Most of the terrain is mountainous with clear, fast-flowing streams that generally carry only small amounts of suspended sediment. The climate of the study region is rather severe. According to Mordoff (1949), air temperatures range from about 40°F below zero to about 100°F (−40° to 38°C), and annual precipitation is usually between 40 and 50 in (1,000 and 1,250 mm). The bedrock consists mainly of felsic metaigneous rocks of Precambrian age such as anorthositic gneiss and granitic gneiss (Fisher and others, 1971) and lesser amounts of marble and gneisses of metasedimentary or metavolcanic origin. The bedrock is covered by an extensive mantle of glacial drift, most of which is derived from the local bedrock. No distinct mercury deposits are known in the region (P. R. Whitney, oral commun., 1971).

STUDY METHODS

Most major lakes and streams in the study area were sampled. Locations of the sampling sites are plotted in figure 1 and are described in table 1.

Two sets of water samples for determination of mercury were collected on November 21–23, 1974, in polyethylene bottles that had been washed with nitric acid and had been rinsed with distilled water. Streamflow in the study area during sampling time was about midway between base flow and high flow. The two sets of water samples were preserved at the time of collection by addition of 1 ml of concentrated nitric acid to each 250-ml sample of water in set 1 and enough potassium permanganate to each 250-ml sample of water in set 2 to make a 0.05-percent solution. Nitric acid was used as the preservative in the 1970–71 study. To determine the amount of mercury that might be induced by reagents and bottles, blank solutions were prepared by adding nitric acid and potassium permanganate to distilled water in the same proportions that they were added to the samples.

Total mercury concentration of unfiltered samples and blanks were determined by the flameless atomic-absorption method (American Society for Testing and Materials, 1974). All samples were analyzed within 6 days after the day of sampling. Mercury concentrations of blank solutions (0.1 μg/l for nitric acid blank and 0.4 μg/l for potassium permanganate blank) were subtracted from sample concentrations to correct for mercury induced by reagents.

RESULTS AND CONCLUSIONS

Mercury concentrations of all samples were less than 0.5 μg/l, the detection limit of the analytical methods. Preference for either treatment was not indicated in this study. However, experimental data of Peter Avotins and E. A. Jenne (written commun., November 1974) indicate that the 0.05-percent potassium permanganate method of sample preservation is effective in preventing significant loss of mercury in water samples. These results agree with the results reported by Buller (1972), which represented various hydrologic conditions. The concentration is considerably less than the recommended limit of 5.0 μg/l mercury for drinking water (New York State Department of Health, 1971) and would probably be considered as trace amounts.

In considering various hydrologic aspects of the study region, the low concentrations of mercury in surface water there are expected. Bedrock and glacial material of the drainage areas are quite resistant to weathering and chemical solution and probably contain only minor amounts of mercury. Data by Rankama and Sahama (1950) indicate that the mercury content of felsic igneous rocks similar to the metaigneous rocks of the study area is less than 100 μg/kg. The lesser amounts of metasedimentary rocks, which may contain greater amounts of mercury and which are generally less resistant to weathering than the metaigneous rocks, are apparently not releasing appreciable amounts of mercury to surface water. Mercury from sources outside the region might conceivably be transported through the atmosphere by wind currents; however, the data do not support this possibility. The author concludes that the concentration of total mercury in surface water of the Adirondack region is generally less than 0.5 μg/l and that this concentration represents a natural background concentration for the region. Concentrations greater than this amount would indicate contamination.

TABLE 1.—*Location of sampling sites in selected streams and lakes of the Adirondack region, New York*

Sampling site[1]	*Location*
1	Hudson River, 1 mi southeast of The Glen, next to State Highway 28.
2	Hudson River at North Creek, at bridge on State Highway 28N.

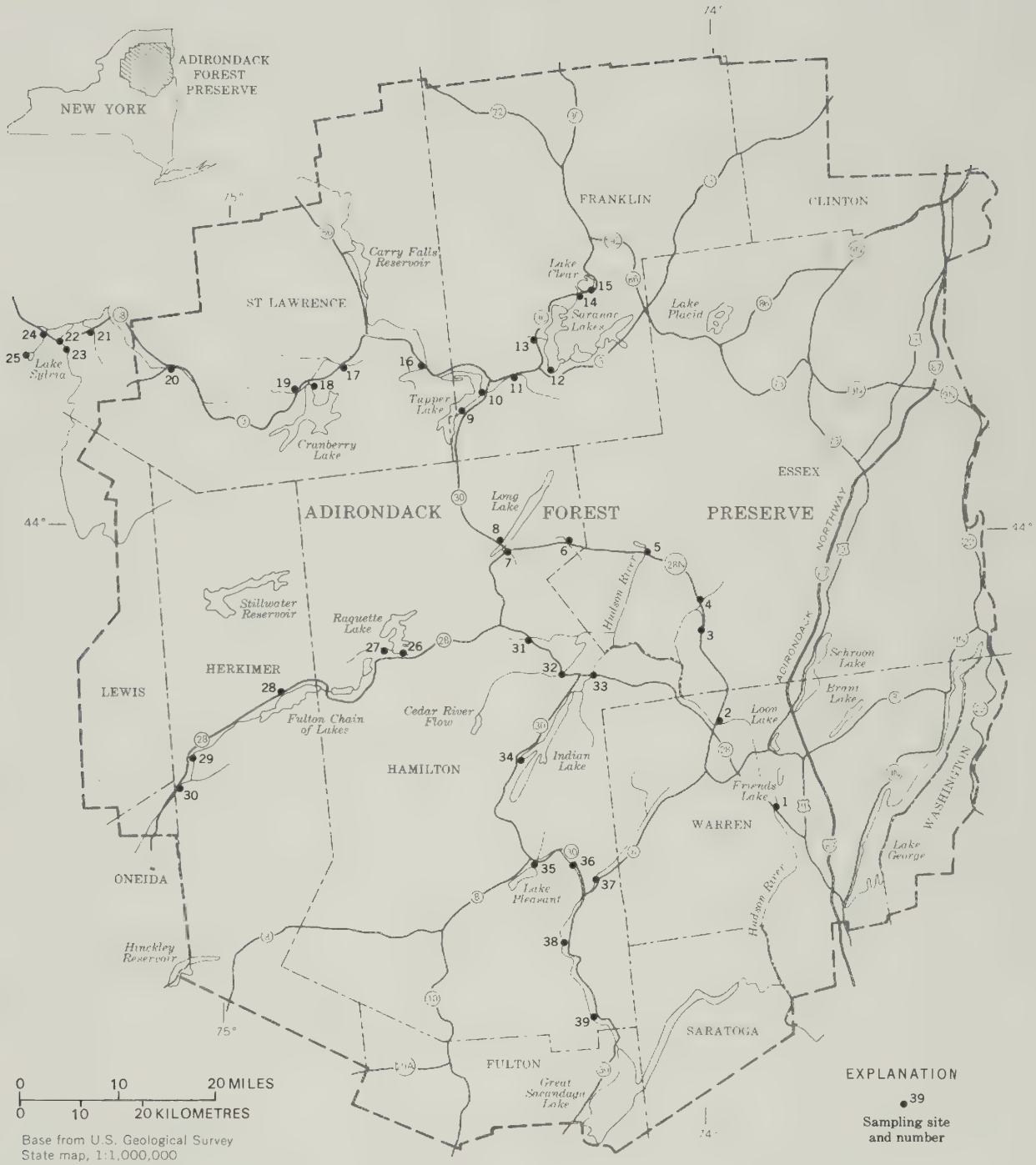

FIGURE 1.—Location of study area and sampling sites in the Adirondack region, New York.

TABLE 1.—*Location of sampling sites in selected streams and lakes of the Adirondack region, New York*—Continued

Sampling site [1]	*Location*
3	Balfour Lake, 4 mi north of Minerva, next to State Highway 28N.
4	Boreas River, 1 mi north of Aiden Lair, at bridge on State Highway 28N.
5	Hudson River, 2 mi east of Newcomb, at bridge on State Highway 28N.

TABLE 1.—*Location of sampling sites in selected streams and lakes of the Adirondack region, New York*—Continued

Sampling site [1]	*Location*
6	Bog, 5 mi west of Newcomb, next to highway markers 1202 and 1030 on State Highway 28N.
7	Stream, ½mi east of the village of Long Lake, next to State Highway 28N.
8	Long Lake at the village of Long Lake, next to State Highway 30.

TABLE 1.—*Location of sampling sites in selected streams and lakes of the Adirondack region, New York*—Continued

Sampling site[1]	Location
9	Tupper Lake at the village of Tupper Lake, 5 mi north of junction of State Highways 421 and 30, next to Highway 30 at water-supply building.
10	Raquette River at the village of Tupper Lake, 1½ mi south of junction of State Highways 3 and 30, next to Highway 30.
11	Raquette River, 3 mi east of the village of Tupper Lake, next to State Highways 30 and 3.
12	Upper Saranac Lake at Wawbeek, next to State Highway 30.
13	Lake, 4½ mi north of Wawbeek, next to State Highway 30.
14	Bog, 4½ mi southwest of the village of Lake Clear, next to State Highway 30.
15	Lake Clear at the village of Lake Clear, next to State Highway 30.
16	Drainage across State Highway 3, 2 mi northwest of Piercefield.
17	South Branch Grass River, 3 mi northeast of the village of Cranberry Lake, at bridge on State Highway 3.
18	Cranberry Lake at the village of Cranberry Lake, next to State Highway 3.
19	Oswegatchie River at the village of Cranberry Lake, at bridge just below dam.
20	Oswegatchie River at Fine at bridge on State Highway 58.
21	Drainage across State Highway 58, 3 mi southwest of Edwards.
22	West Branch Oswegatchie River, 2 mi east of Fowler at bridge on State Highway 58.
23	West Branch Oswegatchie River at Fullerville, at bridge.
24	Turnpike Creek at Highway 58, ½ mi east of Fowler.
25	Lake Sylvia, 1 mi west of Balmat.
26	Raquette Lake 2 mi east of the village of Raquette Lake, next to State Highway 28.
27	Bog, 1 mi southwest of the village of Raquette Lake, next to State Highway 28.
28	Fulton Chain of Lakes, 3 mi west of Eagle Bay, next to State Highway 28.
29	North Branch Moose River, 3 mi north of McKeever, next to State Highway 28.
30	Moose River at McKeever, at bridge on State Highway 28.
31	Rock River, 3 mi east of the village of Blue Mountain Lake, at bridge on State Highways 28 and 30.
32	Cedar River, 2 mi west of the village of Indian Lake, at bridge on State Highway 30–28.
33	Indian River, 1 mi east of the village of Indian Lake, at bridge on State Highway 28.
34	Indian Lake, 8 mi south of Sabael, at drainage line between Lewey Lake and Indian Lake, next to State Highway 30.

TABLE 1.—*Location of sampling sites in selected streams and lakes of the Adirondack region, New York*—Continued

Sampling site[1]	Location
35	Lake Pleasant at Speculator, at bridge on State Highway 30.
36	Sacandaga River, 6 mi east of Speculator, next to State Highway 30, at bridge on side road.
37	East Branch Sacandaga River, 1½ mi northeast of Griffin, next to State Highway 8.
38	Algonquin Lake at Wells, near bridge on State Highway 30.
39	Sacandaga River, 5 mi northwest of Northville, at bridge on State Highway 30.

[1] Sites 1–8 were sampled on Nov. 21, 1974. Sites 9–23 were sampled on Nov. 22, 1974. Sites 24–39 were sampled on Nov. 23, 1974.

REFERENCES CITED

American Society for Testing and Materials, 1974, Standard method of test for total mercury in water: Philadelphia, Annual Book of ASTM Standards, Water, pt. 31, p. 344–350.

Buller, William, 1972, Natural background concentration of mercury in surface water of the Adirondack region, New York, *in* Geological Survey research 1972: U.S. Geol. Survey Prof. Paper 800–C, p. C233–C238.

Dokiya, Y., Yamazaki, S., and Fuwa, K., 1974, Loss of trace elements from natural water during storage: Environmental Letters, v. 7, no. 1, p. 67–81.

Fisher, D. W., Isachsen, Y. W., and Rickard, L. V., 1971, Geologic map of New York, 1970: New York State Mus. and Sci. Service, Map and Chart Ser. No. 15.

Furukawa, K., Suzuki, I., and Tomomura, K., 1969, Decomposition of organic mercurial compounds by mercury-resistant bacteria: Agr. Biol. Chemistry, v. 33, no. 1, p. 128–130.

Hatch, W. R., and Ott, W. R., 1968, Determination of submicrogram quantities of mercury by atomic absorption spectrophotometry: Anal. Chemistry, v. 40, no. 14, p. 2085–2089.

Mordoff, R. A., 1949, The climate of New York State: Cornell Univ. Bull. 764, New York State Coll. Agriculture, 72 p.

New York State Department of Health, 1971, Part 170, Subchapter C—Water supply sources of chapter III, title 10, (health): Official Compilation of Codes, Rules, and Regulations of the State of New York.

Phillips, G. P., Dixon, B. E., and Lidzey, R. G., 1959, The volatility of organo-mercury compounds: Sci. Food Agriculture Jour., v. 10, p. 604–610.

Rankama, Kalervo, and Sahama, T. G., 1950, Geochemistry: Chicago, Univ. Chicago Press, 912 p.

Wood, J. M., Kennedy, F. S., and Rosen, C. G., 1968, Synthesis of methylmercury compounds by extracts of a methanogenic bacterium: Nature, v. 220, no. 5163, p. 173–174.

Jour. Research U.S. Geol. Survey
Vol. 4, No. 2, Mar.–Apr. 1976, p. 227–232

AMINO ACIDS AND GASES IN SOME SPRINGS AND AN OIL FIELD IN CALIFORNIA

By JOHN B. RAPP, Menlo Park, Calif.

Abstract.—Samples of water and gas were collected from six springs and two wells in the Upper Cretaceous Great Valley sequence and Franciscan Formation underlying the Coast Range of northern California and from four oil wells penetrating Tertiary sedimentary rocks in the Kettleman North Dome oil field. Comparison of the dissolved free amino acid compositions of the waters from the two locations show overlapping ranges with many more similarities than differences. The detection of nonprotein amino acids (sarcosine, β-amino *n*-butyric acid, and others) indicates the protein degradation is partly chemical rather than strictly biological. Other low molecular weight degradation products (methane, ethane, nonvolatile organic acids, and other organic chelating agents) were found. This may be one mechanism for the transportation of organic matter from the source rocks to the reservoir rocks of an oil deposit.

The waters of several springs and wells in the Coast Range of northern California contain high concentrations of bicarbonate (7,100 mg/l for Wilbur Springs), chloride (18,200 mg/l for Complexion Spring, 14,000 mg/l for both Murphy samples), ammonium ion (280 mg/l for Wilbur Springs, 210 mg/l for Complexion Spring), and boron (310 mg/l for Wilbur Springs) (Barnes, Hinkle, and others, 1973; U.S. Geological Survey, unpub. data, 1972). These constituents are also high in the oil-field brines from the Kettleman North Dome field in California (well 33–1P, for example, has alkalinity = 2,220 mg/l as bicarbonate, chloride = 19,700 mg/l, ammonium ion = 88 mg/l, and boron = 58 mg/l) (Kharaka and Berry, 1974).

The purpose of this paper is to compare several springs and wells of the Coast Range of northern California with the Kettleman North Dome wells with respect to the dissolved free amino acid compositions of the waters and the composition of the gases which separate from the liquid phase. This study reports the concentrations of the gases and the dissolved free amino acids in six springs, two wells, and four oil-field brines. A summary of the geology and inorganic geochemistry of the area of the springs is given by Barnes, Hinkle, and others (1973), and a similar summary of the Kettleman North Dome area is given by Kharaka and Berry (1974).

Several amino acids have been found in oil-field brines of Paleozoic, Mesozoic, and Cenozoic age from Oklahoma, Colorado, Texas, and Utah (Degens and others, 1964). The concentration of total amino acids reported was between 20 and 230 μg/l. The major amino acids found were serine, glycine, alanine, aspartic acid, the leucines, ornithine, glutamic acid, and threonine. Lesser amounts of unidentified amino acids were found.

The use of ligand-exchange column chromatography to concentrate amino acids from various waters has become widespread recently. In this technique, copper is bound to the chelating resin Chelex 100, and ammonia is complexed with the copper. As the sample passes through the resin column, the amino acids displace the ammonia since they form stronger complexes with the copper. The amino acids are thus bound on the resin and concentrated. Other organics which formed strong complexes with copper would also be concentrated. Siegel and Degens (1966) used the copper-ammonia form of Chelex 100 resin to concentrate amino acids from seawater and used automatic high-pressure ion-exchange chromatography to quantify them. Clark, Jackson, and North (1972) used a combination of the copper-ammonia form of Chelex 100 resin and a cation-exchange resin to concentrate dissolved free amino acids from seawater and used thin-layer chromatography to quantify them. Gardner and Lee (1973) used a combination of the copper-ammonia form of Chelex 100 resin and a cation-exchange resin to concentrate dissolved amino acids in lake waters and used the N-trifluoroacetyl methyl ester derivative of the amino acids and gas chromatography to quantify them.

Acknowledgment.—This research was supported in part by the Defense Advanced Research Projects Agency and was monitored by the U.S. Geological Survey under Order No. 1813, amendment 1.

EXPERIMENTAL METHODS

Apparatus

A Varian Aerograph Model 1440 gas chromatograph having a flame ionization detector and linear temperature programer and a Varian Model A–25 recorder were used. The Pyrex columns used were 1.8 m × 2 mm (ID) TABSORB and 0.9 m × 2 mm (ID) TABSORB HAC (both from Regis Chemical Co.) and 1.8 m × 2 mm (ID) Chromasorb 103 (Johns Manville Co.). All samples were injected directly within the Pyrex column to prevent decomposition in the hot metal injection port.

Derivatives were prepared in tapered glass reaction vials containing a Teflon-faced rubber disk in the screwcap.

A 12-litre stainless-steel container, a stainless-steel pressure-filtration apparatus, and 142-mm-diameter filters with 0.45-μm pore size (all Millipore) were used to collect and filter the samples.

A Finnigan Model 1015 gas chromatograph–mass spectrometer (GC–MS) coupled with a System Industries Model 150 data system, a teletypewriter, and a digital plotter were used to further characterize the amino acids.

Gas analysis was carried out on a Perkin-Elmer Model 154 gas chromatograph having a thermistor detector. Columns used were Waters Associates Porapak Q (150–200 mesh) 1.8 m × 6.4 mm and Linde molecular sieve 13X (40–60 mesh) 0.9 m × 6.4 mm.

Chemicals

Copper-ammonia form of Chelex 100 resin was prepared from Bio-Rad Laboratories Chelex 100 chelating resin (50–100 mesh) according to the method of Siegel and Degens (1966). Ammonium form of Chelex 100 resin was prepared from Chelex 100 resin (100–200 mesh), sodium form, by first converting it to the hydrogen form with 2 *N* HCl, washing with water, and then converting to the ammonium form with 3 *N* NH_4OH.

Bio-Rad AG50X8 (100–200 mesh) resin was cycled from the hydrogen form through the ammonium form (with 7 *N* NH_4OH) to the hydrogen form (with 3 *N* HCl) before being used.

Bio-Rad AG1X4 (100–200 mesh) resin originally in the chloride form, was rinsed with 3 *N* HCl and then was converted to the hydroxide form with NaOH.

All the resins were leached with the same solution which would be used to elute the sample off the resin.

The nitrogen gas used to hasten evaporation was high purity (99.99 percent minimum) and was filtered through charcoal and glass wool.

Field and laboratory procedures

A summary of the procedures used to separate the organic chelating agents is given in figure 1.

The water sample was passed through a 0.45-μm filter which had been leached with at least 1 litre of the water before a 4–litre sample was collected. The pH was adjusted to 9.5 with NaOH. If a precipitate formed, the sample was filtered again. The filtered sample was then passed through a 1.5-cm-diameter chromatographic column containing 10 cm^3 of Chelex 100 resin in the copper-ammonia form at a rate of approximately 8 ml/min. The column was refrigerated until it arrived at the laboratory, at which time it was frozen. The samples were stored frozen at −15°C.

Gases from the springs and wells of the northern Coast Range were collected in glass, gas-tight syringes by displacement of the native water. Gases from the Kettleman North Dome field were collected in evacuated stainless-steel gas-sampling tubes.

The columns were allowed to come to room temperature and rinsed three times with 5 ml of distilled water. A 0.5-cm-diameter column of 3 cm^3 ammonium-form Chelex 100 resin was rinsed twice with 5 ml of distilled water, and was connected to the exit of the copper-ammonia Chelex 100 column. The columns were then eluted with 3 *N* NH_4OH solution at 0.3 ml/min until 50 ml of effluent was collected.

The 3 *N* NH_4OH effluent was distilled in an all-glass apparatus and 40–45 ml of distillate (volatile) was collected. The contents of the flask (nonvolatile) were allowed to cool and quantitatively transferred to a 10-ml graduated centrifuge tube.

The nonvolatile fraction was passed through a 0.5-cm-diameter column of cation-exchange resin in the hydrogen form (3 cm^3 of AG50X8). The column was rinsed with 5 ml distilled water and initial effluent and rinses were collected (nonvolatile acids + neutrals). The column was eluted with 7 *N* NH_4OH and 10 ml of effluent (nonvolatile cations) were collected at 0.2 ml/min. The solution was evaporated to near dryness on a hot water bath with a stream of nitrogen gas passing over the surface of solution. One drop of 3 *N* HCl was added to the sample and the volume adjusted to 4 ml with distilled water.

The sample was then passed through a 0.5-cm-diameter column of anion exchange resin in the hydroxide form (2 cm^3 of AG1X4). The column was rinsed with distilled water until a total of 10 ml of column effluent (nonvolatile amines) was collected. The column was then eluted with 3 *N* HCl and a total of 10 ml of column effluent (amino acids) was collected.

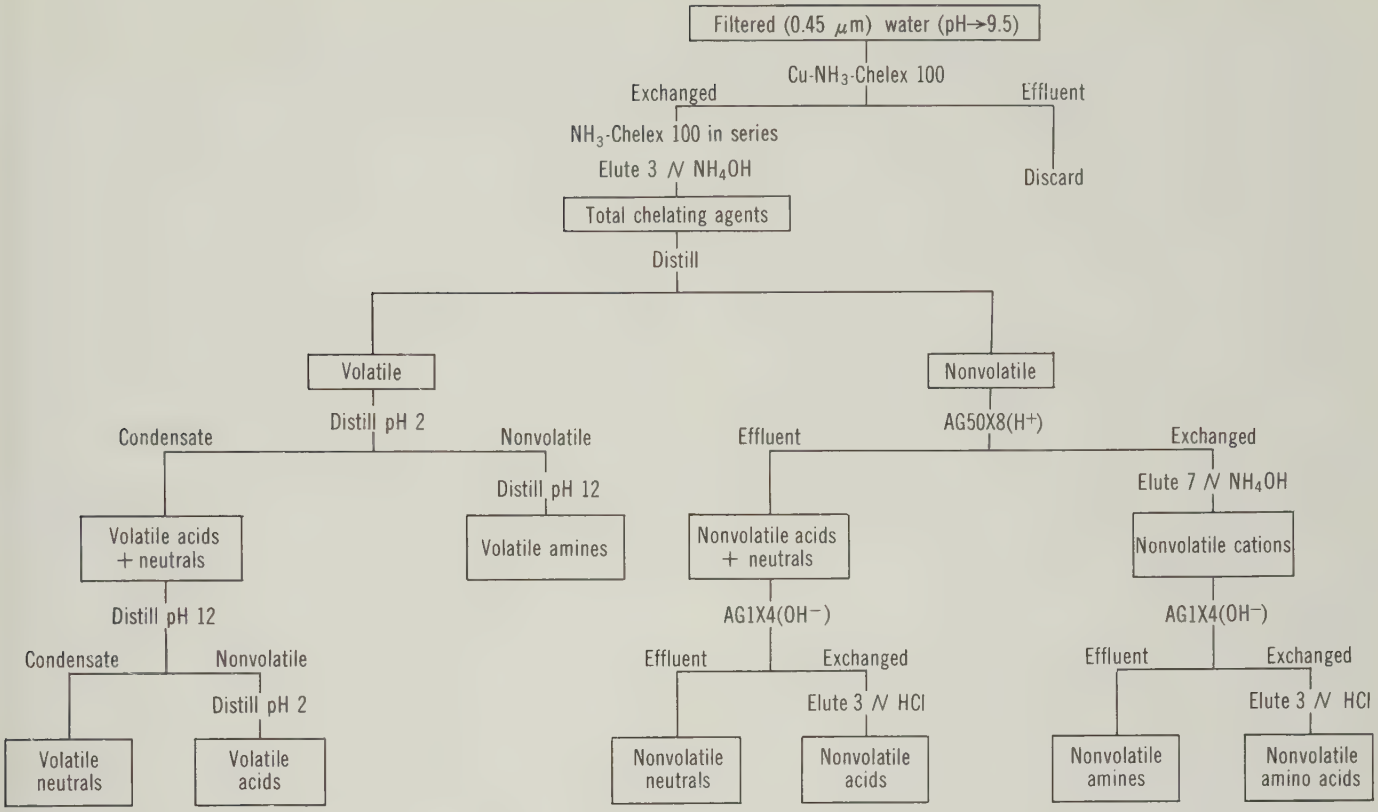

Figure 1.—Separation scheme for organic chelating agents in natural waters.

Some of the nonvolatile (acids + neutrals) fractions were further separated by passing the fraction through a column of AG1X4 (OH^-) resin and collecting the effluent (nonvolatile neutrals). The column was eluted with 3 *N* HCl and the effluent (nonvolatile acids) was collected.

All the volatile samples were analyzed by gas chromatography (direct aqueous injection). A few samples which showed peaks were further separated to partly characterize the material. In the distillations which follow, the sample was adjusted to 50 ml before distillation and 45 ml of distillate was collected. The volatile fraction was adjusted to pH 2 with H_2SO_4 and distilled. The distillate (volatile acids + neutrals) was collected. The solution remaining in the distillation flask was adjusted to pH 12 with NaOH and distilled. The distillate (volatile amines) was collected. The previous distillate (volatile acids + neutrals) was adjusted to pH 12 and distilled. The distillate (volatile neutrals) was collected. The solution remaining in the distillation flask was adjusted to pH 2 and distilled. The distillate (volatile acids) was collected.

Analytical methods

The nonvolatile amines and amino acids fractions were analyzed by gas chromatography after preparation of derivatives. The amines were converted to N-trifluoracetyl derivatives and the amino acids were converted to N-trifluoracetyl *n*-butyl ester derivatives. The micro method of Roach and Gehrke (1969) was followed except the acylation was carried out overnight at room temperature.

The nonvolatile acids fraction was analyzed by gas chromatography after preparation of the *n*-butyl ester derivatives. The derivatization was identical to the first derivatization of the above procedure.

The above derivatives were analyzed on TABSORB (temperature programed 100°–225°C at 4°C/min) and TABSORB HAC (110°–245°C at 8°C/min) gas chromatographic columns with an internal standard of *n*-butyl stearate.

The volatile amines and volatile neutrals fractions were analyzed by gas chromatography on Chromasorb 103 at 150°C with direct aqueous injection.

The amino acids fraction of selected samples was analyzed by gas chromatography–mass spectrometry in order to confirm the identity of the amino acids. The derivative was dissolved in acetone and injected into the GC–MS. The retention times on the TABSORB column and mass spectra of the sample components were compared to standards.

The gases were analyzed by gas chromatography with helium as the carrier gas. Methane, ethane, and carbon dioxide were analyzed on a column of Porapak Q. Nitrogen, oxygen plus argon, and methane were analyzed on a column of Linde molecular sieve 13X.

RESULTS AND CONCLUSIONS

The concentrations of dissolved free amino acids in the samples are given in table 1. The value for alanine through lysine are the original concentrations. The recoveries for the various amino acids were 7 to 50 percent for the whole procedure. The values for aspartic acid, glutamic acid, and sarcosine are the concentrations corrected for the procedural blank only. The reason for reporting in this manner is that the recoveries for aspartic acid, glutamic acid, and sarcosine were low. Gardner and Lee (1973), using a very similar procedure, also reported low recoveries for aspartic and glutamic acids.

Blanks taken through the entire procedure contained very low concentrations of amino acids except for glycine and iminodiacetic acid. These two amino acids are breakdown products of the Chelex 100 and are leached from the resin during the elution procedure. The amount of material leached varies with the period of time between the purification and use of the resin, and also with the length of time it was frozen. Gardner and Lee (1973) observed a compound which eluted from the resin (presumably glycine) which interfered with the glycine analysis. Siegel and Degens (1966) observed two peaks in the blank and attributed them to the imino groups released from the resin. The iminodiacetic acid did not interfere with the analysis since it appeared between aspartic acid and glutamic acid on both gas-chromatography columns. In order to minimize the breakdown of the resin, it is recommended that the columns not be frozen. They should be eluted in the field, or transported back to the laboratory under refrigeration, and then eluted as soon as possible.

The concentrations of the dissolved free amino acids in the water samples from the northern California Coast Range generally are within or near the concentration range of the Kettleman North Dome oil-field brine samples. The major exception is the high concentration of proline in the Grizzly Spring sample and to a lesser amount in the spring in Murphy Canyon and the Wilbur oil test well. The rest of the amino acids in the Grizzly Spring sample are within the concentration range of the Kettleman North Dome samples. The spring in Murphy Canyon and the Wilbur oil test well contain concentrations of amino acids within and greater than the Kettleman North Dome concentration range, whereas Soda Bay Spring contains amino acids within and less than that range except for glycine and sarcosine. These differences are very small compared to the difference between proline in Grizzly Spring and Kettleman North Dome. Generally the Coast Range samples and the Kettleman North Dome samples are very similar. This work supports the proposal that Complexion Spring may be a sample of only slightly altered Jurassic or Cretaceous sea water (Barnes and others, 1972). Degens showed that there is no essential difference in the amino acid distribution between ancient brine waters of apparently marine origin and

TABLE 1.—*Dissolved free amino acid composition, in nanomoles per litre, of spring and well waters*

[The values for alanine through lysine are corrected for procedural blank and percentage recovery. The values for aspartic acid, glutamic acid, and sarcosine are corrected for procedural blank but not for percentage recovery. Township locations and county names are given in parentheses]

Amino acid	Skaggs Spring 1 (NE¼ sec. 25. T. 10 N.. R. 11 W., Sonoma)	Murphy oil test well (SE¼ sec. 22, T. 12 N., R. 3 W., Yolo)	Spring in Murphy Canyon (SW¼ sec. 23, T. 12 N., R. 3 W., Yolo)	Wilbur Springs (NW¼ sec. 28, T. 14 N., R. 5 W., Colusa)	Wilbur oil test well (NW¼ sec. 27, T. 14 N., R. 5 W., Colusa)	Complexion Spring (SW¼ sec. 3. T. 15 N., R. 6 W., Lake)	Soda Bay Spring (NE¼ sec. 6 T. 13 N., R. 8 W., Lake)	Grizzly Spring (SW¼ sec. 2, T. 13 N., R. 6 W., Lake)	Kettleman North Dome wells			
									61–33J (NE¼ sec. 33, T. 21 S., R. 17 E., Fresno)	K333–21Q (SE¼ sec. 21, T. 22 S., R. 18 E., Kings)	33–1P (NW¼ sec. 1, T. 22 S., R. 17 E., Kings)	323–21J (SW¼ sec. 21, T. 21 S., R. 17 E., Fresno)
Alanine	270	270	1,800	140	2,000	170	110	920	170	170	520	1,400
Valine	68	68	280	12	380	43	25	140	25	31	170	560
Glycine	1,200	1,000	1,600	1,600	4,500	4,300	6,800	1,600	1,400	1,900	790	4,100
Isoleucine	30	26	130	13	140	13	9	56	13	9	47	160
Leucine	30	27	150	18	180	15	10	66	15	13	75	250
Proline	32	32	260	21	220	51	21	2,500	29	36	55	51
Threonine	82	61	220	30	180	46	25	72	46	20	0	290
Serine	510	350	730	150	1,200	530	250	310	420	170	58	1,500
Phenylalanine	12	5	34	5	27	7	2	14	5	4	21	26
Ornithine	47	21	78	17	110	20	3	18	23	11	6	120
Lysine	10	4	40	7	33	19	2	13	7	3	0	48
Aspartic acid	14	15	67	7	77	9	4	18	12	3	5	33
Glutamic acid	6	8	97	5	32	9	2	42	2	1	21	48
Sarcosine	12	2	4	17	15	25	24	8	<1	3	2	12

present sea water (Degens and others, 1964). Work on the optical isomers of the amino acids might show if contamination had occurred; for example, from recent biological material such as plant and animal life in the spring, or from fingerprints on equipment. Amino acids formed by organisms are levorotatory. An ancient sample containing amino acids would be racemized from aging and contain equal parts of the dextrorotatory and levorotatory forms, whereas recent biological contamination would be entirely in the levorotatory form.

Other materials found in the amino acids fraction were small amounts of nonprotein amino acids (sarcosine, β-amino n-butyric acid, and others) and plasticizer impurities from laboratory contamination (di-n-butyl phthalate). The presence of the nonprotein amino acids is evidence for a chemical rather than a strictly biological degradation of the original proteins.

The separation scheme presented in figure 1 was used not only to concentrate and separate amino acids but also to partly characterize the other organic chelating agents which were concentrated by this technique. Other organic chelating agents were found in the nonvolatile acids, nonvolatile amines, and volatile neutrals fractions. The nonvolatile acids fraction contained many peaks in similar quantities to the amino acids fraction and are presumably dicarboxylic acids. Only one major peak was measured in the nonvolatile amines fraction and two major peaks were measured in the volatile neutrals fraction. The quantity of material in these two fractions was much less than that in the nonvolatile acids fraction. The other fractions contained very little material. It is recommended that further work be done to identify and measure the material in the nonvolatile acids fraction since it contains a large fraction of the total organic chelating agents.

The analyses of the gases which bubble up in the springs are given in table 2. Complexion Spring had no gas at the times of sampling. The presence of methane and ethane in the samples is evidence that there is degradation of organic matter with release of low molecular weight breakdown products. The carbon dioxide may come from the alteration of carbonate minerals (Barnes, 1970) or from the breakdown of organic matter or both. The oxygen plus argon and the nitrogen are probably air contamination.

The similar composition of free dissolved amino acids in the springs, test wells, and Kettleman North Dome brines, the presence of other dissolved organic chelating agents, and the presence of methane and ethane in the gases bubbling out of the springs and test wells are evidence of the degradation of organic matter with the release of low molecular weight products. This may be one mechanism for the transportation of organic matter from the source rocks to the reservoir rocks of an oil deposit.

TABLE 2.—*Composition, in volume percent, of gases from springs and wells*
[NA, not analyzed]

	O_2+Ar	N_2	CH_4	CO_2	C_2H_6	Date sampled
Skaggs Spring 1	2.8	11	25	62	0.16	10–27–71
	1.2	4.4	28	69	.25	*9–30–70
Skaggs Springs well	1.0	12	49	40	.04	10–27–71
	1.7	13	51	38	----	*9–30–70
Murphy oil test well	.4	4.2	95	.06	.03	5– 4–72
Spring in Murphy Canyon	.3	2.1	98	.1	----	5– 3–72
Wilbur Springs	.3	1.1	3.3	95	----	5– 4–72
	NA	NA	7	93	.001	**4–11–68
Wilbur oil test well	.3	1.3	94	.2	3.1	5– 4–72
Grizzly Spring	.3	1.1	1.6	98	----	9–11–74
	.3	.8	1.0	97	----	*12– 1–69
Soda Bay Spring	.9	2.7	.18	97	----	9–10–74
Kettleman North Dome:						
31–18Q	NA	NA	81	.5	9.4	4–26–72
324–35J	NA	NA	89	1.2	5.6	4–26–72
323–21J	NA	NA	89	1.2	6.0	4–27–72

* Barnes, Hinkle, and others (1973).
** Barnes, O'Neil, and others (1973).

REFERENCES CITED

Barnes, Ivan, 1970, Metamorphic waters from the Pacific tectonic belt of the west coast of the United States: Science, v. 168, p. 973–975.

Barnes, Ivan, Hinkle, M. E., Rapp, J. B., Heropoulos, Chris, and Vaughn, W. W., 1973, Chemical composition of naturally occurring fluids in relation to mercury deposits in part of North-Central California: U.S. Geol. Survey Bull. 1382–A, 19 p.

Barnes, Ivan, O'Neil, J. R., Rapp, J. B., and White, D. E., 1973, Silica-carbonate alteration of serpentine—Wall rock alteration in mercury deposits of the California Coast Ranges: Econ. Geology, v. 68, no. 3, p. 388–390.

Barnes, Ivan, Rapp, J. B., O'Neil, J. R., Sheppard, R. A., and Gude, A. J., III, 1972, Metamorphic assemblages and the direction of flow of metamorphic fluids in four instances of serpentinization: Contr. to Mineralogy and Petrology, v. 35, p. 263–276.

Clark, M. E., Jackson, G. A., and North, W. J., 1972, Dissolved free amino acids in southern California coastal waters: Limnology and Oceanography, v. 17, no. 5, p. 749–758.

Degens, E. T., Hunt, J. M., Reuter, J. H., and Reed, W. E., 1964, Data on the distribution of amino acids and oxygen isotopes in petroleum brine waters of various geologic ages: Sedimentology, v. 3, p. 199–225.

Gardner, W. S., and Lee, G. F., 1973, Gas chromatographic procedure to analyze amino acids in lake waters: Environmental Sci. and Technology, v. 7, no. 8, p. 719–724.

Kharaka, Y. K., and Berry, F. A. F., 1974, The influence of geological membranes on the geochemistry of subsurface waters from Miocene sediments at Kettleman North Dome in California: Water Resources Research, v. 10, no. 2, p. 313–327.

Roach, Don, and Gehrke, C. W., 1969, Direct esterification of the protein amino acids—Gas-liquid chromatography of N-TFA *n*-butyl esters: Jour. Chromatography, v. 44, p. 269–278.

Siegel, Alvin, and Degens, E. T., 1966, Concentration of dissolved amino acids from saline waters by ligand-exchange chromatography: Science, v. 151, p. 1098–1101.

Vol. 4, No. 2, Mar.–Apr. 1976, p. 233–240
Jour. Research U.S. Geol. Survey

SOLUTE TRANSPORT AND MODELING OF WATER QUALITY IN A SMALL STREAM

By S. M. ZAND, V. C. KENNEDY, G. W. ZELLWEGER, and R. J. AVANZINO, Menlo Park, Calif.

Abstract.—An injection of chloride, sodium, and stable strontium was made at a constant rate for 3 hours into Uvas Creek, Santa Clara County, Calif., to determine the mass transport processes in a small stream. Five observation points were selected within a 610-metre reach of the stream below the injection site. Water samples were collected at the observation points during and immediately after the injection. A mathematical model of the stream was obtained by solving analytically and optimally the one-dimensional mass transport equation of the solutes in the stream. Comparison of field results with a simplified mathematical model indicates the dominance of convection in the behavior of sodium and chloride. The concentration of chloride and sodium can be closely simulated by the model. However, strontium cannot be well represented by the simplified model, which contains a first-order decay-type sink.

The primary aim of this experiment was to answer the following questions: (1) Can differences in behavior between reacting and nonreacting species be detected? (2) is it possible to consider chloride as a truly conservative constituent; that is, one with zero source and sink terms? and (3) how well can one represent the result obtained, at least empirically, by means of a simple one-dimensional dispersion model which includes a linear sink?

A small hydrologically simple stream was sought for the initial investigation. Uvas Creek offered the most suitable condition of the numerous streams investigated. The drainage area of the creek above the study reach is about 9 km² and is forested mostly by second growth coast redwood (*Sequoia sempervirens*), madrone (*Arbutus menziesii*), big-leaf maple (*Acer macrophyllum*), and California laurel (*Umbellularia californica*). Annual rainfall in the area is normally 1,000 to 1,400 mm per year, occurring mostly between October and May. There are no housing developments in the watershed. Relief of the watershed is 840 m.

The experimental reach of 610 m on Uvas Creek is accessible by a foot trail along its banks and by a service road that approximately parallels the creek on higher ground. In downstream order, the experimental reach includes an injection point, an initial mixing reach about 15 m in length, and five observation stations (fig. 1). Complete lateral and vertical mixing was assumed within the initial mixing reach. The first two columns in table 1 give the station numbers and their distance from the injection point. The drop in stream elevation from the injection point to the lowermost station in the reach is 19.2 m through a series of pools and riffles. Stream width ranges from about 0.3 to 4 m and the streambed is composed largely of particles greater than 4 mm in diameter. Figures 2 to 5 show representative views of the stream reach. Calcium is the major cation in solution in Uvas Creek water.

EXPERIMENT

This research was done to investigate the processes controlling the mass transport of solutes in a small stream, Uvas Creek above Uvas Canyon County Park in Santa Clara County, Calif. (figs. 1–5). This report presents a mathematical model that was constructed to simulate a 3-h injection test on September 26, 1972, during the low-flow period near the end of the summer dry season.

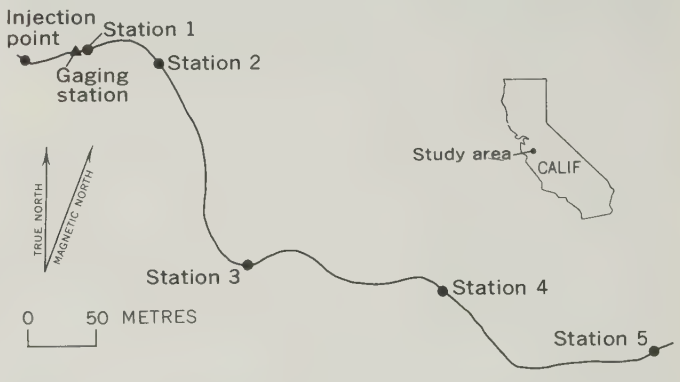

FIGURE 1.—Experimental reach, Uvas Creek, Santa Clara County, Calif.

FIGURE 2.—Aerial view of upper Uvas Creek.

FIGURE 3.—Uvas Creek below station 4.

The selection of injection materials for the Uvas Creek experiment was based on their effectiveness in isolating different transport phenomena, prevention of undue quality degradation, detectibility at low concentrations, ease of handling, and practical feasibility. For the initial experiment in September 1972, chloride, sodium, and stable strontium were selected as the injection materials. Chloride was expected to show the hydrodynamic properties of the experimental reach because of its slight sorption on bed sediments. Sodium and strontium were expected to represent, in addition

FIGURE 4.—Stream reach at station 5.

FIGURE 5.—Typical area of coarser sediments in the study reach.

to the hydrodynamics effect, the effect of differing sorption uptake and release by sediments (sinks and sources) in the reach. The injection materials, consisting of 1,068 g of chloride, 534 g of sodium, and 214 g of strontium, were in dissolved form and were held in a single large container during the 3-h injection. The gravity-fed injection apparatus consisted of a reservoir, tubing, a control valve, and a flowmeter. The rate of injection to the stream was constantly controlled manually through the valve during the injection test.

Sampling for chloride, sodium, and strontium at the different sampling stations began 15 min before the start of the injection and continued for 30 h after the 3-h injection ended. Information was gathered most frequently during the period of greatest change in concentration of injected material. Water samples were collected either manually in plastic bags or by automatic samplers using polycarbonate bottles. The sampling points were at the center points of stream constrictions where mixing was presumed complete.

The flow rate in the creek at the gaging station (fig. 1) was monitored every 15 min using a standard U.S. Geological Survey stream gage. The gage height showed some diurnal fluctuation. However, in the mathematical model of the experiment it was assumed that the discharge could be considered a constant value (0.0125 m^3/s) equal to the average daily flow rate and that there was no significant inflow to or outflow from the stream within the study reach. With these assumptions the percentage losses of chloride, sodium, and strontium were determined and are shown in table 1. A summation period of 15.5 h was used for reasons given later.

TABLE 1.—*Distance and percent recovery of injected material*

Station	Distance from the injection point (metres)	Weight recovered [1] (percent)		
		Chloride	Sodium	Strontium
1	38	100	100	95
2	105	99	97	91
3	281	87	85	64
4	433	82	77	44
5	619	65	53	19

[1] Based on average discharge of 0.0125 m^3/s and 15.5-h time duration.

MATHEMATICAL APPLICATIONS

Mathematical modeling of surface-water quality is in the initial stages of development. Significant examples of work in this area are the studies by Thomann, DiToro, and O'Connor (1974) in large streams, the work of Chen and Orlob (1972) in lakes and estuarine systems, and the studies of Gloyna, Yousef, and Padden (1971) in mass transport of biodegradable and nondegradable materials through a system of flowing and nonflowing research flumes. An informative assessment of estuarine modeling was prepared by Tracor, Inc. (1971), for the Environmental Protection Agency.

Successful mathematical modeling of water quality depends on the intricate relationship between conceptual modeling and complementary experimentation. As described by Weber, Kisiel, and Duckstein (1973), a major shortcoming in this interrelationship is data inadequacy, which may be broken down into insufficient sample size, measurement errors, missing observations, and proxy or secondary data or variables.

The dominant factors controlling the transport of solutes in stream systems can be divided into three groups: those that are primarily physical such as advective and dispersive flow, chemical reactions between dissolved constituents or between dissolved materials and inanimate stream solids, and reactions between dissolved solids and the stream biota. Advective mass transport is caused by the streamflow. Dispersion transport is caused by many factors, among which are turbulence effects and molecular diffusion. Chemical reactions can include sorptive exchange with the sediment and precipitation on or dissolution of the sediment. Biologic influences include the interaction of the solutes with biota living in the water or on the sediments. The contribution of the sediments and biota to the uptake or release of solutes is referred to in the overall mass transport model as sinks or sources of the solutes in the given body of water.

In mathematical modeling of surface-water quality there are two distinctly different approaches. One is the "black-box" type and the other is "structure-imitating." In black-box mathematical modeling the system of concern is isolated, as in a box, and significant variables of the system are assumed to be inputs and outputs of the box. In this type of analysis the internal workings of the system—that is, the processes in operation—are completely neglected. A model constructed using the black-box approach is purely empirical for a particular stream and may fit observed data quite well, yet it may be of little or no value for prediction outside its calibration range.

In the structure-imitating approach, an attempt is made to imitate the internal workings of a given system. To do so, physical laws are utilized to describe the conceptual relationships among significant variables of a system. A purely structure-imitating model may be quite capable of predicting the behavior of the modeled system or of similar systems and permit extrapolation beyond its calibrated range. However, to be complete, such a model must be as complex as the natural system it describes, and this is manifestly impossible.

Approaches commonly used are of the so-called gray type. That is, to a large degree, structure-imitating approaches are utilized in their initial formulation. However, at the parameter evaluation stage (determination of specific mathematical formulae) some degree of "blackness" is utilized. This final stage of black-boxing limits predictive capabilities. In general, the more the internal workings of a system are considered and imitated in mathematical modeling, the better the models can be used as predictive tools.

The approach used in this analysis is considered to be of the gray type. It imitates the convective and dispersive influences to a large degree in a structure-imitating fashion. However, the overall behavior of the sinks of chloride, sodium, and strontium are considered as falling into the first-order decay type; that is, the rate of release of a particular solute to the sinks is directly proportional to the concentration of that constituent in solution. This approach to the chemistry is virtually black box. With additional research, it is expected that more realistic versions of the forms of the sources and sinks of solutes in the given stream can be determined.

The law of conservation of mass, when applied to a stream system, results in the following set of partial differential equations:

$$\frac{\partial c_i}{\partial t}=E\frac{\partial^2 c_i}{\partial x^2}-v\frac{\partial c_i}{\partial x}+\sum_{j=1}^{N_i}S_{ij} \quad i=1,2,\ldots,M \quad (1)$$

when c_i is the concentration of the ith variable; t, time; E, the dispersion coefficient; x, distance; v, average velocity; and S_{ij} represents N_i number of sources or sinks for the ith variable. In the derivation of equation 1, average velocity, cross-sectional area, and the dispersion coefficient in the stream are assumed to be constants. The stream has also been assumed to have M significant variables.

When the sources and the sinks of different variables in a stream behave like chemical reactions with kinetics of the first order, equation 2 results, as follows:

$$\frac{\partial c_i}{\partial t}=E\frac{\partial^2 c_i}{\partial x^2}-v\frac{\partial c_i}{\partial x}+\sum_{j=1}^{M}k_{ij}c_j \quad i=1,2,\ldots,M \quad (2)$$

where k_{ij}, a first-order decay coefficient, represents the influence of jth variable on the ith one. If there are no significant interactions among different variables of a system, equation 2 simplifies to equation 3, as follows:

$$\frac{\partial c_i}{\partial t}=E\frac{\partial^2 c_i}{\partial x^2}-v\frac{\partial c_i}{\partial x}+k_i c_i \quad i=1,2,\ldots,M \quad (3)$$

where k_i represents the first-order decay associated with the ith variable.

The analytical solution of equation 3 for a continuous and constant injection rate of ω, at $x=0$, starting at $t=0$, when $c(\infty,t)=0$, for $t>0$ is obtained by a transformation of the form

$$c(x,t)=y(x,t)\ \exp\left[\frac{ux}{2E}-\left(\frac{u^2}{4E}+k\right)t\right]. \quad (4)$$

This transformation gives the canonical form of equation 3 that is the transient heat conduction equation, shown here as equation 5,

$$E\frac{\partial^2 y}{\partial x^2}=\frac{\partial y}{\partial t}. \quad (5)$$

Back substitution in the analytical solution of equation 5 gives equation 6 that is the analytical solution of equation 3, Ogata (1958).

$$c(x,t)=\frac{\omega}{2\gamma A\Omega}\exp\left(\frac{xv}{2E}\right)\left[\operatorname{erfc}\left(\frac{x+\Omega t}{4Et}\right)\exp\left(\frac{x\Omega}{2E}\right)-\operatorname{erfc}\left(\frac{x-\Omega t}{4Et}\right)\exp\left(-\frac{x\Omega}{2E}\right)\right] \quad (6)$$

where A is the cross-sectional area, $\Omega=v^2+4kE$, γ is the specific weight of the transporting fluid, and erfc is the complementary error function.

INTERPRETATION OF THE DATA

Thinner lines in figures 6, 7, and 8 show the measured concentrations of chloride, sodium, and strontium, respectively, at five observation stations during and shortly after the injection test of 1972. As stated before, the experiment was planned for the end of the rainless period of the year when a low and virtually constant flow was expected. However, the first significant rainfall of the season began approximately 15.5 h after the start of the tracer injection. This rain caused measurable changes in quality and quantity of stream water. Therefore, data obtained from monitoring of the stream after the rainfall could not be used to construct a die-away curve.

With the assumptions as described previously, equation 3 can be used to approximate the concentration distribution of the injected materials as they move downstream. The solution of equation 3 for a square wave injection pulse is equivalent to the summation of the solutions of two imaginary step inputs of the same height, one being a positive step and the other, its time-axis image. The negative step must lag the positive one by the time width of the square wave pulse.

The dispersion coefficient and the first-order decay are two parameters that must be evaluated for the stream and for the solutes. The dispersion coefficient, E, represents the overall hydrodynamic properties of the stream system. The first-order decay coefficient, k,

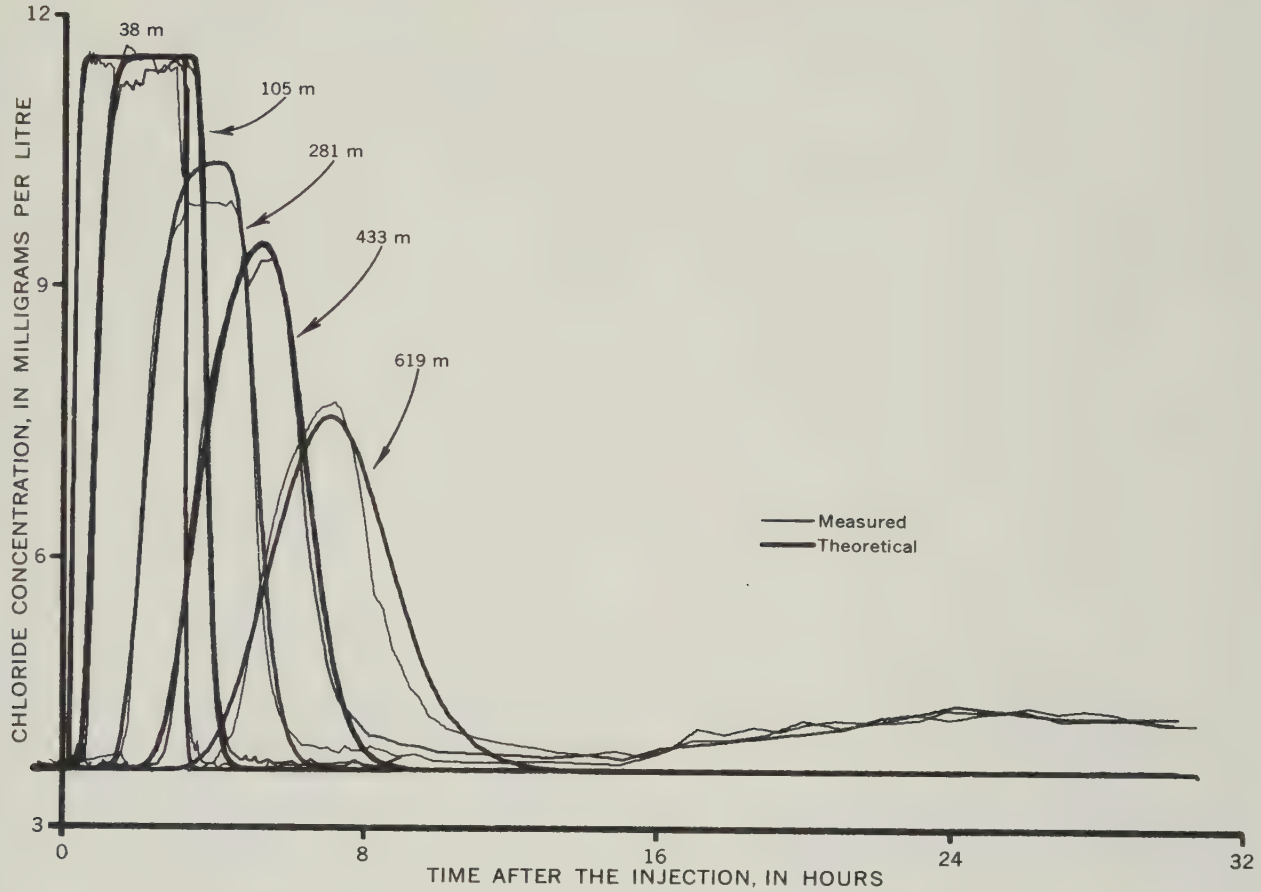

FIGURE 6.—Measured and theoretical concentration of chloride in Uvas Creek on September 26–27, 1972. Measurements in metres are distances from the injection point.

represents the nonhydrodynamic mass transport behavior of the solutes in the stream.

The dispersion coefficient accumulates the effects of many approximations and phenomena. Among its significant contributing components in a one-dimensional approximation of streamflow are the dispersion caused by averaging processes of different variables of the system, turbulent mixing and molecular diffusion. Keefer and McQuivey (1974) examined the relation between turbulent diffusion, dispersion, and the statistical properties of turbulence in an open channel flow, and McQuivey and Keefer (1974) developed a method for predicting longitudinal dispersion coefficients from mean flow parameters. Fischer (1968) utilized a routing method to evaluate the overall dispersion coefficient.

In contrast to published data on the dispersion coefficient, information about decay-type phenomena in stream-water chemistry and biology is relatively poor. This may be attributed to the complex multidimensional nature of the problem. That is, even if we assume that the decay of a substance in a given environment is linearly proportional to its concentration, the value of the decay coefficient is unique for the given substance in its specific environment.

If enough time had been allowed for observation, most of the chloride injected would have returned to the stream, assuming that the stream was not losing an appreciable fraction of flow to the ground water within the study reach. During the experiment it was assumed that the temporary overall loss of chloride from the stream was behaving like a chemical reaction with kinetics of the first order. This assumption permitted the use of the analytical solution for determining the optimum values of parameters E and k.

The following simple optimization routine was utilized to evaluate E and k. Initially, for a constant velocity, arbitrary values were selected for the dispersion and the first-order decay coefficients. With the assumed arbitrary values of E and k, using the analytical solution, the starting theoretical concentration of chloride at different stations was determined. The comparison of the theoretical and the measured concentration according to a given criterion yielded the

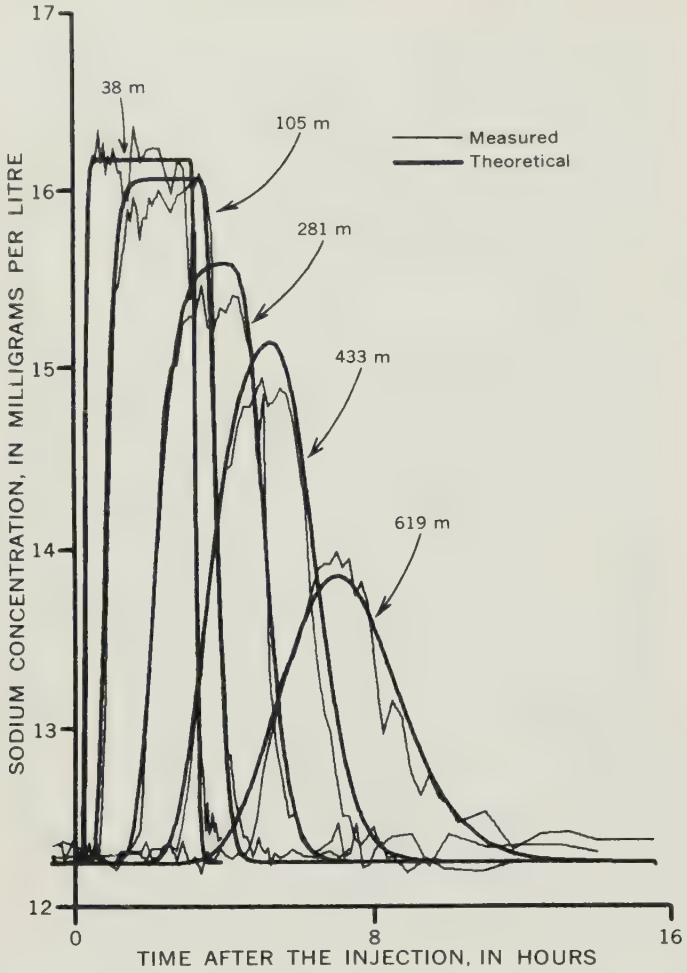

FIGURE 7.—Measured and theoretical concentration of sodium in Uvas Creek on September 26–27, 1972. Measurements in metres are distances from the injection point.

local optimum values of the two parameters. Two criteria were chosen for the optimization, one being the root mean square error of estimate, ERR, equation 7, and the second the percent weight loss, W, equation 8.

$$\mathrm{ERR}=\sum_{i=1}^{N}(C_i-CT_i)^2 \Big/ \sum_{i=1}^{N}(C_i)^2 \qquad (7)$$

where ERR is the root mean square error of estimate, C is the measured concentration, CT is the theoretical concentration, i is the ith value, and N is the number of measured concentrations.

$$W=\left|\frac{M-w}{M}\right|\times 100 \qquad (8)$$

where W is the percent weight loss, M is the total measured weight of the solute passing a given station, and w is the total theoretical weight of the solute passing a given station, or

$$w=\sum_{i=1}^{N} q_i C_i \Delta t, \qquad (9)$$

where q is the flow rate and Δt is the time increment. The outcome of many computer runs utilizing the two optimization criteria indicated similar results.

The mathematical model of the stream is very sensitive to velocity variations. The average velocity from the injection point to each station was adjusted using another simple trial and error optimization procedure. The optimum values for E and k in each cycle were evaluated as mentioned in the preceding paragraph. The starting velocity was the one associated with movement of the center of gravity of the chloride time-concentration curves (figs. 6, 7, and 8). Using the optimum E and k, the velocity was changed until the improvement in the goodness of fit was not significant.

Table 2 shows the average velocity, the optimum values of E, k, root mean square error of estimate (eq 7) and percent weight loss (eq 8) at different stations. Figure 6 shows the plots of measured and theoretical concentration of chloride using the optimum evaluated coefficients at the five stations.

The dispersion coefficient of chloride, as evaluated above, was used for constructing the theoretical models of sodium and strontium. Again, the assumption was made that the sinks for sodium and strontium behaved as chemical reactions with kinetics of the first order. An optimization similar to the one used for chloride was utilized to evaluate the best first-order decay coefficient for sodium and strontium. Table 2 shows the parameters that were evaluated in models of the three solutes. Figures 7 and 8 show the measured and the theoretical concentration of sodium and strontium, respectively, at the five stations.

TABLE 2.—*Velocity, dispersion coefficient, first-order decay coefficient, and associated errors for chloride, sodium, and strontium at five stations*

Station	1	2	3	4	5
Velocity (v) ---m/s--	0.066	0.040	0.037	0.034	0.030
Dispersion coefficient (E) ---m^2/s--	.16	.18	.25	.31	.49
Chloride					
First-order decay coefficient (k) ---$10^5/s$--	0	0	2	2	2
Error (eq 7) ---percent--	6.83	4.10	4.64	3.85	6.05
Error (eq 8) ---percent--	.08	1.01	2.19	6.02	.34
Sodium					
First-order decay coefficient (k) ---$10^5/s$--	0	1	2	2	3
Error (eq 7) ---percent--	2.20	1.47	1.34	1.33	1.09
Error (eq 8) ---percent--	.03	.44	3.21	4.18	3.68
Strontium					
First-order decay coefficient (k) ---$10^5/s$--	8	3	6	6	8
Error (eq 7) ---percent--	14.05	14.51	25.40	29.55	40.71
Error (eq 8) ---percent--	.02	.14	.01	.03	.12

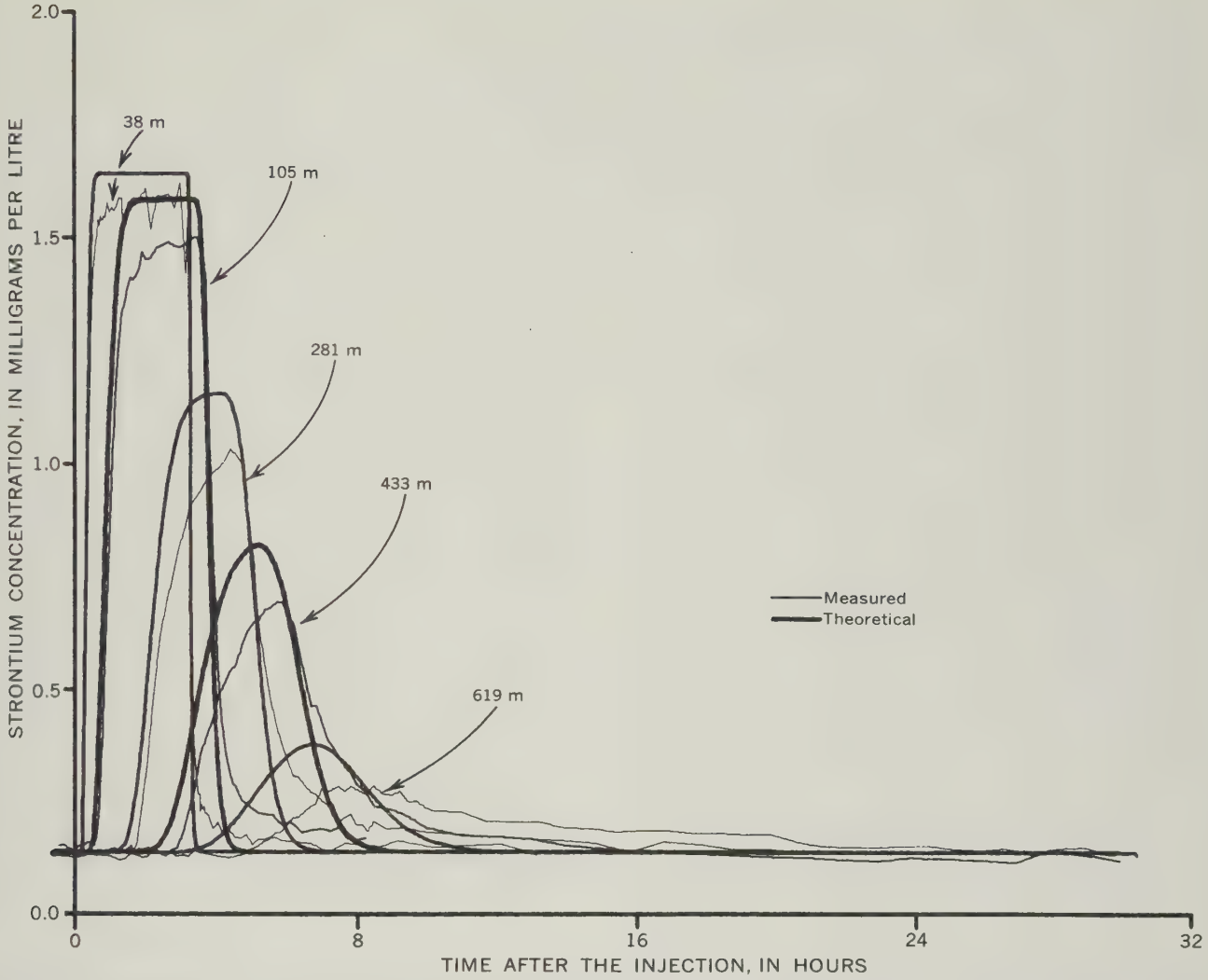

FIGURE 8.—Measured and theoretical concentration of strontium in Uvas Creek on September 26–27, 1972. Measurements in metres are distances from the injection point.

SUMMARY AND CONCLUSION

An injection of chloride, sodium, and stable strontium was made at a constant rate for 3 h to determine the mass transport processes in Uvas Creek, Santa Clara County, Calif., September 26 to 27, 1972. The primary aim of the experiment was to answer the following questions: (1) Can differences in behavior between reacting and nonreacting species be detected? (2) is it possible to consider chloride as truly conservative constituent; that is, one with zero sink terms? and (3) how well can one represent the result obtained, at least empirically, by means of a very simple one-dimensional dispersion model which includes a linear sink of the type $S=kc$?

An analytical solution to the partial differential equation describing the chemical-quality changes in Uvas Creek during tracer addition was made possible by considering the creek as a simplified one-dimensional system. Associated assumptions involved averaging of velocity, concentration, and cross-sectional area in time and space and the use of first-order decay in describing the reaction between the sinks and the solutes in the stream. At the time of the preliminary experiment, knowledge of the stream characteristics was limited, so that these simplified assumptions were required. The experience with the one-dimensional model of the stream indicates its high sensitivity to the variation of stream velocity. This sensitivity causes significant effects on the structure, formulation, and verification of the sink submodels of the solutes in the stream.

The difference between reacting and nonreacting chemical species in the stream is demonstrated by the observations presented in figures 6, 7, and 8. The first significant rainfall of the season prevented determina-

tion of the conservation of chloride during the experiment. However, a later experiment indicated that, if enough time is allowed, the major portion of chloride returns to the stream.

Optimization of the dispersion coefficient and the first-order decay coefficient indicated that the simplified Uvas Creek mathematical model could reasonably well simulate the behavior of chloride and sodium. However, the strontium concentration could not be reproduced as closely as the other two solutes. Neither sodium nor chloride are strongly adsorbed by sediments under the conditions present in Uvas Creek. However, strontium would be expected to compete well with calcium, the major cation in Uvas Creek, for exchange sites on the sediments. Thus, chloride shows little or no reaction with the sediment and is virtually a conservative constituent, whereas sodium is very slightly adsorbed and strontium is rather strongly adsorbed. The "losses" of sodium and strontium relative to chloride observed in the stream study reach during 15.5 h of sampling correlate well with increased adsorption capability.

The simplified mathematical model as described in this report was a useful tool to give a generalized understanding of the behavior of the solutes in the stream during the experiment. The model was not adequate to describe the mass transport of solutes in a structure-imitating fashion. As more data become available, the sources and the sinks of solutes will be examined in detail.

REFERENCES CITED

Chen, C. W., and Orlob, G. T., 1972, Ecologic simulation: Walnut Creek, Calif., Water Resources Engineers, Inc., final rept., 157 p.

Fischer, H. B., 1968, Dispersion predictions in natural streams: Am. Soc. Civil Engineers, Jour. Sanitary Engineering Div., v. 94, no. SA5, Proc. Paper 6169, p. 927–943.

Gloyna, E. F., Yousef, Y. A., and Padden, T. J., 1971, Transport of organic and inorganic materials in small-scale ecosystems, *in* Hem, J. D., ed., Nonequilibrium systems in natural water chemistry: Washington, Am. Chem. Soc., p. 181–193.

Keefer, T. N., and McQuivey, R. S., 1974, Investigation of diffusion in open-channel flows: Jour. Research U.S. Geol. Survey, v. 2, no. 4, p. 501–509.

Ogata, Akio, 1958, Dispersion in porous media: Evanston, Ill., Northwestern Univ., Ph. D. dissert., 121 p.

McQuivey, R. S., and Keefer, T. N., 1974, Simple method for predicting dispersion in streams: Am. Soc. Civil Engineers Proc., Jour. Environmental Eng. Div., v. 100, no. EE4, paper 10708, p. 997–1011.

Thomann, R. V., DiToro, D. M., and O'Connor, D. J., 1974, Preliminary model of Potomac estuary phytoplankton: Am. Soc. Civil Engineers Proc., Jour. Environmental Eng. Div., v. 100, no. EE3, paper 10576, p. 699–715.

Tracor, Inc., 1971, Estuarine modeling: an assessment: Water Pollution Control Research Series 16070DZV, 497 p.

Weber, J. E., Kisiel, C. C., and Duckstein, Lucien, 1973, On the mismatch between data and models of hydrologic and water resources systems: Am. Water Resources Assoc., Water Resources Bull., v. 9, no. 6, p. 1075–1088.

Jour. Research U.S. Geol. Survey
Vol. 4, No. 2, Mar.–Apr. 1976, p. 241–245

THE MEASUREMENT OF ADENOSINE TRIPHOSPHATE IN PURE ALGAL CULTURES AND NATURAL AQUATIC SAMPLES

By W. THOMAS SHOAF and BRUCE W. LIUM, Doraville, Ga.

Abstract.—Three methods for the extraction of adenosine triphosphate (ATP)—neutral dimethyl sulfoxide (DMSO), boiling tris buffer, and butanol-octanol extraction—were equally effective on the alga *Chlorella vulgaris*. Dilution of extracted ATP samples was linear. Filtration of different volumes of samples resulted in proportional values for ATP in the extracts. Measurement of activity by either peak height or integration of the area under the peak were equally sensitive and reproducible. The assay of ATP sample was inhibited by mercuric chloride > cadmium chloride > calcium chloride > potassium or sodium phosphate, and by high concentrations of the extractant DMSO. Analysis of ATP in aquatic environments led to the problem of transferring a sample from the field to the laboratory without obtaining a change in ATP concentration. Membrane filtration of the sample followed by chilling at 4°C, slow freezing at −20°C, or freezing on dry ice were ineffective in maintaining a constant level of ATP. Chilling caused a marked increase in ATP, whereas slow freezing caused a significant loss of ATP. Freezing on dry ice was variable but generally resulted in large losses of ATP. Quick freezing by immersion of filter and algae in liquid nitrogen and storage on dry ice maintained a constant ATP level. Field extraction of the ATP followed by quick freezing in an acetone–dry-ice bath maintained the ATP in a convenient and stable form.

An estimate of the quantity of living micro-organisms (biomass) in an aquatic environment can be a useful tool to assess water quality. Both phytoplankton and microzooplankton biomass can be estimated by direct microscopic determination of volume and number. Other micro-organisms (for example, bacteria) have been estimated by various plating techniques (colony counting) and extinction-dilution techniques. The techniques are often time consuming, expensive, and subject to inherent sources of error. Some of the major problems include the following: Direct microscopic counting of bacteria may yield higher estimates because of the difficulty in distinguishing bacteria from bacteria-sized inert particles. There is also the inability to differentiate between viable and nonviable cells, and the problems of cell aggregation, for bacteria and algae. Low estimates may be produced by plating and extinction techniques which are selective because of the chemical composition of the media and inherent physical parameters such as temperature and pressure. The extinction-dilution technique may also be biologically selective in that only types capable of growth in specialized media will grow to measureable size.

For a total biomass determination, it would be desirable to measure some biochemical that is present in all living cells but is not associated with nonliving particulate material. This cellular constituent must have a short survival time after death, so that it would be specific for viable biomass. It must likewise be present proportional to some measure of the total biomass for all microorganisms—algae, bacteria, fungi, and protozoans. Sensitive and accurate methods for its detection should be available.

The biochemical which seems to meet these requirements best is adenosine triphosphate (ATP). ATP is the primary energy donor in cellular life processes. Its central role and biological and chemical stability make it an excellent indicator of the presence of living material. The level of endogenous ATP, which is the amount of ATP per unit biomass in bacteria (Allen, 1973), algae (Holm-Hansen, 1970), and zooplankton (Holm-Hansen, 1973), is relatively constant when compared to the cellular organic carbon content in several species and throughout all phases of the growth cycle. In studies where cell viability was determined (Hamilton and Holm-Hansen, 1967; Dawes and Large, 1970), the concentration of ATP per viable cell remained relatively constant during periods of starvation. The quantity of ATP, therefore, can be used to estimate total living biomass.

This report compares instrumentation for measurement of ATP and procedures for extraction from living cells in natural aquatic samples. It describes changes that may occur in the ATP concentration of a natural sample from the time it is removed from its natural environment until the time it is assayed in the laboratory, and how to prevent this change. Compounds that interfere with the assay are also described.

MATERIALS AND METHODS

Water.—Fresh glass-distilled water was used for the preparation of all reagents. The water was assayed for ATP activity before being used as a reagent. Deionized and older unautoclaved distilled water frequently contained significant and variable amounts of ATP and were not suitable.

Buffer preparation.—Morpholinopropane sulfonic (MOPS) acid buffer (sodium salt), 0.01 *M*, at pH 7.4, was prepared with freshly distilled water, autoclaved, and capped until used.

ATP standards.—ATP was prepared at a concentration of 0.1 μg/ml in 0.5 mmol/l (ethylenedinitrilo) tetraacetic acid disodium salt (Na_2EDTA), 5 mmol/l $MgSO_4$, and 5 mmol/l Tris-Cl at pH 7.7 using freshly distilled water. One half millilitre was placed in 6×49 mm glass vials, capped, and quick frozen in an acetone–dry-ice bath. The standards were then maintained at −20°C until used. A vial was thawed once and then discarded after use.

Algae.—Chlorella vulgaris was obtained from Dr. John Heiss, Georgia Institute of Technology, and grown on the medium used for the provisional algal assay procedure (Bartsch, 1971).

Extraction procedure.—A modification of the neutral dimethyl sulfoxide (DMSO) procedure described in the E. I. Dupont De Nemours & Co. (1974) luminescence biometer manual was utilized throughout, except where compared to the boiling tris-buffer method and the butanol-octanol method. The neutral DMSO procedure utilizes the Dupont filter stand and self-supporting membrane filters (13-mm diameter, 0.45-μm pore size). The filter assembly is placed in the stand and rinsed with 1 ml of 0.01 *M* MOPS, pH 7.4. A volume of sample is placed on the filter and filtered. The cells are then immediately rinsed with 1 ml of 0.01 *M* MOPS, pH 7.4. Adhering droplets are shaken from the bottom of the filter assembly. A clean graduated tube is placed in the filter stand to collect the extract. A 0.2 ml mixture of 90 percent DMSO and 10 percent 0.01 *M* MOPS, pH 7.4, is added to the filter assembly so that all cells are covered. After 20 s, the vacuum is applied and the sample is filtered "dry." One millilitre of 0.01 *M* MOPS, pH 7.4, is added to the filter assembly. After 10 s the vacuum is applied and the sample is filtered dry. One millilitre of 0.01 *M* MOPS, pH 7.4, is again added to the filter assembly. After 10 s the vacuum is applied and the sample is filtered dry. The final volume, approximately 2.2 ml, is recorded and used in the calculations for initial concentration. The sample is mixed well and assayed.

The boiling tris-buffer and butanol-octanol methods were tested without filtration. The boiling tris method consisted of pipeting a volume of sample (usually 100 μl) into 5.9 ml of boiling 0.05 *M* Tris-Cl, pH 7.7, in a 15-ml graduated tube. After 2 min the sample is cooled, volume adjusted to 6 ml, and mixed. The sample is then assayed. The method was modified from that described by Hamilton and Holm-Hansen (1967). The butanol-octanol extraction method is as described in the Dupont instruction manual.

Analysis.—Very sensitive methods of ATP analysis have been developed from McElroy's (1947) finding that luminescence in fireflies has an absolute requirement for ATP. ATP is determined by measuring the amount of light produced when ATP reacts with reduced luciferin (LH_2) and O_2 in the presence of firefly luciferase and magnesium, producing adenosine monophosphate (AMP), inorganic pyrophosphate (PPi), oxidized luciferin (L), H_2O, CO_2, and light (hv), by the following reaction:

$$ATP + O_2 + LH_2 \xrightarrow[Mg^{+2}]{\text{luciferase}} AMP + PPi + L + H_2O + CO_2 + hv.$$

The bioluminescent reaction is specific for ATP and the reaction rate is proportional to the ATP concentration with 1 photon of light emitted for each molecule of ATP hydrolyzed. When ATP is introduced to suitably buffered enzyme and substrates, a light flash follows which decays in an exponential fashion (fig. 1). Either the peak height of the light flash or integration of the area under the decay curve can be used to form standard curves.

Enzyme-substrate mixture.—The mixture contains 100 Dupont units of purified luciferase, 0.71 mmol/l luciferin, 10 mmol/l magnesium sulfate, and 10 mmol/l morpholinopropane sulfonic acid, at pH 7.4, in a volume of 100 μl. This solution was stable at room temperature (22°–24°C) for at least 4 h, and could be used for longer periods, even the next day if ATP standards were reanalyzed. The enzyme-substrate solution was not used for ATP analysis until at least 15 min after it was dissolved, as the background luminescence decreased rapidly during this period. Unless otherwise stated, a 10-μl aliquot of sample containing the ATP was injected into the standard 100-μl volume of enzyme substrate in a cuvette (50-mm length by 5-mm ID). The injector was a Hamilton (Model 705–N) 50-μl syringe equipped with a Shandon Reprojector (Model SAA1350) to aid in achieving a rapid and reproducible delivery rate.

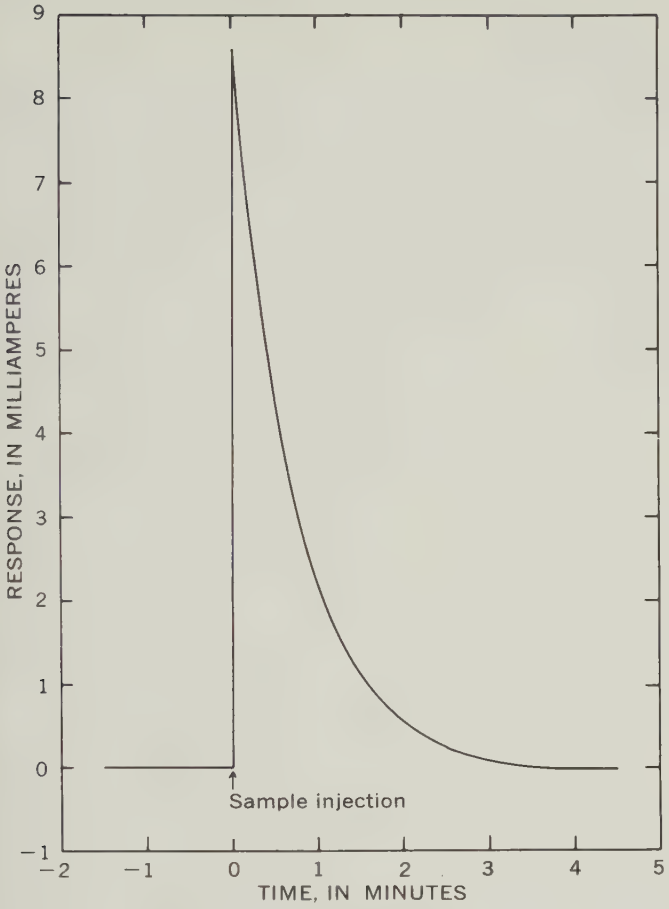

FIGURE 1.—Light-emission curve when a sample containing ATP is injected into the luciferin-luciferase mixture.

RESULTS AND DISCUSSIONS

Comparison of instruments.—The Luminescence Biometer, Model 760 (Dupont Instrument Co.), is specifically designed to measure the peak height of the luminescent reaction. It provides five decades of range with automatic range selection. A signal to the photomultiplier tube is amplified and utilized to charge a memory capacitor. The signal is presented 3 s after the onset of light emission on a digital display that gives the concentration of ATP directly.

The ATP photometer, Model 2000 (JRB, Inc.) is designed to measure either the peak height of emitted light or integrate a part of the area under the reaction curve. The integral mode measures the area under the curve for a 60-s period after a 15-s delay. The peak height mode measures the light emitted during the first 6 s of the reaction. The instrument provides six decades of range with automatic range selection. The amplified signal is presented on a digital display as counts per minute, a value proportional to the ATP concentration.

The Chem-Glow photometer, Model J4–7441, and integrator-timer, Model J4–7462 (American Instrument Co.), can measure peak height or integrate area under the response curve. Four decades of range selection are provided. The range selection is manual for peak height measurements, and if the range selected is inappropriate, the reaction must be repeated after changing the range. The integrator-timer will integrate the area under the curve for 1, 3, 5, 10, 20, 30, or 60 s and has more than three decades of automatic range change.

All three instruments could detect amounts of ATP as low as 10^{-15} mol (5×10^{-13} g). Reproducibility with all three instruments was very good. The peak height measurements were more dependent on a uniform rate of delivery and mixing of ATP in the luciferin-luciferase solution. The instruments produced linear responses from approximately 10^{-12} to 10^{-15} mol of ATP. A representative standard curve using the ATP photometer is seen in figure 2. The slope of this curve was approximately 1, whereas the absolute value obtained varied from one enzyme preparation to the next.

ATP extracts.—Three extraction procedures were tested: Neutral dimethyl sulfoxide (DMSO), boiling tris buffer, and butanol-octanol extraction. These methods and the algae used are described in detail in the "Materials and Methods" section. The boiling tris-buffer and butanol-octanol methods were used to test

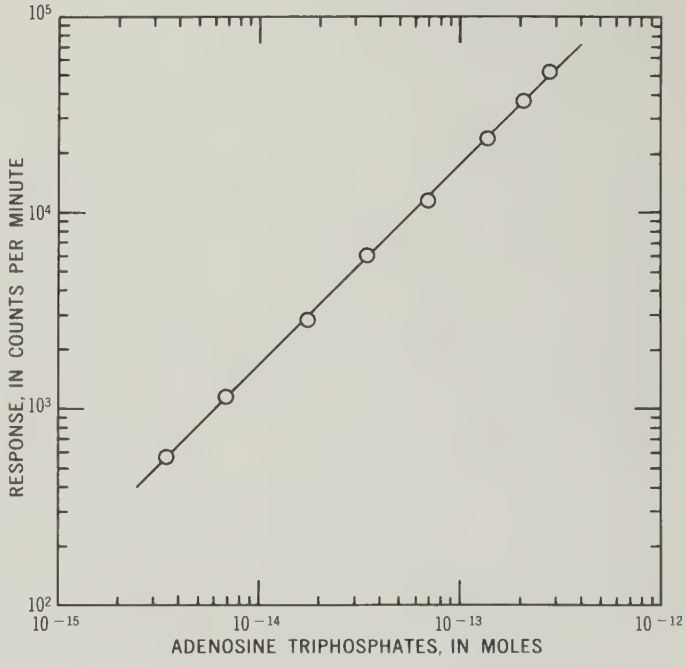

FIGURE 2.—ATP standard curve. Counts per minute were determined by a 1-min integration using the ATP photometer. ATP was assayed in the liquid scintillation vials provided with the instrument. The assay mixture contained 100 μl of the luciferin-luciferase mixture and varying amounts of ATP. The total volume was 500 μl.

ATP extraction, without concentration of the algae. Both methods produced the same amounts of ATP. The neutral-DMSO method was tested with and without concentration of algae (by membrane filtration). In both procedures the total amount of ATP was the same and this value was identical to those obtained by the other two methods, boiling tris-buffer and butanol-octanol extraction. Attempts to reextract ATP from the samples filtered for neutral-DMSO extraction indicated that no significant extractable ATP remained. The fact that all three methods yield the same ATP content and that no additional ATP is extractable indicated that all the soluble ATP is being extracted. These procedures work well for a number of algae and bacteria, but one extractant may not be suitable for all organisms.

The neutral-DMSO extraction method was more rapid and convenient and was used for the experiments described in this report. The method eliminates the use of a boiling apparatus in the field, which may not only be difficult to maintain, but whose boiling temperature (and thus extraction efficiency) would vary with altitude. The neutral-DMSO method also eliminates the possible problem of heat-gradient formation (and thus lower recovery of ATP) when the amount of filtered biomass placed in the boiling tris buffer is large. The neutral-DMSO method does not require a centrifuge as does the butanol-octanol method.

Linearity with dilution and volume filtered.—Several laboratory cultures of algae and the biomass of natural water samples were examined to determine the reliability of diluting an extracted ATP sample, and of filtering different volumes of a water sample. The ATP concentration found in diluted extracts was proportional to the dilution factor, and the final values of ATP per unit volume of algal culture were consistent. Results of an experiment of this type using *Chlorella vulgaris* given in table 1 show linearity over a dilution range that is 100 fold. The dilution solution was 0.01 *M* MOPS buffer, pH 7.4, and was free of ATP.

Aliquots of decreasing size of a natural water sample or laboratory culture gave proportionally decreasing values for ATP in their extracts. Results of an experiment using *Chlorella vulgaris* are given in table 2. The range of volumes filtered is 100 fold. This consistency and linearity with dilution of extract and variation of volume filtered should be useful when performing routine analyses of ATP.

Inhibitors of the ATP assay.—The neutral- DMSO extractant inhibits the luciferase enzyme (table 3) by about 25 percent. This inhibition may be eliminated by a 10-fold dilution of the neutral-DMSO extractant with low-response distilled water before analyzing for ATP content.

Several metal salts also inhibit the enzymatic determination of ATP (table 4). This inhibition can usually be eliminated, however, by washing the filtrate with 0.01 *M MOPS* buffer immediately after completing filtration. Although high concentrations of most salts will inhibit the reaction, a few were very potent inhibitors. Mercuric ion was the most potent, reducing the amount of ATP measured to 28 percent of the correct amount (table 4) at a concentration of 8.3 μmol/l mercuric

TABLE 1.—*Effect of dilution of extracted ATP*

Dilution	Micrograms of ATP per litre	
	Observed	Predicted (from undiluted)
None	141.0	141.0
1/2	70.5	70.5
1/4	34.5	35.3
1/10	13.9	14.1
1/20	6.0	7.1
1/100	1.4	1.4

TABLE 2.—*Effect of filtering various sample volumes*

Volume filtered (μl)	Micrograms of ATP per litre	
	Observed	Predicted (from initial volume)
2,500	125.0	125.0
1,000	51.5	50.0
250	12.4	12.5
100	5.2	5.0
25	1.3	1.3

TABLE 3.—*Effect of the neutral dimethyl sulfoxide (DMSO) extractant on the luciferin-luciferase reaction*

Dilution of extractant	Response (percent)	Dilution of extractant	Response (percent)
None added[1]	100	1/3	91
1/10	102	1/2	89
1/8	96	Undiluted	75
1/6	95		

[1] 10 μl of low-response water without DMSO.

NOTE:—The standard volume and concentration of luciferin-luciferase was used. Then 10 μl of low-response water or the appropriate dilution of 90 percent neutral DMSO was injected into the luciferin-luciferase solution and mixed. Samples were immediately assayed by injection of 10 μl of 0.1 μg ATP per millilitre. The Dupont luminescence biometer was used to measure peak height response.

TABLE 4.—*Inhibition of the ATP assay*

Compound	Final concentration in assay cuvette	Activity (percent)
Distilled water	---	100
Mercuric chloride	8.3 μmol/l	28
Cadmium chloride	0.42 mmol/l	38
Calcium chloride	4.2 mmol/l	63
Potassium phosphate (pH 7.4)	21 mmol/l	33
Sodium phosphate (pH 7.4)	21 mmol/l	41

NOTE.—The standard volume and concentration of luciferin-luciferase was used. Then 10 μl of low-response water or the appropriate inhibitor was added and mixed. Samples were then immediately assayed by addition of 10 μl of 0.1 μg ATP per millilitre.

chloride. Of those tested, cadmium was the next most potent, followed by calcium, and sodium and potassium phosphate.

Stability of sample.—The stability of the sample from the time it is collected to the time it is assayed is critical when measuring ATP in natural aquatic environments. The ATP content of a laboratory culture *Chlorella vulgaris* (grown on the media described in Materials and Methods) is stable for at least 2 h when removed from an environmental chamber at 24°C and 4,300 lm/m² (lumens per square metre) of cool, white fluorescent light and placed at room temperature (24°C) under less intense light of approximately 1,000 lm/m². However, natural aquatic samples when removed from their natural environment, even if maintained in dim light and with no significant change in temperature, may not maintain a constant level of ATP. This can result from the sample containing a significant population of growing bacteria, protozoans, fungi, or heterotrophically growing algae. Thus the ATP content of natural aquatic samples must be either determined immediately or properly preserved.

Placing a liquid culture of *Chlorella vulgaris* in the dark at ice-water temperature, such as might be required for shipment to a laboratory, resulted in a marked loss of ATP. As a possible alternative, the stability of membrane-filtered samples was examined. Algae filtered on 0.45-μm membrane filters and placed in a refrigerator (dark) at 4°C did not maintain a constant ATP level. The ATP increased (fig. 3) so that after 94 h, approximately 1.9-fold more ATP was present than when initially filtered. A similar effect has been reported in leaves of *Chenopodium rubrum* and *Phaseolus vulgaris* (Jones, 1970). The next approach was to freeze the filtered samples by placing the filter in a freezer at −12°C. The ATP level dropped rapidly and by the end of a 94-h period only about 14 percent of the ATP remained (fig. 3). Attempts to freeze the filtered algae on dry ice and store in the freezer at −12°C resulted in even a more rapid loss of ATP (fig. 3). The ATP content of filtered algae could be kept stable if the filter and algae were dipped into liquid nitrogen (<−196°C) immediately after filtration, and then transferred to and maintained on solid carbon dioxide (<−78°C). This procedure, although convenient and effective in the laboratory, would be less desirable as a field procedure. Because the ATP extracted from the algae was stable when frozen at freezer temperatures (−10 to —20°C), the best approach to insure that one obtains an accurate measure of ATP is to extract the ATP from the sample in the field (as described in "Materials and Methods"). The extracted ATP can then be quick frozen by immersion of a tube of ATP extract into an acetone–dry-ice bath and then maintained in a frozen state.

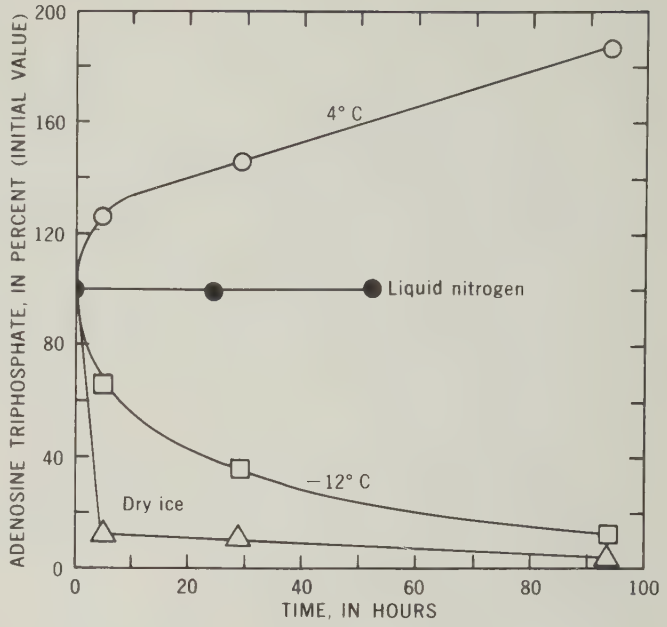

FIGURE 3.—ATP concentration in *Chlorella vulgaris* as a function of time after filtration. A liquid culture of *Chlorella vulgaris* was filtered and the ATP extracted using the neutral-DMSO technique as described in "Materials and Methods."

REFERENCES CITED

Allen, P. D., 1973, Development of the luminescence biometer for microbial detection: Devel. Indust. Microbiology, v. 14, p. 67–73.

Bartsch, A. F., 1971, Algal assay procedure—bottle test: Corvallis, Oreg., U.S. Environmental Protection Agency, 82 p.

Dawes, E. A. and Large, P. J., 1970. Effect of starvation on the viability and cellular constituents of *Zymomonas anaerobia* and *Zymomonas mobilis*: Jour. Gen. Microbiology, v. 60, p. 31–40.

E. I. DuPont De Nemours Co. (Inc.), 1974, Instruction manual —760 luminescence biometer: Wilmington, Del., E. I. DuPont De Nemours & Co. (Inc.), 22 p.

Hamilton, R. D., and Holm-Hansen, O., 1967, Adenosine triphosphate content of marine bacteria: Limnology and Oceanography, v. 12, p. 319–324.

Holm-Hansen, O., 1970, ATP levels in algal cells as influenced by environmental conditions: Plant Cell Physiology, v. 11, p. 689–700.

——— 1973, Determination of total microbial biomass by measurement of adenosine triphosphate, *in* Stevenson, L. H., and Colwell, R. R., eds, Estuarine Microbial Ecology: Columbia, S.C., Univ. South Carolina Press, p. 73–89.

Jones, P. C. T., 1970, The effect of light, temperature, and anaesthetics on ATP levels in the leaves of *Chenopodium rubrum* and *Phaseolus vulgaris*: Jour. Experimental Botany, v. 21, p. 58–63.

McElroy, W. D., 1947, The energy source for bioluminescence in an isolated system: Natl. Acad. Sci. Proc., v. 33, p. 342–346.

Jour. Research U.S. Geol. Survey
Vol. 4, No. 2, Mar.–Apr. 1976, p. 247–251

DETERMINATION, STORAGE, AND PRESERVATION OF LOW MOLECULAR WEIGHT HYDROCARBON GASES IN AQUEOUS SOLUTION

By D. J. SHULTZ, J. F. PANKOW,[1] D. Y. TAI,[1] D. W. STEPHENS,
and R. E. RATHBUN, Bay Saint Louis, Miss.

Abstract.—A gas chromatograph with a flame ionization detector was used in conjunction with a stripping chamber and cold trap apparatus to measure microgram-per-litre quantities of low molecular weight hydrocarbon gases in water samples. Glass bottles with ground-glass stoppers were used to store the samples. Formalin was added to stop bacterial activity and preserve samples with no measurable losses for as much as 7 days.

The development by Tsivoglou and others (1965, 1968) of a tracer technique for measuring reaeration coefficients of streams was a significant contribution to experimental studies of the oxygen cycle of streams. The development by Swinnerton and Linnenbom (1967) of a gas chromatographic technique for measuring very small quantities of low molecular weight hydrocarbon gases in water samples suggested the possibility of using these gases as a tracer for oxygen.

This report describes modifications of the Swinnerton and Linnenbom (1967) technique together with techniques developed for sample storage and preservation of microgram-per-litre quantities of ethylene and propane in aqueous solution.

ANALYTICAL PROCEDURE

The analytical procedure consists of (1) introducing an aliquot of a water sample into a stripping chamber, (2) stripping the dissolved gases from the water with a stream of helium gas, (3) trapping the gases in a cold trap, (4) desorbing the gases from the trap by warming, and (5) flushing the gases into a gas chromatograph equipped with a flame ionization detector. A single gas, ethylene, was used in most of the initial work; however, in several instances ethylene and propane were used together. Figure 1 is a diagram of the stripping and gas chromatographic system; the steps of the procedure are described in the following paragraphs.

[1] General Electric Co., Bay Saint Louis, Miss.

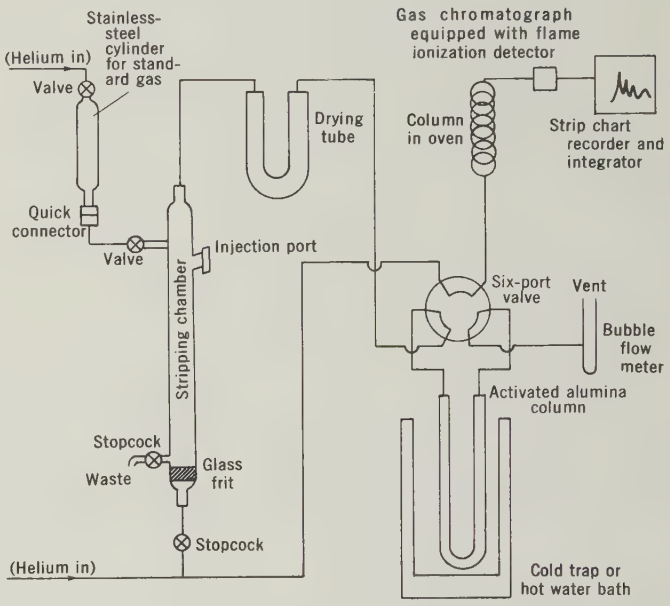

FIGURE 1.—Stripping and gas chromatographic system in the stripping mode.

Introduction of sample into stripping chamber

A sample (30 ml or less) is introduced into the stripping chamber through the Teflon septum of the injection port with a glass syringe. The syringe is filled by pouring the sample into the syringe barrel rather than filling by suction.

Sample stripping

The dissolved hydrocarbon and atmospheric gases are stripped from the sample and flushed into the cold trap by a stream of helium gas flowing through the glass frit in the bottom of the stripping chamber. The stripping time is a function of temperature, sample volume, helium flow rate, and pressure inside the stripper (Kroopnick, 1971). Additional time is necessary for flushing of the stripped gases into the cold trap. For samples of 30 ml or less, a stripping time of 15

min with a helium flow rate of 30 ml/min gives quantitative recovery of the hydrocarbon gases for the stripping chamber used in this work. Figure 1 shows the system in the stripping mode.

Sample trapping

The gases leaving the stripping chamber are dried by flowing through a drying tube filled with anhydrous calcium sulfate (fig. 1). The dry gases then flow into a U-tube cold trap consisting of a 0.3-m (1.0-ft) length of 6.4-mm (0.25-in) OD stainless-steel tubing packed with activated alumina. Liquid nitrogen is used as the refrigerant for the cold trap. At the temperature of liquid nitrogen, any methane present in the water samples will also be trapped. Should the methane concentration greatly exceed that of ethylene, the methane and ethylene peaks may overlap. This has not been a problem thus far in field applications. If samples have interfering methane concentrations, a dry ice and acetone slurry can be substituted for liquid nitrogen. At the temperature of this slurry, the higher boiling point hydrocarbons will be trapped while methane will not.

Trap flushing

After the stripping process is completed, the six-port valve (fig. 1) is switched so that the helium carrier gas for the chromatograph passes through the cold trap. The refrigerant is replaced with a 70°C water bath causing the hydrocarbon gases to vaporize and elute into the gas chromatograph.

Sample analysis

A Varian Aerograph, Moduline Series 2800, gas chromatograph equipped with a flame ionization detector is used.

Separation of the hydrocarbon gases is accomplished with two columns in series. The first, for separation of ethylene and ethane, consists of a 1.2-m (4.0-ft) length of 6.4-mm (0.25-in) OD stainless steel tubing packed with activated alumina coated 10 percent by weight with DC 200 (silicone oil). The second, for separation of the saturated C_2, C_3, and C_4 hydrocarbons, consists of a 3.0-m (10-ft) length of 6.4-mm (0.25-in) OD stainless steel tubing packed with Chromosorb P coated 20 percent by weight with SE–30 (methyl silicone). The oven temperature is maintained at 30°C and the detector temperature at 200°C. The helium carrier-gas flow rate is 70 ml/min, and the hydrogen and air flow rate for the detector are 30 and 300 ml/min, respectively. The signal from the electrometer is recorded on a potentiometric strip chart recorder operated at 1 mV full scale and a chart speed of 5 mm/min. Unless otherwise noted, the peak areas were integrated with a mechanical ball and disk integrator with printout. Figure 2 is a chromatogram of river water containing methane, ethylene, and propane. The methane is natur-

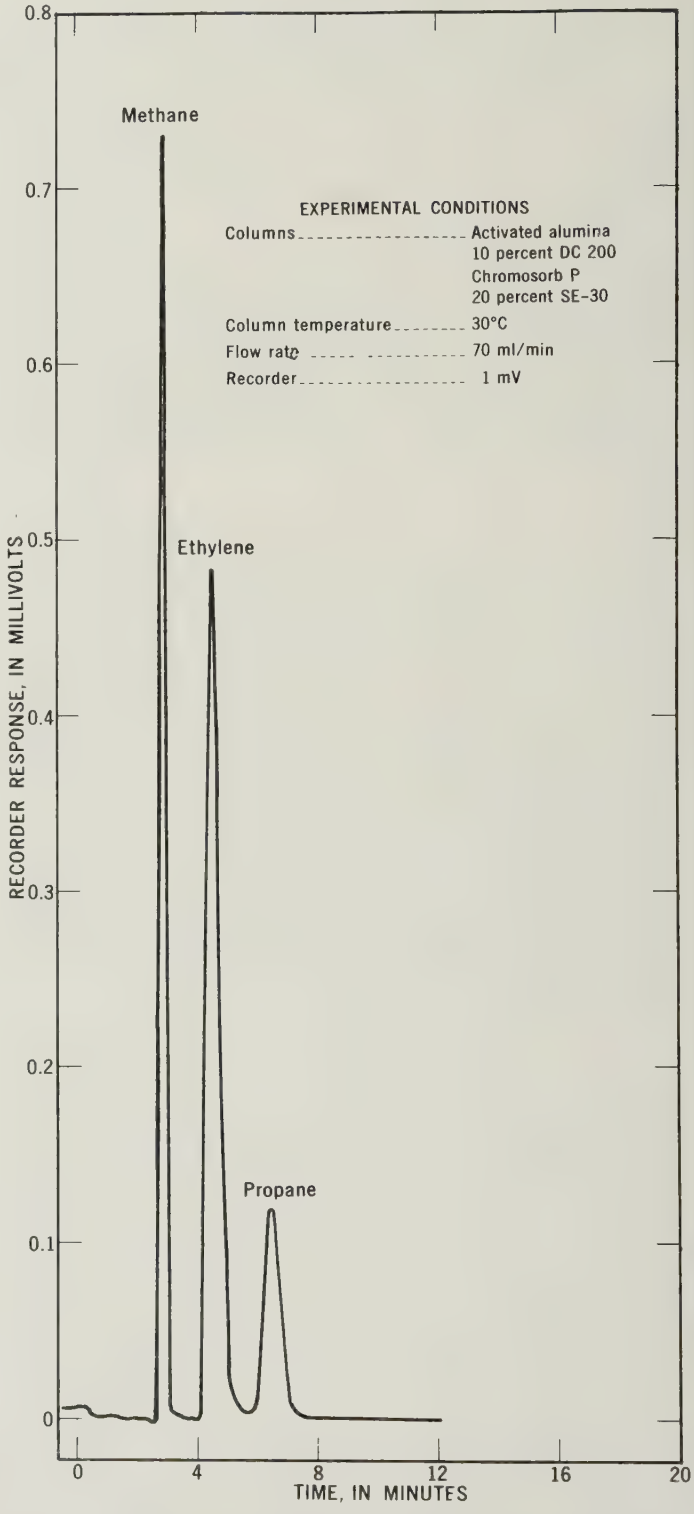

FIGURE 2.—Chromatogram of a river water sample containing naturally occurring methane and artificially added concentrations of ethylene and propane.

ally occurring, the ethylene and propane were added for a field measurement of the reaeration coefficient. Concentrations of the ethylene and propane were 6.17 and 1.58 μg/l, respectively.

A commercial calibration gas mixture certified to contain 11.0 μg/g each of ethylene and propane and 10.5 μg/g of butane in nitrogen is used as an instrument standard. A sample of this gas is analyzed at the beginning and end of each day and whenever operating conditions of the chromatograph are changed. A stainless steel sample cylinder of known volume is filled with a known pressure of the gas standard using the apparatus shown in figure 3. The sample cylinder is placed in the stripping apparatus at the position indicated in figure 1, and the standard gas sample is analyzed by the same procedure described previously for the water samples.

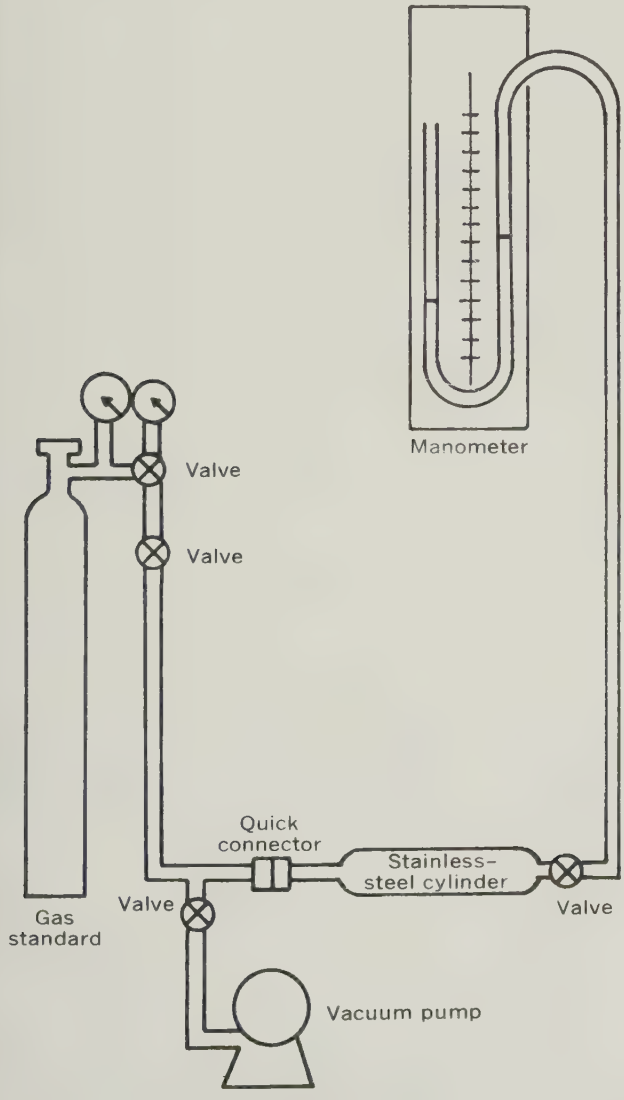

FIGURE 3.—Apparatus for filling the standard gas cylinder.

The weight of each of the three hydrocarbons (ethylene, propane and butane) in the sample of standard gas is calculated from the ideal gas law

$$W = PV_c F/RT, \quad (1)$$

where W is the weight of the particular hydrocarbon, in micrograms,
P is the gas pressure in the cylinder, in atmospheres,
V_c is the volume of the cylinder, in litres,
F is the microgram content of the particular hydrocarbon gas in the gas mixture per gram-mole of nitrogen,
T is the temperature, in kelvins, and
R is the ideal gas law constant, in litre-atmosphere per gram-mole-kelvin

The detector response for a particular hydrocarbon is calculated from

$$S_W = W/A_c, \quad (2)$$

where S_W is the detector response in micrograms per unit area,
W is the weight of hydrocarbon in micrograms, determined from equation 1, and
A_c is the peak area in arbitrary area units.

If an instrument parameter such as electrometer attenuation, electrometer range, recorder chart speed, or recorder sensitivity is changed, then another standard gas sample is analyzed and S_W is recalculated.

Absolute concentrations of dissolved hydrocarbons in a sample may be calculated from

$$H = A_s S_W/V_s, \quad (3)$$

where H is the concentration of the particular hydrocarbon in the sample, in micrograms per litre,
A_s is the peak area of the particular hydrocarbon in the sample, in arbitrary area units,
S_W is the detector response for the particular hydrocarbon, and
V_s is the volume, in litres, of the sample injected for analysis.

SAMPLE CONTAINER

Hydrocarbon losses were found to occur in the presence of substances such as soft rubber and some stopcock greases. This precludes use of many common water-sample containers. At present a 60-ml glass bottle with a ground-glass stopper is being used. There are at least three processes by which losses of dissolved hydrocarbon gases could occur from glass bottles with ground-glass stoppers. First, there could be adsorption

of the hydrocarbons onto the glass surface. There is, however, no evidence in the literature suggesting that this occurs. Second, there could be loss of the hydrocarbons as the result of an unsatisfactory seal around the ground-glass stopper. Third, losses of the hydrocarbons could occur when the stopper is removed for transfer of the sample to the syringe.

Data from two experiments designed to determine if losses of the hydrocarbons occur in the bottles during storage are presented in table 1. In the first set, ethylene and propane were used with distilled water; in the second set, ethylene was used with water from the East Pearl River, Miss. Samples were obtained from a well-mixed reservoir. The bottles were filled to overflowing by a siphon extending to the bottom of the bottles, after which they were stoppered.

TABLE 1.—*Evaluation of the glass bottle as a sample container*

Bottle set	Days elapsed after preparation	Number of replicates	Mean concentration (μg/l)	
			Ethylene	Propane
1a ------	0	2	11.9	14.1
b ------	1	2	11.6	14.2
c ------	8	2	11.9	14.2
2a ------	0	10	9.88	---
b ------	1	10	9.74	---
c ------	6	10	10.4	---

Consideration of results shows that there were no apparent losses of dissolved hydrocarbons in either experiment. This suggests that losses as a result of unsatisfactory seals, desorption during sample transfer, or adsorption on glass surfaces must be small. We concluded, therefore, that the 60-ml bottles with ground-glass stoppers are satisfactory sample containers.

SAMPLE PRESERVATION

The ability to store the samples for several days without loss of the hydrocarbon gases from bacterial degradation is necessary. Formalin (37 percent formaldehyde, 11 percent methanol, in water) and hexachlorophene (6 g/l in 1.1 *M* potassium hydroxide) as well as refrigeration were investigated as a means of preserving the samples. Five sets of six bottles each were filled with river water containing dissolved ethylene and propane, using a siphon as previously discussed. Approximately 90 mg of leaf litter was placed in each bottle of sets 2, 3, 4, and 5 prior to filling. Previous work had shown that losses of ethylene and propane occur during storage in the presence of the leaf litter, apparently because of bacterial activity. One millilitre of formalin was placed in each bottle of set 2, and 2 ml of the hexachlorophene solution was added to each bottle of set 3. Set 4 was refrigerated, and sets 1, 2, 3 and 5 were stored in a constant-temperature water bath at 26°C. Two samples from each set were analyzed the day of preparation, 5 days after preparation, and 7 days after preparation. The results are shown in table 2. The concentrations of the samples containing hexachlorophene and formaldehyde were corrected for dilution. The values shown in table 2 are the mean values of the two replicates analyzed on a specific day.

TABLE 2.—*Evaluation of sample preservatives*

Set	Concentration (μg/l)					
	Day of preparation		5 days after preparation		7 days after preparation	
	Ethylene	Propane	Ethylene	Propane	Ethylene	Propane
1 (water only) ---	11.6	11.2	10.1	10.3	10.5	10.5
2 (formalin) ----	11.2	10.7	11.4	10.8	11.6	10.4
3 (hexachlorophene) -	11.3	10.8	11.0	10.2	11.4	10.3
4 (refrigerated) --	10.9	10.7	8.24	7.6	8.18	9.34
5 (no preservation) --	9.74	10.6	7.84	10.2	11.3	9.60

Both formalin and hexachlorophene were effective in preventing hydrocarbon losses; however, refrigeration was not satisfactory. Set 4 which was refrigerated had comparable variation to set 5 which was not preserved in any way. The concentration of methane increased in the samples of set 5 with increasing time after preparation, suggesting bacterial activity. There was also some methane generation in the refrigerated samples of set 4.

As a result of this preservative study, the procedure of adding 1 ml of formalin to each 60-ml sample was adopted.

PRECISION OF THE PROCEDURE

Precision was determined by replicate analyses of seven different sets of samples of ethylene dissolved in water. The bottles were filled from a well-mixed reservoir by submerging and allowing the water to flow slowly into the bottles. The type water used is noted in column three of table 3. The river water was obtained from the East Pearl River, Miss. Results are presented in table 3.

The coefficient of variation ranges from 1.3 to 6.9 and averages 4.0 percent for the seven sets. These values are indicative of the overall error involved in filling the bottles, injecting the sample into the stripping chamber, stripping the hydrocarbon gases from the sample, integrating the peaks of the output signal, and variations within the instrumental system.

TABLE 3.—*Precision of the analytical procedure*

Sample set	Number of samples	Type of water	Coefficient of variation (percent)
1	3	Distilled	3.1
2	3	----do	6.8
3	3	----do	1.3
4	4	Tap	6.9
5	10	River	2.9
6	10	----do	4.0
7	10	----do	3.3

MODIFICATION OF THE PROCEDURE

Modifications were made to the procedure and the apparatus shown in figure 1 to reduce the time required for sample analysis. These modifications consist of replacing the six-port valve with an eight-port valve and replacing the mechanical ball and disk integrator with a digital integrator. The eight-port valve allows the use of two cold traps so that a second sample can be stripped while the first sample elutes through the gas chromatograph. This increases the number of samples that can be analyzed in 1 day by about 40 percent.

The digital integrator is more precise than the mechanical ball and disk integrator and requires no operator attendance during analysis. In addition, a sample peak that exceeds the recorder scale is still accurately integrated. This is especially important for field samples where the concentration is unknown, and only one analysis can be made per sample bottle.

Table 4 shows the results of replicate analyses made on 17 samples with the modified procedure. The samples were siphoned from a well-mixed reservoir containing ethylene and propane in distilled water. Comparison of the results for the two traps shows that there is no significant difference between the two sets of data at the 95 percent confidence level. Combining the two sets of data gives an overall coefficient of variation of 1.8 percent for ethylene and 2.0 percent for propane.

TABLE 4.—*Evaluation of the two-trap modification*
[Concentrations are in micrograms per litre]

Trap A		*Trap B*	
Ethylene	*Propane*	*Ethylene*	*Propane*
8.49	9.05	8.51	9.26
8.49	8.96	8.18	9.06
8.43	8.90	8.66	9.26
8.44	9.14	8.67	9.12
8.48	9.22	8.37	8.94
8.41	8.69	8.41	8.94
8.34	8.71	8.82	9.31
8.58	9.00		
8.37	8.88		
8.41	9.03		

CONCLUSIONS

A gas chromatograph with a flame ionization detector, in conjunction with a stripping chamber–cold trap arrangement, was used to measure microgram-per-litre quantities of low molecular weight hydrocarbon gases in aqueous solution. The coefficient of variation averaged 4.0 percent for replicate analysis of seven sets of samples containing concentrations of ethylene in the microgram-per-litre range. Modifications to the system designed to reduce the time required for sample analysis gave a coefficient of variation of 1.8 percent for ethylene and 2.0 percent for propane for one set of samples.

A glass bottle with a ground-glass stopper was used as a sample container. Samples can be stored for at least 6 days with no measurable loss of the hydrocarbon gases due to the sample container. Samples containing 1 ml of formalin and leaf litter showed no measurable loss of dissolved ethylene and propane within experimental error over a 7-day period, whereas control samples showed losses.

REFERENCES CITED

Kroopnick, P. M., 1971, Oxygen and carbon in the oceans and atmosphere—stable isotopes as tracers for consumption, production, and circulation models: San Diego, California Univ., Scripps Inst. of Oceanography, Ph. D. dissert., 241 p.

Swinnerton, J. W., and Linnenbom, V. J., 1967, Determination of the C_1 to C_4 hydrocarbons in sea water by gas chromatography: Jour. Gas Chromatography, v. 5, p. 570–573.

Tsivoglou, E. C., O'Connell, R. L., Walter, C. M., Godsil, P. J., and Logsdon, G. S., 1965, Laboratory studies, part I of tracer measurements of atmospheric reaeration: Water Pollution Control Federation Jour., v. 37, no. 10, p. 1343–1362.

Tsivoglou, E. C., Cohen, J. B., Shearer, S. D., and Godsil, P. J., 1968, Field studies, part II of tracer measurement of stream reaeration: Water Pollution Control Federation Jour., v. 40, no. 2, pt. 1, p. 285–305.

*U.S. GOVERNMENT PRINTING OFFICE: 1976 211-295/4 1-3

RECENT PUBLICATIONS OF THE U.S. GEOLOGICAL SURVEY

(The following books may be ordered from the Branch of Distribution, U.S. Geological Survey, 1200 South Eads Street, Arlington, VA 22202 (an authorized agent of the Superintendent of Documents, Government Printing Office). Prepayment is required. Remittances should be sent by check or money order payable to U.S. Geological Survey. Give series designation and number, such as Bulletin 1368–A, and the full title. Prices of Government publications are subject to change. Increases in costs make it necessary for the Superintendent of Documents to increase the selling prices of many publications offered. As it is not feasible for the Superintendent of Documents to correct the prices manually in all the previous announcements and publications stocked, the prices charged on your order may differ from the prices printed in the announcements and publications)

Professional Papers

433–P. Discharge and flow distribution, Columbia River estuary, by G. A. Lutz, D. W. Hubbell, and H. H. Stevens, Jr. 1975. p. P1–P31. $1.15.

437–D. Land subsidence due to ground-water withdrawal, Arvin-Maricopa area, California, by B. E. Lofgren. 1975. p. D1–D55; plates in pocket. $3.55.

560–I. Geology of the Arabian Peninsula—Jordan, by Friedrich Bender. 1975. p. I1–I36; plates in pocket. $1.25.

574–F. Background geochemistry of some rocks, soils, plants, and vegetables in the conterminous United States, by J. J. Connor and H. T. Shacklette, *with sections on* Field studies, by R. J. Ebens, J. A. Erdman, A. T. Miesch, R. R. Tidball, and H. A. Tourtelot. 1975. p. F1–F168. $3.30.

712–C. Hydrogeologic and hydrochemical framework, south-central Great Basin, Nevada-California, with special reference to the Nevada test site, by I. J. Winograd and William Thordarson. 1975. p. C1–C126; plates in pocket. $5.75.

769. Bedrock geology and ore deposits of the Palmer quadrangle, Marquette County, Mich., by J. E. Gair; *with a section on* The Empire Mine, by Tsu-Ming Han. 1975. 159 p.; plates in pocket. $7.50.

792. Reconnaissance geology of Chichagof, Baranof, and Kruzof Islands, southeastern Alaska, by R. A. Loney, D. A. Brew, L. J. P. Muffler, and J. S. Pomeroy. 1975. 105 p.; plates in pocket. $5.

818–B. Mineralization halos and diagenesis in water-laid tuff of the Thomas Range, Utah, by D. A. Lindsey. 1975. p. B1–B19. $1.90.

851. Soil slips, debris flows, and rainstorms in the Santa Monica Mountains and vicinity, southern California, by R. H. Campbell. 1975. 51 p. $1.70.

857. Diagenesis and stratigraphy of the Lisburne Group limestones of the Sadlerochit Mountains and adjacent areas, northeastern Alaska, by G. V. Wood and A. K. Armstrong. 47 p.; 12 plates showing fossils. $2.25.

870–A. The channels and waters of the Upper Salmon River area, Idaho, by W. W. Emmett. 1975. p. A1–A116. $3.05.

873. Cambrian and Ordovician rocks of southern Arizona and New Mexico and westernmost Texas, by P. T. Hayes, assisted by G. C. Cone. 1975. 98 p.; plate in pocket. $3.75.

901. Explanatory text to accompany the geologic map of the United States, by P. B. King and H. M. Beikman. 1974. 40 p. $1.25.

907–A, B. A, Grade and tonnage relationships among copper deposits, by D. A. Singer, D. P. Cox, and L. J. Drew. p. A1–A11; *and* B, Geochemical exploration techniques applicable in the search for copper deposits, by M. A. Chaffee. 1975. B1–B26. $1.60.

914. Geologic considerations for redevelopment planning of Managua, Nicaragua, following the 1972 earthquake, by H. R. Schmoll, R. D. Krushensky, and Ernest Dobrovolny. 1975. 23 p. 90¢.

917. A numerical model of material transport in salt-wedge estuaries—Part 1, Description of the model, by H. B. Fischer—Part 2, Model computation of salinity and salt-wedge dissolved oxygen in the Duwamish River estuary, King County, Wash., by J. D. Stoner, W. L. Haushild, and J. B. McConnell. 1975. 36 p. $1.25.

924. Hurricane Agnes rainfall and floods, June–July 1972, by J. F. Bailey, J. L. Patterson, and J. L. H. Paulhus. 1975. 403 p. $9.10.

926–A. Geology and resources of base-metal vanadate deposits, by R. P. Fischer. 1975. p. A1–A14. 75¢.

926–B. Vanadium resources in titaniferous magnetite deposits, by R. P. Fischer. 1975. p. B1–B10. 70¢.

966. The Geologic Retrieval and Synopsis Program (GRASP), by R. W. Bowen and J. M. Botbol. 1975. 87 p. $2.05.

Bulletins

1389. Stratigraphic and structural relationships of the Brimfield Group in northeast-central Connecticut and adjacent Massachusetts, by J. D. Peper, M. H. Pease, Jr., and V. M. Seiders. 1975. 31 p. 70¢.

1397–A. Mineral resources of the Teton Corridor, Teton County, Wyo., by J. D. Love, J. C. Antweiler, and F. E. Williams. 1975. p. A1–A51; plate in pocket. $2.20.

1405–A. Changes in stratigraphic nomenclature by the U.S. Geological Survey, 1974, by G. V. Cohee and W. B. Wright. 1975. p. A1–A36. 70¢.

1405–E. McGowan Creek Formation, new name for Lower Mississippian flysch sequence in east-central Idaho, by C. A. Sandberg. 1975. p. E1–E11. 40¢.

1411. Latin America's Petroleum prospects in the energy crisis, by B. F. Grossling. 1975. 40 p. 70¢.

1412. Coal resources of the United States, January 1, 1974, by Paul Averitt. 1975. 131 p. $1.60.

Water-Supply Papers

1827–G. Effects of organic solutes on chemical reactions of aluminum, by C. J. Lind and J. D. Hem. 1975. p. G1–G83. $1.35.

2030. Summary of floods in the United States during 1969, by J. K. Reid and others. 1975. 173 p. $1.90.

2153. Quality of surface waters of the United States, 1970, Part 3. Ohio River basin. 1975. 444 p. $3.90.

U.S. GOVERNMENT
PRINTING OFFICE
PUBLIC DOCUMENTS DEPARTMENT
WASHINGTON, D.C. 20402

OFFICIAL BUSINESS
PENALTY FOR PRIVATE USE $300

POSTAGE AND FEES PAID
U.S. GOVERNMENT
PRINTING OFFICE
375

U.S.MAIL

Special
fourth-class
rate books